Quantum coherence in the integer quantum Hall regime

Preden Roulleau

HAL Id: tel-00348151

https://tel.archives-ouvertes.fr/tel-00348151v2

Submitted on 3 Jan 2010

Université Pierre et Marie Curie - Paris 6

THESE

présentée le 19 novembre 2008 pour l'obtention du

Doctorat de l'Université Pierre et Marie Curie - Paris 6
Spécialité Physique Quantique

par

Preden ROULLEAU

Etude de la cohérence quantique dans le régime d'effet Hall quantique entier

Composition du jury

Rapporteurs :	Markus Buttiker
	Marc Sanquer
Examinateurs :	Moty Heiblum
	Klaus Ensslin
	Benoît Doucot
Directeurs de thèse :	D. Christian Glattli
	Patrice Roche

CEA-Saclay DSM / DRECAM / SPEC - 91191 Gif Sur Yvette Cedex

Table des matières

Chapitre 1

Remerciements

Ces trois années de thèse à Saclay ont été pour moi trois belles années. J'y ai découvert le métier de chercheur avec ses moments de doutes quand " tout fout le camp ", et ses moments " magiques " lorsque la nature révèle enfin ses secrets.

Cette aventure n'aurait pas été possible sans la direction de Patrice Roche. Patrice m'a d'abord enseigné la rigueur scientifique. Il a toujours pris soin de m'expliquer la physique mésoscopique dans ses moindres détails, et nos discussions ont été d'une grande richesse scientifique. Il a aussi été un encadrant exceptionnel qui m'a toujours soutenu dans les périodes les plus dures, qui a corrigé avec tact mes principaux défauts tout en valorisant mes qualités.

J'ai découvert la physique mésoscopique grâce à Christian Glattli. C'est lui qui a jeté les bases de ce qui deviendra pour moi une révélation. Christian a toujours été à mon écoute pendant ses trois années et j'ai pu bénéficier de sa connaissance profonde de la physique mésosopique.

Fabien Portier et Xavier Waintal ont été d'un grand soutien pendant cette thèse. Fabien déborde d'idées et nos échanges scientifiques ont été extrêmement fructueux. Xavier, même s'il n'a pas directement été impliqué dans l'expérience m'a éclairé sur les subtilités du " champ " scientifique. Xavier a aussi été un partenaire de randori exceptionnel quasi quotidien (en général après la pause déjeuner, conférences inclues).

Toutes ces expériences réalisées sur le Mach Zehnder n'auraient pas été possibles sans les " golden hands " du LPN : Dominique Mailly et GianCarlo Faini. La difficulté de ces expériences reposait en grande partie sur l'extrême complexité de l'échantillon : j'ai pu bénéficier pendant ma thèse d'une série d'échantillons exceptionnelle. Dominique Mailly et GianCarlo Faini ont toujours apporté un angle nouveau à nos mesures, et notre partenariat fut d'une grande richesse scientifique. Enfin j'aimerais remercier Ulf Gennser pour nous avoir fourni le gaz 2D et pour son aide lors de la relecture des articles.

J'ai eu l'honneur d'avoir dans mon jury de thèse des grands noms de la physique mésoscopique. J'ai été très honoré de la présence de Moty Heiblum et j'aimerais le remercier d'avoir fait le déplacement depuis Israel. Moty Heiblum a ce génie de pouvoir dévoiler la beauté de la physique mésoscopique dans ce qu'elle a de plus simple. J'aimerais également remercier Markus Buttiker et Marc Sanquer tous deux rapporteurs de ma thèse, pour la

Chapitre 2

Résumé de la thèse

Contents

2.1 Introduction

FIGURE 2.1 – Représentation schématique du double MZI proposée par Samuelsson *et al.* [74]. Les électrons sont injectés au niveau des contacts 2 et 3, A, B, C et D étant des lames séparatrices. La mesure de corrélation électronique croisée est effectuée entre les contacts 5 et 8. ϕ est la phase accumulée le long de chaque trajectoire électronique. Par exemple ϕ_1 est la phase accumulée le long des bords entre les lames séparatrices C et A. La mesure de bruit en corrélation croisée entre les contacts 5 et 8 est sensible à la phase Aharonov-Bohm à deux électrons : $\phi = \phi_1 + \phi_2 - \phi_3 - \phi_4$

L'objectif de cette thèse est d'observer la violation des inégalités de Bell pour un conducteur mésoscopique. Le principe général s'inspire de l'expérience réalisée en 1982 par Aspect *et al* [9]. Cette expérience a été proposée pour la première fois en 2004 par Samuelsson *et al* [74][60]. Nous avons représenté figure 1 le schéma de cette expérience appelé double interféromètre de Mach Zehnder (MZI). Contrairement à l'expérience d'Aspect *et al.* deux sources électroniques distinctes sont utilisées (numérotées 2 et 3 sur la figure 2.1). Considérons dans un premier temps l'onde électronique émise par le réservoir 2. Elle sera soit transmise soit réfléchie par la première lame séparatrice C. Si elle est transmise, elle accumulera la phase ϕ_1 jusqu'à la prochaine lame séparatrice notée A. Si elle est réfléchie, elle accumulera la phase ϕ_3 jusqu'à la prochaine lame séparatrice notée B. Considérons maintenant l'onde électronique émise par le réservoir 3. Elle sera soit transmise soit réfléchie par la première lame séparatrice D. Si elle est transmise, elle accumulera la phase ϕ_2 jusqu'à la prochaine lame séparatrice notée A. Si elle est réfléchie, elle accumulera la phase ϕ_4 jusqu'à la prochaine lame séparatrice notée B. On effectue ensuite une mesure de corrélation électronique entre les contacts 5 et 8. La mesure sur le contact 5 ne permet pas de différencier l'électron émis par le réservoir 2 de l'électron émis par le réservoir 3. On peut donc montrer que la mesure de corrélation électronique va "sélectionner" la partie intriquée de l'état à deux électrons. Cette mesure de la partie intriquée de l'état à deux électrons est sensible à la différence de phase : $\phi_1+\phi_2-\phi_3-\phi_4$. Lorsque l'aire définie par ce chemin électronique est soumise à un champs magnétique perpendiculaire, on peut faire varier cette différence de phase via le champ magnétique appliqué. La partie intriquée sera révélée par des oscillations Aharonov Bohm dans une mesure à deux électrons, le bruit. Une fois ces oscillations observées, il s'agit de régler les différentes lames séparatrices afin d'obtenir l'état maximalement intriqué, pour finalement procéder à la violation des inégalités de Bell.
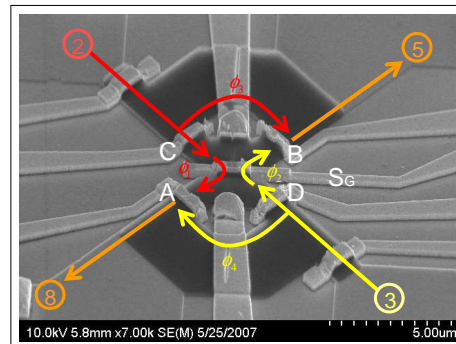
FIGURE 2.2 – Les notations sont similaires à la figure 1. On note cependant ici la présence d'une lame séparatrice centrale (notée S_G) qui, lorsqu'elle est fermée, sépare le double MZI en deux simples MZI, de façon a optimiser les réglages (étant convenu qu'il est plus facile d'obtenir des oscillations Aharonov Bohm à un électron qu'à deux électrons). Une fois cette la lame séparatrice ouverte, on retrouve la configuration double MZI.

Expérimentalement nous n'appliquerons pas directement la géométrie proposée par Samuelsson *et al.*. On peut montrer[60] que le double MZI peut être décomposé en deux MZI simples séparés d'une lame séparatrice. Un réglage optimal du simple MZI [37] permet

d'observer des oscillations Aharonov Bohm à un électron. Une fois que les deux simples MZI sont réglés afin d'obtenir la visibilité maximale, on ouvre le lame sépatrice centrale pour se retrouver dans la configuration double MZI. Nous allons discuter maintenant des outils mésoscopiques nécessaires à l'élaboration d'un MZI électronique.

2.2   Montage expérimental

Pour construire un MZI en physique mésoscopique nous avons besoin de deux éléments : d'un faisceau d'électrons et de lames séparatrices. Pour obtenir un faisceau électronique nous travaillerons en régime Hall quantique, dans un gaz bidimensionnel(AsGa/GaAlAs). Nous savons en effet qu'en régime Hall quantique le transport électronique a lieu dans des canaux de bord que l'on peut se représenter comme des conducteurs 1D chiraux. En effet les électrons soumis à un champs magnétique perpendiculaire ont une trajectoire cyclotron. Si loin des bords la vitesse moyenne des électrons est nulle, au bord de l'échantillon , les électrons seront soumis au potentiel de bord. La représentation semi classique que l'on peut se faire de ce phénomène est montrée figure 2.3.
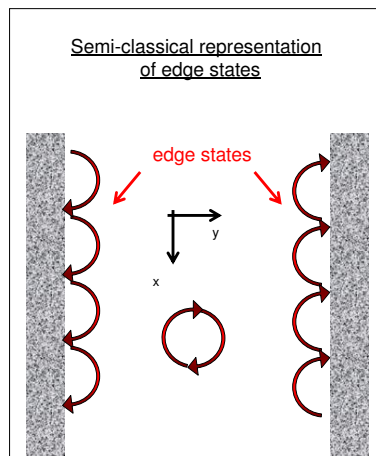
FIGURE 2.3 – Représentation semi classique des canaux de bord en régime Hall quantique. La trajectoire des électrons dans le bulk peut être décrite par une trajectoire cyclotron. Le long des bords de l'échantillon, le centre de l'orbite cyclotron dérive.

Le long des bords les électrons rebondissent et le centre de l'orbite cyclotron dérive : en moyenne la vitesse de dérive des électrons le long des bords n'est pas nulle. Si l'on considère maintenant l'hamiltonien de l'électron dans un gaz 2D soumis à un champ magnétique perpendiculaire, on peut montrer que les niveaux d'énergie sont discrets (niveaux de Landau). Lorsque l'on se rapproche des bords de l'échantillon, les niveaux de Landau vont être déformés par le potentiel de confinement. Le transport électronique aura lieu au croisement entre ces niveaux de Landau courbés et l'énergie de Fermi. Le nombre de canaux de bord est égal au nombre de croisements entre niveaux de Landau et énergie de Fermi. Nos résultats ont été obtenus à facteur de remplissage 2 (ν=2) : deux niveaux d'énergie

croisent le niveau de Fermi, on travaille avec deux canaux de bord. Pour ce qui est des lames séparatrices électroniques, les contact ponctuels quantiques (CPQ) sont parfaitement adaptés. Nous avons représenté figure 2.4(a) une vue SEM d'un CPQ.
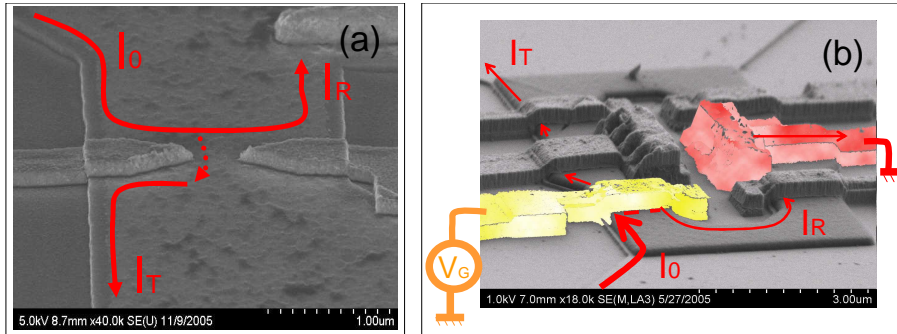
FIGURE 2.4 – (a) Vue SEM d'un CPQ. Une partie de l'onde électronique est réfléchie (transmise) notée I_R (notée I_T). (b) Vue SEM d'un CPQ dans la partie centrale du MZI. En jaune nous avons représenté le pont qui connectent les deux grilles du CPQ, en rouge un contact ohmique connecté à la masse. Dans cette représentation, une partie de l'onde électronique est transmise vers le deuxième CPQ. La partie réfléchie pourra être collectée par le contact à la masse.

Figure 2.4(b) ce même CPQ mais intégré dans le MZI : en jaune un pont qui permet de connecter les deux grilles du CPQ. En appliquant une tension négative sur le CPQ, on dépléte localement sous le CPQ et on augmente le couplage entre canaux contre propageants. On peut ainsi contrôler de manière très précise la probabilité de transmission ou de réflexion d'une onde électronique. Nous avons désormais tous les outils pour comprendre le principe général du MZI. Nous en avons représenté une vue SEM figure 2.5.
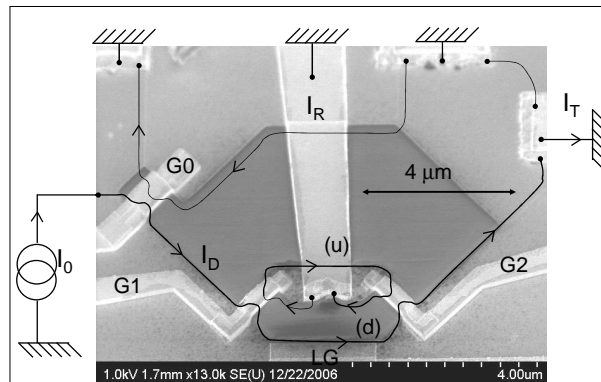
FIGURE 2.5 – Vue SEM du MZI électronique. G0, G1 et G2 sont des CPQ qui servent de lames sépratrices. G0 permet une dilution du courant injecté, G1 et G2 sont les deux lames séparatrices de l'interféromètre. LG est une grille latérale qui permet la variation de l'aire de la surface définie par (u) and (d). Le petit contact ohmique central entre les deux bras du MZI permet de collecter le courant rétrodiffusé à la masse grâce à un long pont en or.

$G1$ et $G2$ sont les deux lames séparatrices de l'interféromètre. Lorsqu'il est réléchi (transmis) par $G1$ l'électron passe par le chemin (u) (resp. (d)) pour ensuite être recombiné

en $G2$. Si on considère maintenant l'approche à une particule du formalisme Landauer-Buttiker, l'amplitude de transmission t à travers le MZI est la somme de deux amplitudes de transmission correspondant aux chemins (u) et (d). Pour des amplitudes de transmission et de réflexion t_i et r_i du $i$ème CPQ (avec $|r_i|^2 + |t_i|^2 = 1$), l'amplitude de transmission est donnée par :

$$t = t_1 e^{i\phi_d} t_2 - r_1 e^{i\phi_u} r_2.$$

où ϕ_u (ϕ_d) est la phase accumulée le long du chemin supérieur (inférieur) . On obtient la probabilité de transmission :

$$T = T_1 T_2 + R_1 R_2 + \sqrt{T_1 T_2 R_1 R_2} sin\varphi(\epsilon) \tag{2.1}$$

où $\varphi(\epsilon) = \phi_u - \phi_d$ et $T_i = | t_i |^2 = 1 - R_i$. $\varphi(\epsilon)$ est le flux du champs magnétique à travers l'aire définie par les deux trajectoires à l'énergie ϵ. On dispose donc de deux manières pour observer les franges d'oscillations : soit en faisant varier le champs magnétique soit en faisant varier l'aire définie par les deux trajectoires grâce à la grille latérale (notée LG sur la figure 2.5).

2.3 Visibilité à tension finie

La mesure de bruit en corrélation croisée, pour sélectionner la partie intriquée de l'état à deux électrons, se fait à tension finie. Avant de réaliser cette mesure, il s'agit donc de comprendre la visibilité [1] de la conductance à tension finie. La visibilité n'est pas censée dépendre de la tension drain-source appliquée, mais la première expérience [37] a montré une décroissance monotone de la visibilité avec la tension appliquée. Cette première expérience réalisée à facteur de remplissage 2 (deux canaux de bords) ne permettait pas de séparer les deux canaux de bords envoyés sur le MZI. Plus récemment, le groupe du Weizmann a ajouté un CPQ (noté G0 sur la figure 2.5) qui permettait de séparer les deux canaux de bord et de n'envoyer qu'un seul canal à la tension V_{ds} sur le MZI. Cette modification a entraîné l'apparition d'un comportement assez spectaculaire de la visibilité avec la tension : une structure en lobes. Nos premières mesures réalisées sur un échantillon de taille moyenne (aire de $14\mu m^2$) et instable n'ont révélées qu'un seul lobe. Nous avons montré que l'on pouvait très bien ajuster cette structure en lobe en supposant une enveloppe Gaussienne de la conductance (voir figure 2.6(a)).

Plus récemment nous avons réalisé les mêmes mesures sur un échantillon de grande taille stable (aire de $35\mu m^2$) et à faible champ (mais toujours à facteur de remplissage 2) et nous avons obtenu une structure avec plusieurs lobes. L'ajout d'un terme cosinus donne l'enveloppe du cas mutli-lobes, mais demeure à ce jour inexpliqué (voir figure 2.6(b)). Cette approche heuristique nous a permis de comprendre le couplage entre deux canaux de bord. De récents travaux sur la dépendance de la visibilité en fonction de la transmission du premier beam splitter (G1) en l'absence de grille (G0) [15] ont montré une augmentation

---

1. La visibilité est définie par $\frac{T_{max} - T_{min}}{T_{max} + T_{min}}$
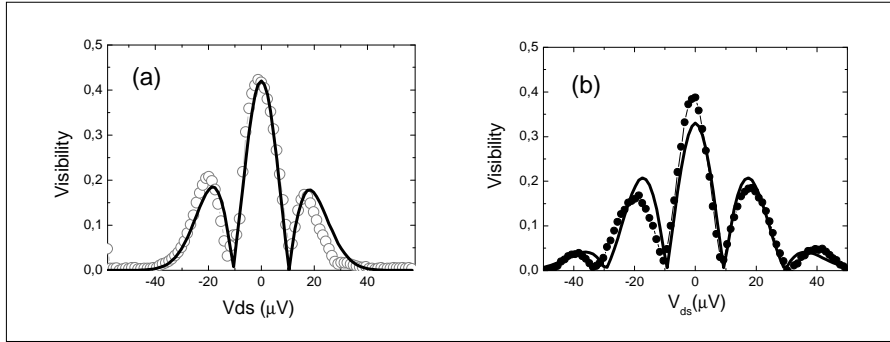
FIGURE 2.6 – (a) Les cercles noirs représentent la visibilité du canal interférant. La courbe noire représente notre formule qui suppose une enveloppe Gaussienne de la conductance.(b)Les points noirs représentent la visibilité du canal interférant. La courbe noire représente notre formule qui suppose une enveloppe Gaussienne de la conductance multipliée d'un terme cosinus à ce jour inexpliqué.

inattendue de la visibilité autour de la valeur V_{ds}=0 pour certaines valeurs de T_1 (transmission de G_1). Nous avons montré que ce comportement pouvait être compris en considérant le couplage entre le canal interférant et le canal voisin. Les fits en excellent accord avec l'expérience (voir figure 2.7) nous ont permis de dégager une énergie caractéristique qui augmente avec T_1.
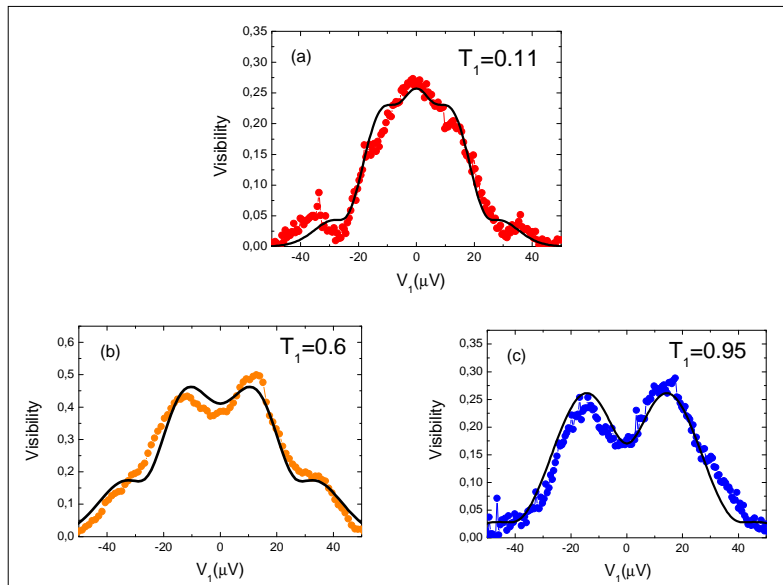
FIGURE 2.7 – Les points représentent les visibilités en fonction de V_1 pour différentes valeurs de la transmission T_1 lorsque la première grille $G0$ est ouverte. On observe également une augmentation de la visibilité autour de $V_1 = 0V$ pour T_1 proche de 1. Les courbes sont les fits en considérant le couplage entre canaux de bord. Ces fits nous permettent d'extraire une énergie caractéristique qui augmente avec T_1.

Ce résultat est très différent de ce qui a pu être observé lorsque les deux canaux de

bord sont séparés (le canal interne est réfléchi par $G0$). On peut montrer dans ce cas que cette énergie caractéristique ne dépend que très peu de T_1.

2.4 Longueur de cohérence phase à facteur de remplissage 2 ($\nu = 2$)

L'expérience sur le double MZI nécessite de savoir si la longueur de cohérence de phase électronique est plus grande que le chemin à deux particules parcouru dans le MZI. La longueur de cohérence de phase électronique est la longueur caractéristique pour laquelle l'électron conserve sa cohérence de phase. Si des expériences se sont intéressées à cette longueur de cohérence [35], aucune n'a déterminé la valeur exacte de l_φ à $\nu = 2$. Pour extraire cette longueur de cohérence, nous avons mesuré la visibilité des oscillations en fonction de la température. Deux conditions sont nécessaires pour déterminer l_φ. La première est de pouvoir varier la taille de l'interféromètre : l'équipe du LPN (Dominique Mailly et Giancarlo Faini, ainsi que Ulf Gennser pour les couches 2D) a donc fabriquer des échantillons de 3 tailles différentes, avec à chaque fois un rapport d'échelle dans les tailles. Dans un deuxième temps, il s'agit de s'assurer que la baisse de la visibilité en fonction de la température n'est pas causée par le "thermal smearing". Le "thermal smearing" est dû aux fluctuations des trajectoires électroniques avec la température : si la différence entre les trajectoires électroniques supérieure et inférieure n'est pas nulle, on peut être sensible au "thermal smearing". Nous avons montré par des arguments de rigidité de phase sur une large gamme d'énergie, que l'on pouvait exclure tout "thermal smearing". La figure 2.8 montre la visibilité en échelle logarithmique en fonction de la température pour un échantillon de petite, moyenne et grande taille.

On observe une dépendance exponentielle de la visibilité en fonction de la température, avec une dépendance en champ magnétique qui est la même pour chaque échantillon, ce qui nous permet d'écrire :
$$\nu = \nu_0 e^{-2L/l_\varphi}$$

avec
$$l_\varphi \propto T^{-1}$$

On trouve $l_\varphi \sim 20\mu m$ à 20 mK. Se posent alors deux questions : pourquoi a-t-on une longueur de cohérence finie, et d'où vient cette dépendance en champ magnétique ?

2.5 Origine de la longueur de cohérence de phase finie

Pourquoi a-t-on une longueur de cohérence finie, et d'où vient cette dépandance en champ magnétique ? Dans notre cas, puisque l'on travaille avec deux canaux de bord, le canal interférant est fortement couplé au canal adjacent. Nous avons étudié de manière systématique ce couplage entre canaux. Pour ce faire, nous avons polarisé le canal adjacent, afin de l'utiliser comme une véritable grille latérale. Nous avons représenté figure 2.9(a) la
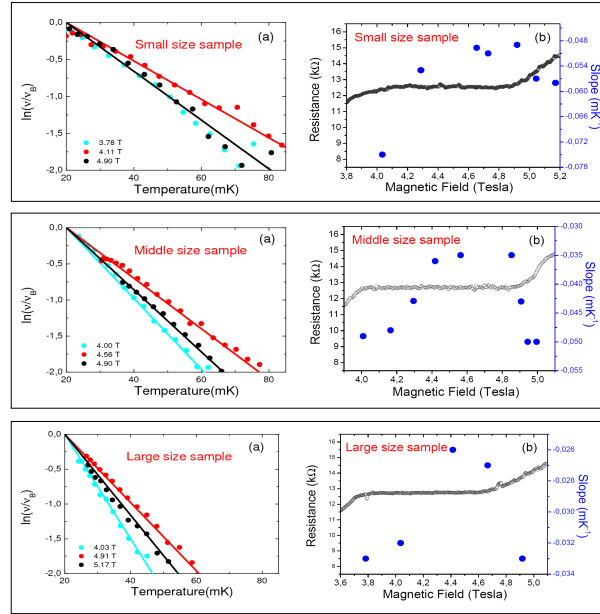
FIGURE 2.8 – (a) $\ln(\nu/\nu_B)/(T - T_B)$. en fonction de la température pour trois champs magnétiques différents, pour les échantillons de taille petite, moyenne et grande. On note ν la visibilité, et ν_B la visibilité à la température minimale T_B.(b) Dépendance de $\ln(\nu/\nu_B)/(T - T_B)$ avec le champ magnétique.

conductance différentielle en fonction de la tension V_2 appliquée sur le canal adjacent : on observe des oscillations Aharonov Bohm.

La tension nécessaire pour ajouter une phase de 2π est appelé paramètre de couplage V_0 : nous avons mesuré ce paramètre de couplage sur tout le plateau $\nu = 2$. Ce que nous voulons montrer maintenant, c'est que les fluctuations thermiques du canal adjacent sont responsables de la longueur de cohérence finie. En considérant V_0 le couplage entre canaux et $4k_B T R_Q$ le bruit Johnson Nyquist du canal adjacent, on montre que l'on peut écrire la visibilité :

$$\nu = \nu_0 e^{-T/T_\varphi},$$

avec :

$$T_\varphi^{-1} = \frac{2 \times 8\pi^2 k_B R_Q}{V_0^2 \Delta\nu}, \tag{2.2}$$

où $\Delta\nu$ est la bande passante, seul paramètre inconnu du problème. Pour extraire cette bande passante, nous avons procédé à une deuxième expérience. Nous avons partitionné le canal adjacent, tout en lui appliquant une tension de bias V_2. Nous avons étudié la visibilité du canal interférant en fonction du bruit de partition généré par le canal adjacent. On montre cette fois que la visibilité peut s'écrire :

$$\nu = \nu_0 e^{-T_0(1-T_0)(V_2-2k_B T/e)/V_\varphi}, \tag{2.3}$$

avec

$$V_\varphi^{-1} = \frac{4\pi^2 e R_Q}{V_0^2} \Delta\nu,$$
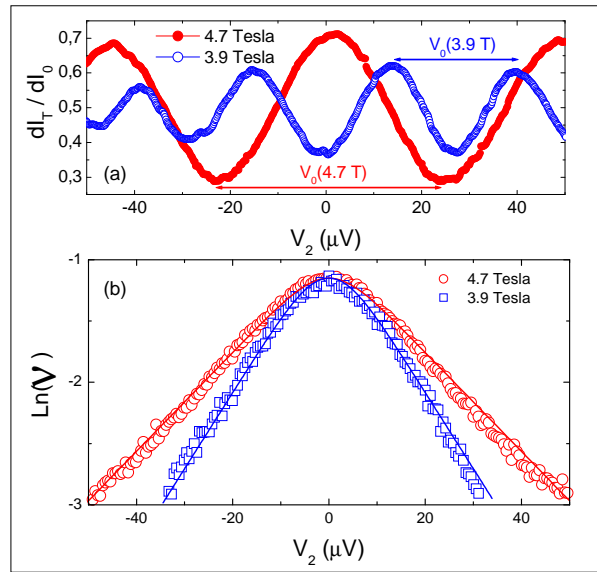
FIGURE 2.9 – **a) :**Balayage en phase en variant V_2 avec $T_0 = 1$ pour deux champs magnétiques différents à 3.9T et 4.7T. La périodicité V_0 dépend du champ magnétique. **b) :** Diminution de la visibilité en fonction de V_2 à $T_0 = 1/2$ pour deux champs magnétiques différents 3.9T et 4.7T. Les lignes en trait plein sont des fits aux données expérimentales $V = V_0 e^{-2\pi^2 \Delta S_{22} \Delta \nu / V_0^2}$ avec une température électronique de 25mK (pour une température de frigo égale à 20mK) et $T_0 = 1/2$. A fort tension drain source le fit $\nu = \nu_0 \exp(-T_0(1 - T_0)V_2/V_\varphi)$ nous permet de déterminer V_φ pour différents champs magnétiques.

où T_0 est la transmission du canal adjacent, $\Delta \nu$ la même bande passante et V_φ un paramète de déphasage. Nous avons représenté figure 2.9(b), le logarithme de la visibilité en fonction de V_2 à T_0 fixé à 1/2, et figure 2.10 le logarithme de la visibilité en fonction de T_0 pour différents V_2.
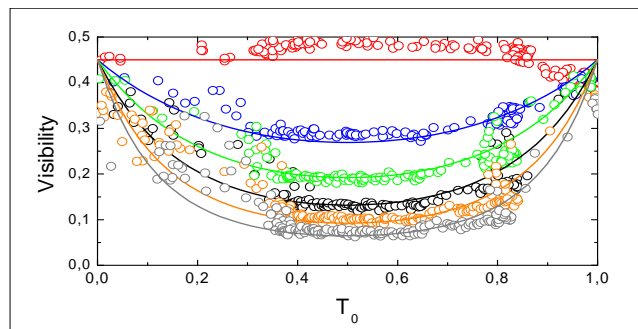
FIGURE 2.10 – (couleur sur la figure)Dépendance de la visibilité en fonction de T_0 pour V_2=0, 21, 31, 42, 53 et 63 μV de haut en bas. Les lignes en trait plein sont les fits aux données expérimentales en utilisant l'équation 2.3 avec $V_\varphi = 7.2\mu V$ et T=25mK.

L'excellent accord avec la formule 2.3 confirme notre approche (approximation Gaussienne du problème). Cette expérience nous permet d'extraire V_φ sur tout le plateau $\nu = 2$. Puisque l'on connaît V_0, nous sommes capables d'extraire de V_φ la bande passante, tous
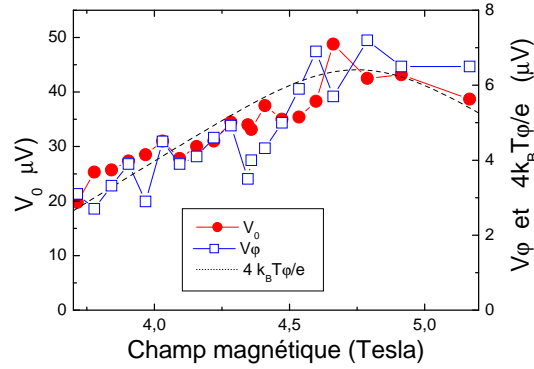
FIGURE 2.11 – (couleur sur la figure) V_0 et V_φ en fonction du champ magnétique. La courbe en pointillée est le comportement général de $4k_B T_\varphi/e$ (échelle à droite) mesuré sur le même échantillon.

les paramètres du problème étant maintenant connus.

Revenons maintenant à notre hypothèse première qui est que les fluctuations thermiques du canal adjacent sont responsables de la longueur de cohérence finie. Si cette hypothèse est vraie on devrait obtenir d'après 2.2 et 2.4 :

$$eV_\varphi = 4k_B T_\varphi \tag{2.4}$$

où T_φ a été mesurée dans la précédente partie. Nous avons représenté figure 1.11 l'ensemble de nos résultats sur le plateau $\nu = 2$. On vérifie bien la relation 2.4 sur tout le plateau : notre hypothèse première est vérifiée. La dépendance de la longueur de cohérence en fonction du champs magnétique provient elle de la variation du paramètre de couplage V_0 sur la plateau. Cette déviation vient probablement d'une longueur de trajectoire électronique effective variant avec B.

2.6   "Voltage Probe"

Nous décrivons dans cette partie une expérience du type "which path". Le détecteur est composé d'une petit contact ohmique flottant que l'on couple à un MZI par l'intermédiaire d'une grille latérale (voir figure 2.12).

Lorsque la grille latérale est ouverte tous les électrons du bras inférieur vont être absorbés par le contact ohmique flottant puis vont être réémis avec une phase aléatoire. On s'attend donc à voir la visibilité diminuer avec la transmission T_P de la grille latérale. On montre qu'elle s'écrit :

$$\nu = \nu_0 \times \sqrt{R_P} \tag{2.5}$$

où R_P=1-T_P. Figure 2.13, nous avons représenté en point rouge la visibilité renormalisée en fonction de R_P=1-T_P, la courbe noire étant le fit associé à la formule 2.5 : l'accord est parfait.
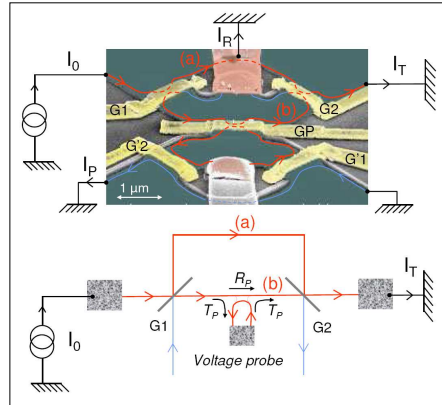
FIGURE 2.12 – Montage expérimental : le bras inférieur (b) du MZI peut être connecté à un contact ohmique flottant qui joue le rôle de voltage probe. Les CPQ G1 et G2 sont les lames séparatrices qui séparent et recombinent les trajectoires électroniques. Le CPQ GP permet de contrôler la probabilité de transmission T_P vers le contact de probe. G'1 et G'2 sont deux CPQ additionnels qui sont pincés pendant l'expérience.
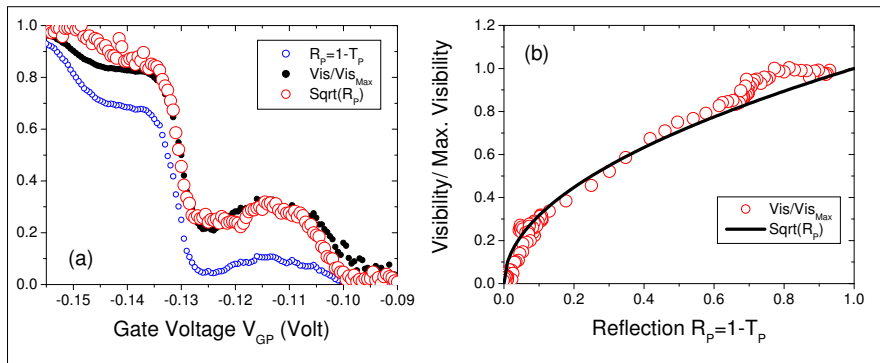
FIGURE 2.13 – (a) Visibilité renormalisée, R_P et $\sqrt{R_P}$ en fonction de V_{GP}, la tension appliquée sur GP. (b) Visibilité renormalisée en fonction de R_P. La courbe noire est la loi en $\sqrt{R_P}$ prédite par la théorie.

Cette expérience nous a permis de suivre la variation en phase causée par un état localisé prêt du CPQ et à le modéliser grâce à une approche du type matrice de scattering. Enfin des mesures de bruit réalisées avec la grille latérale ouverte nous ont permis de confirmer la relaxation en énergie dans un contact ohmique flottant.

Chapitre 3

Introduction

Contents

The goal of this thesis was the observation of the Bell's inequalities violation in a mesoscopic conductor. The violation of Bell's inequality is the answer to an intense debate between Bohr and Einstein during the 20's. Einstein had doubts about the probabilistic interpretation of the quantum physics defended by Bohr and the school of Copenhague. In 1935, Einstein published his famous article :"Can Quantum-Mechanical description of physical reality be considered complete?" [27]. In this article Einstein *et al.* show that quantum physics predicts state of two particles, with strong correlations in position and velocity. In particularly this EPR state predicts that if we measure the position or the velocity of one of the particle, we can extract the position or the velocity of the other one. According to Einstein *et al*, since the two particles can be arbitrary far away from each other, the measurement of one particle can not modify the state of the other one. Einstein *et al.* have deduced that each particle owns the precise value of its position and velocity before the measurement. Since quantum physics can not give simultaneously the velocity and the position, quantum physics is not complete. Bohr immediately replied [54], explaining that such a state can not be described as two individual states : the entangled state was born. The entangled state constitutes a unique object whatever the distance between the two electrons.

In 1965, Bell [13] discovered that the "EPR" state described by Einstein should lead to a contradiction with quantum mechanics. This article was all the more important that it opened new possibilities to give an experimental answer. If Bohr's representation of quantum mechanics was the correct one, in certain conditions, Bell's inequality (later defined) could be violated. A major experiment which has shown that indeed Bell's inequality could be violated with an entangled state of photons has been realized by Aspect *et al.* in 1982 [9].

The initial objective of this thesis was to realize the electronic analog of the Aspect *et al.* experiment.

In a first part, I will define the entanglement, and I will show that for a certain tuning of the polarizers (optical device used in the Aspect *et al.* experiment), the Bell's inequality can be violated. I will then introduce the violation of Bell's inequality in mesoscopic physics and describe the type of geometry that would enable us to observe this effect.

3.1   Toward Bell's inequality in mesoscopic physics

3.1.1   Definition of the entanglement

We call tensorial product of two spaces E_1 and E_2, the space E noted $E_1 \bigotimes E_2$ generated by the basis obtained "juxtaposing" vectors of the two basis $|\Phi_n^1\rangle$ and $|\Phi_p^2\rangle$:

$$|\Phi_{n,p}\rangle = |\Phi_n^1\rangle \bigotimes |\Phi_p^2\rangle$$

We consider now two vectors of E_1 and E_2 : $|\Phi_1\rangle$ and $|\Phi_2\rangle$. Then :

$$|\Phi\rangle = |\Phi_1\rangle \bigotimes |\Phi_2\rangle$$

is by definition a vector of E.

However the reciprocal is wrong : there exists some vectors that can not be factorized in E and written as a tensorial product $|\Phi_1\rangle \bigotimes |\Phi_2\rangle$. Such a state $|\Phi\rangle$ is entangled.

3.1.2   EPR Paradox and Bell's inequality

We start with the singlet state :

$$|\Phi\rangle = \frac{1}{\sqrt{2}}(|+_z\rangle|-_z\rangle - |-_z\rangle|+_z\rangle)$$

This state is an entangled state. We now suppose that particles 1 and 2 are spatially separated. The particle 1 is sent to Bob, the particle 2 to Alice. If Bob makes a measurement of the polarization of the particle 1 along the axis z, he will be able to forecast the particle 2 state. For example, if he measures +1, he will deduce that particle 2 is in the state $|-_z\rangle$. There is a perfect correlation. It exists examples of perfect correlations in the classical world. We consider a black and a white ball. One of the ball is given to Bob. He observes

it, and notices that it is white : it deduces that Alice has the black one. But this example is based on a fundamental hypothesis : each ball owns the information "I form a pair white ball-black ball". Could we imagine the same hypothesis, but with an entangled system ? For example the pair $|+_z\rangle|-_z\rangle$ would own the information "I form the pair $(|+_z\rangle, |-_z\rangle)$", information that each particle would conserve when they are spatially separated. It means here that the system owns some hidden variables.

More generally, if we note $A(\overrightarrow{a})$ (resp. $B(\overrightarrow{b})$), the measurement along $\overrightarrow{a}$ [1] (resp. $\overrightarrow{b}$), the most general way to model this hidden variable is to write these measurements as $A(\lambda, \overrightarrow{a})$($B(\lambda, \overrightarrow{b})$) where λ is the hidden variable. I now make the hypothesis that each hidden variable has a certain probability distribution $P(\lambda)$ with :

$$\int d\lambda P(\lambda) = 1 \text{ and } P(\lambda) \geq 0$$

The values taken by $A(\lambda, \overrightarrow{a})$ and $B(\lambda, \overrightarrow{b})$ are :

$$A(\lambda, \overrightarrow{a}) \pm 1 \text{ and } B(\lambda, \overrightarrow{b}) \pm 1$$

The average value of the resulting product is then written :

$$E_Q(\overrightarrow{a}, \overrightarrow{b}) = \int d\lambda P(\lambda) A(\lambda, \overrightarrow{a}) B(\lambda, \overrightarrow{b})$$

I now consider 4 vectors $\overrightarrow{a}, \overrightarrow{a'}, \overrightarrow{b}, \overrightarrow{b'}$ and I introduce :

$$s(\lambda) = A(\lambda, \overrightarrow{a})B(\lambda, \overrightarrow{b}) + A(\lambda, \overrightarrow{a'})B(\lambda, \overrightarrow{b}) + A(\lambda, \overrightarrow{a'})B(\lambda, \overrightarrow{b'}) - A(\lambda, \overrightarrow{a})B(\lambda, \overrightarrow{b'})$$

This can be written in a different way :

$$s(\lambda) = (A(\lambda, \overrightarrow{a}) + A(\lambda, \overrightarrow{a'}))B(\lambda, \overrightarrow{b}) - (A(\lambda, \overrightarrow{a}) - A(\lambda, \overrightarrow{a'}))B(\lambda, \overrightarrow{b'})$$

since $A(\lambda, \overrightarrow{a}) = \pm 1$ and $B(\lambda, \overrightarrow{b}) = \pm 1$, we immediately deduce that $s(\lambda) = \pm 2$ or s=0. Hence Bell's inequality [13] :

$$|E_Q(\overrightarrow{a}, \overrightarrow{b}) + E_Q(\overrightarrow{a'}, \overrightarrow{b}) + E_Q(\overrightarrow{a'}, \overrightarrow{b'}) - E_Q(\overrightarrow{a}, \overrightarrow{b'})| \leq 2 \tag{3.1}$$

The theory of the hidden variables leads thus to the Bell's inequality 2.1. We are going to show that these inequality can be violated by the measurement of an entangled state, confirming Bohr's interpretation of quantum physics.

---

1. In optics, it can be, for example, the direction of a polarizer.

3.1.3   Violation of the Bell's inequality

I first express $E_Q(\overrightarrow{a}, \overrightarrow{b})$ as a function of $\overrightarrow{a}$ and $\overrightarrow{b}$, the direction of the two polarizers. In the plane xOz, $\overrightarrow{a}$ is defined by the angle θ_1 with the X axis :

$$|+_{\overrightarrow{a}}\rangle = \cos(\theta_1)|+\rangle + \sin(\theta_1)|-\rangle$$

$$|-_{\overrightarrow{a}}\rangle = -\sin(\theta_1)|+\rangle + \cos(\theta_1)|-\rangle$$

(we get similar results for $\overrightarrow{b}$ with the angle θ_2). I now express $|\Phi\rangle$ in the eigenstates basis $|\pm_{\overrightarrow{a}}\rangle$ for the particle 1 and $|\pm_{\overrightarrow{b}}\rangle$ for the particle 2, we get :

$$|\Phi\rangle = \frac{1}{\sqrt{2}}(\sin(\theta_2-\theta_1)|+_a, +_b\rangle + \cos(\theta_2-\theta_1)|+_a, -_b\rangle - \cos(\theta_2-\theta_1)|-_a, +_b\rangle + \sin(\theta_2-\theta_1)|-_a, -_b\rangle)$$

I deduce from this expression the probability to measure, for example, +1 for the particle 1 and +1 for the particle 2 (noted $P(+_a, +_b)$). $E_Q(\overrightarrow{a}, \overrightarrow{b})$ is given by :

$$E_Q(\overrightarrow{a}, \overrightarrow{b}) = P(+_a, +_b) + P(-_a, -_b) - P(-_a, +_b) - P(+_a, -_b)$$

This finally gives

$$E_Q(\overrightarrow{a}, \overrightarrow{b}) = -\cos(2(\theta_2 - \theta_1)) \tag{3.2}$$

We consider now the configuration of the figure 3.1. It is straightforward to show that :

$$|E_Q(\overrightarrow{a}, \overrightarrow{b}) + E_Q(\overrightarrow{a'}, \overrightarrow{b}) + E_Q(\overrightarrow{a'}, \overrightarrow{b'}) - E_Q(\overrightarrow{a}, \overrightarrow{b'})| = |\cos(6\theta) - 3\cos(2\theta)|$$

If we choose $\theta = \pi/8$ then :

$$|\cos(6\theta) - 3\cos(2\theta)| = 2\sqrt{2} > 2$$

For certain values of θ, Bell's inequality are violated. The hidden variables theory combined with the principle of locality does not apply for entangled states. An entangled state can not be interpreted as two individual states. It is a unique state composed of two particles.

3.2   Electronic entanglement in the two-particle interferometer

In the previous part, we have used very general arguments to prove that for a certain geometric configuration of the polarizers, the measurement of an entangled state violates Bell's inequality. In this part, I will detail how this experiment can be realized. I will show that for an ingenious mesoscopic conductors geometry [74][73], we can obtain the mesoscopic analogous of the optical experiment realized by Aspect *et al.* in the 80's to violate Bell's inequality. [9].
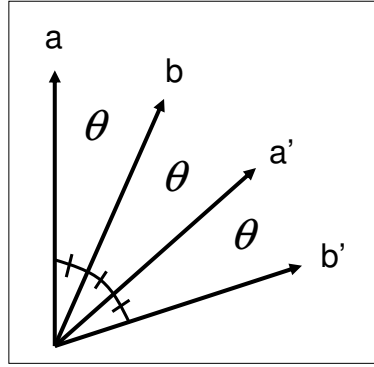
FIGURE 3.1 – Geometric configuration to violate Bell's inequality. Measurements are realized along **a**,**b**,**a'**,**b'**, the different directions of the polarizers. The angle between **a** and **b**, **a'** and **b**, **a'** and **b'** is equal to θ. The angle between **a** and **b'** is equal to 3θ. For $\theta = \pi/8$ we obtain the maximally entangled state.

Entanglement in mesoscopic conductors

We are interested here in the system described figure 3.2. Electrons emitted by reservoirs 1 and 2 can be either transmitted to B or reflected to A. In the following, we will focus on electronic correlations between regions A and B.
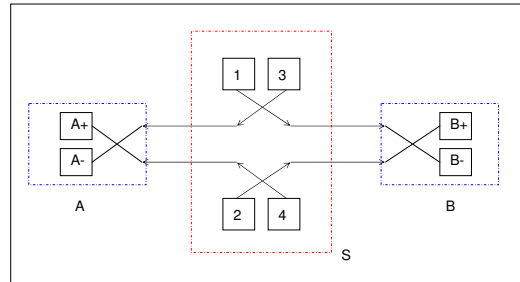
FIGURE 3.2 – Schematic representation of the conductor. A region source (S) composed of the injection (reservoirs 1 and 2) and two beam splitters. Injected electrons are sent towards region A and B. Region A(resp. B) is composed of one beam splitter and two detectors : ohmic contacts A+ and A- (resp. B+ and B-).

Noise measurements and post-selection of an entangled state

The injected state is :

$$|\Psi\rangle = a_1^+ a_2^+ |0\rangle$$

where a_i^+ is the creation operator of a particle at the ith contact. We introduce the operators b_{An} and b_{Bn} that model electrons emitted by the contact n after the beam splitter from the region S and that propagate respectively toward regions A and B. We can relate these states to the injected states with the scattering matrix :

$$\begin{pmatrix} b_{A1} \\ b_{B1} \end{pmatrix} = \begin{pmatrix} r & t' \\ t & r' \end{pmatrix} \begin{pmatrix} a_1 \\ a_3 \end{pmatrix}$$

and

$$\begin{pmatrix} b_{A2} \\ b_{B2} \end{pmatrix} = \begin{pmatrix} r & t' \\ t & r' \end{pmatrix} \begin{pmatrix} a_2 \\ a_4 \end{pmatrix}$$

The injected state thus becomes :

$$|\Psi\rangle = [r^2 b_{A1}^+ b_{A2}^+ + t^2 b_{B1}^+ b_{B2}^+ + rt(b_{A1}^+ b_{B2}^+ - b_{A2}^+ b_{B1}^+)]|0\rangle$$

The cross correlation noise measurement [2] gives a no null result only for the two particles states, where one particle is in the region A and the other in B. Consequently, the noise measurement selects the state :

$$|\Psi_0\rangle = rt[|1\rangle_A\rangle|2\rangle_B - |2\rangle_A\rangle|1\rangle_B]$$

which is an entangled state. Since the scattering matrix is unitary, the beam splitter has a transmission coefficient toward the ohmic contact A+ : t=$\sin(\theta_A)$ (B+ : t=$\sin(\theta_B)$), and a reflexion coefficient toward A- : r=$\cos(\theta_A)$(B- : r=$\cos(\theta_B)$). We obtain then :

$$\begin{pmatrix} |A+\rangle \\ |A-\rangle \end{pmatrix} = \begin{pmatrix} \cos(\theta_A) & -\sin(\theta_A) \\ \sin(\theta_A) & \cos(\theta_A) \end{pmatrix} \begin{pmatrix} |2_A\rangle \\ |1_A\rangle \end{pmatrix}$$

and

$$\begin{pmatrix} |B+\rangle \\ |B-\rangle \end{pmatrix} = \begin{pmatrix} \cos(\theta_B) & -\sin(\theta_B) \\ \sin(\theta_B) & \cos(\theta_B) \end{pmatrix} \begin{pmatrix} |2_B\rangle \\ |1_B\rangle \end{pmatrix}$$

We introduce the quantity :

$$P_{\alpha\beta} = S_{\alpha\beta} \times \frac{h}{-4e^2 V}$$

where $S_{\alpha\beta} \sim \langle \delta I_\alpha I_\beta \rangle$ is the cross correlated power noise spectrum, and α (resp. β) is A+ (resp. B+) or A- (resp. B-). We obtain then :

$$P_{A+B-} = P_{A-B+} = \frac{1}{2}[\sin^2(\theta_A)\sin^2(\theta_B) + \cos^2(\theta_A)\cos^2(\theta_B) + 2\sin(\theta_A)\sin(\theta_B)\cos(\theta_A)\cos(\theta_B)\cos(\phi_0)]$$

and

$$P_{A+B+} = P_{A-B-} = \frac{1}{2}[\cos^2(\theta_A)\sin^2(\theta_B) + \sin^2(\theta_A)\cos^2(\theta_B) - 2\sin(\theta_A)\sin(\theta_B)\cos(\theta_A)\cos(\theta_B)\cos(\phi_0)]$$

$$(3.3)$$

---

2. I will detail the cross correlation measurement in the Chapter 4. For the moment, we just want to determine the electronic correlation between region B and A without worrying about the actual way it can be done.

where ϕ_0 is a phase term. We suppose first that $\phi_0=0$. The previous expressions now becomes :

$$P_{A+B-} = P_{A-B+} = \frac{1}{2}\cos^2(\theta_A - \theta_B) \text{ and } P_{A+B+} = P_{A-B-} = \frac{1}{2}\sin^2(\theta_A - \theta_B)$$

One can realize that the electronic and the optical problems are similar through the correlation function :

$$E(\theta_A, \theta_B) = P_{A+B-} - P_{A-B+} - P_{A+B+} + P_{A-B-}$$
$$E(\theta_A, \theta_B) = \cos(2\theta_A)\cos(2\theta_B) + \sin(2\theta_A)\sin(2\theta_B)$$

which has the same form as formula 2.1. We know that the Bell's inequality is given by $-2 \leq S_B \leq 2$ where :

$$S_B = E(\theta_A, \theta_B) - E(\theta'_A, \theta_B) + E(\theta_A, \theta'_B) + E(\theta'_A, \theta'_B)$$

For $\theta_A=\pi/8$, $\theta_B=\pi/4$, $\theta'_A=3\pi/8$, $\theta'_B=\pi/2$, we obtain $S_B = 2\sqrt{2}$ and Bell's inequality are maximally violated.

3.3 From the simple Mach Zehnder Interferometer to the two-particle interferometer

In the previous part, I have described the general geometry of a mesoscopic conductor that would enable us to violate Bell's inequality. Here, I present the double "MZI" [3], a feasible sample that fulfills all the conditions to violate Bell's inequality. We will show that before tuning the beam splitters to obtain the maximal violation, we must check that noise measurements probe the entangled part of the state. In order to do that, we will vary the Aharonov-Bohm phase defined by the different electronic trajectories and will show that the entangled part of the state can be revealed by Aharonov-Bohm oscillations in the cross-correlated noise measurements.

A schematic representation of the sample [74] is represented figure 2.3.

3.3.1 The two-particle Aharonov-Bohm effect

Contrary to the simple electronic MZI [37], two incoherent electronic sources inject a current in the MZI. If we now compare this geometry to the one described in the previous part (figure 3.2), we notice that it is very similar. The region S is now composed of the ohmic contacts 2 and 3 that will inject electrons, with C and D the beam splitters that will partition electrons. The regions A and B are now composed of the ohmic contacts 5 and 8 (the detectors), with A and B the beams splitters. The noise measurements are realized between ohmic contacts 5 and 8. We are going to detail the state measured by

_____

3. Association of two single MZI.
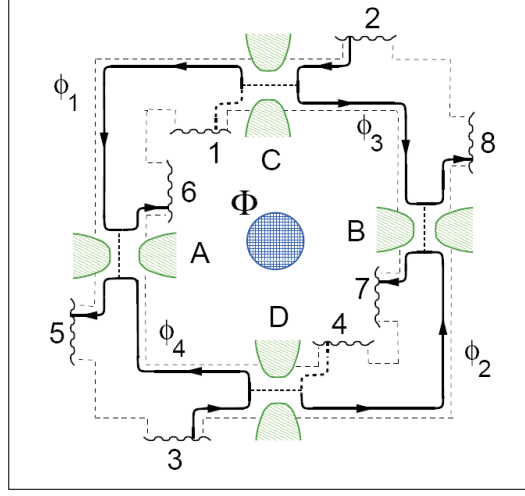
FIGURE 3.3 – Schematic representation of the double MZI proposed by Samuelsson et al. [74] . Electrons are injected from contacts 2 and 3. Cross correlation noise measurements are realized between contacts 5 and 8. Keeping in mind the notations of the figure 3.2, the source S is composed of ohmic contacts 2 and 3 and beam splitters C and D. Region A is composed of beam splitter A and ohmic contacts 5 and 6. Region B is composed of beam splitter A and ohmic contacts 7 and 8. ϕ is the phase accumulated along the trajectory of an edge. For example ϕ_1 is the accumulated phase along the outer edge between the beam splitters C and A. Cross correlation noise measurement between contacts 5 and 8 is sensitive to the two electrons Aharonov-Bohm phase $\phi = \phi_1 + \phi_2 - \phi_3 - \phi_4$

this cross correlation noise measurement and show that it depends on the "two electrons Aharonov-Bohm" phase.

We introduce $f(\epsilon)$ the Fermi distribution of reservoirs 2 and 3, and $f_0(\epsilon)$ the Fermi distribution of the other reservoirs. We want to calculate the correlation current between contacts 5 and 8. The general expression of the noise between contacts α and β can be written as :

$$S_{\alpha\beta} = \frac{-2e^2}{h}\Sigma_{\gamma\delta} \int dE(s_{\alpha\gamma}^+ s_{\alpha\delta} s_{\beta\delta}^+ s_{\beta\gamma})(f_\gamma - f_0)(f_\delta - f_0)$$

$$S_{58} = \frac{-2e^2}{h}\int dE|s_{52}^* s_{82} + s_{53}^* s_{83}|^2 (f - f_0)^2$$

(3.4)

where $s_{\alpha\beta}$ is the scattering amplitude between contacts α and β. When the gates transmissions are equal to $1/2$:

$$S_{58} = \frac{-e^2}{4h}|eV|[1 + cos(\phi_1 + \phi_2 - \phi_3 - \phi_4)]$$

where ϕ_1 is the phase accumulated between QPCs C and A, ϕ_2 between QPCs D and B, ϕ_3 between QPCs C and B, ϕ_4 between QPCs D and A (see figure 2.3). We suppose now that we can add a magnetic flux through the sample. Due to the chirality of the electronic trajectories, we obtain a positive contribution of the magnetic flux for the phases ϕ_1 and ϕ_2, and a negative one for the phases ϕ_3 and ϕ_4. The global contribution related to the

magnetic flux is thus equal to $\phi_1 + \phi_2 - \phi_3 - \phi_4 = \oint \overrightarrow{dl}.\overrightarrow{A}$ where $\overrightarrow{A}$ is the potential vector. Varying the magnetic flux through the double MZI, we should observe two electrons Aharonov-Bohm oscillations.
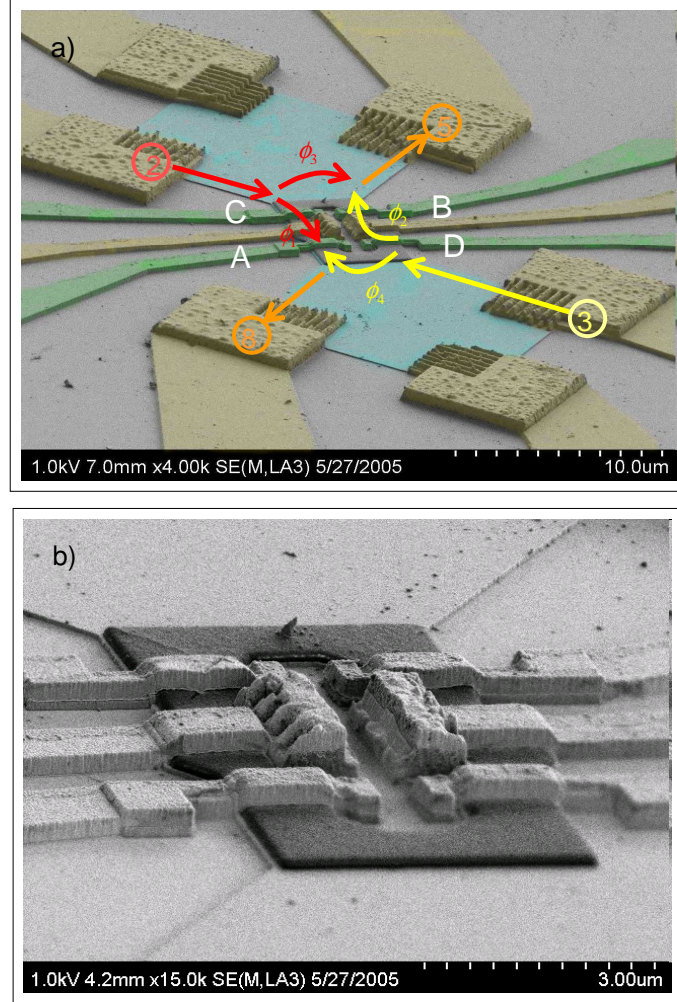
FIGURE 3.4 – (a) Schematic representation of the first version of our double MZI . There is no side gate to tune each simple MZI separately. Electrons are collected via small inner ohmic contacts in yellow on the figure.(b) Zoom of the central part of the double MZI with four gates, and two ohmic contacts connected to the ground. The advantages of this sample was the very short length of the trajectory. The disadvantage was the impossibility to tune the interferometer using conductance measurements.

Once two-electron Aharonov-Bohm oscillations measured, how can we violate Bell's inequality ? Comparing formula 3.4 to 3.2 obtained in the previous part, we then obtain :

$$P_{58} \sim \frac{1}{2}[\sin^2(\theta_A)\sin^2(\theta_B) + \cos^2(\theta_A)\cos^2(\theta_B) + 2\sin(\theta_A)\sin(\theta_B)\cos(\theta_A)\cos(\theta_B)\cos(\phi_0)]$$

with $\phi_0 = \phi_1 + \phi_2 - \phi_3 - \phi_4$ and T_A=1-R_A=$\sin^2(\theta_A)$ (T_B=1-R_B=$\sin^2(\theta_B)$). Consequently

once P_{58} measured, we have to set $\phi_0{=}0$, to reproduce the measurement with P_{67}, P_{68} and P_{57} tuning $\theta_A{=}\pi/8$, $\theta_B{=}\pi/4$, $\theta'_A{=}3\pi/8$ and $\theta'_B{=}\pi/2$.

3.3.2   Technical realization
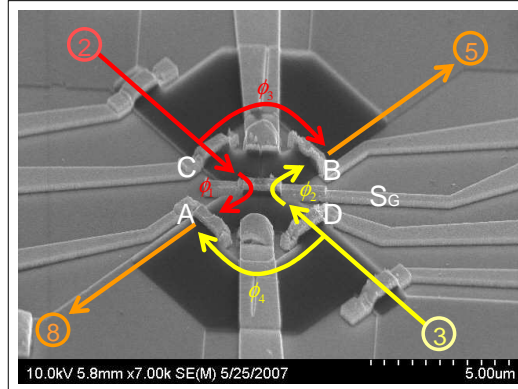
FIGURE 3.5 – Schematic representation of the second version of our double MZI. Electrons are injected from contacts 2 and 3. Cross correlation noise measurements are realized between contacts 5 and 8. Keeping the notations of the figure 3.2, the source S is composed of ohmic contacts 2 and 3 and beam splitters C and D. Region A is composed of beam splitter A and ohmic contact 5. Region B is composed of beam splitter A and ohmic contact 8. ϕ is the phase accumulated along the trajectory of an edge. For example ϕ_1 is the phase accumulated along the outer edge between the contacts C and A. Cross correlation noise measurement between contacts 5 and 8 should be sensitive to the two electrons Aharonov-Bohm phase $\phi = \phi_1 + \phi_2 - \phi_3 - \phi_4$. A side gate ($S_G$) enables us to separate the upper MZI from the lower one. We should first tune separately each simple MZI to obtain the highest visibility and then open the side gate and realize noise measurements, as it has been done recently by the Weizmann group [60].

We started the experiment with a sample which was exactly the one proposed by Samuelsson *et al* [74]. These samples (see figure 3.4) had the advantage to be very compact hence leading to very short electronic trajectories. However these samples suffered from a strong disadvantage : it was impossible to tune the magnetic field and/or the gate voltage to obtain the highest visibility using conductance measurements. We have chosen then a configuration pioneered by the Weizmann group [60] (see figure 3.5). The trick is to separate two simple MZI by a gate : when the gate is closed, we tune separately the two MZI using conductance measurements, to obtain the highest visibility on each. When the gate is opened we get the double MZI configuration [60] and can perform noise measurements.

3.4   Conclusion

This chapter was a general introduction to this thesis. We have shown that it is theoretically possible to violate Bell's inequality with a mesoscopic conductor. We have described the geometry to achieve this experiment. Starting with two simple MZI tuned in order to measure the highest visibility, we open the central gate and obtain the Double MZI

configuration. We will then probe the entangled part of the state via electronic shot noise measurements These measurements will be realized at finite bias voltage and finite temperature. Consequently before measuring the noise, we need to study the visibility in a simple MZI as a function of the sample size, magnetic field and applied bias.

1. We first have to extract a coherence length, since when we will open the central gate, the surface of the interferometer will be doubled : we have to ensure that the two electrons state remains coherent on the whole surface.

2. We have to find a magnetic field where this coherence length is the longest. This study of the coherence length will give us the temperature dependence of the visibility : we will then be able to know if the electronic temperature of our fridge (20mK) will be low enough to measure the two electrons Aharonov-Bohm effect.

3. Finally since the noise measurements are realized at finite bias voltage, we must understand the voltage bias dependence of the visibility. Recent experiments have shown that the voltage bias dependence of the visibility was not monotonous [57] : such results must be explained before performing noise measurements.

After all these preliminary studies, we will be able to answer this question : do we have the noise sensitivity to violate Bell's inequality with our experimental set up ?

Chapitre 4

The electronic MZI

Contents

4.1 Introduction

This part is an introduction to the electronic MZI and the experimental set up. We will first recall the historical experiment of the MZI realized in optics and we will explain its general principle. In optics, interferometers are composed of beams splitters, mirrors and source of photons. To realize interference experiments in mesoscopic physics which are somehow a copy of the one realized in optics, we must find an experimental set up which produces beam-like electronic motion, beam splitters, mirrors. We will show that the edge states in the quantum Hall regime are 1D wires whose position can be easily controlled. In a second step, we will take up the question of the beam splitters : we will show that the quantum point contacts (QPC) are good candidates to mimic beam splitters. Then, we will describe the geometry of the electronic MZI and explain how the conductance and noise measurements are performed.

In a last part, we will detail the method that we have followed to obtain the highest visibility on samples with a stable phase (several hours) and also with samples presenting phase fluctuations.

4.2 From optics to mesoscopic physics : description of the optical MZI
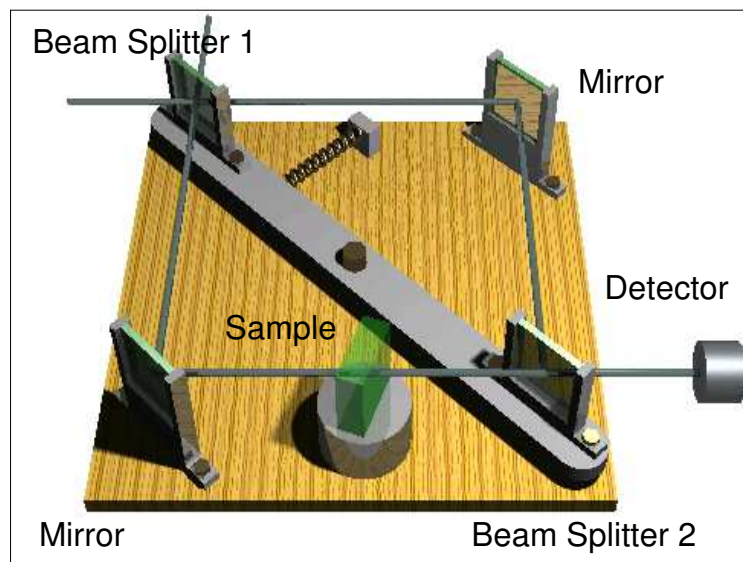
FIGURE 4.1 – Schematic view of the optical MZI. A collimated beam is split by a first half-silvered mirror (represented in grey). The two resulting beams (the "sample beam" and the "reference beam") are each reflected by a mirror (in black on the figure). The two beams are recombined on a second half-silvered mirror and then enter in the detector.

The Mach Zenhder interferometer[1] is a device which has been used for the first time to determine the phase shift caused by a small object placed in the path of one of two collimated beams issued from a coherent light source.

A collimated beam is split by a half-silvered mirror (a beam splitter). The two resulting beams (the "sample beam" and the "reference beam") are each reflected by a mirror. The two separated beams are then recombined on a second half-silvered mirror and then enter in the detector.

Because the coherence length of photons is larger than the size of the interferometer , the transmission amplitude t through the MZI is the sum of the two complex transmission amplitudes corresponding to upper path and down path of the interferometer. For transmission and reflection amplitudes t_i and r_i for the ith beam splitter (with $|r_i|^2+|t_i|^2=1$ (i=1,2)), the transmission amplitude t through the MZ is given by :

$$t = t_1 e^{i(\delta ke + kL_u)} r_2 - r_1 e^{ikL_d} t_2.$$

where k is the wave vector of the monochromatic light, δk the wave vector variation due to the inserted object and e the thickness of this object[2]. It leads to the transmission probability :

$$T = T_1 R_2 + R_1 T_2 + \sqrt{T_1 T_2 R_1 R_2} sin(\varphi)$$

where $\varphi(k) = k(L_u - L_d) + \delta ke$ and $T_i=|t_i|^2 = 1 - R_i$.

To reveal oscillations, one has to vary the length difference between the two trajectories by moving one mirror, or to introduce a phase shift by adding a sample along one of the path.

One of the major difficulties when making an optical interferometer was to obtain a focussed light beam and a monochromatic one, such that the coherence length of the source (inversely proportional to its spectral width) is longer than the interferometer. For several decades, the LASER has been very useful as it provides directly a focussed monochromatic light.

Here, one wants to make interferences with electrons : the electronic wave function replaces the electromagnetic one. If interferences with electrons have already been realized in mesoscopic conductors [19][77], it is impossible to impose strictly two trajectories for electrons without chirality[3](at least in conductors). This problem is circumvented here by breaking the time reversibility of trajectories with a magnetic field. We will show that when submitted to a perpendicular magnetic field, the electronic transport in 2D high mobility electron gas is chiral and occurs along edge states which are 1D conductors. Consequently, we will be able to control the trajectories of electrons just by designing the edge of the sample. Another major difficulty when making an optical interferometer is the tuning of beam splitters. The collimation of the transmitted and reflected beams must be very precise, and the transmission of each beam splitter has to be set to $1/2$ in order to obtain

_____

1. Named after physicists Ludwig Mach and Ludwig Zehnder (1891) [47][89].
2. The sign minus in the reflection is a consequence of the unitary of the scattering matrix.
3. Motion in one direction, like a photon beam.

the highest visibility. In mesoscopic physics, we will show that QPCs enable us a very accurate tuning of the electronic beams transmissions. Last, ohmic contacts will serve as detectors of electrons, and detection will be realized via voltage measurement between two ohmic contacts.

4.3   An electronic beam : the edge state of the Integer Quantum Hall regime

Before describing the edge states properties, I will give a brief introduction of the quantum Hall effect. Then, I will describe the electronic transport in the quantum Hall regime and show that the transport occurs in 1D wires along the sample edges : the edge states.

4.3.1   The classical Hall effect

Classical Dynamics of electrons submitted to a magnetic field

We consider a 2D gas of electrons submitted to a perpendicular magnetic field $\overrightarrow{B}$. We introduce the complex notation z=x+iy to study the position of electrons. The dynamic of electrons under the Lorentz force is :

$$m\ddot{x} = -eB\dot{y} \text{ and } m\ddot{y} = eB\dot{x}$$

or $\ddot{z} = i\omega_c\dot{z}$ with ω_c=eB/m^*, where ¨denotes the second time derivative, and m^* the effective mass. The solution of this simple equation is given by :

$$z = C - \frac{iv_0}{\omega_c}e^{i\omega_c t}$$

For non zero values of v_0, the trajectory of the particle describes a cyclotron orbit with a frequency ω_c. The center of this orbit C is fixed.

Transport

In the classical Hall regime, the conductivity tensor $\hat{\Sigma}$ (defined by $\overrightarrow{j} = \hat{\Sigma}\overrightarrow{E}$) is equal to [7][38] :

$$\hat{\Sigma} = \frac{\Sigma}{1 + \omega_c^2\tau^2} \begin{pmatrix} 1 & -\omega_c\tau \\ \omega_c\tau & 1 \end{pmatrix}$$

where Σ is the conductivity at zero magnetic field, Σ=$n_s e^2\tau/m^*$, τ being the Drude collision time. We deduce from that expression the resistivity tensor :

$$\hat{\rho} = (\hat{\Sigma})^{-1} = \rho \begin{pmatrix} 1 & \omega_c\tau \\ -\omega_c\tau & 1 \end{pmatrix}$$

with $\rho = \Sigma^{-1}$ the resistivity at zero magnetic field. The longitudinal resistivity is given by the diagonal elements of the tensor, and the Hall resistance (or transverse resistance) by its non-diagonal elements. We note that in the classical regime, the longitudinal resistance is not affected by the magnetic field and the Hall resistance is given by :

$$\rho_{xy} = \rho \omega_c \tau = \frac{1}{n_s e} B$$

The classical Hall resistance varies linearly with the magnetic field and offers the possibility to measure the electronic density. This classical description of the Hall effect is adapted for $\omega_c \tau \ll 1$. The transition with the quantum Hall effect occurs when the collision time τ of the electrons is larger than the inverse of the cyclotron frequency and the temperature of the system $T \ll \hbar \omega_c$.

4.3.2   The quantum Hall effect

The discovery of the Quantum Hall effect in 1980 by Von Klitzing [39] has been an important step in the comprehension of the electronic transport in 2D systems. Von Klitzing *et al.* have characterized the variations of the longitudinal resistivity ρ_{xx}, and of the transverse resistivity ρ_{xy} of a two-dimensional gas with the applied magnetic field. If in average ρ_{xy} followed a linear slope with B as predicted by the classical approach, Von Klitzing has observed some plateaus at 1.5K. These plateaus in the curves ρ_{xy} have the remarkable property to appear at values equal to $\frac{h}{e^2} \times \frac{1}{\nu}$ where ν is an integer : this quantification is the mark of a quantum phenomenon (figure 4.2).
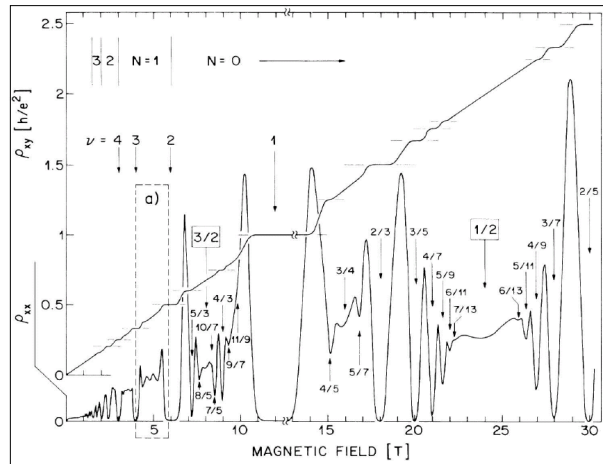
FIGURE 4.2 – Hall and longitudinal resistance as a function of the magnetic perpendicular field. We note the integer Hall plateaus, and the Shubnikov-de-Haas oscillations between two plateaus. The longitudinal resistance is null on the Hall plateaus.

For each plateau, Von Klitzing noticed that ρ_{xx} vanishes : the electronic transport is no longer dissipative. He also observed some peaks of ρ_{xx} while ρ_{xy} was evolving continuously between two plateaus. These oscillations are the expression of a well known phenomena for electrons submitted to a uniform magnetic field : the Shubnikov-de-Haas oscillations. [28].

4.3.3   Electrons without spin

To explain the origin of these plateaus, we first consider the simple case of an electron moving in a 2D system, submitted to a perpendicular magnetic field. Here, we will neglect electronic interactions. The Hamiltonian of the system is given by :

$$H_0 = \frac{1}{2m^*}(\overrightarrow{p} - e\overrightarrow{A})^2 = \frac{\Pi^2}{2m^*} = \frac{1}{2m^*}(\Pi_x^2 + \Pi_y^2)$$

with m^* the electron effective mass, e=$-|e|$ its charge, $\overrightarrow{p}$ its moment, and $\overrightarrow{A}$ the potential vector. In the cylindric gauge, $\overrightarrow{A} = \frac{1}{2}\overrightarrow{B} \wedge \overrightarrow{r}$ with $\overrightarrow{B}$ the magnetic field, we can show that the hamiltonian is quadratic in position and in moment. The problem is thus analog to an harmonic oscillator in two dimensions, Π_x and Π_y being conjugate :

$$[\Pi_x, \Pi_y] = \frac{-i\hbar^2}{l_m^2}$$

where $l_m = \sqrt{\hbar/eB}$ is the cyclotron length. We introduce the operators a and $a^\dagger$ defined by :

$$a = \frac{l_m}{\hbar\sqrt{2}}(\Pi_x - i\Pi_y) \text{ and } a^\dagger = \frac{l_m}{\hbar\sqrt{2}}(\Pi_x + i\Pi_y) \text{ leading to } [a, a^\dagger] = 1$$

The Hamiltonian H_0 becomes :

$$H_0 = \hbar\omega_c(\frac{1}{2} + a^\dagger a)$$

The energy spectrum of this Hamiltonian is given by $\varepsilon_n = \hbar\omega_c(n + \frac{1}{2})$. These discrete energy levels are called Landau levels. The charged particles can only occupy orbits with discrete energy values : between two Landau levels, there are no available states. As the density of state falls to zero between 2 Landau levels, it would mean that the system should be a perfect insulator. In fact, the explanation of the Hall plateau is a little bit more sophisticated. As an example the sample edges and the disorder play a crucial role. Since H_0 does not depend of the position of the center of the cyclotron orbit, energy levels must be degenerated. The quantum operator that describes the position of the center of the cyclotron orbit is defined by :

$$C = z + i\frac{\Pi}{m^*\omega_c} \text{ which leads to } [C_x, C_y] = il_m^2$$

where z=x+iy stands for the position of the cyclotron orbit. $2\pi l_m^2$ represents the area of one flux quantum ϕ_0=h/eB. We now introduce operators b and $b^\dagger$:

$$b = \frac{1}{l_m\sqrt{2}}(C_x + iC_y) \text{ and } [b, b^\dagger] = 1$$

We can easily verify that [a,b]=[a†,b]=[H,b]=0, and thus diagonalize the Hamiltonian in the eigenstates basis of operators a and b. The eigenstates basis of H_0 can be written :

$$|n, m\rangle = \frac{(a^\dagger)^n (b^\dagger)^m}{\sqrt{n!m!}}|0,0\rangle \text{ and } \varepsilon_n = (n + \frac{1}{2})\hbar\omega_c$$

Expressing a and b in function of z,$\overline{z}$,$\partial/\partial z$ and $\partial/\partial\overline{z}$, one can show that [46] :

$$\Psi_{0,0} = \frac{1}{\sqrt{2\pi l_m^2}} e^{-\frac{z\overline{z}}{4l_m^2}}$$

$$\Psi_{0,m} = \frac{z^m}{\sqrt{2\pi l_m^2}\sqrt{2^m m!}} e^{-\frac{z\overline{z}}{4l_m^2}}$$

We can now calculate the number of states per unity of surface for a Landau level, for example the first one (n=0). The area occupied by all the states of the first level is given by :

$$\pi\langle m, 0|z\overline{z}|0, m\rangle = 2\pi l_m^2(0 + m + 1)$$

The area occupied by a state is exactly the area of a flux quantum h/eB. We define the filling factor ν by :

$$\nu = \frac{n_s}{n_{\phi_0}}$$

with n_s the electronic density and n_{ϕ_0} the flux quantum density. Each state occupies a flux quantum : when there is one electron per flux quantum the Landau level is full.

4.3.4   Electrons with spin

When we consider the spin of the electrons, we simply add the Zeeman energy to the solutions of the Hamiltonian H_0 :

$$\epsilon_{n,\pm} = \hbar\omega_c(n + \frac{1}{2}) \pm \frac{1}{2}g^*\mu_B B$$

with μ_B the Bohr's magneton, and g^* the gyromagnetic factor of Landé. Consequently , when the temperature is low enough compared to $g^*\mu_B B$, we will observe odd plateaux of the quantum Hall effect.

4.3.5   Hall resistance and Shubnikov-de-Haas oscillations

If we now consider the semi-classical approach of the transport developed in the previous part (part 4.3.1), the longitudinal resistance ρ_{xx} depends of the inverse of the collision time : $\rho_{xx} \sim 1/\tau$. When the Fermi energy is located between two Landau levels, there is a gap for the excitations and the electronic density of state at the Fermi level is zero. We expect thus a divergence of τ between two Landau levels. This results in oscillations of the longitudinal resistance, called Shubnikov de Haas oscillations (see figure 4.2).When all the

states of a Landau level are full, the density of states $n_s = \nu n_{\phi_0}$. Still in the semi classical representation, the Hall resistance ρ_{xy} now reads :

$$\rho_{xy} = \frac{B}{n_s e} = \nu^{-1}\frac{B}{n_{\phi_0}e} = \frac{1}{\nu}\frac{h}{e^2}$$

When the Fermi level is located between two Landau levels, ν is an integer. The Hall resistance only depends of h and e.

4.3.6   Edge states

In the bulk, electrons are not submitted to edge potentials, they follow circular trajectories with a null average drift velocity. When we get closer to the edges, electrons are submitted to the confining potential. The total energy being the sum of the Landau energy and the confining potential, Landau levels are bent. When the Landau levels cross the Fermi energy, one-dimensional gapless excitation modes form, which correspond to electrons drifting along the edge of the sample. The drift velocity is not zero, electrons are moving along the edges .
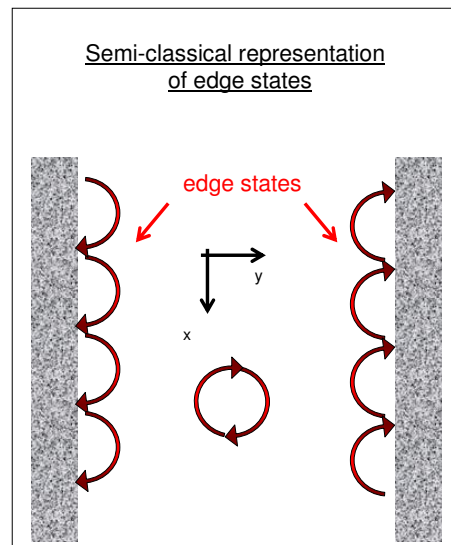
FIGURE 4.3 – Semi classical representation of edge states in the quantum Hall regime. The trajectory of electrons in the bulk can be described by a cyclotron trajectory. Along the edge of the sample, the center of the cyclotron orbit is drifting.

In the semi classical representation of edge states in the quantum Hall regime shown in figure 4.3, the trajectory of electrons in the bulk can be described by cyclotron trajectories. Along the edge of the sample, the center of the cyclotron orbit is drifting. The relation between the drift velocity and the confining potential can be obtained in the following way. We consider a sample designed in a 2D gas, submitted to a perpendicular magnetic field.

We model the edges of the sample by a repulsive potential for electrons : we note V(z) this edge potential. The Hamiltonian becomes :

$$H = \hbar\omega_c(a^\dagger a + 1/2) + V(z)$$

If we suppose that Landau levels are barely coupled by this potential, we can write the Hamiltonian projected on a Landau level :

$$H_n = \langle n|H|n\rangle = \hbar\omega_c(n + \frac{1}{2}) + V(\widetilde{C_x, C_y})$$

The first part of the Hamiltonian corresponds to a the cyclotron rotation of the electron, while the second part represents the effect of the edge potential on the center of the cyclotron orbit (C_x, C_y).

We consider the very simple case of an harmonic edge potential :

$$V(\widetilde{C_x, C_y}) = \frac{1}{2}m^*\omega_0^2(y_0 - W_0)^2$$

where W_0 is the center of the parable. Using the relation $y_0 = i\frac{\hbar}{eB}\frac{\partial}{\partial x_0} = \frac{\hbar}{eB}k_0$ (x_0 and y_0 are conjugate variables), the Hamiltonian becomes :

$$H = \hbar\omega_c(n + \frac{1}{2}) + \frac{\hbar^2}{2m^*(\omega_c/\omega_0)^2}(k_0 - \frac{W_0}{l_m^2})^2$$

The first part of this Hamiltonian describes the cyclotron trajectory of the electrons, the second part the drift of the center of the cyclotron orbit along the edges of the sample. Energies of the eigenstates are given by :

$$\epsilon_n(k) = \hbar\omega_c(n + \frac{1}{2}) + \frac{\hbar^2}{2m^*(\omega_c/\omega_0)^2}(k_0 - \frac{W_0}{l_m^2})^2$$

The drift velocity of the electrons becomes :

$$v_d(k_0) = \frac{1}{\hbar}\frac{dE(n, k_0)}{dk_0} = \frac{\hbar^2}{m^*(\omega_c/\omega_0)^2}(k_0 - \frac{W_0}{l_m^2})$$

Due to the edge potential, electrons along the edge of the sample have a non null drift velocity, while in the bulk the edge potential being equal to zero the drift velocity is null : electronic transport occurs along edges of the sample. We define an edge state when its energy is equal to the Fermi energy. There are as many edge states as occupied Landau level in the bulk (see figure 4.4).

In this thesis, we have been principally worked at filling factor ν=2, with two edge states and a Hall resistance equal to 12.9kΩ (see figure 4.5).
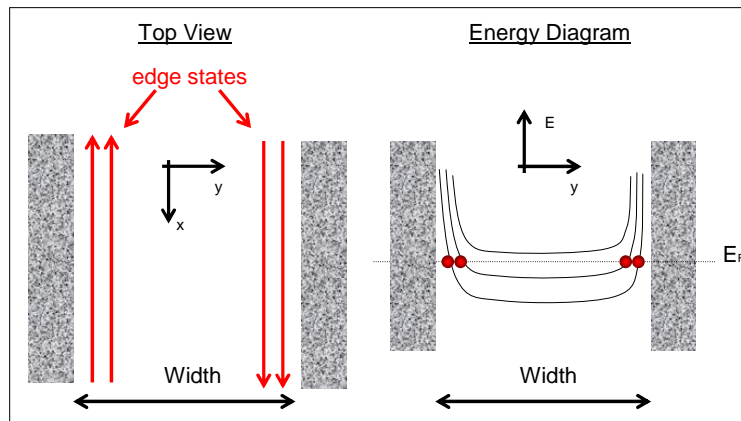
FIGURE 4.4 – Edge states representation as a function of landau levels. Due to confining edge potential (here we have represented a confining potential null in the center of the sample, varying on the edges),the Landau levels are bent, gapless excitations form on the edge where the Landau levels cross the Fermi energy. Hence, the electronic transport occurs at these crossing. From one edge to the other, the direction of the electronic trajectory is inverse : the electronic transport is chiral.
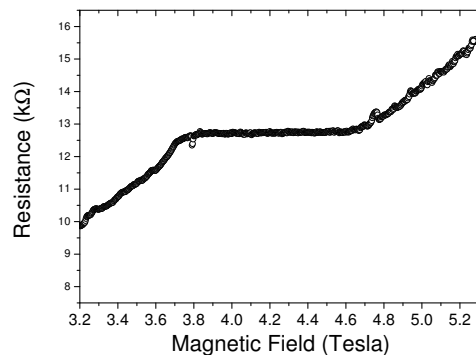
FIGURE 4.5 – Two points measurement of the Hall resistance realized in a MZI. Most of our results presented in this thesis have been obtained at filling factor $\nu=2$, with two edge states and a Hall resistance equal to 12.9kΩ.

4.4   Electronic Beam Splitter : the Quantum Point Contact

In this part, we will show that the QPC enables us to manipulate easily electronic modes either by reflecting or partially transmitting them. They are, as a consequence, a perfect candidate for the beam splitter in the electronic MZI. [4] We give in annexe A a more detailed description of the QPC via the introduction of the the scattering matrix in the Landauer-Buttiker formalism.

_____

4. The QPC will be also used to sweep the phase of the MZI.

4.4.1   The Quantum Point contact
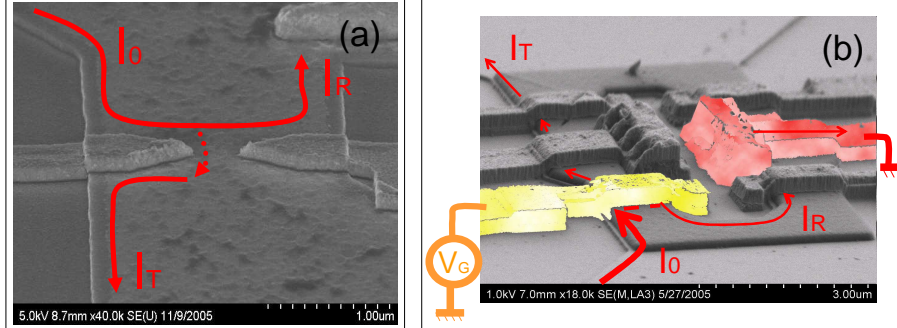
FIGURE 4.6 – (a) Top SEM view of a QPC. A part of the electronic wave is reflected (transmitted) noted I_R (noted I_T). (b) Top SEM view of a QPC in the MZI. We have colored in yellow the Au metallic bridge that connects both gates of the QPC, and in red the grounded ohmic contact. In this representation a part of the edge state is transmitted toward the second beam splitter. The reflected part of the current can be collected by the grounded ohmic contact.
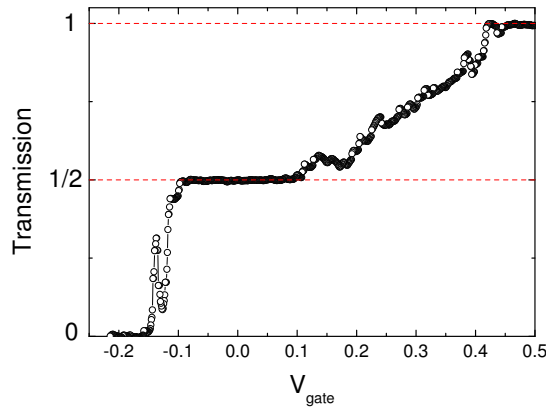
FIGURE 4.7 – Transmission behavior of a quantum point contact with the gate voltage at filling factor ν=2. For a gate voltage of +0.5V (when the sample is cooled down, gates are biased with +0.5V) both edge states are transmitted, the transmission is equal to 1. When the gate voltage is null, the transmission is equal to 1/2, only the outer edge state is transmitted, the inner one being totally reflected. Since, we will reveal Aharonov Bohm oscillations on the outer edge state, with a transmission equal to T_{out}=1/2, gate voltages usually applied in our experiments are $\sim$ -0.15V.

The first experimental realization of the QPC, with the observation of the conductance plateaus (giving the number of transmitted modes) has been realized by Van Wees *et al.* at Delft University in 1988 [83][85].

The Quantum Point Contact (see figure 4.6) is composed of split gates evaporated on the surface of a wafer containing the 2DEG [5].

_____

5. These two gates are fabricated by electronic lithography which enables to reach a very small distance between them ($\sim 280nm$).

Most of our results have been obtained at filling factor $\nu = 2$, meaning that two edge states are injected into the interferometer. We measure the transmission defined by $T = dI_T/dI_0$ with I_T the transmitted current and I_0 the injected current into the sample. Varying the gate voltage, we modify the electronic density under the QPC and the coupling between two counter propagating edge states. If the quantum point contact is opened, both edge states will be transmitted and T_{in}(transmission of the inner edge state) $=T_{out}$ (transmission of the outer edge state)=1 (see figure 4.7). When the filling factor beneath is equal to 1, we reflect one edge state while the other one is transmitted : in that case the transmission of the outer channel T_{out} will be equal to 1 while the transmission of the inner channel T_{in} will be equal to 0. This can be seen in Fig. 4.7 for values of V_{gate} between -0.05 and 0.1. At pinch off ($V_{gate} \leq$-0.15 on Fig.4.7), both edge states are reflected. For intermediary values of the gate voltage, we will be able to set the transmission of an edge state to 1/2 for example.

4.5   The electronic Mach Zehnder Interferometer

4.5.1   Description
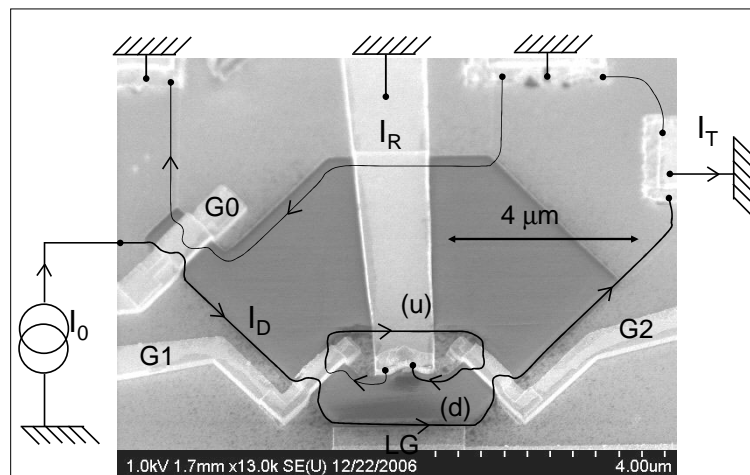
FIGURE 4.8 – SEM view of the electronic MZI with a schematic representation of the outer edge state. G0, G1, G2 are quantum point contacts which mimic beam splitters. The pairs of split gates defining a QPC are electrically connected via a Au metallic bridge deposited on an insolator (SU8). G0 allows a dilution of the impinging current, G1 and G2 are the two beam splitters of the MZI interferometer. LG is a side gate which allows a variation of the length of the lower path (b). The small ohmic contact in between the two arms collects the back scattered current I_R to the ground through a long gold bridge.

The electronic MZI is the electronic counterpart of the optical one[37][69][45], quantum point contacts (QPC) functioning as beam splitters and ohmic contacts as detectors[6]. As

_____

6. Ohmic contacts enable us to link the surface of the sample and the 2D gas located at 100nm under the surface. To fabricate them, we realize a deposit of an alloy gold, nickel germanium, and we heat during

shown schematically in Figure 4.8 QPC G_1 splits the incoming edge current to two paths (u) and (d). The two electronic trajectories will follow the edge of the sample designed to assure a zero length difference between the upper(u) and down(d) trajectories. They recombine on QPC G_2. This leads to interferences which are visible in the measured transmitted current. The reflected part of current is collected with a inner tiny ohmic contact grounded. I_T, the transmitted current is the measured quantity. The lateral gate LG will act as a side gate which allows a variation of the length of the lower path (d).

An additional QPC G_0 will enable us to dilute the impinging current and to reflect the inner edge state. Note that the upper trajectory is very far from the opposite edge (several μm) to avoid any interaction between the interfering edge state and the counter-propagating one.[7] At the beginning of my thesis, when we have tested the different MZI, there was always a broken QPC or ohmic contact. Thus, we have decided to optimize each cooling down of a sample : each sample was in reality composed of two MZI separated by the side gate, both MZI being strictly symmetric. We were able then to test two electronic MZI during each cooling down. Since the fabrication process is now very well mastered by Dominique Mailly and Gian Carlo Faini, the fabrication success rate is very high ($\sim 80\%$).

4.5.2   Fabrication process

The main difficulty of the experiment is indeed the fabrication of the samples which combine several QPC in a tiny region. The fabrication of the samples has been realized by Dominique Mailly and Giancarlo Faini at LPN, Marcoussis. They succeeded to put several gold gates at the top of a 2D electron gas, the electronic gas (provided by Ulf Gennser) being located at a distance of 100nm from the QPC. Furthermore, we will see that in the electronic MZI, we will need 4 QPC's + air bridges which reinforces the experimental realization difficulty. The first step in the characterization of a sample, is to verify that all the QPC correctly answer to a gate voltage. Moreover, as represented on figure 4.6(b), the reflected part of current will be collected by the grounded ohmic contact. When testing QPC, we will also verify that inner ohmic contacts are perfectly grounded. If not, some current will be re-emitted into the MZI, altering the visibility.

4.5.3   The two dimensional electron gas

A two-dimensional electron gas, or 2DEG, is formed when a crystal heterostructure (here GaAs/AlGaAs) is made such that free electrons feel a strongly confining potential in one direction. The electrons so confined are effectively reduced to two degrees of freedom.

1mn at 450˚C. The alloy will diffuse inside the GaAs to finally reach the 2D gas. We connect this ohmic contacts to the measurement set up via gold microweld realized with an ultrasound bounding machine. The ohmic contacts have a niche shape to maximize the exchange length between the contact and the 2D gas, and to reduce the resistance between the 2D gas and the contatc.

7. We will see that Sukhorukov *et al.* [79] have considered this long range interaction between the interfering edge state and the counter propagating one to justify the lobe pattern of the visibility with the applied bias (see Chapter 5).

Heterojunctions GaAs/AlGaAs used to fabricate our samples have been realized by epitaxy which consists in depositing atoms on a heated crystal wafer [1][30]. MZIs were patterned using e-beam lithography on a high-mobility two-dimensional electron gas with a sheet density of $n_S = 2.0 \times 10^{11}$ cm^{-2} and a mobility $= 2.5 \times 10^6$ cm^2/Vs).

4.5.4   Aharonov Bohm oscillations

Using the single particle approach of the Landauer-Buttiker formalism, the transmission amplitude t through the MZI is the sum of the two complex transmission amplitudes corresponding to paths (u) and (d) of the interferometer. t_i and r_i being the transmission and reflection amplitude of the ith QPC (with $|r_i|^2 + |t_i|^2 = 1$), the transmission amplitude of the MZI is given by :

$$t = t_1 e^{i\phi_d} t_2 - r_1 e^{i\phi_u} r_2.$$

where ϕ_u (ϕ_d) is the phase accumulated along the upper path (down path). It leads to a transmission probability at the energy ϵ :

$$T = \mid t \mid^2 = T_1 T_2 + R_1 R_2 + \sqrt{T_1 T_2 R_1 R_2} \sin(\varphi(\epsilon)) \tag{4.1}$$

where $\varphi(\epsilon) = \phi_u - \phi_d$ and $T_i = \mid t_i \mid^2 = 1 - R_i$.

$\varphi(\epsilon)$ is the AB flux across the area defined by the position of the edge state at the energy ϵ on the paths (u) and (d). This phase is related to the phase at energy ϵ_F by the relation [8][25] :

$$\varphi(\epsilon) = \epsilon \Delta L / (\hbar v_D) + \varphi_{\epsilon_F}$$

with v_D the drift velocity, $\Delta L = L_u - L_d$ ($L_u(L_d)$ are the length of the trajectories (u) and (d)) and :

$$\varphi_{\epsilon_F} = 2\pi \frac{e}{h} \phi_{AB}(\epsilon_F)$$

The visibility of the oscillation is defined as :

$$\nu = \frac{T_{max} - T_{min}}{T_{max} + T_{min}}$$

where $T_{max}(T_{min})$ is the maximum (minimum) transmission. When nothing reduces the visibility (noise, finite coherence length), the visibility is simply determined by the tranmissions T_1 and T_2 :

$$\nu = \frac{\sqrt{T_1 T_2 R_1 R_2}}{T_1 T_2 + R_1 R_2}$$

The maximum visibility is obtained for $T_1 = T_2 = 1/2$.

---

8. We consider here a simple non interacting approach of the electronic transport at $\nu = 2$. We will see that the non interacting approach is not sufficient since it does not explain the lobe structure of the visibility with bias (see Chapter 5).

4.6 Experimental technics

In this part we detail the experimental technics we used. It will contain usual conductance measurement technics as well as noise measurement technics. At the end of this part, we will explain the different way we used to determine the visibility from our measurement set up.

4.6.1 Conductance measurements
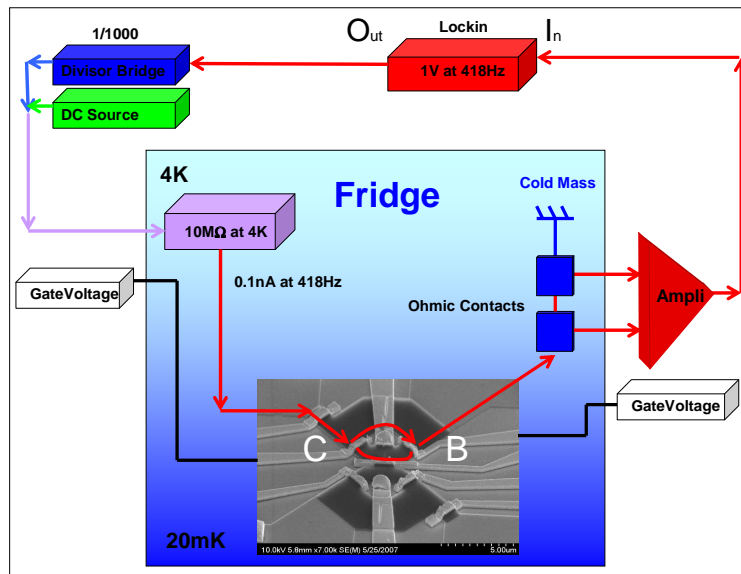
FIGURE 4.9 – Conductance measurement based on lockin detection. We also have the possibility to apply a DC voltage in parallel with the AC signal generated by the lockin. Amplifiers are at room temperature, while the 10MΩ resistance is thermalized at 4K. Ohmic contacts are used as current-tension converters. Gates voltages are filtered via low pass filters.

The conductance measurement of Aharonov Bohm oscillations is represented in figure 4.9. We measure the differential transmission through the MZI by standard lock-in techniques[9]. An alternating current at frequency f_0=418 Hz is sent on the sample. The output voltage contains an alternating component synchronized to the excitation and a noisy component. This output signal is amplified with low noise amplifier[10], and demodulated with the reference signal at the frequency f_0[11]. The measured signal is finally the response of the system excited at the frequency f_0, around the energy eV, where V is the DC bias applied in addition to the tiny excitation. Finally what we measure is the differential conductance

---

9. Model 5210, EGG Princeton Applied Research.

10. LI 75A

11. The lock-in amplifier realizes an average of the output signal during a time constant τ, and strongly reduces the bandwidth defined by $\sim 1/\tau$ and hence the noise.

defined by :

$$G(eV) = \frac{dI}{dV}(eV)$$

The AC excitation must be low enough. Indeed the AC excitation is the energy range on which we probe the system. If one wants to be able to observe temperature dependent properties, it is necessary that :

$$eV_\sim \ll k_B T$$

In our experiment, the lowest electronic temperature was $\sim$ 20 mK, which imposes $V_\sim \ll 2\mu V$. On the other hand, to have the best sensitivity we must choose a value of $V_\sim$ close to this limit. Typically we injected an AC current of 0.1nA in our sample, which gives at $\nu = 2$, for a 12.9kΩ input resistance, $V_\sim \sim 1.3\mu V$.

Regarding the AC signal frequency, it must be out of the interval of noise measurements ($\omega_0/2\pi \leq$ 1kHz), and one must avoid multiples of 50 Hz. In some experiments [12] realized on the MZI, we have used two lock-ins with 2 excitations frequencies $\omega_1/2\pi$=418 Hz and $\omega_2/2\pi$=619 Hz. To protect the experiment from microwave pollution, the fridge is inside a copper box that prevent electromagnetic waves from reaching the sample.

4.6.2   Noise measurements

The voltage between two ohmic contacts of the electronic MZI is amplified with a low noise amplifier, that can be modelled by a source of current noise in parallel with a source of voltage noise. It implies that when we measure the output signal autocorrelation, we cannot neglect the component due to the voltage noise of the amplifier. To eliminate this voltage noise, we realize cross correlation measurements [40][72]. We have represented figure 4.11 the general principle of cross correlation measurements. The voltage between the measured ohmic contact and the grounded ohmic contact of the MZI is amplified by amplifier 1 and amplifier 2, then the spectrum analyzer performs the cross correlation of these two amplified output signals.

We are now going to show the advantages of using a cross correlation measurement compared to an auto correlation measurement. We note $\langle V_{N,1}^2 \rangle$(resp. $\langle V_{N,2}^2 \rangle$) and $\langle I_{N,1}^2 \rangle$(resp. $\langle I_{N,2}^2 \rangle$) the voltage and current noise of the amplifier 1 (resp. 2). We note R_W the resistance of the two amplification lines , T_W the temperature of the wires (that we suppose equal for both lines). Finally , we note V_1 (V_2) the voltage output tension for each line.

If only one line is used, the general principle of the noise measurement is represented figure 4.10.

When we calculate the total noise, we have to take into account the voltage and current noise of the amplifier. We thus obtain :

$$\langle V^2 \rangle = G^2(\langle V_s^2 \rangle + \langle V_W^2 \rangle + \langle V_N^2 \rangle + (R_W + R_s)^2 \langle I_N^2 \rangle) \tag{4.2}$$

---

12. See Chapter 6, Part : Study of the coupling between the inner and outer edge state. When we wanted to measure the transmission of the inner and outer edge state independently, we have used two lock ins with two different frequencies of excitation.
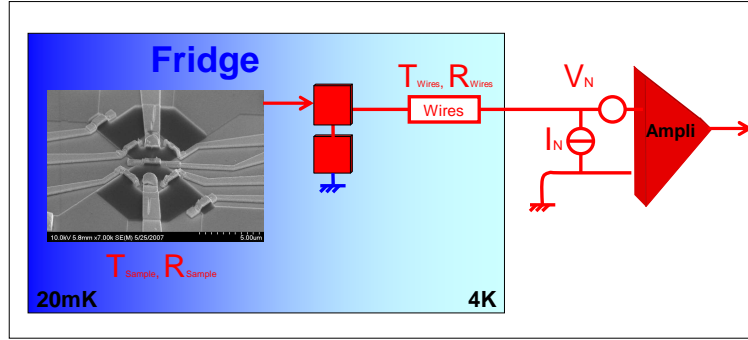
FIGURE 4.10 – Unique amplification line set up. We model it by an amplifier of gain G, a voltage and a current source noise. The auto correlation noise measurement is sensitive to Jonhson Nyquist noise due to the wires, and also to the voltage noise of the amplifier.

with R_s the resistance of the sample. In this formula $\langle V_W^2 \rangle$ is simply given by the Johnson Nyquist noise :

$$\langle V_W^2 \rangle = 4k_B T_W R_W \Delta f$$

where Δf is the frequency interval where noise measurements are performed. We want to extract $\langle V_s^2 \rangle$, but our measurement is also sensitive to other parasite noises, and above all to the Johnson Nyquist noise due to wires and to the voltage noise of the amplifiers.

When both amplification lines are used, as represented figure 4.11, one obtains for the autocorrelation noise :
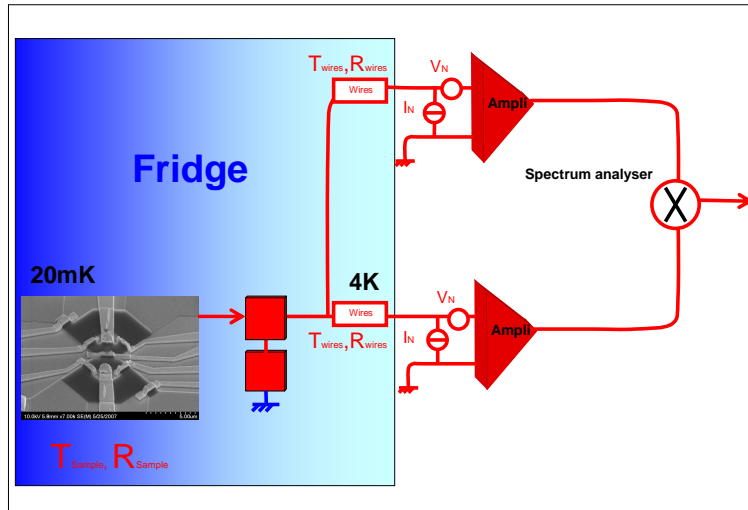
FIGURE 4.11 – Two amplification lines set up. Both amplified signals are sent on the spectrum analyzer that performs the cross correlation. Thanks to the cross correlation, the measurement is not sensitive anymore to the voltage noise of amplifiers and to the Johson Nyquist noise of the wires.
n

$$\langle V_1^2 \rangle = G_1^2(\langle V_s^2 \rangle + \langle V_{W,1}^2 \rangle + \langle V_{N,1}^2 \rangle + (R_W + R_s)^2 \langle I_{N,1}^2 \rangle + (R_s)^2 \langle I_{N,2}^2 \rangle) \qquad (4.3)$$

and for the cross correlation :

$$\langle V_1 V_2 \rangle = G_1 G_2 (\langle V_s^2 \rangle + R_s(R_W + R_s)\langle I_{N,1}^2 \rangle + R_s(R_W + R_s)\langle I_{N,2}^2 \rangle) \tag{4.4}$$

We first notice that if the auto correlation is always sensitive to the voltage noise of the amplifiers, it has disappeared in the cross correlation noise. Both Jonhson Nyquist noise of the wires 1 and 2, and voltage noise of amplifiers 1 and 2 are not correlated, only the current noise remains. Since $R_s I_N \ll V_N$ in our case, the sensitivity of the cross correlation measurement is higher than for an auto correlation measurement.

4.6.3   Measuring the visibility in the MZI

We recall the formula of the transmission probability through the MZI :

$$T = T_1 T_2 + R_1 R_2 + \sqrt{T_1 T_2 R_1 R_2} \cos \varphi(\epsilon) \tag{4.5}$$

where $\varphi(\epsilon) \propto \phi_{AB}(\epsilon)$. Consequently to observe oscillations, we must vary the Aharonov-Bohm (AB) flux through the surface defined by the two arms of the interferometer. We have realized measurements on samples of three different sizes : a small one (area of $8.5\mu m^2$), a medium one (area of $17\mu m^2$) and a large one (area of $34\mu m^2$). Two methods are possible to vary the AB phase [13] : either by varying the area defined by the paths (u) and (d) using a lateral gate or exploiting the gradual decay of the magnetic field in persistent mode at a rate of about ~ 0.11mT/hour ($\sim$ one quantum flux every 80 minutes on the small MZI (area of $8.5\mu m^2$)). The side gate has the huge advantage to reveal oscillations very fast (5 seconds compared to 80 minutes for the gradual decay of the magnetic field).

Indeed, if exploiting the gradual decay of the magnetic field in persistent mode is adapted for noise measurements (time constants are very long), for conductance measurement we want to be able to compare magnetic field/side gate methods very quickly.

Unfortunately to sweep one quantum flux with the current source of the magnetic coil, we need a $\sim 10^{-4}$A sensitivity. This sensitivity is not reached on our Oxford current source [14] . We have then added a current source in parallel, and have verified the two methods (magnetic field/side gate) on the same time scale ($\sim$ 5sec for one oscillation).

We have represented figure 4.12 the two equivalent ways to reveal oscillations.

Tuning of the beam splitters in the MZI

We have noticed that applying a positive gate voltage (0.5V) while cooling down, strongly enhanced the maximum visibility [18]. [15] Moreover, we have shown that to obtain the

---

13. We will see in the Chapter 7 that it is possible to reveal oscillations, by biasing the inner edge state. We actually have three methods to observe oscillations.

14. We have a $\sim 10^{-2}$A sensitivity on the Oxford current source.

15. Our cooling down is very fast, from the room temperature to 4K in 30mn. From 4K to 40mK in 5 hours. The positive voltage on the gates enables us to avoid any instabilities on the QPC and to obtain high visibility.
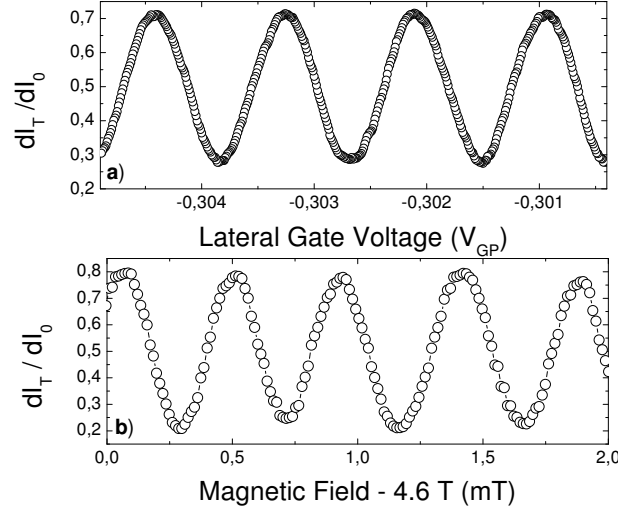
FIGURE 4.12 – **a)** dI_T/dI_0 as a function of the lateral gate voltage. **b)** dI_T/dI_0 as a function of the magnetic field. The interferences period is 0.46 mT which corresponds to a surface defined by the arms equal to 8.5 μm^2, in good agreement with the designed geometry of the MZI (7.25 μm^2). Interferences obtained at 4.6T and 20mK.

highest visibility, we had to tune very precisely the two beam splitters G_1 and G_2 to 1/2. To realize a precise tuning, we have always used the following method : if the first beam splitter G_1 is tuned to $T_1=1/2$, then the transmitted signal must be independent of G_2. Indeed, the average transmitted current is given by :

$$\langle I_T \rangle_\varphi = I_0 \langle T_1 T_2 + R_1 R_2 + \sqrt{T_1 T_2 R_1 R_2} \sin \varphi(\epsilon) \rangle_\varphi$$

or

$$\langle I_T \rangle_\varphi = I_0 (T_1 T_2 + (1 - T_1)(1 - T_2))$$

where I_0 is the injected current into the MZI, which can also be written :

$$I_T = (1 - T_1 + (2T_1 - 1)(T_2))I_0$$

If $T_1 > 1/2$, I_T increases with T_2. If $T_1 < 1/2$, I_T decreases with T_2, and if $T_1 = 1/2$, it is constant. Once T_1 is tuned to 1/2 following this method, we know that T_2 is set to 1/2 for the maximum of visibility [16]. With this method, we have reached up to 65% of visibility (obtained on the smallest sample at 18mK).

Measuring the visibility on a noisy sample

The first sample on which we have observed interferences had an unstable AB phase whose exact origin remains unknown. We have then developed an original method [68] to

_____

16. We have verified that $T_2=1/2$ obtained with this method corresponds to $T_2=1/2$ obtained independently.

measure the visibility, when instabilities (low frequency phase fluctuations) prevent direct observation of the periodic interference pattern obtained by changing the magnetic flux through the MZI (or the side gate).
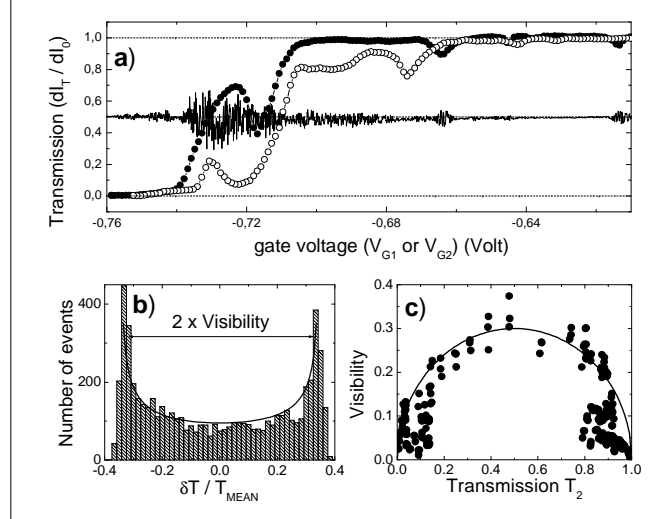
FIGURE 4.13 – Results obtained at 20 mK and 619Hz (lockin frequency) **a)**Transmission $T = dI_T/dI_0$ as a function of the gate voltages V_{G1} and V_{G2} applied on G1 and G2. ($\circ$) $T = T_1$ versus V_{G1}. ($\bullet$) $T = T_2$ versus V_{G2}. The solid line is the transmission T obtained with T_1 fixed to $1/2$ while sweeping V_{G2} : transmission fluctuations due to interferences with low frequency phase noise appears. **b)** Stack histogram on 6000 successive transmission measurements as a function of the normalized deviation from the mean value. The solid line is the distribution of transmission expected for a uniform distribution of phases. **c)**Visibility of interferences as a function of the transmission T_2 when $T_1 = 1/2$. The solid line is the $\sqrt{T_2(1 - T_2)}$ dependence predicted by the theory.

We have followed the usual method (see preceding part) to reveal oscillations : we have fixed the transmission T_1 to $1/2$ while sweeping the gate voltage of G2 (solid line of figure (4.13**a**)). Whereas for a fully incoherent system T should be $1/2 \times (R_2 + T_2) = 1/2$, we have observed large temporal transmission fluctuations around $1/2$. We show in the following that they result from the interferences, expected in the coherent regime, but in presence of large low frequency phase noise. This is revealed by the probability distribution of the transmissions obtained when making a large number of transmission measurements for the same gate voltage. Figure 4.13 (b) shows a histogram of T when making 6000 measurements (each measurement being separated from the next by 10 ms). The histogram of the transmission fluctuations $\delta T = T - T_{mean}$ displays two maxima very well fitted using a probability distribution

$$p(\delta T/T_{mean}) = \frac{1}{2\pi \sqrt{1 - (\frac{\delta T}{T_{mean}})^2 \frac{1}{\nu^2}}}$$

(the solid line of figure (4.13 b)). This distribution is obtained assuming interferences :

$$\delta T = T_{mean} \times \nu \sin(\varphi) \tag{4.6}$$

and a uniform probability distribution of φ over $[-\pi, +\pi]$. Then 4.6 leads to a probability distribution of δT equal to :

$$p(\delta T) = T_{mean} \times \nu \cos(\varphi)^{-1} p(\varphi) = \frac{1}{2\pi \sqrt{1 - \sin(\varphi)^2}}$$

Note that the peaks around $|\delta T/T_{mean}| = \nu$ have a finite width. They correspond to the Gaussian distribution associated with the detection noise which has to be convoluted with the previous distribution.

Although no regular oscillations of transmission can be observed due to phase noise, we can directly extract the visibility of the interferences by calculating the variance of the fluctuations (the approach is similar to measurements of Universal Conductance Fluctuations via the amplitude of 1/f noise in diffusive metallic wires). All the results have been obtained using the following procedure : we measured $N = 2000$ times the transmission and calculated the mean value T_{mean} and the variance $\langle \delta T^2 \rangle$. It is straightforward to show that the visibility is

$$\nu = \sqrt{2} \frac{\sqrt{\langle \delta T^2 \rangle - \langle \delta T^2 \rangle_0}}{T_{mean}}$$

where $\langle \delta T^2 \rangle_0$ is the measurement noise which depends on the AC bias amplitude, the noise of the amplifiers and the time constant of the lock-in amplifiers (fixed to 10 ms, lockin frequency $\sim$ 619 Hz), measured in absence of the quantum interferences. As expected when $T_1 = 1/2$, the visibility extracted by our method is proportional to $\sqrt{T_2(1 - T_2)}$, definitively showing that fluctuations result from interferences(see figure 4.13c).

This method was the one we used on an unstable sample to study the finite bias visibility of the interferences. Since then, we succeeded to obtain stable interferences. One can notice that this method can also be applied for stable samples : sweeping very fast the side gate, one just has to measure the amplitude of the output resulting oscillation.

4.7   Conclusion

In this part, we have shown how to build an electronic Mach Zehnder and what are the experimental techniques involved in this PhD. At the beginning of my PhD, the fabrication process and the method of observations were not settled. We tried at least 30 samples at low temperature before observing noisy oscillations. Two years later, I succeeded to observe oscillations with 65% visibility which has been a record during two months, before the work of the Weizmann group [60] where they obtained 90% at 10mK. Fabrication technics and observation methods are now well mastered. We are ready to study the physics of the MZI.

High visibility in an electronic Mach–Zehnder interferometer with random phase fluctuations

P. Roulleau[a], F. Portier[a], D.C. Glattli[a,1], A. Cavanna[b], G. Faini[b], U. Gennser[b], D. Mailly[b], P. Roche[a,*]

[a]*Nanoelectronic group, Service de Physique de l'Etat Condensé, CEA Saclay, F-91191 Gif-Sur-Yvette, France*
[b]*CNRS, Laboratoire de Photonique et Nanostructures, Route de Nozay, F-91460 Marcoussis, France*

Available online 17 October 2007

Abstract

We present an original method to measure the visibility of interferences in an electronic Mach–Zehnder interferometer in the presence of low frequency phase fluctuations. We studied the visibility of the interferences as a function of the energy and showed a gaussian variation of the decoherence and/or phase averaging at finite energy. This gaussian variation leads to a visibility modulation with a single side lobe.
© 2007 Elsevier B.V. All rights reserved.

Quantum information experiments have been a fruitful field of research in quantum optics partially thanks to the extremely long coherence length of the light. Under peculiar conditions, it is possible to realize experiments in quantum conductors which mimic the optical ones. A beamlike electron motion can be obtained in the integer quantum hall effect (IQHE) regime using a high mobility two dimensional electron gas in a high magnetic field at low temperature. In the IQHE regime, the electrons carrying the current drift along the sample edge equipotential and are described as one-dimensional gapless excitation modes called edge channels. The number of these edge channels corresponds to the number of filled Landau levels in the bulk. The chirality of the excitations yields to long collision times between quasi-particles, making edge states very suitable for quantum interferences experiments like the electronic Mach–Zehnder interferometer (MZI) [1–3]. Surprisingly, despite some experiments which show that equilibrium length in chiral wires is rather long [4], very few

is known about the coherence length or the phase averaging in these "so perfect" chiral uni-dimensional wires. In particular, while in the very first MZI experiment the interference visibility showed a monotonic decrease with voltage bias [1], in a recent paper, a lobe structure was observed in the variations of the visibility with bias voltage [5]. It is then difficult to conclude on the universality of these results and more experiments are highly needed.

We report here on an original method to measure the visibility v of interferences in a MZI when low frequency phase fluctuations prevent direct observation of the periodic interference pattern obtained when changing the electronic phase with a magnetic or an electric field. We studied the visibility at finite energy and we showed that the decoherence and/or phase averaging is proportional to $\exp(-V^2/2V_0^2)$, where V is the applied bias voltage.

The MZI geometry was patterned using e-beam lithography on a high mobility two dimensional electron gas in a GaAs/Ga$_{1-x}$Al$_x$As heterojunction with a sheet density $n_S = 2.0 \times 10^{11}$ cm^{-2} and a mobility of 2.5×10^6 cm^2/V s. The experiment was performed in the IQHE regime at filling factor $n_S h/eB = 2$ (magnetic field $B = 5.2$ T). Quantum point contacts (QPC) controlled by gates G0, G1 and

---

*Corresponding author. Tel.: +33 169087216; fax: +33 169088786.
E-mail address: patrice.roche@cea.fr (P. Roche).
[1]Also at Laboratoire Pierre Aigrain, Ecole Normale Supérieure, Paris.
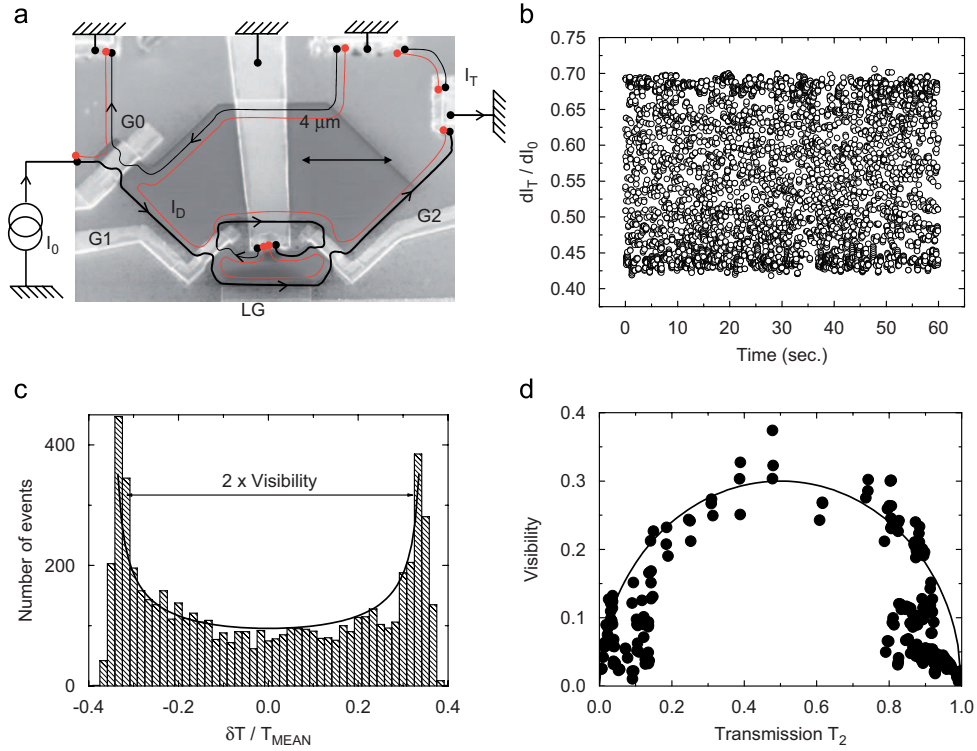
Fig. 1. (a) SEM view of the electronic Mach–Zehnder with a schematic representation of the edge state. The pairs of split gates defining a QPC (G0, G1 and G2) are electrically connected via a Au metallic bridge deposited on an insolator (SU8). G0 allows a dilution of the impinging current, G1 and G2 are the two beam splitters of the Mach–Zehnder interferometer. LG is a lateral gate which allows to vary the length of the lower path. (b) When the transmission T_1 and T_2 of beam splitters G1 and G2 are tuned to $\sim \frac{1}{2}$, the transmission through the MZI, $T = \mathrm{d}I_T/\mathrm{d}I_0$ fluctuates with time around the mean value $T_1 T_2 + R_1 R_2 \sim \frac{1}{2}$. (c) A stack histogram of the fluctuations reveals a distribution which results from a uniform distribution of phase noise convoluted with the measurement noise (see text). (d) Fixing $T_1 = \frac{1}{2}$, the visibility is proportional to $\sqrt{T_2(1 - T_2)}$ (the solid line).

G2 define electronic beam splitters with transmissions T_0, T_1 and T_2, respectively. In all the results presented here, the interferences were studied using the outer edge state schematically drawn as black lines in Fig. 1(a), the inner edge state being fully reflected by all the QPCs. The two arms defined by the mesa are 8 μm long and enclose a 14 μm² area. The current which is not transmitted through the MZI, $I_B = I_D - I_T$, is collected to the ground with a small ohmic contact. The impinging current I_0 can be diluted thanks to the beam splitter G0 whose transmission T_0 determines the dilution. We measure the differential transmission through the MZI by standard lock-in techniques using a 619 Hz frequency 5 μV$_{\mathrm{rms}}$ AC bias V_{AC} superimposed to the DC voltage V. The transmission T is defined as $\mathrm{d}I_T/\mathrm{d}I_0$.

When both beam splitters G1 and G2 are set to transmission $\frac{1}{2}$, and at low temperature (18 mK), we observed large temporal transmission fluctuations around $\frac{1}{2}$ (see Fig. 1b) which result from the interferences, expected in the coherent regime, but in presence of large low frequency phase noise. This is revealed by the probability distribution of the transmissions obtained when making a

large number of transmission measurements for the same gate voltage (Fig. 1b). The histogram of the transmission fluctuations is well fitted (Fig. 1c) using a probability distribution $p(\delta T/T_{\mathrm{mean}}) = 1/(2\pi\sqrt{1 - (\delta T/T_{\mathrm{mean}})^2/v^2})$ obtained assuming a uniform probability distribution of the phase φ over $[-\pi, +\pi]$, therefore demonstrating the signature of coherent interferences. The deduced visibility[2] varies with the beam splitters transmissions as expected within the Landauer–Buttiker theory (Fig. 1d).

The visibility depends on the bias voltage with a one side lobe structure shown in Fig. 2a. A fit, which is almost perfect for the whole range of T_0 (dilution), is

$$v = v_0 \mathrm{e}^{-V^2/2V_0^2} \left| 1 - \frac{V I_D}{V_0^2 \, \mathrm{d}I_D/\mathrm{d}V} \right|, \qquad (1)$$

[2] To deduce the visibility, we measured 2000 times the transmission and calculated the mean value T_{mean} and the variance $\langle \delta T^2 \rangle$. It is straightforward to show that the visibility is $v = \sqrt{2}\sqrt{\langle \delta T^2 \rangle - \langle \delta T^2 \rangle_0}/T_{\mathrm{mean}}$, where $\langle \delta T^2 \rangle_0$ is the variance of T due to measurement noise.

a
b
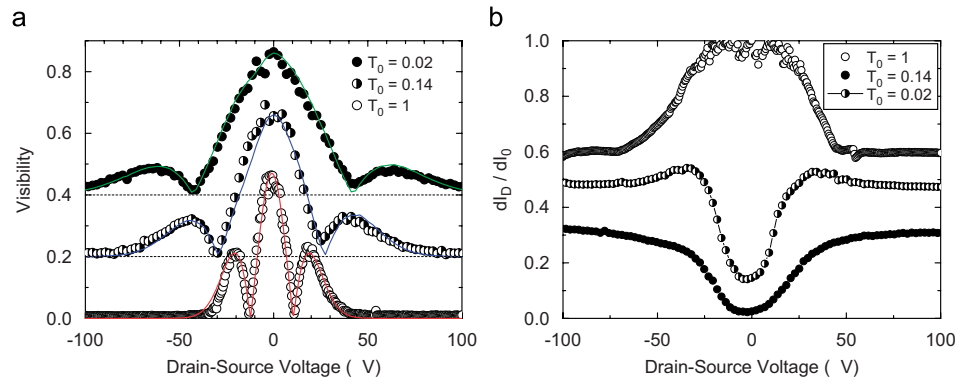
Fig. 2. (a) Visibility as a function of the drain–source voltage $V = I_0 h/e^2$ for three different values of T_0. The curves are shifted for clarity. The energy width of the lobe structure is modified by the dilution whereas the maximum visibility at zero bias is not modified. Solid lines are fits to the date using Eq. (1). From top to bottom, $T_0 = 0.02$ and $V_0 = 31\,\mu V$, $T_0 = 0.14$ and $V_0 = 22\,\mu V$, $T_0 = 1$ and $V_0 = 11.4\,\mu V$. (b) $dI_D/dV \times h/e^2 = dI_D/dI_0$ versus applied voltage for $T_0 = 1$, 0.14 and 0.02.

where V_0 a fitting parameter and v_0 the visibility at zero bias. Eq. (1) is obtained upon assuming that the decoherence and/or phase averaging is proportional to $\exp(-V^2/2V_0^2)$ (namely a phase noise $\delta\varphi^2 \propto V^2$). In such a case, the coherent contribution to the current $I_\sim$ is proportional to $I_D \times \exp(-V^2/2V_0^2)$. The measured coherent part of the overall transmission, $T_\sim = h/e^2\,dI_\sim/dV$ gives a visibility corresponding to formula (1) with a zero value and a π shift of the phase when $VI_D/(V_0^2\,dI_D/dV) = 1$. One can see in Fig. 2a that the fit with Eq. (1) is very good, even when the conductance is non-linear (dI_D/dI_0 varies with V, shown in Fig. 2b), definitively demonstrating that the existence of a single side lobe can be explained within our approach. Furthermore, there is a clear increase of the robustness V_0 when increasing the dilution, not shown here [6].

One may ask how robust is the lobe structure, well fitted by our approach. We indicate here some properties which may help to find the underlying mechanism responsible for the gaussian phase averaging. First of all, varying the transparencies of the beam splitter G1 and G2 does not change the energy scale. Increasing the temperature does not alter the lobe structure. It reduces the visibility at zero bias, but it merely adds a scaling factor. The variations of the finite bias visibility normalized by the zero bias value are not modified. However, we should point out that sometimes the lobe structure is not symmetric. This is particularly true when one applies a dc bias on the inner edge state which, in principle, does not participate to interferences. Moreover, when G0 is completely open, that is when the inner edge state is injected into the interferometer with the same bias as the outer one, the lobe

structure disappears, and the interferences have a larger visibility at finite bias. It means that we observe the lobe structure when only the outer edge carries current, namely when there is a finite spin current. As we also observe the lobe structure at filling factor one, this may indicate that finite spin current could play a role through, for example, nuclear spin fluctuations. At this stage we cannot conclude. It may be also possible that the physics of phase averaging mechanism occurs at the beam splitter when the filling factor in the depleted region beneath the QPC is less than one. However, if it was the case, we should observe a variation of the energy scale when varying the beam splitter transmission which, we do not observe. Finally, we also observed an increase of V_0 with the dilution. This effect remains puzzling but it has been reproduced on many samples.

To conclude, in addition to a new method to measure the visibility of interferences in presence of low frequency random phase fluctuations, we show for the first time that edge channels decoherence is well accounted by a phase noise proportional to V^2 which, combined to the measurement procedure, leads to a visibility modulation with a single side lobe [6].

References

[1] Y. Ji, et al., Nature 422 (2003) 415.
[2] P. Samuelsson, E.V. Sukhorukov, M. Büttiker, Phys. Rev. Lett. 92 (2004) 026805.
[3] I. Neder, et al., arXiv:0705.0173.
[4] T. Machida, et al., Solid State Commun. 103 (1997) 441.
[5] I. Neder, et al., Phys. Rev. Lett. 96 (2006) 016804.
[6] P. Roulleau, et al., Phys. Rev. B 76 (2007) 161309.

Chapitre 5

Finite bias visibility

Contents

5.1   Introduction

In this part, I investigate the finite bias properties of the MZI. This study is of importance as it will be necessary to apply a finite bias for noise measurements [1]. In principle, the visibility of the conductance oscillations should be independent of the bias. The reason is the following one : when one measures the differential transmission at finite bias V, one probes the differential transmission trough the MZI at energy eV. As a result, the phase of interferences may change (only if the arms of the interferometer are of different length) but, the amplitude of the visibility should not. Surprisingly, since the very first experiment of Ji *et al.* [37], a monotonous decrease of the visibility with the bias has been observed. Few years latter, in the same group, Neder at al. [57] have observed an intriguing lobe behavior in the visibility as a function of the bias, instead of a monotonous decrease. When we started our own study on the MZI, there was neither confirmation of these strange behaviors, nor theoretical explanation, apart from the theory of Sukorukov and Cheianov [79] who proposed a mechanism based on long range interaction between the two counter propagating edge states of the upper part of the MZI. I will present here a partial confirmation of the observation of Neder *et al.* [57]. I will show that our observations can be explained assuming a gaussian decrease of the visibility with bias voltage. This gaussian envelope (so far unexplained) leads to a one side lobe structure of the differential visibility which we observe at the upper end of the $\nu = 2$ plateau and at $\nu = 1$.

In this chapter, I will first describe the existing experiment to extract the general properties of the lobes. Then I will detail our experimental results and compare them with previous experiments. We have proposed a Gaussian envelope of the visibility in the case of one side lobe. With two side lobes, an additional term is necessary (unexplained). Finally, I will carry out a critical approach of the different theories proposed and show that some of them can explain the experimental observations, but never in a complete satisfactory way.

As you will see, the Gaussian envelope that we have observed and the analysis that we have proposed has been since used by other experimental groups, demonstrating an universality of this behavior.

5.2   Unexpected behavior of the visibility at finite bias

In the very first experiment [37](figure 5.1), the visibility voltage was monotonously decreasing with the applied bias. In this pioneering experiment, there was no partition gate G_0 to reflect the inner edge state. In a second experiment, the inner edge state was reflected and the visibility revealed an unexpected behavior with the bias : a lobe pattern.

---

1. As an example, the two ahoronov bohm oscillations, observed by Neder *et al.*, have been observed for $V = 8\mu V$ [60].

We will see why the reflection of the inner edge state is of importance to reveal side lobe structures.

5.2.1   The very first experiment : a monotonous decrease
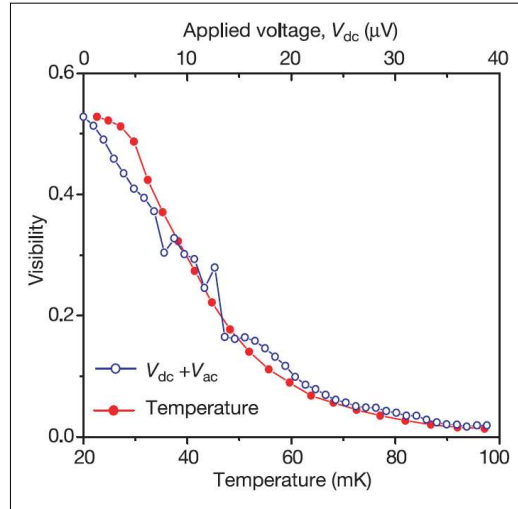
FIGURE 5.1 – The first experiment using the electronic MZI [37]. Visibility as a function of temperature for $V=0V$ (red plot), and as a function of V at the base temperature of the fridge (blue plot). Both gates G_1 and G_2 were set to T1 $\sim$ T2 $\sim$ 0.5(Ji *et al.* [37]).

Ji *et al.* [37] were the first to study the dependence of the visibility with the bias. They found a monotonous decay of it with the applied voltage (figure 5.1). To account for this decay, Ji *et al.*[37] pointed out two voltage dependent dephasing mechanisms. One might be due to low frequency noise (1/f type due to moving impurities), which might be induced by a higher current, leading to fluctuation in the area and consequently, to phase smearing. The other could be related to the self consistent potential contour at the edge. Since it depends on the local density of the electrons in the edge state, fluctuations in the density due to partitioning are expected to lead to fluctuations in the Ahoronov Bohm area enclosed by the two paths and hence to phase randomization. For example, for B $\sim$ 5.5T a mere 1$\sim$2 angstroms shift of the edge suffices to add one flux quantum into the enclosed area. Indeed these both mechanisms were plausible. The last one does correspond to recent theories [88][55] where the charge noise due to the partitioning by the first beam splitter generate phase randomization. I will detail this later.

5.2.2   One channel biased : an unexpected lobe pattern

In a second experiment [57] of the Weizmann group , most of the measurements were conducted at $\nu = 2$, with two edge channels. However, unlike in the first experiment, the inner edge was now totally reflected by G_0 and only the outer edge channel was injected into the MZI.

For zero DC bias on S2 and transmissions $T_1(T_2)$ of $G_1(G_2)$ equal to 1/2 (see figure 5.15 for the notations), the maximum visibility was $\sim 60\%$. In figure 5.2(a), I have represented a two-dimensional color plot of the AC voltage measured by Neder *et al.* [57] as a function of the modulation gate and the applied DC bias for ν=2. Figures 5.2(b) (ν=2) and (c) (ν=1) provide the normalized amplitude (visibility) and phase of the AB oscillations at different values of DC bias. Two features are common to Figures 5.2 (b) and (c). The visibility evolves in a form of a decaying lobe pattern with increasing V, dipping to zero periodically at specific biasing voltages. The phase is constant throughout each lobe but slips abruptly by $+\pi$ or $-\pi$ at each zero. The lobes are more pronounced at ν=2 than at ν=1. This behavior of a beating visibility and a rigid phase presents an energy scale of $\sim 10\mu eV$.

5.3   General properties of the lobe structure

Before looking at parameters which affect the lobe structure, I have to say here that the structure is temperature independent. It means that we recover exactly the same curve as a function of V for different temperature, once renormalized to the zero bias visibility.

5.3.1   Magnetic field dependence

One parameter which affects the lobe structure is the magnetic field. Neder *et al.* [57], have observed than the width of the lobe structure increases with the magnetic field, as I have shown in figure 5.3 (figure 3 of ref.[[57]]). A multiple side lobe structure has never been observed at filling factor 1. Indeed it raises an interesting question : is the presence of several edge states necessary for a multiple side lobe ? One actually cannot answer to that question as the increase of the lobe width with the magnetic field may also explain the disappearance of the multiple side lobes : at higher magnetic field a multiple side lobe may exist, but it is simply hidden by the general visibility decrease.

More recently, Litvin *et al.*[44] have studied this magnetic field dependence on a larger range of the magnetic field from the end of the plateau $\nu = 2$ to the beginning of the plateau $\nu = 1$. They found that the largest distance between the zeros was found around $\nu = 1.5$ and reduces, when ν moves from $\nu = 1.5$ to $\nu = 1$ or $\nu = 2$. For $\nu > 1.5$ more than one pair of side lobes can be observed (see figure 5.4(a)). To fit their data, they consider the product of an oscillatory function and a Gaussian envelope. They obtained this fit mixing our approach [2](see part 5.4.2) and Levkivskyi and Sukhorukov's result [43] which predicts an additional cosine term combined with the expected visibility [3], which finally gives :

$$\nu_I = \nu_{I0}|cos(\pi V/V_L)|exp(-V^2/2V_{lob}^2)$$

This formula contains the parameters V_L as the period of the cosine term and V_{lob} as the characteristic width of the envelope. In figure 5.4(b), I have plotted their measured

---

2. We will show later that they did not apply exactly our approach.
3. We will discuss this point in 5.7.3.
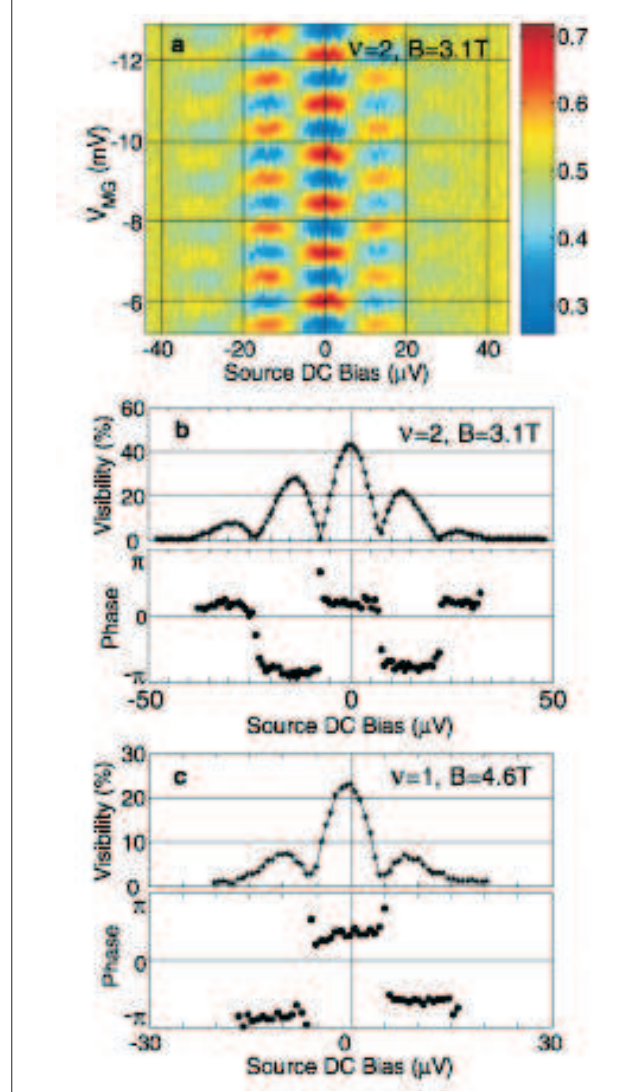
FIGURE 5.2 – Interference oscillations and visibility. (a) Two dimensional color plot of the differential transmission as a function of the applied DC bias.(b). The visibility and the phase of the interference pattern at ν=2 as a function of the applied DC bias. Five major lobes are visible, each $\sim 14\mu V$ wide. The phase at each lobe is constant and slips abruptly by π at each node. (c) A similar graph at ν =1 exhibiting only 3 major lobes (or one side lobe) with similar stick-slip phase behavior (Neder *et al.* [57]).

magnetic field dependence of V_{lob} and V_L. Both energy scales increase from the end of $\nu = 2$ to reach a maximum at $\nu = 1.5$, and then decrease to $\nu = 1$. It is important to underline the differences between results obtained by Neder *et al.* and Litvin *et al.* When
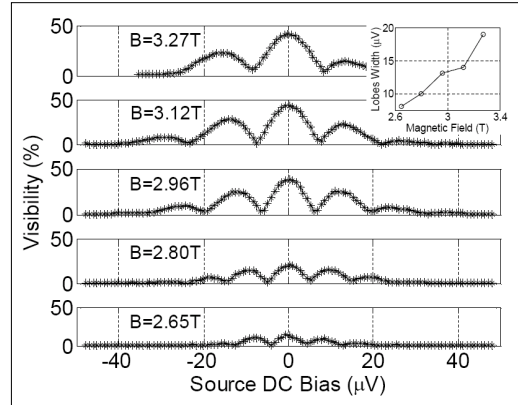
FIGURE 5.3 – Evolution of the lobe structure with the magnetic field. For lower magnetic field, the maximum visibility is lower, but one can observe multi side lobes. At the end of the plateau $\nu = 2$, the visibility is higher, but one notes only one side lobe. (Neder *et al.* [57]).

Neder *et al.* studied the magnetic field dependence of the lobe pattern, they found that the periodicity of the lobe increased from the beginning of the plateau $\nu = 2(\sim 10\mu V)$ to reach $\sim 20\mu V$ at the end (see inset of the figure 5.3). Considering the figure 5.2(c), at $\nu = 1$ the lobe width $\sim 10\mu V$ which means that for intermediary values of the magnetic field (between $\nu = 2$ and $\nu = 1$) the lobe width observed by Neder *et al.* should decrease. For Litvin *et al.* the periodicity of oscillations is given by V_L. The general behavior of V_L with the magnetic field is the same : it increases first and then decrease around $\nu = 1.5$. But they begin to observe oscillations at the very end of the plateau $\nu = 2$, raising the question of their definition of the homogeneity of the electronic density within the sample [4]. Moreover, their lobe width are in average $\sim 20\mu V$, the double of Neder *et al.* This energy scale seems sample [5] dependent.

5.3.2   Dependence on the dilution

A way to check whether the lobe structure is affected by e-e interaction between edge states, or within one edge state is to dilute the incoming beam. This can be done by partly reflecting the interfering edge channel with G_0. Neder *et al.*[56] were the first to be interested in the T_0 dependence of the lobe pattern . I have represented their results in the figure 5.5 : for an occupation of 20% [6], the higher order lobes stretched out to higher voltages and weakened significantly, but the main lobe remained almost invariant compared to $T_0=1$. It is interesting to note that they did not try to dilute more their impinging beam : their

_____

4. Their geometry is different from the one of Neder *et al.* It may explain why their definition of the filling factor in their sample is not the same than in the interferometer. It is quite surprising that they do not observe oscillations on the plateau $\nu = 2$ (as Neder *et al.* we observe oscillations on the whole plateau), but this discrepancy between their and our results remain, to date, unexplained.

5. Or size dependent, but unfortunately the area of the Neder *et al.* sample seems not to be specified in [57].

6. Namely the transmission T_0 is set to 0.2.
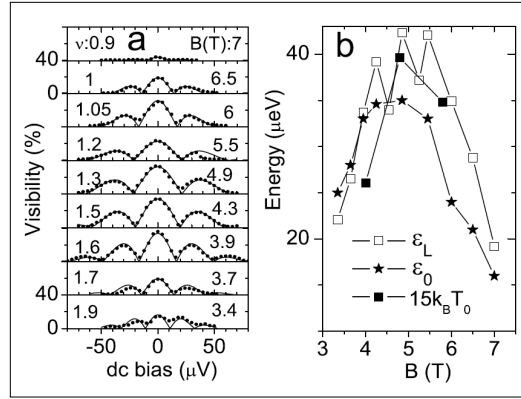
FIGURE 5.4 – Differential visibility of the small MZI. (a) Lobe structures at different magnetic fields. General behavior is the same than Neder *et al.*, supposing a shift in their definition of filling factor 2 (b) Characteristic energies V_L and V_{lob} as a function of the magnetic field. Their lobe width are in average $\sim 20\mu V$ (Litvin *et al.*[44]).*In this figure* $\epsilon_L \equiv V_L$ *and* $\epsilon_0 \equiv V_{lob}$

minimum occupation is 20% meaning that they tune the transmission T_0 to 0.2. We have studied the dilution effect below this occupation of 20% and we have found that, in that case, the main lobe is strongly affected by the dilution.
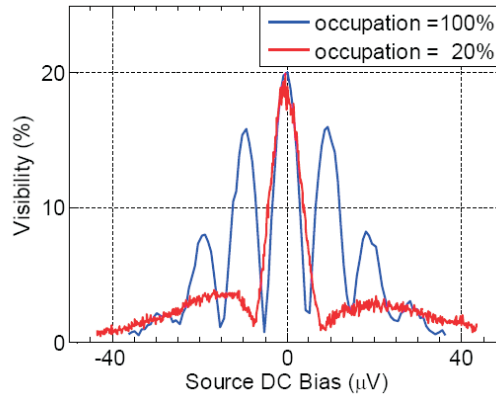
FIGURE 5.5 – The effect of beam dilution on the lobe pattern of the visibility. The dilution was performed by reflecting a part of the impinging channel with G_0. When the occupation of the incoming edge channel was reduced to 20 %, the higher order lobes stretched and vanished while the main lobe remained almost unaffected (Neder *et al.* [56]).

5.3.3   Two channels biased

In a recent experiment [15] Bieri *et al.* have studied the dependence of the visibility with the tranmission of the first beam splitter (G_1) when both edge states are fed with

the same bias [7]. They were mainly interested in the regime of weak tunneling ($T_{1,out} \to 0$) and weak backscattering ($T_{1,out} \to 1$). In their experiment, only one side lobe seems to be resolved. In the weak tunneling regime (WT) (figure 5.6(a)), they observe a lobe structure analogous to the one reported by the other groups [57][68][44]. The phase gradually evolves at small bias-voltage and a more complex curved pattern is observed at larger bias voltages (figure 5.6(b)).

The visibility dependence with DC bias in the weak backscattering(WB) limit is very different. In this regime, the visibility first increases with increasing DC bias, while at larger bias voltages the visibility decreases. (figure 5.6(a))

Bieri *et al.* have realized several tests to check that this effect is intrinsic and does not depend on the beam splitter properties. [8]

We will show next, that this effect can be well understood within a simple model of capacitive coupling between the inner and outer edge state. In particular, and this is the main point, Bieri *et al.* have made the statement that they observed only one side lobe and that in the WB this one side lobe was affected. I think that this is not correct. In particular, I will show that in reality there is a double side lobe structure, the first lobe being hidden. Indeed, since they do not have a partition gate G_0, they cannot separate the inner edge state from the outer one. Consequently they are mixing several phenomena : lobe structure and capacitive coupling effects. Taking into account the inner edge state, we will show that the increase of the visibility at finite bias simply results from the capacitive coupling between the two edge states. I will show how one can fit their results with such a model.
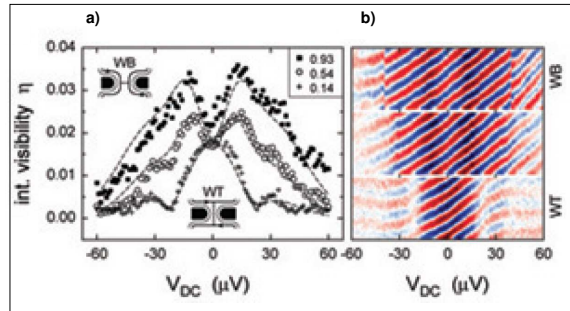
FIGURE 5.6 – (a) Dependence of the "intrinsic" visibility [15] for three different T_1 values (T_1 =0.93, 0.54 and 0.14) and QPC G_2 fixed. In the weak backscattering limit the visibility first grows with increasing the bias, whereas it decays in the opposite case of weak tunneling. The curves are guide to the eyes. (b)Phase evolution as a function of the bias in the WB, WT and intermediate regime. (Bieri *et al* [15])

---

7. Like in the very first electronic MZI of Ji *et al.*[37], Bieri *et al.*[15] did not include a partition gate G_0.

8. They have reversed the magnetic field, the first(second) beam splitter becoming the second (first) beam splitter. They have verified that this effect always depended on the first beam splitter.

5.4 Our experimental results

5.4.1 Phase rigidity and visibility

Measurements realized on a middle size interferometer

Our first measurements of the visibility dependence with the bias voltage have been realized on a middle size interferometer, at 4.8 Tesla (end of the Hall plateau at ν=2). The two arms defined by the mesa are 8 μm long and enclose a 14 μm^2 area.The first measurements of the lobe pattern have been realized on a noisy sample, following the method developed in the part 4.6.3. We have verified that we obtained the same results on a stable middle size sample. I have represented in figure 5.8(a) the visibility versus the DC bias voltage. We observe here only one side lobe structure. Figure 5.8(b) shows that the phase is constant throughout each lobe but slips abruptly by $+\pi$ or -π at each zero.
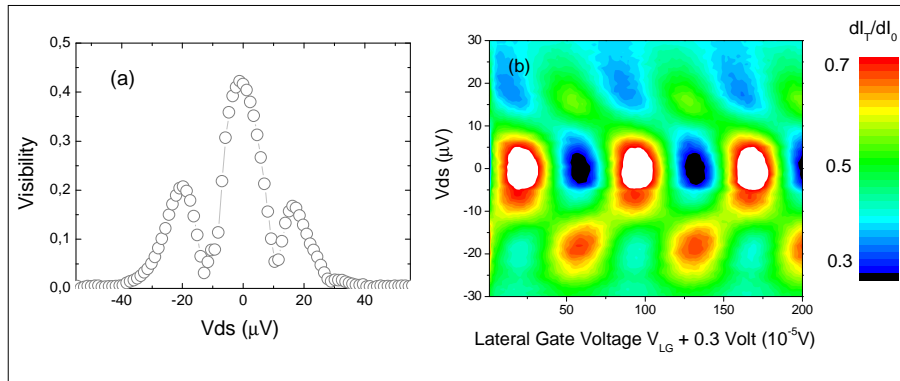
FIGURE 5.7 – (a) The visibility of the interference pattern at ν=2 as a function of the applied DC bias. Only three major lobes are visible. (b) Two dimensional color plot of the $\sim 400Hz$ AC MZI transmission as a function of the applied DC bias (V_{ds}) and the lateral gate voltage, at filling factor $\nu = 2$ with transmission $T_1 = T_2 \sim 1/2$. The phase at each lobe is constant but slips abruptly by π at each node.

This first experiment did not reveal multi side lobe, although the sensitivity of our measurements was high enough to observe a second one if it existed. We obtain a lobe width of $\sim 20\mu V$ at the end of the plateau $\nu = 2$ close to the one obtained by Neder *et al.* (see inset of figure 5.3), but very different from the one obtained by Litvin *et al.*(see figure 5.4(b)). We have also realized measurements at $\nu = 1$ and have observed a lobe structure (only one side lobe) (see figure **??**).

Measurements realized on a large size interferometer

We have also probed the finite bias visibility on a large size interferometer, at a lower magnetic field (4.28 Tesla)(beginning of the plateau ν=2). The two arms defined by the mesa are 11.3μm long and enclose a 35.5μm^2 area. This experiment has revealed multi side lobe as represented figure 5.9. If we now compare it to other groups results, we observe a multi side lobe at the beginning of the plateau at $\nu = 2$ once again in agreement with Neder
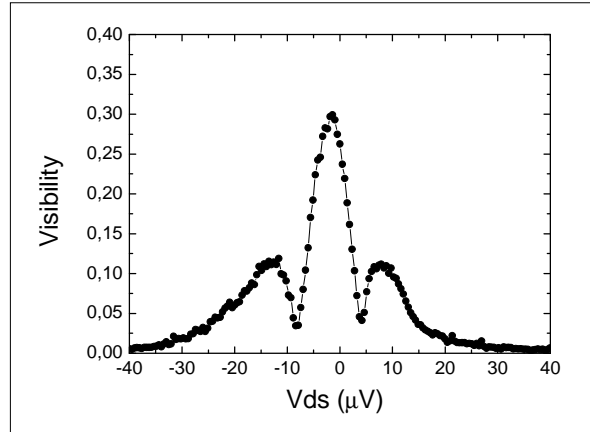
FIGURE 5.8 – The visibility of the interference pattern at ν=1 as a function of the applied DC bias. Only three major lobes are visible. Compared to $\nu = 2$, we notice a lobe width slightly smaller $\sim 13\mu V$.

et al.(see inset of figure 5.3),but still in disagreement with Litvin *et al.* (see figure 5.4(b). However if we consider the central lobe width, we find a periodicity $\sim 20\mu V$ comparable to the one obtained with the middle size sample at the end of the plateau, whereas Neder *et al.* and Litvin *et al.* both find a magnetic field dependence of this energy scale. However, we have measured the lobe structure only for two values of B (at $\nu = 2$) and for two sample sizes : there may be (most probably) a size dependence of the lobe width. A more systematic study with different sizes on the whole plateau $\nu = 2$ should be realized to answer this question (I did not realize this study) .
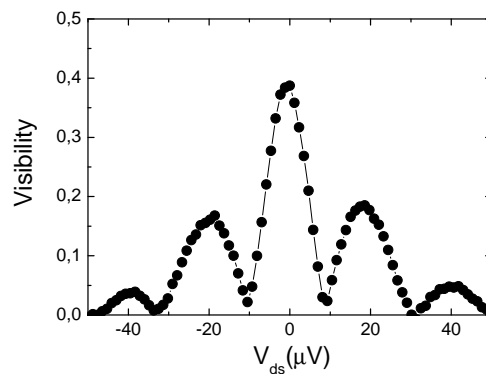
FIGURE 5.9 – The visibility of the interference pattern at ν=2 as a function of the applied DC bias for a larger sample (35.5μm^2 area) and at a magnetic field of 4.28 Tesla. There, two side lobes are visible.

5.4.2   A Gaussian shape visibility

Since no theory was available to understand the lobe structure[9], we aimed to find a general expression that could fit our data. When we worked on that fit, we had carried out measurements only at the upper end of the $\nu = 2$ plateau, hence we considered only one side lobe. Also in our very first experiment realized on the noisy sample, we did not observe multi side lobes. We have found an almost perfect fit for this lobe structure whose origin can be explained as following. I start with the general formula of the interfering part of the current $I_\sim$ at the bias voltage V, assuming that there is a stochastic distribution of the phase φ during the measurement. Hence $I_\sim$ writes :

$$I_\sim = \frac{e^2}{h} V \sqrt{T_1 R_2 T_2 R_1} \langle \sin(\varphi) \rangle$$

where $\langle \rangle$ denotes the average of $\sin(\varphi)$ over the phase distribution. I now assume a Gaussian phase averaging with a variance $\langle \delta\varphi^2 \rangle$. $\langle \sin(\varphi) \rangle$ becomes :

$$\langle sin(\varphi) \rangle = \sin(\langle \varphi \rangle) e^{-\langle \delta\varphi^2 \rangle / 2}$$

$\langle \varphi \rangle$ being given by $\langle \varphi \rangle = \langle \varphi_0 \rangle + \frac{eV \Delta L}{\hbar v_D}$. Our sample being designed with $\Delta L = 0$, the mean value $\langle \varphi \rangle$ does not depend of the bias. Then I will assume that the variance is given by :

$$\langle \delta\varphi^2 \rangle = \frac{V^2}{V_{lob}^2}$$

with V_{lob} a fitting parameter. The Gaussian distribution of the phase then leads to :

$$I_\sim = \frac{e^2}{h} V \sqrt{T_1 R_2 T_2 R_1} \sin(\langle \varphi \rangle) e^{-\frac{V^2}{2V_{lob}^2}}$$

where $\langle \varphi \rangle$ is the mean value of the phase distribution. The differential conductance $G_\sim = \frac{dI_\sim}{dV}$ is thus :

$$\frac{dI_\sim}{dV} = \frac{e^2}{h} \sqrt{T_1 R_2 T_2 R_1} \sin(\langle \varphi \rangle) e^{-\frac{V^2}{2V_{lob}^2}} |1 - \frac{V^2}{V_{lob}^2}| \tag{5.1}$$

in the following $\langle \varphi \rangle$ will be noted φ

Such behavior gives a zero visibility accompanied with a π shift of the phase when $V^2/V_{lob}^2 = 1$. I have represented in figure 5.10(a) a fit to our data with $V_{lob} \sim 11\mu$ V. One can remark that the fit is excellent. In fact, our approach is in very good agreement with all our data, except for our observation of multiple side lobes.

To fit the multi lobe pattern, we introduce an additional term :

$$I_\sim \approx eV \times e^{-V^2/2V_{lob}^2} \cos(V/V_c) \times \sin(\varphi) \tag{5.2}$$

---

9. There is a theory of Sukhorukov *et al.*[79] which explains the lobe structure considering the long range interaction between two counter propagating edge states. However this theory should not apply when the spatial separation between the counter propagating edge states is large compared to the length of the interfering path which is the case in our samples.
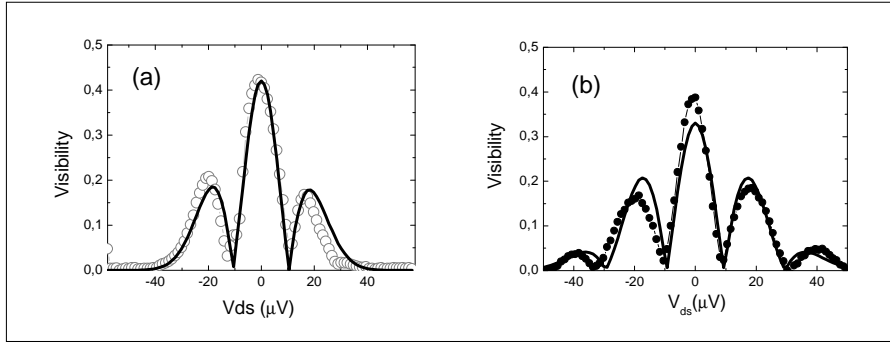
FIGURE 5.10 – (a) In blacks circles the visibility as a function of the bias. In black solid line, I have plotted the formula 5.1. We obtain $V_{lob} \sim 11\mu V$.(b) In blacks dots the visibility for the sample which presented multiple side lobes. In black solid line, we have plotted our formula 5.2. We obtain $V_c \sim 13\mu V$, $V_{lob} \sim 14\mu V$.

where V_c is an unknown parameter. The Gaussian approximation approach regarding the phase is always valid but the $\cos(V/V_c)$ term adds another oscillating term in the differential visibility. The expression of the differential conductance now becomes :

$$\frac{dI_\sim}{dV} \propto (-\frac{V}{V_c}\sin(V/V_c) + \cos(V/V_c)(1 - \frac{V^2}{V_{lob}^2})) \times e^{-V^2/2V_{lob}^2} \times \sin(\varphi) \qquad (5.3)$$

I have represented figure 5.10(b) formula 5.3 fitting our experimental data, with $V_c \sim 13\mu V$ and $V_{lob} \sim 14\mu V$. It is noteworthy that this fit (Gaussian envelope) has worked for many different samples with different sizes and different magnetic fields. It makes us confident on the existence of a Gaussian shape of the visibility. As I have previously mentioned, this kind of Gaussian profile has been recently used in a paper by Litvin at al. to analysis their results. I have to stress here that we do not have precise idea on the origin of these terms. But the lobe structure is not *unexpected* when there is only one side lobe structure. It simply results from a particular attenuation of the interfering part of the current combined to the measurement of the differential conductance. This gives an access to a typical energy scale eV_{lob} whose general properties are :
  – It is not modified by the transmission of the first beam splitter [10]
  – It is not modified by the transmission of the second beam splitter.
  – It is not affected by the temperature (when varying the temperature between 20 and 100mK) [11].
  – It exists at $\nu = 1$.
  – It also exists when there is multiple side lobes. It suggests that we are in presence of two effects : a Gaussian envelope and an additional term (unexplained) [12].

─────────────────

10. When the inner edge state is reflected. We will see that when both edge states are fed with the same bias, eV_{lob} varies with the transmission of the first beam splitter.

11. Once renormalized to the zero bias visibility.

12. Since this additional term is a cosine, we could think about a beating between two modes. This possibility is the key point of the Levkivshyi and Sukhorukov's [43] approach.

In a previous part (5.3.1), I have shown that Litvin *et al.*[44] have proposed a very close expression to fit multi side lobes :

$$\frac{dI_\sim}{dV} \sim eV \times e^{-V^2/2V_{lob}^2} |\cos(\pi V/V_L)| \times \sin(\varphi)$$

with $\pi \times V_c = V_L$. We recognize in this expression the Gaussian envelope and an additional cosine term directly inspired by Levkivskyi and Sukhorukov's [43] (see also formula 5.16 in this chapter). However if this additional term has been theoretically obtained for the differential conductance, I think that this is not correct to add the Gaussian envelop to the differential conductance. For the differential conductance, one obtains necessarly a different expression [13].

Finally, I have proposed a general expression that could fit the lobe pattern of the visibility with the bias voltage. In the case of multi side lobes, an additional unexplained term is necessary. A more detailed study at different magnetic field would allow to understand evolutions of V_c and V_{lob} explaining why at high magnetic field only one lobe is observed.

5.4.3   Influence of the dilution
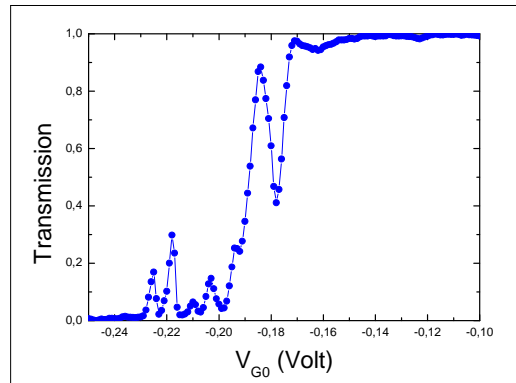
FIGURE 5.11 – The transmission of the outer edge state $T_{0,out}$ as a function of the gate voltage applied, T_1 and T_2 being tuned to 0. The transmission varies from 0 to 1 for gate voltages between -0.16V and -0.23V.

In this part, I study the impact of a diluting beam on the lobe pattern. Up to now, T_0 was set to 1. I will show that when the impinging current is diluted (T_0 close to zero, see also figure 5.11) the lobe width increases, which in other words means that the energy scale, responsible for the Gaussian envelop, is slightly modified. When the impinging current is diluted the formula 5.1 is lightly modified since the diluted current I_D is no more proportional to V. This is not due directly to the dilution, but to the fact that the transport becomes non linear. In the most general case, and above all, when T_0 is close to 0,

---

13. The derivative of the Gaussian envelope with V adds another term in he expression of the visibility.

dI_D/dV varies with V. To take into account these non linearities of I_D, one must write that the interfering current is proportional to I_D :

$$I_\sim \propto I_D \times \sin(\varphi)e^{-\frac{V^2}{2V_{lob}^2}}$$

The differential conductance thus becomes :

$$\frac{dI_\sim}{dV} \propto |1 - \frac{VI_D}{V_{lob}^2 dI_D/dV}|e^{-\frac{V^2}{2V_{lob}^2}}\sin(\varphi), \tag{5.4}$$

a formula which is exactly the same that 5.1 when $\frac{I_D/V}{dI_D/dV}$=1.
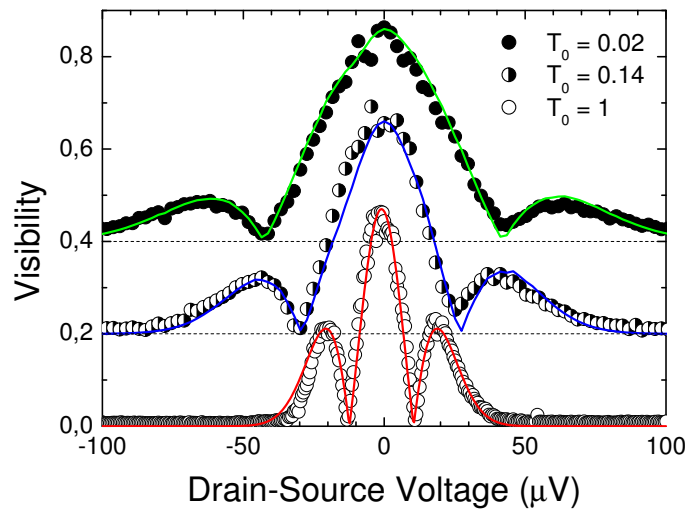
FIGURE 5.12 – Visibility of the interferences as a function of the drain-source voltage $I_0 h/e^2$ for three different values of T_0. The curves are shifted for clarity. The energy width of the lobe structure is modified by the dilution whereas the maximum visibility at zero bias is not modified. Solid lines are fits using equation (1). From top to bottom, $T_0 = 0.02$ and $V_0 = 31~\mu V$, $T_0 = 0.14$ and $V_0 = 22~\mu V$, $T_0 = 1$ and $V_0 = 11.4~\mu V$.

I have represented in figure 5.12 our experimental data in dots for different transmissions. We first notice the strong impact of dilution on the lobe width : the lobe width is enhanced when the transmission T_0 decreased. The agreement between our model and the experimental data is very good on the whole range of T_0, definitively showing that the existence of one side lobe, as observed in the experiment of [57] at $\nu = 2$ (for the highest fields) and at $\nu = 1$, can be explained within our simple approach a Gaussian envelope.

We have summarized our results in figure 5.13, where we have represented V_{lob} on the whole range of the transmission T_0 for two different samples (a noisy one and a stable one).

We first note that V_{lob} increases with the dilution, namely when the transmission T_0 at zero bias decreases. An impact of the dilution has already been observed as it suppressed multiple side lobes [56] (arXiv version of [57]), but the conclusion was that the width of the central lobe was barely affected. Here, dilution plays a clear role, which is nevertheless not
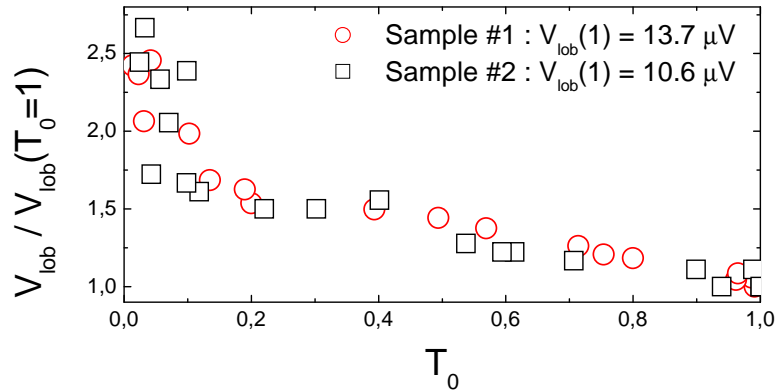
FIGURE 5.13 – V_0 obtained by fitting the visibility with equation (1), normalized to V_0 at $T_0 = 1$, as a function of T_0 at zero bias.

easy to explain. At first, we thought that the length between the partition gate and the MZI was smaller that the coherence length [69] and hence we expected the energy redistribution to be negligible. This argument that we had used is merely wrong. Indeed at zero bias, the coherence length is long but we do not know if it is actually true at finite bias. For example, the Gaussian envelope could arise from a short inelastic collision process. Then, the dilution effect could result from a redistribution in the wire leading "de facto" to an apparent increase of the energy scale associated to the lobe structure. In figure 5.14, we have represented in blue dots experimental data plotting now T_0 not defined at zero bias but for the V_{ds} that minimizes the visibility, and in red line the expected $1/T_0$ dependence of the V_{lob} assuming a complete redistribution of the wire. Then, it may indicate that there is a partial redistribution

5.5 Coupling between the inner and outer edge state

In this part, I will study the capacitive coupling between the inner and outer edge state. I will show why in the very first experiment, Ji *et al.*[37] did not observe the lobe pattern. I will also explain the "unexpected" enhancement of the visibility obtained by Bieri *et al.* [15].

Terminology *: I will introduce T_0 as the "global" transmission of the edge states. If I call $T_{0,in}(T_{0,out})$ the transmission of the inner (outer)edge state, I will define $T_0 = T_{0,in} + T_{0,out}$. As the channels are opened one by one, $T_0 = 2$ when $T_{0,in} = 1$ and $T_{0,out} = 1$, $T_0 = 1$ when $T_{0,in} = 0$ and $T_{0,out} = 1$, $T_0 = 0$ when $T_{0,in} = 0$ and $T_{0,out} = 0$*

5.5.1 Modelling the capacitive coupling between edge states

I consider in this part the coupling between the inner and outer edge state, which in a mean field approximation can be simply viewed as a capacitive coupling . The experimental way that I used to feed the edge states with different bias is represented in figure 5.15. I
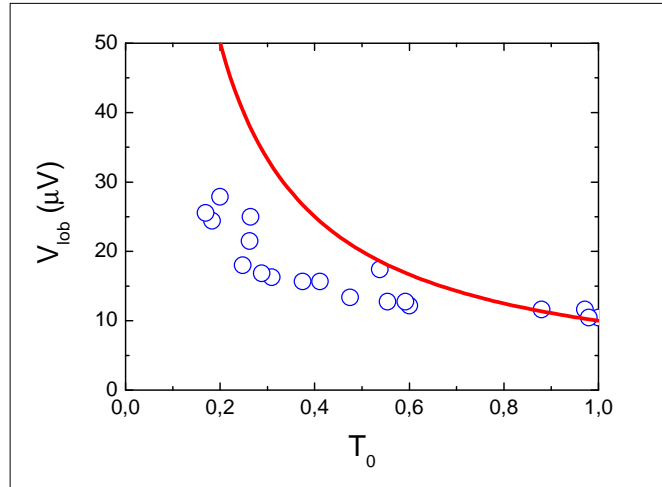
FIGURE 5.14 – In blue dots V_{lob} obtained by fitting the visibility with equation 5.4, as a function of T_0. Now T_0 is defined for the V_{ds} that minimizes the visibility. Assuming a complete redistribution of the wire, we should obtain a $1/T_0$ dependence of the V_{lob}(represented in red solid line). These data seem to indicate a partial redistribution in the wire.
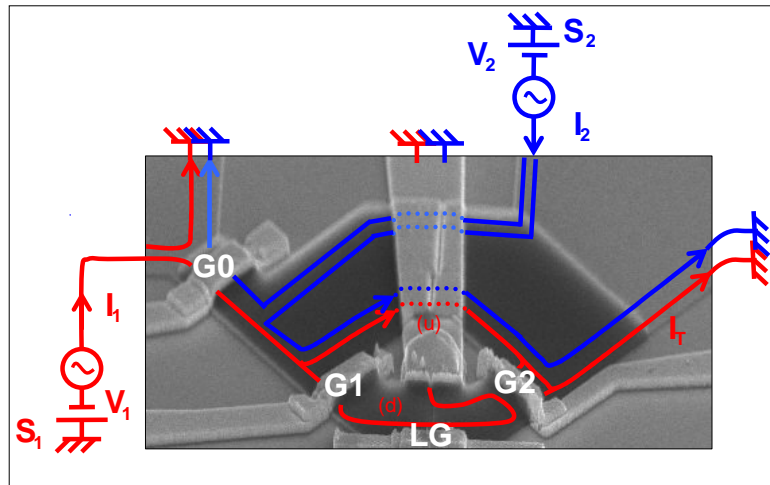
FIGURE 5.15 – Tilted scanning electron microscope view of the device, with schematic representation of the edge states. On this representation the gate G_0 is set to transmission $T_0=1$. Two edge states are injected into the MZI : the outer edge-state drawn in red (bias voltage V_1), and the inner one drawn in blue (bias voltage V_2). In our experiment, I have superimposed small AC signals at different frequencies on source S_1 and S_2 in order to measure by standard lock-in technics the components of the total transmitted current which oscillate synchronously at these two frequencies.

have represented in blue the inner edge state, in red the outer interfering edge state.

The first experiment showing the coupling between the inner and outer edge state has been performed by Neder *et al.*[58]. They used the inner edge as a "which path"

detector to perform path determination in a two-path electron interferometer [14], leading to full suppression of the interferences. This article was the first to reveal the interactions between the inner and outer edge state, in a MZI. We propose here an approach based on a simple mean field approximation that allows to catch **almost** all the picture of the lobe structure when the two edge states are fed with the same bias. Indeed the mean field approximation does not lead to a lobe structure. However assuming that it exists, I will show that the coupling between edge states(cross talk effects) modifies their observation. I will show that this can explain both the results by Bieri *et al* and also the absence of a lobe structure in the pioneering experiment of Ji *et al* [37].

To study the interaction between the inner and the outer edge state, I first tune the transmission of the first partition gate T_0 to $T_0=1$ and $T_{1,out}=T_{2,out}=1/2$ (see figure 5.16).
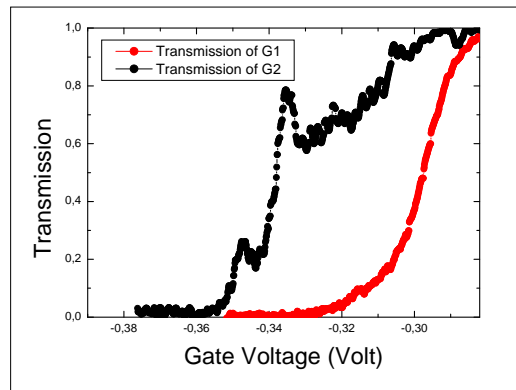
FIGURE 5.16 – In red dots, the transmission of the first gate G1 as a function of the gate voltage applied. In black dots the transmission of the second gate G2. Since interferences are obtained on the outer edge state, transmissions vary between 1 and 0. To obtain the maximum visibility G1 and G2 are tuned to 1/2 namely, -0.335V for G2 and -0.295V for G1.

Then, I measure the visibility of the outer edge state emitted from S_1 and its capacitively induced signal on the inner edge state emitted from S_2 [15].

When I have derived the formula 5.2 , I have assumed that the charges in the inner edge state did not modify the phase of the electrons in the outer edge state : this hypothesis is not correct [16]. When I apply a DC bias voltage on S_2 (the way it is done is schematically represented in figure 5.15), electrons of the inner edge state modify the potential seen by the electrons in the outer channel, and hence their phase. In this picture, the inner edge state can be viewed as a lateral gate. This is shown in the figure 5.17 where I have revealed the interferences on the inner edge state by varying the voltage applied on the outer one. From this measurement, I determine the **coupling** parameter V_0, which is the periodicity of the oscillation pattern revealed by this method.

---

14. The "which path" words are the one used by Neder *et al.*[58] .

15. Experimentally, I use two lock-in with two different excitation frequencies : one for each edge state.

16. Fortunately, if the inner edge state is reflected, which was the case up to now, neglecting the interaction with the inner edge state still gives the good result for the visibility.
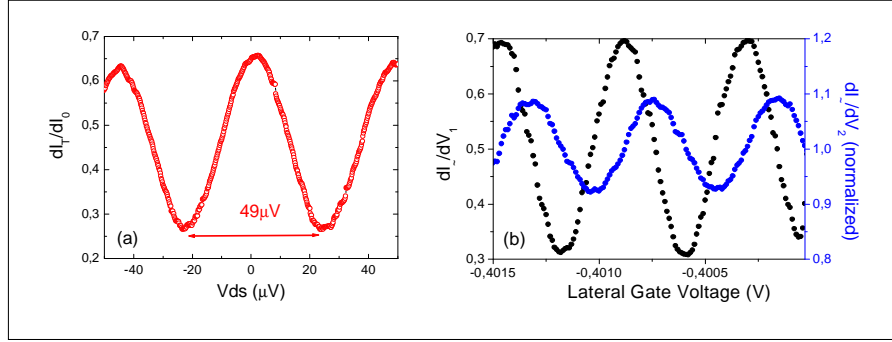
FIGURE 5.17 – (a)Observation of the capacitive coupling between the inner edge state and the outer edge state. These measurements are made on the large sample, at 4.66T. The first beam splitter G_0 is set to $T_0=1$, whereas beam splitters G1 and G2 are both set to $T_1=T_2\sim1/2$ in order to have the biggest visibility. A DC voltage is then applied on the inner edge state (drawn in blue on figure 5.15). As one can remark, the interferences are revealed by varying V_2, the voltage applied on the inner edge state. The period of the interferences obtained by this method is called V_0. It characterizes the coupling between the two edge states. (b) The DC voltage applied on the inner edge state is now suppressed. I study here separately the impact of V_2 and V_1 by measuring the differential conductance dI_T/dV_1 and dI_T/dV_2 using lock-in technics. One observes that the oscillations of dI_T/dV_1 versus the lateral gate voltage are in quadrature with the one revealed in dI_T/dV_2. Although the inner edge state is just going along the MZI, it reveals oscillations in phase quadrature with the reference signal of the outer edge state. This behavior is a direct consequence of the capacitive coupling between the two edge states.

When I include this coupling in the phase of the oscillation. The formula 5.2 becomes :

$$I_\sim \approx I_D e^{-V_1^2/2V_{lob}^2} \times \cos(\phi - \frac{2\pi}{V_0} \times V_2)$$

where V_1 (V_2) is the bias voltage applied on $S_1(S_2)$. From this last formula, one can immediately remark that when the two edge states are fed with the same bias ($V_2 = V_1$), $dI_\sim/dV_1$ contains a term resulting from the capacitive coupling. This case is obtained when $T_0 = 2$. Let first assume that $V_2 \neq V_1$, in practice obtained when $T_0 = 1$. In such a case :

$$\frac{dI_\sim}{dV_1} \sim (1 - \frac{V_1^2}{V_{lob}^2})e^{-V_1^2/2V_{lob}^2} \times \cos(\phi - \frac{2\pi}{V_0} \times V_2) \tag{5.5}$$

$$\frac{dI_\sim}{dV_2} \sim \frac{2\pi}{V_0} \times V_1 e^{-V_1^2/2V_{lob}^2} \times \sin(\phi - \frac{2\pi}{V_0} \times V_2) \tag{5.6}$$

Figure 5.17(b) I have represented in black dots $\frac{dI_\sim}{dV_1}$ for the outer edge state, and in blue dots $\frac{dI_\sim}{dV_2}$ for the inner edge state with $V_1=1.2\mu V$ and $T_0=1$. Both signals are in quadrature, in good agreement with formulas 4.5 and 4.6. Now that we have observed and characterized the coupling between the inner and outer edge state, we are going to treat the case when $T_0=2$. The physics remaining the same, we can guess that the measured current will be the sum of two terms 4.5 and 4.6.

5.6 Discussion regarding the visibility

5.6.1 Only one edge channel is biased

When G_0 is tuned to transmission $T_0=1$, the lobes are well defined and the phase is rigid with a π shift when the visibility is zero. However for $T_0=2$, lobes almost disappear and the phase is not rigid anymore [57]. Recently, E.Bieri *et al.*[15] have shown that at $T_0=2$ an unexpected enhancement of the visibility could be obtained for a transmission of T_1 close to 1. I will show that this result can be explained with the coupling that I have characterized in the previous chapter.

I have first set $T_0=1$ and $T_2=0.65$ and studied the visibility versus V_1 for three values of T_1 : 0.96, 0.6 and 0.12 (since $T_0=1$, the outer edge state sees a grounded inner edge state).

As I have shown in the previous part, for this large sample at this magnetic field, one observes a multi side lobe structure. Considering the formula 5.2, and the capacitive coupling between the inner and outer edge state, the interfering part of the current becomes

$$I_\sim \propto I_D e^{-V_1^2/2V_{lob}^2} \cos(V_1/V_c) \times \cos(\varphi - \frac{2\pi}{V_0} \times V_2)$$

which finally gives :

$$\frac{dI_\sim}{dV_1} \propto (-\frac{V_1}{V_c}\sin(V_1/V_c) + \cos(V_1/V_c)(1 - \frac{V_1^2}{V_{lob}^2}))e^{-V_1^2/2V_{lob}^2} \times \cos(\phi - \frac{2\pi}{V_0} \times V_2) \quad (5.7)$$

$$\frac{dI_\sim}{dV_2} \propto \frac{2\pi}{V_0} \times V_1 \cos(V_1/V_c)e^{-V_1^2/2V_{lob}^2} \times \sin(\phi - \alpha V_2) \quad (5.8)$$

From which , I deduce a visibility of the interferences equal to :

$$\nu_1 = \nu_0 \mid -\frac{V_1}{V_c}\sin(V_1/V_c) + \cos(V_1/V_c)(1 - \frac{V_1^2}{V_{lob}^2}) \mid e^{-V_1^2/2V_{lob}^2} \quad (5.9)$$

$$\nu_2 = \nu_0 \mid \frac{2\pi}{V_0} \times V_1 \cos(V_1/V_c) \mid e^{-V_1^2/2V_{lob}^2} \quad (5.10)$$

where ν_0 is the visibility at zero bias.

I have represented figure 5.18 the visibility ν_1 and ν_2 for the different transmissions of T_1. The dots are the experimental data while the solid lines are fit to the data using formulas 5.9 and 5.10. The very good agreement between our formula and our experimental data validates our approach. I can extract from these fit parameters the V_c, V_0 and V_{lob}.

I first notice that V_{lob} does not depend on the transmission of the first gate G_1 in good agreement with results described in the literature [68][56]. Secondly V_c is not modified by the transmission : for $T_1=0.1$, 0.6 and 0.9, $V_c \sim 13.9\pm0.2\mu V$, $\sim 14\pm0.2\mu V$, $\sim 13.9\pm0.2\mu V$. Finally, V_0 is constant and equal to $\sim 32.5\mu V$. Indeed we can show independently that V_0 should not vary with T_1 and V_1. I have represented the conductance as a function of the bias voltage V_2 applied on the inner edge state for different values of V_1 ($T_1 = 0.6$) in figure 5.19. From this color plot one can extract V_0 for each value of V_1 : V_0 is constant equal
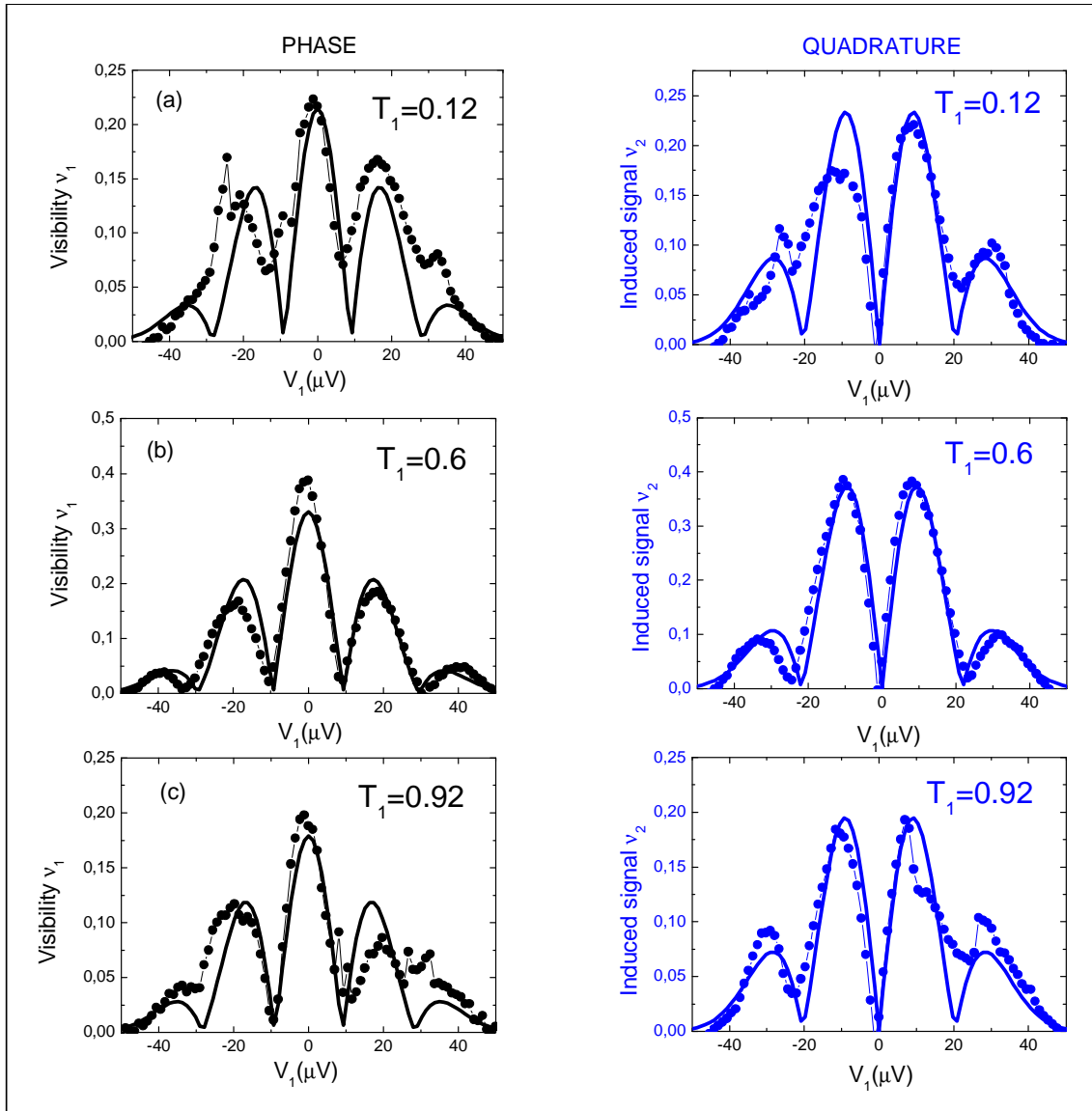
FIGURE 5.18 – B=4.28T. For the whole measurements G_0 is set to T_0=1, and beam splitter G2 is set to T_2=0.65. In black dots(solid line) experimental data(fit) for the interfering edge state (outer edge state). In blue dots(solid line) experimental data(fit) for the induced signal on the inner edge state. (a) T_1 is set to 0.12. I obtain $V_c \sim 13.9\mu V$, $V_{lob} \sim 14\mu V$ and $V_0 \sim 32.5\mu V$ (b) T_1 is set to 0.6. I obtain $V_c \sim 13\mu V$, $V_{lob} \sim 14\mu V$ and $V_0 \sim 32.5\mu V$ (c) T_1 is set to 0.92. I obtain $V_c \sim 13.9\mu V$, $V_{lob} \sim 14\mu V$ and $V_0 \sim 32.5\mu V$

to $\sim$ 32.5 μV. Figure 5.20, I have shown V_0 for three different values of V_1 (-18μV, 0μV, 18μV) and T_1 (0.12, 0.6, 0.92). I obtain a constant value of V_0 equal to $\sim$ 32.5 μV. [17]

---

17. However, if V_0 is constant with V_1 and T_1, we can show that V_0 is magnetic field (and size) dependent (see Chapter 7).
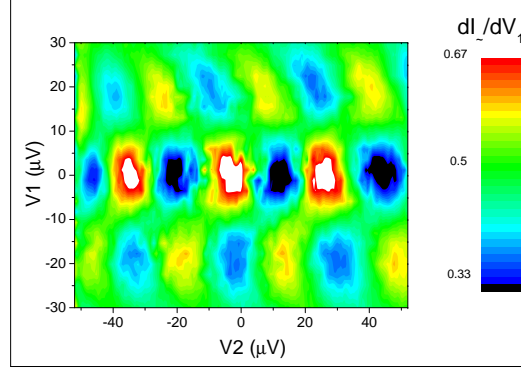
FIGURE 5.19 – Color Plot of the differential conductance as a function of the bias V_1 and V_2 for $T_1 = 0.6$. One can observe a π shift of the phase coinciding with the annulation of the visbility. This figure reveals that the capacitive coupling between the inner and outer edge state is independent of the bias voltage V_1 .
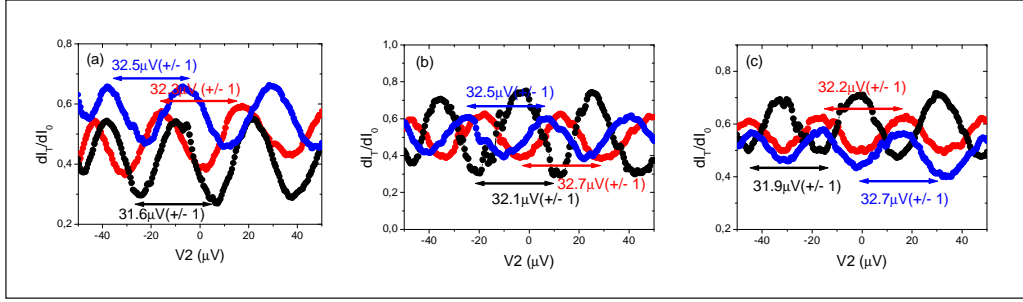
FIGURE 5.20 – Conductance oscillations versus the bias voltage V_2 applied on S_2, for different values of V_1 and T_1. In blue V_1=-18μV, in black V_1=0μV and in red V_1=18μV. (a) T_1=0.12 (b) T_1=0.6 (c) T_1=0.92. In these regimes V_0 remains constant $\sim 32.5\mu V$.

5.6.2 Two edge states are biased

Transmission evolution

When G_0 is fully opened the inner and outer edge state are fed with the same bias, thus I simulate in that way the very first experiment of Ji *et al.*[37] and Bieri *et al.*[15]. To calculate the visibility, I need to take into account the induced signal on the inner edge state :

$$\frac{dI_\sim}{dV} \propto \sqrt{[\cos(V_1/V_c)(1 - \frac{V_1^2}{V_{lob}^2}) - \frac{V_1}{V_c}\sin(V_1/V_c)]^2 + [\frac{2\pi}{V_0} \times V_1\cos(V_1/V_c)]^2} e^{-V_1^2/2V_{lob}^2}\cos(\theta)$$

(5.11)

with

$$\theta = \phi - \frac{2\pi}{V_0} \times V_1 - \arctan(\frac{\frac{2\pi}{V_0} \times V_1\cos(V_1/V_c)}{\cos(V_1/V_c)(1 - \frac{V_1^2}{V_{lob}^2}) - \frac{V_1}{V_c}\sin(V_1/V_c)})$$

(5.12)
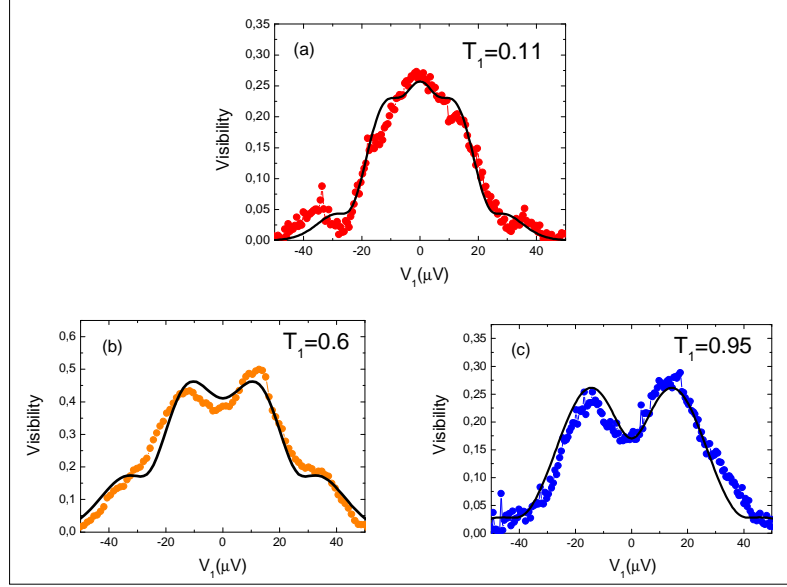
FIGURE 5.21 – B=4.28T, V_2=0V, G_0 is set to T_0=2, and beam splitter G2 is set to T_2=0.65 (except for (b) where T_2=0.68). In dots the visibility of the output signal. In black solid line, our fit using formula 5.11(a) T_1=0.11. I obtain $V_c = 12.9 \pm 0.2\mu V$, $V_{lob} = 11.9 \pm 0.1\mu V$ and $V_0 = 37\mu V$ (b) T_1=0.6. I obtain $V_c = 14.9 \pm 0.2\mu V$, $V_{lob} = 16.2 \pm 0.2\mu V$ and $V_0 = 37.35 \pm 1.3\mu V$ (c) T_1=0.95. I obtain $V_c = 23.2 \pm 0.4\mu V$, $V_{lob} = 19.1 \pm 0.4\mu V$ and $V_0 = 38.4 \pm 1.5\mu V$.

I tune the partition gate to T_2=2 and the second gate G_2 to T_2=0.65. Both channels are now equally biased to V_1. I study the dependence of the visibility with V_1 and I repeat the experiment for three different transmissions of the first gate G_1 : 0.11, 0.6, 0.95. I obtain on figure 5.21 similar results than a recent observation of E.Bieri *et al.*[15]. For large transmissions (larger than 1/2), I notice an enhancement of the visibility when increasing the bias voltage. This enhancement is more pronounced when T_1 gets closer to 1. In that case, the visibility is not maximum for V_1=0 but for $V_1 \sim 15\mu V$. If I now fit these data with our formula 5.11, I obtain a perfect agreement for each transmission. V_0 is once again constant as a function of $T_1 (\sim 37\mu V)$ [18] but the others parameters are significantly evolving with the transmission T_1. V_c is respectively equal to $12.9 \pm 0.2\mu V, 14.9 \pm 0.2\mu V, 23.2 \pm 0.4\mu V$ for T_1 equal to 0.11, 0.6 and 0.95 respectively. Similarly, V_{lob} increases from $11.9 \pm 0.1\mu V$ to $16.2 \pm 0.2\mu V$ and $19.1 \pm 0.4\mu V$. I have finally extracted two characteristic energies that both increase with the transmission of the first gate G_1 as one can remark in figure 5.21.

Phase evolution

The formula 5.12 gives us the evolution of the phase with the bias voltage applied on S_1. When T_0=2 it has been observed [57][15] that the phase was not rigid anymore. This observation raises the question whether the phase rigidity is affected by the presence of

---

18. We note however a small difference with our previous determination of V_0 when T_0=1 ($V_0\sim 32.5\mu V$)

an inner edge state biased at the same potential, or is sill present simply hidden by the capacitive coupling between the two edge states.
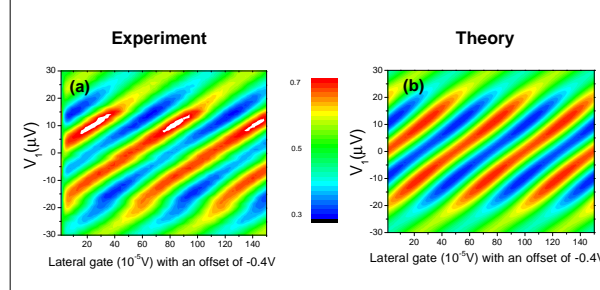
FIGURE 5.22 – Color plot of the MZI transmission versus V_1 and the voltage applied on the lateral gate . The X axis represents the lateral gate voltage, and the Y axis the bias voltage V_1. The color plot indicates maximum and minimum of Ahoronov Bohm oscillations. (a) Experimental evolution of the phase with the bias voltage V_1 when T_0 is tuned to 2. Contrary to $T_0=1$ when the phase is rigid, the phase now increases linearly with the bias voltage.(b) Color plot of the MZI transmission versus V_1 calculated with our formula 5.12. We notice a perfect agreement between our model and experimental data.

I have measured the phase evolution with the bias voltage V_1, and found (see figure 5.22(a)) a linear increase of it. I have compared this result with our formula 5.12. We get a perfect agreement between our model and experimental data (figure 5.22(b)).

This result is very important since it definitively confirms that the π shift always occurs when visibility cancels. It means that, in reality the phase remains the same on the whole interval of V_{ds} and that we observe π shift because we measure the absolute value of the visibility.

One channel biased versus two channel biased

When only one channel was biased we have shown (figure 5.18) that V_c and V_{lob} did not depend on the first beam splitter transmission T_1.

When two edge states are biased, we can extract V_c, V_{lob} and V_0 for each transmission. Since we know all the parameters of the capacitive coupling between the inner and outer edge state, we can subtract from the global signal the expected induced signal ν_2 and focus on the "true" visibility ν_1. We have represented in figure 5.23(a) this expected visibility for $T_1 = 0.11$ and $T_1 = 0.95$ deduced from formula 5.7, including the fact that V_c depends on T_1. We notice a strong impact of the first beam splitter to the lobe structure. This is rather surprising as the lobe structure does not depend on the first beam splitter when only on edge is biased. We aimed to confirm this difference trying to entirely simulate the case when both edge states are fed by the same ohmic contact. Now $T_0 = 1$, and we apply the same bias on S_1 and S_2 (in figure 5.18, we had tuned T_0 to 1, but the inner edge state was grounded). We have represented our results in figure 5.23(b). We note an increase of the lobe width with the transmission : even if the effect is very small, the general trend is in agreement with our predictions. To conclude, when both edge states are equally biased, the lobe structure depends of the transmission T_1.
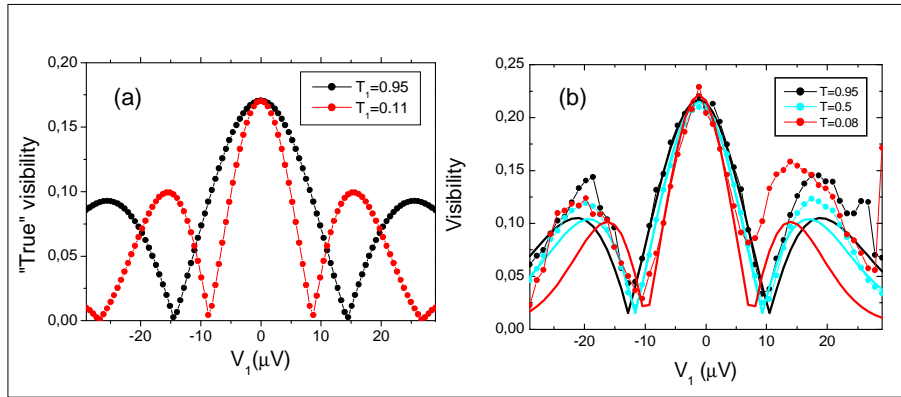
FIGURE 5.23 – **a) :** "True" visibility expected if we subtract from the global signal the expected induced signal for two different transmissions T_1 : 0.11 and 0.95. Contrary to the case when only one edge state is biased, here the lobe structure clearly depends on the first beam splitter transmission. **b) :** $T_0 = 1$, and we apply the same bias on S_1 and S_2. We note an increase of the lobe width with the transmission : even if the effect is very small, the general trend is in agreement with our predictions.

5.6.3 The lobe eraser
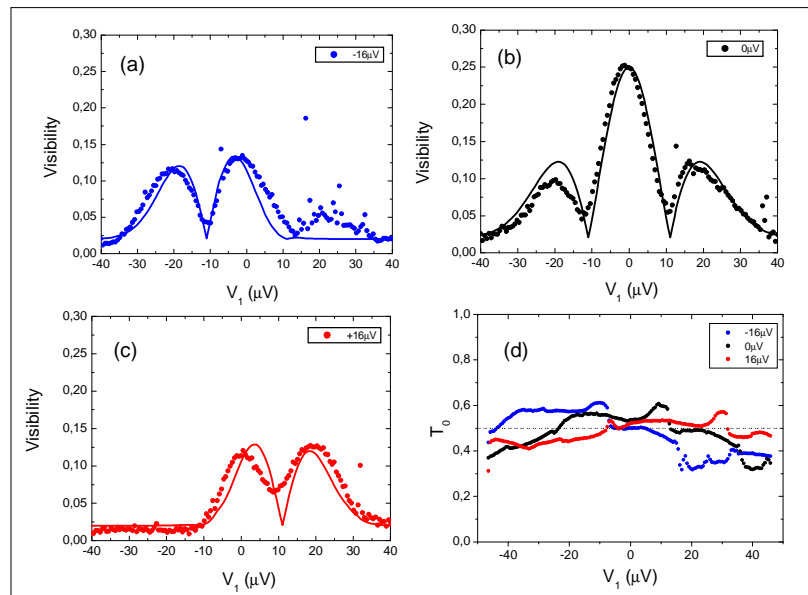
FIGURE 5.24 – $T_{0,ou}$ is tuned to 1/2. In dots the experimental data, in solid lines a guide to the eye. The two steps shape of the distribution function strongly affects the visibility **a)**$V_2 = -16\mu V$. **b)**$V_2 = 0\mu V$. **c)**$V_2 = +16\mu V$.**d)**Mean value of the transmission of T_0 with the bias voltage (T_0 supposed to be tuned to 1/2)

Now that I have shown that the capacitive coupling between the edge states was responsible for experimental artefacts when the two edge states are biased with the same voltage, I will investigate the limitations of this approach. In particular, what happens when the

inner and outer edge state are fed with two different bias, leading to a particular two step distribution function in the wire. This may gives us some knowledge on the mechanism responsible for the Gaussian envelope and/or why the multiple side lobe is affected by T_1 when both edge are biased.
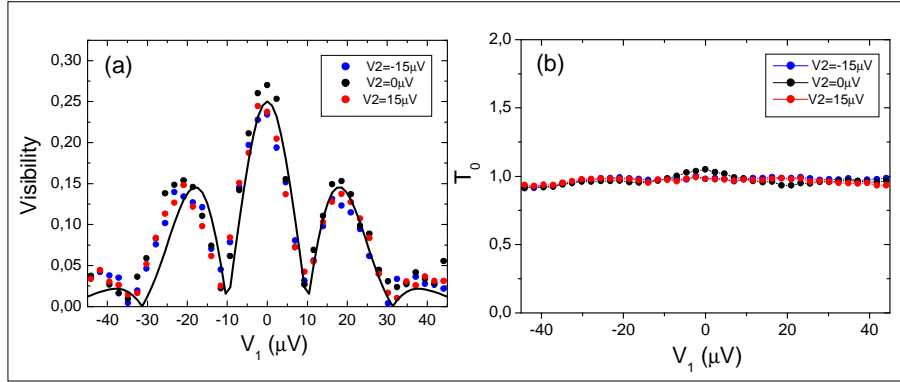
FIGURE 5.25 – Same experiment but T_0 is now tuned to 1.**a)** The visibility does not depend anymore on V_2. In black solid line : fit using formula 5.9. **b)** Mean value of the transmission of T_0 with the bias voltage (T_0 supposed to be tuned to 1)

In this experiment, G_1 and G_2 are tuned to $T_{1,out} \sim T_{2,out} \sim 1/2$. G_0 is now set to $T_{0,out} = 1/2$, so half part of the current is emitted from S_1, the other one from S_2 leading to a two steps shape of the distribution function. I will apply different voltage on S_2 (-16μV, 0μV, +16μV) and will study the impact on the lobe structure.

I observe an unexpected result : we can erase one lobe of the lobe pattern without affecting the other one. When we apply a positive(negative) bias, the lobe corresponding to the negative(positive) bias is erased. This is clearly shown in figure 5.24a)b)c). In addition, I have plotted (see figure 5.24d))the transmission as a function of the bias to show that this effect does not arise from a variation of the transmission probability. Here, this is clear that this is a two step distribution which is responsible for this behavior. As an example, if one realizes an experiment where S_2 is biased but with $T_0=1$ (no two step distribution), the lobe structure is clearly not affected (see figure 5.25). This is a very interesting result for which we do not have a clear explanation. However, it shows that some inelastic processes in the wire itself are involved in the Gaussian shape. This should be explored in the future.

5.6.4 The lobe width : comparison between the inner and outer edge state

I have compared the lobe pattern obtained with the outer edge state ($T_{1,out}=T_{2,out}=1/2$) and the inner edge state ($T_{1,out}=T_{2,out}=1$ and $T_{1,in}=T_{2,in}=1/2$) on the same sample. The energy width of the lobe structure is modified : for the inner edge state $V_{lob,in}= 6.4\mu$V, whereas for the outer edge state $V_{lob,out}= 11.6\mu$V. This brings us new information for the theory interested in the lobe structure. When considering the theory of Levkivskyi and Sukhorukov's [43], the lobes arise from beating between two coupled excitations in the
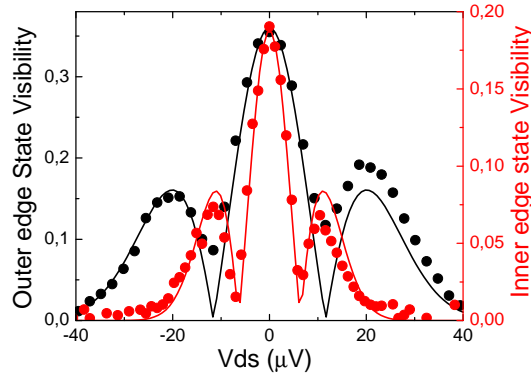
FIGURE 5.26 – In black dots, the visibility of the interferences of the outer edge state as a function of the drain-source voltage applied on it. T_0 is set to 1, and beam splitters G1 and G2 are both set to $T_{1,out}=T_{2,out}=1/2$. In red dots, the visibility of the interferences of the inner edge state as a function of the drain-source voltage applied on it. T_0 is set to 1, and beam splitters G1 and G2 are both set to $T_{1,in}=T_{2,in}=1/2$. Solid lines are fits using equation 5.1. Unexpectedly, the energy width of the lobe structure is modified : for the inner edge state $V_{lob,in}= 6.38\mu V$, whereas for the outer edge state $V_{lob,out}= 11.6\mu V$.

inner and outer edge state. The collective excitations should not depend on the edge state in which electrons are injected. Consequently, the lobe structure should not depend on the edge state (I will discuss this theory in details in the next chapter). One of the parameter that may change between the inner and outer edge state would be the drift velocity. The drift velocity depends on the local confining potential. Our observations may be related to a smaller (because the energy scale is smaller) drift velocity in the inner state, compared to the outer one. However, we do not have proof of this.

5.7 Theoretical approach

We detail here different theoretical models that have been proposed to explain properties of the visibility with the applied bias voltage as a function of the transmission of G_0.

5.7.1 The non interacting model

In a theoretical paper, Chung *et al.* [25] have studied the effect of a voltage eV on the visibility. This paper treats the non interacting case. It serves to understand what is the impact of a finite temperature on the visibility. They first calculated how the phase should vary with the energy when there is a length difference ΔL. For that purpose, they have introduced the parameter s which measures directly the path length, i.e. *x(s)*, *y(s)*(coordinates of the electron). In addition at *s*, they introduce local coordinate $s_\perp$ perpendicular to the equipotential line. In these coordinates, an edge state that follows the

equipotential line at a small energy ϵ away from E_F acquires the additional phase :

$$\delta\varphi = \int ds \frac{\Delta s_\perp}{l_B^2}$$

where $l_B^2 = \hbar/eB$ and $e(dU/ds_\perp)\Delta s_\perp = \epsilon$. Moreover, we know that the potential gradient $dU/ds_\perp$ is related to the local electric field by F(s) = -dU/ds$_\perp$. From this relation we can define the drift velocity of the guiding center of the cyclotron orbit at point s of the edge state $v_D(s)$, with $v_D(s)$= F(s)/B. Thus a small increase in energy leads to a phase increment given by :

$$\delta\varphi = \frac{e}{\hbar v_D} \int ds F(s)\Delta s_\perp$$

which gives finally :

$$\delta\varphi = \frac{\epsilon \times \Delta L}{\hbar v_D} \qquad (5.13)$$

where I have introduced ΔL, the length difference between the upper and down arm of the MZI. One can then calculate the spectral current density :

$$j(\epsilon) = \frac{e}{h}[f(\epsilon) - f_0(\epsilon)][T_1T_2 + R_1R_2 + 2\sqrt{T_1T_2R_1R_2}\cos(\epsilon/Ec + \Theta_{AB})]$$

with Θ_{AB} the Ahoronov Bohm (AB) phase through the area defined by the position of the edge state at the Fermi energy, $f_0(\epsilon)$ the distribution function of the grounded terminal, f(ϵ) = $f_0(\epsilon - eV)$ the distribution function of terminal injecting the current and $Ec = \hbar v_D/\Delta L$. The current is given by :

$$I = \int j(E)dE$$

or

$$I = \frac{e}{h}[(T_1T_2 + R_1R_2)eV + \sqrt{T_1T_2R_1R_2} \times \frac{4\pi k_B T}{sinh(\frac{k_B T\pi}{E_c})}sin(\frac{eV}{2E_c})\cos(\frac{eV}{2E_c} + \Theta_{AB})] \quad (5.14)$$

Experimentally, we measure the differential conductance, which within this theory is related to T and V in the following way :

$$\frac{dI}{dV} = \frac{e}{h}[(T_1T_2 + R_1R_2)e + \sqrt{T_1T_2R_1R_2} \times \frac{2\pi k_B T}{E_c \times sinh(\frac{k_B T\pi}{E_c})}\cos(\frac{eV}{E_c} + \Theta_{AB})] \qquad (5.15)$$

In the non interacting approach, the visibility does not depend on the voltage. However this model gives a temperature dependence via the *sinh*, which leads to an exponential dependence of the visibility with the temperature (also called thermal smearing) when $k_B T > E_c$. We will study the consequences of the thermal smearing in the Chapter 7.

5.7.2   Interaction between counterpropagating edge states

In 2007, Sukhorukov *et al.* [79] proposed a model attempting to explain the lobe structure at $\nu = 1$. They noticed that an important feature of the MZI setup [56][69][44] was the existence of a counterpropagating edge state (labeled as ϕ_3 in Figure 5.27), which closely approaches the edge state forming the upper arm of the interferometer (labeled as ϕ_2 in Figure 5.27) and could strongly interacts with it [19]. Being localized inside a finite interval of the length L, the interaction leads to a resonant scattering of collective charge excitations (plasmons), which carry away the phase information. As a result, interferences vanish at certain values of bias accompanied by a π shift of the phase. However, this theory fails to explain observations at $\nu = 2$ for the following reasons. At $\nu = 2$, when interferences are realized on the outer edge state, the inner one should screen the interactions with the counter propagating one. Moreover, in our experiment we have measured the same lobe width as Neder *et al.*[56] even though in our sample, the counter propagating edge state is much more distant. This interaction between edge states and the differences between $\nu = 1$ and $\nu = 2$ raises an interesting question that I have already mentioned. The one side lobe structure observed at $\nu = 1$ and $\nu = 2$ only needs a Gaussian envelope. However, the multiple side lobe structure has only been observed at $\nu = 2$. Does it mean that 2 neighboring edge states are necessary to explain the multiple side lobes? This is in fact the other model proposed by Sukhorukov that I will explain in the following.
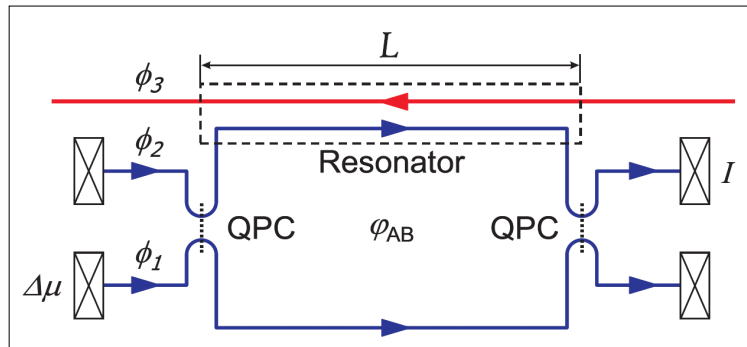
FIGURE 5.27 – The main hypothesis of the Sukhorukov *et al.* theory [79] is that the counter propagating state (red line on the figure) closely approaches the upper branch of the MZI interferometer (inside the resonator shown by a dashed box) and strongly interacts with it

5.7.3   Short range interactions

More recently, Levkivskyi and Sukhorukov [43] have proposed another model based on strong Coulomb interactions between the neighbor edge states to explain the evolution of the lobe structure at $\nu = 2$. This model only considers the regimes of weak tunneling

---

19. In our case the two counter propagating edge states are separated by several μm ($\sim 5\mu$m). Such an interaction is unlikely.

($T_1 \longrightarrow 0$) or weak backscattering ($T_1 \longrightarrow 1$) for which bozonisation technics and perturbation development are allowed. One of the goal of this theory [43] is to explain the unexpected enhancement of the visibility when both edge states are biased, around a zero bias, observed by Bieri *et al.*[15]. In their model, they consider very short range intra edge state interactions and two edge states interactions. Diagonalizing the Hamiltonian, describing the coupling, they find that coulomb interaction at $\nu = 2$ leads to the separation of the spectrum into collective excitations. They obtain two modes : a fast mode (that carries the charge) with a speed u and a slow (dipole) one with a speed v. The corner stone of this approach is that the electron is decomposed exactly in the same proportion (when $u \gg v$) in the two modes. Then, there are two excitations of same amplitude but with different velocity : this leads naturally to beating effects. They consider then two experiments : one edge state biased or two edge states biased.

Only one edge channel is biased

They suppose first, that only one edge channel is biased (experimentally occurs when T_0=1, namely the inner edge state is reflected) and that T_1 is much smaller than 1/2 corresponding to the weak tunneling regime (they obtain same results in the weak backscattering regime if $\Delta L = 0$).

They first calculate the variation of the Aharonov Bohm phase with the potential ($\Delta\mu = eV$)

$$\frac{\partial \Delta\phi_{AB}}{\partial \Delta\mu} = \frac{u + \nu}{2u\nu}\Delta L$$

Therefore, for the symmetric interferometer, ΔL=0, the phase shift is independent of the bias. This may explain the phenomenon of phase rigidity observed [56][69][44], if one assumes that the interferometer is symmetric. However, this conclusion is exactly the same that we obtain when considering non-interacting quasi particle. Regarding the visibility, this model gives :

$$|\nu| = |\cos(\Delta\mu L/(2v))| \tag{5.16}$$

where L is the length of one arm of the interferometer. It simply describes the beating between the two interferences leading to periodic zeros of the visibility with the bias. This approach seems to contradict some experimental results. First, the period of the calculated visibility is $\sim$ to v/L, and should thus depend on the size of the interferometer in contradiction with our data since we have shown that for the middle and large MZI, we obtained the same lobe width. [20] This model is unfortunately only valid in the weak backscattering (tunneling) regime. However, it is known that far from the perturbative limit, the theory does not apply. If one tries to extend their theory to higher (smaller) value of T_1, we can show that the visibility will be $\sim$ to $v/((1 - 2T_1) \times L)$ in contradiction with experiments where it has been shown that the lobe pattern did not depend on T_1 [68] [57].

_____

20. Note however that the lobe patterns have not been realized at the same magnetic field, which prevent us from concluding definitively.

Two edge states are biased

Levkivskyi and Sukhorukov[43] also considered the case when both edge states are biased at the same potential (T_0=2), in the weak tunneling regime. In this case the visibility can be found exactly :

$$|\nu| = |J_0(\Delta\mu\Delta L/2\nu)| \qquad (5.17)$$

The visibility of the calculated oscillations is shown in figure 5.28. One can see that in contrast to the case when only one channel is biased, the central lobe is approximatively twice wider than side lobes, apparently in agreement with experimental observations [15]. Moreover, the width of lobes is determined by the new energy scale ϵ'=$v/\Delta L$. Finally inside the lobes the phase shift $\Delta\phi_{AB} = \Delta\mu(L_D + L_U)/2v$ always grows linearly with bias, so no phase rigidity should be observed.

This result contradicts two experimental observations. First, we have shown (see part 5.6.2) that in reality the one side lobe observed in the weak tunneling regime by the Basel group was in reality a multi side lobes simply hidden by the capacitive coupling between the inner and outer edge states. The assertion "the central lobe is approximatively two times wider than side lobes" arises in fact from the trivial capacitive coupling. What is more problematic is the new energy scale ϵ'=$v/\Delta L$ which must be very large for symmetric MZI. In our case, the litography precision enable us to have $\Delta L = 0$ and we have shown that energy scales were comparable whether only one edge state was biased or two.
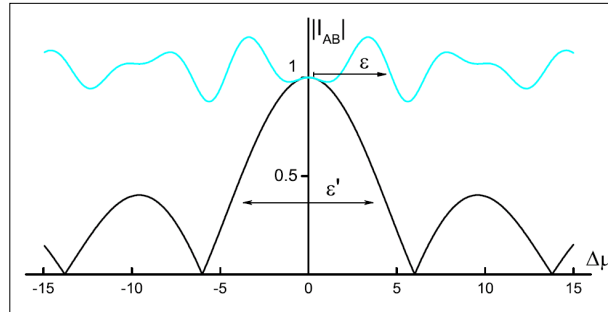
FIGURE 5.28 – The intrinsic visibility of interferences in the case when two edge channels are biased for strongly asymmetric interferometer, L_D=1.8L_U. In the model of Levkivskyi and Sukhorukov[43], the visibility is plotted as a function of bias $\Delta\mu$ in units of v/L_U for the regime of weak tunneling (black line) and for the regime of weak backscaterring (blue line)

In the weak backscattering regime and for a symmetric MZI, Levkivskyi and Sukhorukov[43] obtain the following expression of the visibility :

$$|\nu| = |\Delta t/t_0 + (1 - \Delta t/t_0)e^{i\Delta\mu t_0}|$$

where $t_0 = L/v$ is the propagation time of the slow mode between two QPCs, and Δt is defined by :

$$\Delta t = 2\pi\partial_{\Delta\nu}(Q1_U L_U - Q1_D L_D)$$

with $Q1_U(Q1_D)$ the charge of the upper(down) trajectory and $\partial_{\Delta\nu}$ the derivative as a function of $\Delta\nu$. Whether the visibility grows or decays depends on the sign of the second term. However in the weak backscattering or tunneling regime and for $\Delta L=0$, Levkivskyi and Sukhorukov[43] find that this formula gives a constant visibility. They had to consider a strongly asymmetric interferometer with $L_D = 1.8L_U$ to observe the enhancement of the visibility for small bias voltages (see figure 5.28). Contrary to Bieri *et al* experiment, our MZI is symmetric and we also obtain an enhancement of the visibility. This model is not appropriate.

5.8 Shot noise generated by the first beam splitter

These works propose that the dephasing in the MZI is due to the shot noise generated by the partition of the edge channel at the first QPC. Neder *et al* [55] and Youn *et al* [88] consider that the shot noise generated at the input beam splitter of the MZI leads to an ensemble of nonequilibrium electron density configurations in the two arms. Then the electron interaction within each arm induces configuration-specific phase shifts of an interfering electron, and the ensemble average of the phase shifts leads to nonequilibrium dephasing. The combined effect of the shot noise and the interaction results in lobe patterns and phase jumps. Both works are similar except that Neder *et al* [55] consider a regime of stronger interaction strength than Youn *et al* [88]. Now, we will focus on Youn *et al* [88] results, since they are particularly interested in the T_1 dependence of the visibility which can be easily compared to the experiments. In figure 5.29 I have represented their results :
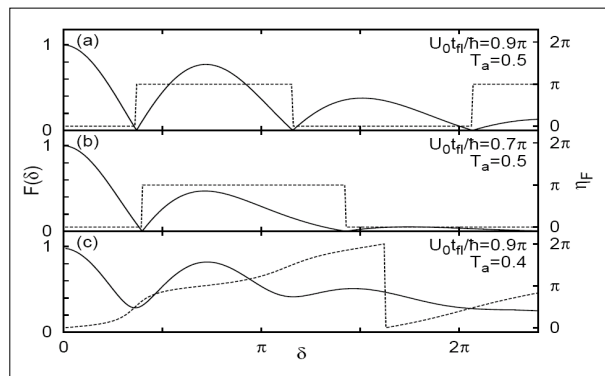
FIGURE 5.29 – Visibility F (solid curves) and phase shift η_F (dashed) of dI/dV , as a function of δ (δ is a parameter proportional to the bias). We notice a strong dependence of the lobe pattern with the transmission of the first gate (not observed in the experiments)

the general behavior of the visibility and phase with the bias. This approach reveals the multi side lobe pattern. But their visibility also strongly depends on T_1 (see figure 5.29(c)) although experiments do not show such a dependence when one channel is biased [68] [57]. Since interaction in the wire itself may be the origin of the multiple side lobes, I will describe in more details this approach.

5.8.1 Discussion of this model

This section is the result of a fruitful debate between Dr.Sim [88] and me.

The simplest way to understand the effect of shot noise within their model is to consider the case when N≪ 1, with N the number of packets that have significant weight in the arms. Thus for N≪ 1, only one packet has significant weight and the nonequilibrium ensemble has two representative elements in each of which the nonequilibrium density appears in the upper (down) arm with probability $R_1(T_1)$. The electron in the upper path generates a phase shift $e^{i\delta}$, the electron in the down path generates a phase shift $e^{-i\delta}$. Thus the interfering part of the current $I_\sim$ is corrected by a dephasing factor D equal to :

$$D = |R_1 e^{i\delta} + T_1 e^{-i\delta}| = \sqrt{cos^2\delta + (R_1 - T_1)^2 sin^2\delta} \qquad (5.18)$$

We are now going to discuss this formula. However, it is important to precise that we measure $dI_\sim/dV$ and hence the relation between this parameter D and the lobe structure that we observe in the differential conductance is not straightforward. In particular, the first dip of the visibility on $dI_\sim/dV$ interferences occurs at a voltage somewhere between 0 and the value at which D has the first dip.

G1 dependence of the lobe width

The formula 5.18 implies a strong dependence of the lobe width with the first beam splitter. Even if the factor D has been obtained for N≪ 1 and for the MZI conductance, this factor gives the general trends of the visibility. Indeed, when they consider a more general model with N≤3, the lobes in D of the N≪ 1 case are maintained, though lobes now acquire a decaying envelope. Consequently all the discussion of the Youn *et al.* model will be based on the expression 5.18 of D. We have represented in figure 5.30, the evolution of D with the transmission T_1 of the first beam splitter G_1. D shows lobe patterns with periodic minima. The lobe width of this lobe pattern does not depend on the T_1. However, the minima strongly increase as T_1 deviates from 0.5.

I have thus measured the visibility with the bias V_{ds} for three different transmissions of the first beam splitter : T_1=0.12, 0.6, and 0.92. I find no dependence of the lobe width with the transmission T_1 (see figure 5.31)(confirmed by Neder et al. [56]). Moreover for T_1 equal 0.12 we note a small increase of the minima compared to T_1=0.6 in agreement with formula 5.18 that predicts an increase of the minima as T_1 deviates from 0.5 (unfortunately, I don't have the exact expression of the visibility used by Youn *et al* [88] for their numerical simulations. I can only compare general trends.). However for T_1=0.92, we find well defined minima. Finally, we have found a transmission close to 1 where the visibility vanishes, in disagreement with Youn *et al* [88] model.

5.8.2 An asymmetric configuration

I am now considering another asymmetric configuration : a voltage probe experiment (for more details see chapter 8). As represented in figure 5.33, I have studied the lobe
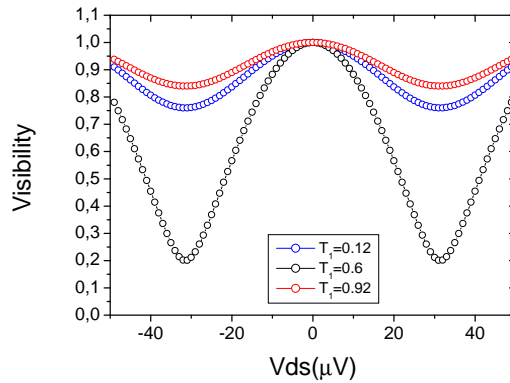
FIGURE 5.30 – Non equilibrium dephasing factor D ([88]) for different transmissions of the first beam splitter G_1. The lobe width does not depend on the transmission T_1. However the minima increase as T_1 deviates from 0.5
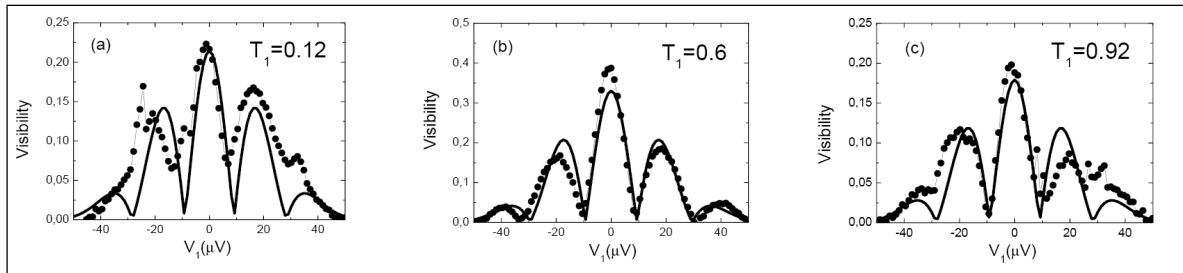
FIGURE 5.31 – Visibility as a function of the bias V_{ds} for different transmissions of the first beam splitter. In solid lines, fits using formula 5.7 (a) T_1 is set to 0.12.(b) T_1 is set to 0.6.(c) T_1 is set to 0.92. The lobe width does not depend on the transmission of the first beam splitter.
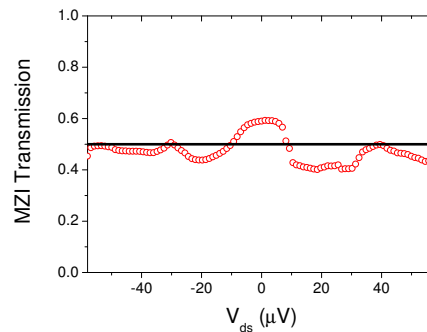
FIGURE 5.32 – MZI transmission for different values of V_{ds}. The mean transmission is equal to 1/2 confirming the good tuning of T_2 to 1/2.

width as a function of V_{ds} for different value of transmission T_P toward the probe. If the voltage probe is a good one, its voltage V_P is $V_P = T_1 V_{ds} = (1/2)V_{ds}$. The voltage probe is another source generating an nonequilibrium ensemble of electron density configurations
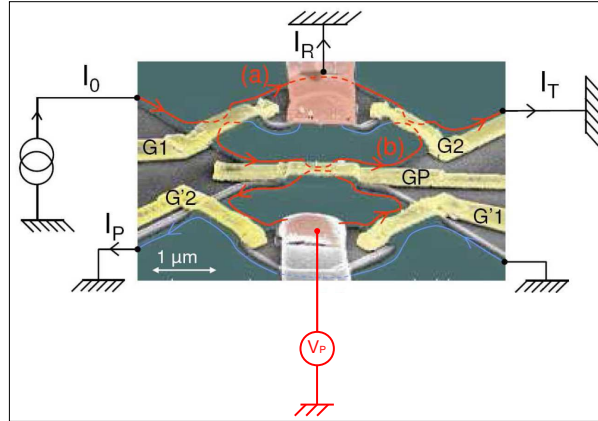
FIGURE 5.33 – Schematic representation of the probe configuration. The upper MZI is connected to a floating ohmic contact (for more details see chapter 8) via a gate probe. We are interested in the evolution of the lobe width of the lobe pattern when we open the probe gate, breaking thus the symmetry of the problem.
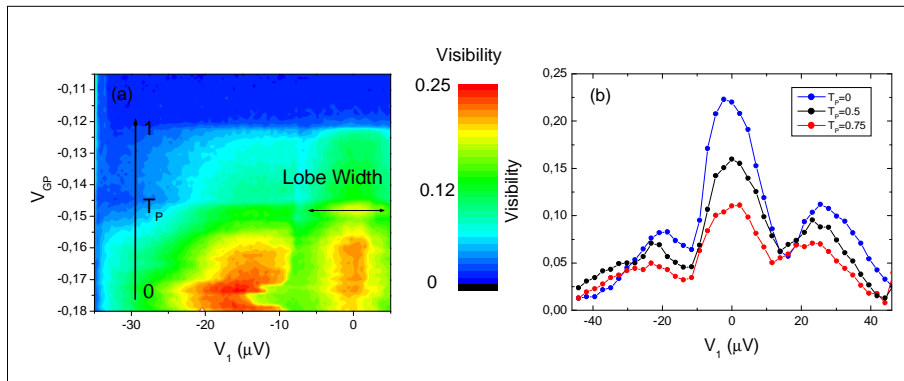
FIGURE 5.34 – Visibility as a function of V_{ds} for a MZI connected to a floating ohmic contact via a probe gate (transmission T_P). When T_P=1 the probe gate is opened. We do not observe any dependence of the lobe width with T_P.(a) color plot of the visibility as a function of V_{ds} and V_{GP}. When V_{GP}=-0.18 the gate is closed and T_P=0, When V_{GP}=-0.1 the gate is opened T_P=1. We pass then continuously from T_P=0 to T_P=1. We notice a small asymmetry of the lobe pattern, since the visibility is larger for V_{ds}=-15μV than for V_{ds}=+15μV. The lobe width is constant.(b) Lobe pattern of the visibility as a function of V_{ds} for three different values of T_P : 0, 0.5 and 0.75. We can notice here that the lobe pattern is not perfectly symmetric (visibility stronger for negative bias than for 0 bias). The visibility is not exactly equal to zero between two maxima, I do not know exactly why.

in the MZI. Then, the MZI with the voltage probe is a complicated nonequilibrium circuit with two nonequilibrium voltages V_{ds} and V_P. As the potential (voltage) along the lower arm (that coupled to the probe) is fluctuating in time due to the shot noise at the first beam splitter, there exists time-dependent current flow from the probe to the drain or from the source to the probe, depending on the scattering event at the first beam splitter. Any interfering electron should be then affected by the time-dependent current flow. Based on the above argument, we are going to derive the factor D for the MZI with the voltage

probe, when N $\ll 1$ (for $R_1=T_1=0.5$) (result obtained by Dr. Sim) :

$$D = |T_P(R_1 e^{i(\delta-\delta_p)} + T_1 e^{-i(\delta-\delta_p)}) + R_P(R_1 e^{i\delta} + T_1 e^{-i\delta})| \tag{5.19}$$

$$D = |T_P cos(\delta - \delta_p) + R_P cos(\delta)| \tag{5.20}$$

The first term of Eq. 4.18 comes from the event A where the nonequilibrium electron injected from the source exists in the upper arm (with probability R_1) and at the same time a nonequilibrium electron is injected from the probe into the lower arm (with probability T_P). In this event A, the electron in the upper arm generates the phase shift $e^{i\delta}$ to an interfering electron, while the electron injected into the lower arm from the probe gives another phase shift $e^{-i\delta_P}$. Here δ_P is proportional to $V_P = (1/2)V_{ds}$ and to the path length between the probe beam splitter and the second beam splitter of the MZI, and does not depend on R_P and T_P. The second term of Eq. 4.18 comes from the event B where the nonequilibrium electron injected from the source exists in the lower arm (with probability T_1) and it partially moves toward the probe passing through the probe beam splitter (with probability T_P). In this event B, the nonequilibrium electron gives the phase shift of $e^{-i\delta_P}$. Similarly, the third term of Eq. 4.18 comes from the event C where the nonequilibrium electron injected from the source exists in the upper arm (with probability R_1) and at the same time no nonequilibrium electron is injected from the probe into the lower arm (with probability R_P). For this event C, the phase shift is simply $e^{i\delta}$. Finally, the fourth term of Eq. 4.18 comes from the event D where the nonequilibrium electron injected from the source exists in the lower arm (with probability T_1) and it fully moves toward the drain without passing through the probe beam splitter (with probability R_P). For this event D, the phase shift is $e^{-i\delta}$. In the limit of $T_P= 0$, equation 4.18 corresponds to the expression that we have obtained previously for a MZI without probe. Experimentally, we do not observe any dependence of the lobe width with T_P, as expected from 5.8.2.

5.9   Conclusion

In a first part, I have summarized different experimental observations regarding the visibility variation with the voltage. In the very first experiment Ji *et al.* observed a monotonous decay of the visibility since the two edge states were fed by the same ohmic contact. Biasing only the outer edge state with an additional beam splitter G_0, Neder *et al.* observed an unexpected lobe structure of the visibility.

We have observed single side lobe and multi side lobes. We have shown that the single side lobe could be understood supposing a Gaussian phase averaging. We have proposed a simple model to explain recent observations of Bieri *et al.* We have shown that, taking into account the capacitive coupling between the inner and outer edge state, the enhancement observed by Bieri *et al* was not so unexpected. Still, we have extracted two energy scales which increase with the transmission T_1. Finally, I have compared our results with the different theories available in the literature. Although each of them gives rise to an

oscillation in the visibility, it seems that none can explain why the lobes are not affected by the transmission of the first beam splitter and why there is a Gaussian envelop. Our results suggest that we are probably in front of two effects : a Gaussian envelop, which gives the general trend of the visibility at $\nu = 2$ and also at $\nu = 1$ and "something else" which appears at low magnetic field with two edge states. If it is the latter case, interaction between the edge states seems to be the most plausible candidate for multiple side lobes.

Finite bias visibility of the electronic Mach-Zehnder interferometer

Preden Roulleau, F. Portier, D. C. Glattli,[*] and P. Roche[†]

Nanoelectronic Group, Service de Physique de l'Etat Condensé, CEA Saclay, F-91191 Gif-Sur-Yvette, France

A. Cavanna, G. Faini, U. Gennser, and D. Mailly

CNRS, Phynano Team, Laboratoire de Photonique et Nanostructures, Route de Nozay, F-91460 Marcoussis, France

We present an original statistical method to measure the visibility of interferences in an electronic Mach-Zehnder interferometer in the presence of low frequency fluctuations. The visibility presents a single side lobe structure shown to result from a Gaussian phase averaging whose variance is quadratic with the bias. To reinforce our approach and validate our statistical method, the same experiment is also realized with a stable sample. It exhibits the same visibility behavior as the fluctuating one, indicating the intrinsic character of finite bias phase averaging. In both samples, the dilution of the impinging current reduces the variance of the Gaussian distribution.

PACS number(s): 85.35.Ds, 73.43.Fj

Nowadays quantum conductors can be used to perform experiments usually done in optics, where electron beams replace photon beams. A beamlike electron motion can be obtained in the integer quantum Hall effect (IQHE) regime using a high mobility two dimensional electron gas in a high magnetic field at low temperature. In the IQHE regime, one-dimensional gapless excitation modes form, which correspond to electrons drifting along the edge of the sample. The number of these so-called edge channels corresponds to the number of filled Landau levels in the bulk. The chirality of the excitations yields long collision times between quasiparticles, making edge states very suitable for quantum interference experiments like the electronic Mach-Zehnder interferometer (MZI).[1–3] Surprisingly, despite some experiments which show that equilibrium length in chiral wires is rather long,[4] very little is known about the coherence length or the phase averaging in these "perfect" chiral unidimensional wires. In particular, while in the very first interference MZI experiment the interference visibility showed a monotonic decrease with voltage bias, which was attributed to phase noise,[1] in a more recent paper, a surprising nonmonotonic decrease with a lobe structure was observed.[5] A satisfactory explanation has not yet been found, and the experiment has so far not been reported by other groups to confirm these results.

We report here on an original method to measure the visibility of interferences in a MZI, when low frequency phase fluctuations prevent direct observation of the periodic interference pattern obtained by changing the magnetic flux through the MZI. We studied the visibility at finite energy and observed a single side lobe structure, which can be explained by a Gaussian phase averaging whose variance is proportional to V^2, where V is the bias voltage. To reinforce our result and check if low frequency fluctuation may be responsible for that behavior, we realized the same experiment on a stable sample: we also observed a single side lobe structure which can be fitted with our approach of Gaussian phase averaging. This proves the validity of the results, which cannot be an artifact due to the low frequency phase fluctuations in the first sample. In both samples, the dilution of the impinging current has an unexpected effect: it de-

creases the variance of the Gaussian distribution.

The MZI geometry is patterned using *e*-beam lithography on a high mobility two dimensional electron gas in a GaAs/Ga$_{1-x}$Al$_x$As heterojunction with a sheet density $n_S = 2.0 \times 10^{11}$ cm^{-2} and a mobility of 2.5×10^6 cm^2/Vs. The experiment was performed in the IQHE regime at filling factor $\nu = n_S h/eB = 2$ (magnetic field $B = 5.2$ T). Transport occurs through two edge states with an extremely large energy redistribution length.[4] Quantum point contacts (QPCs) controlled by gates G0, G1, and G2 define electronic beam splitters with transmissions $\mathcal{T}_0$, $\mathcal{T}_1$, and $\mathcal{T}_2$, respectively. In all the results presented here, the interferences were studied on the outer edge state schematically drawn as black lines in Fig. 1, the inner edge state being fully reflected by all the QPCs. The interferometer consists of G1, G2, and the small central ohmic contact in between the two arms. G1 splits the incident beam into two trajectories (a) and (b), which are recombined with G2 leading to interferences. The two arms defined by the mesa are 8 μm long and enclose a 14 μm^2 area. The
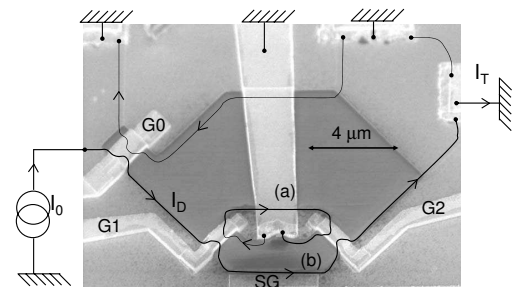
FIG. 1. Scanning electron microscope view of the electronic Mach-Zehnder interferometer with a schematic representation of the edge state. G0, G1, G2 are quantum point contacts which mimic beam splitters. The pairs of split gates defining a QPC are electrically connected via an Au metallic bridge deposited on an insulator (SU8). G0 allows a dilution of the impinging current, G1 and G2 are the two beam splitters of the Mach-Zehnder interferometer. SG is a side gate which allows a variation of the length of the lower path (b).

current which is not transmitted through the MZI, $I_B = I_D - I_T$, is collected to the ground with the small ohmic contact. An additional gate SG allows a change of the length of the trajectory (b). The impinging current I_0 can be diluted thanks to the beam splitter G0 whose transmission $\mathcal{T}_0$ determines the diluted current $dI_D = \mathcal{T}_0 \times dI_0$. We measure the differential transmission through the MZI by standard lock-in techniques using a 619 Hz frequency 5 μV_{rms} ac bias V_{ac} superimposed to the dc voltage V. This ac bias modulates the incoming current $dI_D = \mathcal{T}_0 \times h/e^2 \times V_{ac}$, and thus the transmitted current in an energy range close to eV, giving the transmission $\mathcal{T}(eV) = dI_T / dI_0$.

Using the single particle approach of the Landauer-Büttiker formalism, the transmission amplitude t through the MZI is the sum of the two complex transmission amplitudes corresponding to paths (a) and (b) of the interferometer; $t = t_0 \{ t_1 \exp(i\phi_a) t_2 - r_1 \exp(i\phi_b) r_2 \}$. This leads to a transmission probability $\mathcal{T}(\epsilon) = \mathcal{T}_0 \{ \mathcal{T}_1 \mathcal{T}_2 + \mathcal{R}_1 \mathcal{R}_2 + \sqrt{\mathcal{T}_1 \mathcal{R}_2 \mathcal{R}_1 \mathcal{T}_2} \sin[\varphi(\epsilon)] \}$, where $\varphi(\epsilon) = \phi_a - \phi_b$ and $\mathcal{T}_i = |t_i|^2 = 1 - \mathcal{R}_i$. $\varphi(\epsilon)$ corresponds to the total Aharonov-Bohm (AB) flux across the surface $S(\epsilon)$ defined by the arms of the MZI, $\varphi(\epsilon) = 2\pi S(\epsilon) \times eB/h$. The surface S depends on the energy ϵ when there is a finite length difference $\Delta L = L_a - L_b$ between the two arms. This leads to a variation of the phase with the energy, $\varphi(\epsilon + E_F) = \varphi(E_F) + \epsilon \Delta L / (\hbar v_D)$, where v_D is the drift velocity. When varying the AB flux, the interferences manifest themselves as oscillations of the transmission; in practice this is done either by varying the magnetic field or by varying the surface of the MZI with a side gate.[1,5,6] The visibility of the interferences defined as $\mathcal{V} = (\mathcal{T}_{MAX} - \mathcal{T}_{MIN}) / (\mathcal{T}_{MAX} + \mathcal{T}_{MIN})$ is maximum when both beam splitter transmissions are set to $1/2$. In the present experiment the MZI is designed with equal arm lengths ($\Delta L = 0$) and the visibility is not expected to be sensitive to the coherence length of the source $\hbar v_D / \max(k_B T, eV_{ac})$. Thus the visibility provides a direct measurement of the decoherence and/or phase averaging in this quantum circuit.

In Ref. 1, 60% visibility was observed at low temperature, showing that the quantum coherence length can be at least as large as several micrometers at 20 mK (and probably larger if phase averaging is the limiting factor). At finite energy (compared to the Fermi energy), the visibility was also found decreasing with the bias voltage.[1,5,6] This effect is not due to an increase of the coherence length of the electron source which remains determined by eV_{ac} or $k_B T$.[7] In a first experiment, a monotonic visibility decrease was found, which was attributed to phase averaging, as confirmed by shot noise measurements.[1] Nevertheless, it remains unclear why and how the phase averaging increases with the bias. In a recent paper, instead of a monotonic decrease of the visibility, a lobe structure was observed for filling factor less than 1 in the QPCs.[5] No noninteracting electron model was found to be able to explain this observation, and although interaction effects have been proposed,[8] a satisfactory explanation has not yet been found to account for all the experimental observations. So far, two experiments have shown two different behaviors, raising questions about the universality of these observations. Here, we report experiments where different samples give consistent results, with a fit to the data clearly
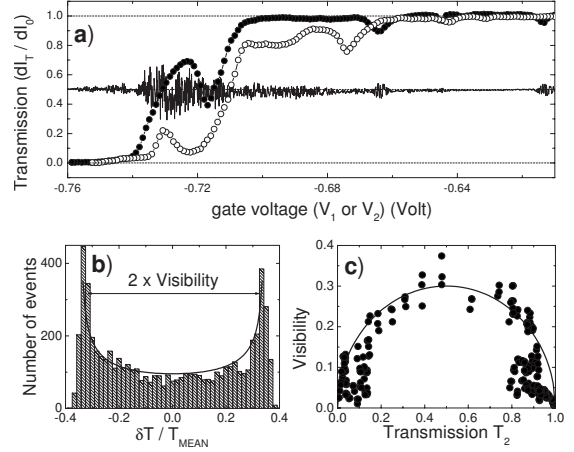
FIG. 2. Sample 1: (a) Transmission $\mathcal{T} = dI_T/dI_0$ as a function of the gate voltages $V1$ and $V2$ applied on G1 and G2. ($\bigcirc$) $\mathcal{T} = \mathcal{T}_1$ vs $V1$. ($\bullet$) $\mathcal{T} = \mathcal{T}_2$ vs $V2$. The solid line is the transmission $\mathcal{T}$ obtained with $\mathcal{T}_1$ fixed to $1/2$ while sweeping $V2$: transmission fluctuations due to interferences with low frequency phase noise appear. (b) Stack histogram on 6000 successive transmission measurements as a function of the normalized deviation from the mean value. The solid line is the distribution of transmission expected for a uniform distribution of phases. (c) Visibility of interferences as a function of the transmission $\mathcal{T}_2$ when $\mathcal{T}_1 = 1/2$. The solid line is the $\sqrt{\mathcal{T}_2(1 - \mathcal{T}_2)}$ dependence predicted by the theory.

demonstrating that our MZI suffers from a Gaussian phase averaging whose variance is proportional to V^2, leading to the single side lobe structure of the visibility.

We have used the following procedure to tune the MZI. We first measure independently the two beam splitters' transparencies vs their respective gate voltages, the inner edge state being fully reflected. This is shown in Fig. 2(a) where the transmission ($\mathcal{T}_1$ or $\mathcal{T}_2$) through one QPC is varied while keeping unit transparency for the other QPC. This provides the characterization of the transparency of each beam splitter as a function of its gate voltage. The fact that the transmission vanishes for large negative voltages means that the small ohmic contact in between the two arms can absorb all incoming electrons, otherwise the transmission would tend to a finite value. This is very important in order to avoid any spurious effect in the interference pattern. In a second step we fix the transmission $\mathcal{T}_1$ to $1/2$ while sweeping the gate voltage of G2 [solid line of Fig. 2(a)]. Whereas for a fully incoherent system the $\mathcal{T}$ should be $1/2 \times (\mathcal{R}_2 + \mathcal{T}_2) = 1/2$, we observe large temporal transmission fluctuations around $1/2$. We show in the following that they result from the interferences, expected in the coherent regime, but in the presence of large low frequency phase noise. This is revealed by the probability distribution of the transmissions obtained when making a large number of transmission measurements for the same gate voltage. Figure 2(b) shows a histogram of $\mathcal{T}$ when making 6000 measurements (each measurement being separated from the next by 10 ms). The histogram of the transmission fluctuations $\delta\mathcal{T} = \mathcal{T} - \mathcal{T}_{mean}$ displays two maxima very well fitted using a probability distribution $p(\delta\mathcal{T}/\mathcal{T}_{mean})$
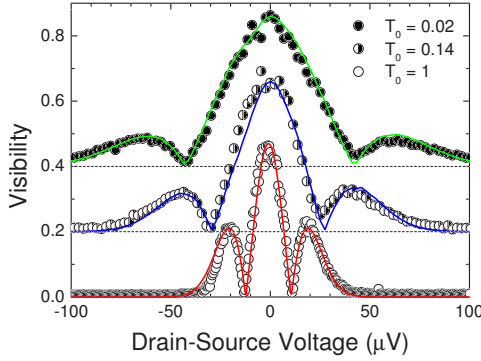
FIG. 3. (Color online) Sample 1: Visibility of the interferences as a function of the drain-source voltage $I_0 h/e^2$ for three different values of $\mathcal{T}_0$. The curves are shifted for clarity. The energy width of the lobe structure is modified by the dilution whereas the maximum visibility at zero bias is not modified. Solid lines are fits using Eq. (1). From top to bottom, $\mathcal{T}_0=0.02$ and $V_0=31$ μV, $\mathcal{T}_0=0.14$ and $V_0=22$ μV, $\mathcal{T}_0=1$ and $V_0=11.4$ μV.

$=1/[2\pi\sqrt{1-(\delta\mathcal{T}/\mathcal{T}_{mean})^2/\mathcal{V}^2}]$ [the solid line of Fig. 2(b)]. This distribution is obtained assuming interferences $\delta\mathcal{T}=\mathcal{T}_{mean}\times\mathcal{V}\sin(\varphi)$ and a uniform probability distribution of φ over $[-\pi,+\pi]$. Note that the peaks around $|\delta\mathcal{T}/\mathcal{T}_{mean}|=\mathcal{V}$ have a finite width. They correspond to the Gaussian distribution associated with the detection noise which has to be convoluted with the previous distribution.

Although no regular oscillations of transmission can be observed due to phase noise, we can directly extract the visibility of the interferences by calculating the variance of the fluctuations (the approach is similar to measurements of universal conductance fluctuations via the amplitude of $1/f$ noise in diffusive metallic wires).[10] As expected when $\mathcal{T}_1=1/2$, the visibility extracted by our method is proportional to $\sqrt{\mathcal{T}_2(1-\mathcal{T}_2)}$, definitively showing that fluctuations result from interference: we are able to measure the visibility of fluctuating interferences [see Fig. 2(c)].

The visibility depends on the bias voltage with a lobe structure shown in Fig. 3, confirming the pioneering observation.[5] Nevertheless, there are marked differences. The visibility shape is not the same as that in Ref. 5. We have always seen only one side lobe, although the sensitivity of our measurements would be high enough to observe a second one if it existed. Moreover, the lobe width (see Fig. 3) can be increased by diluting the impinging current with G0, whereas no such effect is seen for G1 and G2. This apparent increase of the energy scale cannot be attributed to the addition of a resistance in series with the MZI because G0 is close to the MZI, at a distance shorter than the coherence length.

An almost perfect fit for the whole range of $\mathcal{T}_0$ (dilution) is

$$\mathcal{V}=\mathcal{V}_0 e^{-V^2/2V_0^2}\left|1-\frac{VI_D}{V_0^2 dI_D/dV}\right|,\qquad (1)$$

where V_0 is a fitting parameter. Equation (1) is obtained when assuming a Gaussian phase averaging with a variance
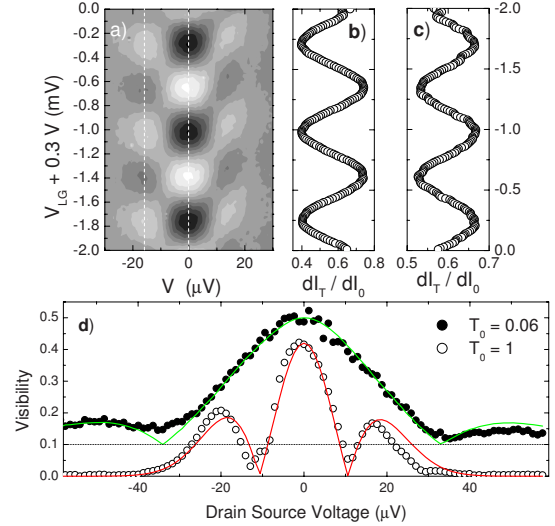
FIG. 4. (Color online) Sample 2: (a) Gray plot of the transmission $\mathcal{T}$ as a function of the bias voltage V and the side gate voltage V_{SG}. Note the π shift of the phase when the visibility reaches 0. (b), (c) $\mathcal{T}$ as a function of the side gate voltage for two different values of the drain source voltage corresponding to the dashed line of (a) (0 and 16 μV, respectively). (d) Lobe structure of the visibility fitted using Eq. (1) for a diluted and an undiluted impinging current.

$\langle\delta\varphi^2\rangle$ proportional to V^2 and a length difference ΔL small enough to neglect the energy dependence of the phase in the observed energy range $eV\ll\hbar v_D/\Delta L$. In such a case, the interfering part of the current $I_\sim$ is thus proportional to $I_D\sin(\varphi)$. The Gaussian distribution of the phase leads to $I_\sim\propto I_D\sin(\langle\varphi\rangle)e^{-\langle\delta\varphi^2\rangle/2}$, where $\langle\varphi\rangle$ is the mean value of the phase distribution. The measured interfering part of the transmission, $\mathcal{T}_\sim=h/e^2 dI_\sim/dV$, gives a visibility corresponding to formula (1) when $\langle\delta\varphi^2\rangle=V^2/V_0^2$. Such behavior gives a nul visibility accompanied with a π shift of the phase when $VI_D/(V_0^2 dI_D/dV)=1$. When $\mathcal{T}_0\sim 1$, I_D is proportional to V and the width of the central lobe is simply equal to $2V_0$. However, in the most general case, dI_D/dV varies with V. One can see in Fig. 3 that the fit with Eq. (1) is very good, definitively showing that the existence of one side lobe, as observed in the experiment of Ref. 5 at $\nu=2$ (for the highest fields) and at $\nu=1$, can be explained within our simple approach. Concerning multiple side lobes, we cannot yet conclude if they do arise from long range interaction as recently proposed by Ref. 8 Our geometry is different from the one used in the earlier experiment[5] and the coupling between counterpropagating edge states, thought to be responsible for multiple side lobes,[8] should be less efficient here.

To check if low frequency fluctuations have an impact on the finite bias phase averaging, we have studied another sample, with the same geometry and fabricated simultaneously (sample 2), which exhibits clear interference pattern [see Figs. 4(a)–4(c)]. As one can remark in Fig. 4(d), the lobe structure is well fitted with our theory, definitively showing that the Gaussian phase averaging is not associated with low frequency phase fluctuations.
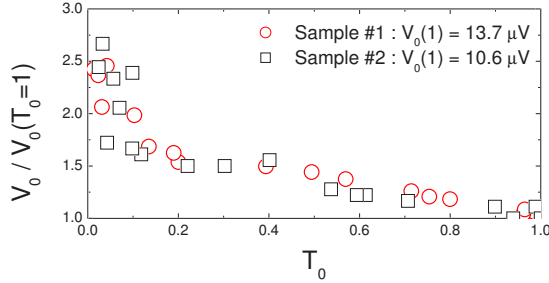
FIG. 5. (Color online) V_0 obtained by fitting the visibility with Eq. (1), normalized to V_0 at $\mathcal{T}_0 = 1$, as a function of $\mathcal{T}_0$ at zero bias.

It is noteworthy that V_0 increases (see Fig. 5) with the dilution, namely when the transmission $\mathcal{T}_0$ at zero bias decreases. An impact of the dilution was already observed as it suppressed multiple side lobes[9] (arXiv version of Ref. 5), but the conclusion was that the width of the central lobe was barely affected. Here, dilution plays a clear role whose $\mathcal{T}_0$ dependence is the same for the two studied samples, once normalized to the not diluted case. This dilution effect is

nevertheless not easy to explain. For example, mechanisms like screening, intra-edge scattering, and fluctuations mediated by shot noise should have maximum effect at half transmission, in contradiction with Fig. 5. More generally, it is difficult to determine if the process responsible for the phase averaging introduced in our model is located at the beam splitters, or is uniformly distributed along the interfering channels. However, setting $\mathcal{T}_1 = 0.02$ or 0.05, keeping $\mathcal{T}_2 = 0.5$, leaves the lobe width unaffected. This shows that, if located at the quantum point contacts, the phase averaging process is independent of transmission.

To summarize, we propose a statistical method to measure the visibility of "invisible" interferences. We observe a single side lobe structure of the visibility on stable and unstable samples which is shown to result from a Gaussian phase averaging whose variance is proportional to V^2. Moreover, this variance is shown to be reduced by diluting the impinging current. However, the mechanism responsible for such type of phase averaging remains yet unexplained.

---

*Also at LPA, Ecole Normale Supérieure, Paris.

†patrice.roche@cea.fr

[1] Y. Ji, Y. Chung, D. Sprinzak, M. Heiblum, D. Mahalu, and H. Shtrikman, Nature (London) **422**, 415 (2003).

[2] P. Samuelsson, E. V. Sukhorukov, and M. Büttiker, Phys. Rev. Lett. **92**, 026805 (2004).

[3] I. Neder, N. Ofek, Y. Chung, M. Heiblum, D. Mahalu, and V. Umansky, Nature (London) **448**, 333 (2007).

[4] T. Machida, H. Hirai, S. Komiyama, T. Osada, and Y. Shiraki, Solid State Commun. **103**, 441 (1997).

[5] I. Neder, M. Heiblum, Y. Levinson, D. Mahalu, and V. Umansky, Phys. Rev. Lett. **96**, 016804 (2006).

[6] L. V. Litvin, H.-P. Tranitz, W. Wegscheider, and C. Strunk, Phys. Rev. B **75**, 033315 (2007).

[7] V. S.-W. Chung, P. Samuelsson, and M. Büttiker, Phys. Rev. B

72, 125320 (2005).

[8] E. V. Sukhorukov and V. V. Cheianov, arXiv:cond-mat/0609288, Phys. Rev. Lett. (to be published).

[9] I. Neder, M. Heiblum, Y. Levinson, D. Mahalu, and V. Umansky, arXiv:cond-mat/0508024 (unpublished).

[10] All the results on the visibility reported here on sample 1 have been obtained using the following procedure: we measured $N = 2000$ times the transmission and calculated the mean value $\mathcal{T}_{mean}$ and the variance $\langle \delta \mathcal{T}^2 \rangle$. It is straightforward to show that the visibility is $\mathcal{V} = \sqrt{2} \sqrt{\langle \delta \mathcal{T}^2 \rangle - \langle \delta \mathcal{T}^2 \rangle_0} / \mathcal{T}_{mean}$, where $\langle \delta \mathcal{T}^2 \rangle_0$ is the measurement noise which depends on the ac bias amplitude, the noise of the amplifiers, and the time constant of the lock-in amplifiers (fixed to 10 ms), measured in the absence of the quantum interferences.

Chapitre 6

The Coherence Length at $\nu{=}2$

Contents

6.1 Introduction

In the physics of quantum conductors, one of the basic length scale which gives a limitation to the manifestation of quantum effects, is the so-called quantum coherence length l_φ. It characterizes the length on which an excitation exchanges information with other degrees of freedom and hence looses its phase coherence. l_φ has been extensively studied in diffusive wires in the last decade. It has been shown to result from electron electron interaction as predicted by Altshuler-Aronov-Khmelnitsky [5], leading to a $T^{-1/3}$ temperature dependence of l_φ in 3D diffusive wires [29]. Surprisingly, very little was known about the coherence length in the Integer Quantum Hall Regime (IQHE), where transport occurs through one dimensional chiral wires localized on the edge of the sample (the edge states). In principle, for such ballistic wires, one expects the chirality to prevent energy exchange processes, leading to a very long coherence length. An important step towards

the determination of the coherence length in the quantum Hall regime has been realized by Ji. *et al* [37] with the MZI. Since they obtained interferences with an interferometer's area of $45\mu m^2$, this experiment has set a lower bound $\sim 10\mu m$ at 20mK to the coherence length. Indeed, to determine the coherence length several conditions are required. The first one is to realize quantum interferences, as a finite coherence length will have a direct impact on the visibility of these interferences. In a second step, one has to measure the dependence of the visibility with different parameters (the bias, the temperature, the magnetic field). In this chapter, I will essentially study the dependence with the temperature. Once we obtain a visibility which depends on these parameters, it is not clear that we have measured a coherence length. Hence, one has to vary the size L on which interference occurs and check if the visibility follow some exp($-L/l_\varphi$) law. Last, one has to check that the visibility decrease does not come from spurious effect like it is the case with the so called thermal smearing [1].

In a first part we will describe an experiment realized by Hansen *et al.* [35] who have determined the coherence length in a 2D electron gas [2](at zero magnetic field) fulfilling the different necessary conditions for that. They were able to probe different interferometers size. Then they have subtracted the effect of thermal smearing to their temperature dependence of the visibility to finally estimate the coherence length. I have chosen to present this experiment because it provides the first measurement of l_φ in a ballistic conductor, which has shown an unexpected $1/T$ dependence of l_φ. I think that this experiment is a perfect introduction to our experiment since we will follow a similar procedure. We will measure the decrease of the visibility for different interferometers of different sizes, then we will show that this decrease is not due to thermal smearing. Then, we will be able to extract a precise value of the coherence length.

6.2 Methodology
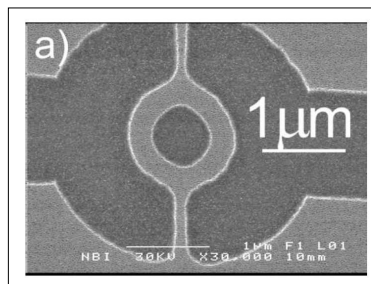
FIGURE 6.1 – SEM image of the ring before gate deposition. In the dark areas the donor layer is etched away. The quantum wires defining the arms of the ring are etched 280 nm wide, while the wires connecting the ring to the 2DEG reservoirs are 100 nm wide.

_____

1. We will define thermal smearing in the part 6.4.
2. GaAs/GaAlAs heterostructure.

    In 2001, the group of Lindelhof [35] has studied the decoherence in mesoscopic Aharonov-Bohm rings, in 2D systems (GaAs/GaAlAs heterostructure). Even if this experiment has been realized at zero magnetic field, it is a useful example since it aimed to extract a precise coherence length treating the case of thermal smearing. In their Aharonov-Bohm rings (a SEM view of their rings is represented in figure 6.1), the interference of numerous paths leads to conductance oscillations (revealed via a top gate) of period h/e in the magnetic field flux enclosed by the paths. Measuring the visibility of the AB oscillations enables to probe the coherence in their system. The trick here, is to study trajectories which have enclosed the AB ring up to $n = 6$ time. As electrons have a strong probability of being reflected in the constrictions, electrons tend to perform many turns in the loop. This is observed as peaks in the Fourier spectra of the magnetoconductance at multiples ne/h of the fundamental AB frequency. As higher harmonics correspond to electrons that have performed more turns around the loop, they decay faster with increasing T : it is the basis of their determination of l_φ. In figure 6.2(a) we have shown their results, for different temperatures. We can observe a little bump even at 6e/h meaning that they are sensitive enough to detect electrons that have enclosed the ring up to 6 times.
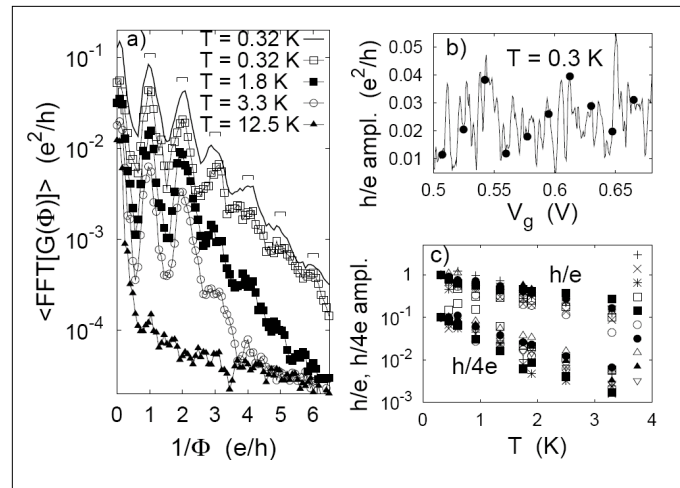
FIGURE 6.2 – a) Fourier spectra at different temperatures, as a function of inverse magnetic flux, $\Phi = B\pi r^2$ through the ring. Since the phase of AB oscillations depends on the gate voltage applied on the ring, the spectra have been averaged for 10 different gate voltages. The spectrum marked with a thick line results from an average of 500 gate voltages and is offset vertically for clarity. b) Amplitude of h/e oscillations as a function of gate voltage. The filled circles mark the 10 gate voltages used in the further analysis. c) Amplitude of h/e and h/4e oscillations for 10 different gate voltages V_g, normalized to 1 and 0.1 at T = 0.3 K, as a function of temperature. The gate voltage increases from $V_g = 0.51$ V to 0.67 V in order of the symbols plotted to the right.

    In figure 6.2(c), they have represented the temperature dependence of the harmonic amplitude for n=1 and n=4 : clearly the visibility decrease is more pronounced for n=4. They summarize their results for n=1..6 in figure 6.3.

    They assume then the visibility to be :

$$\nu_n = e^{-nL/L_\phi(T)} \tag{6.1}$$
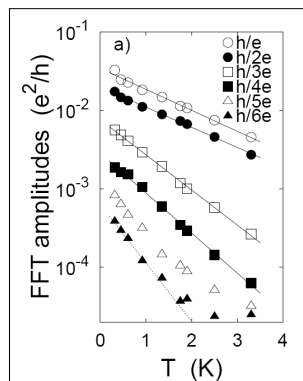
FIGURE 6.3 – Measured amplitudes of the h/ne oscillations, n = 1 to 6, on a semi-log scale as a function of temperature. Straight lines are fits with $a_n\exp(-b_n/\text{T})$.

where $L_\phi(T)$ is the coherence length, and L is half the circumference of the ring. The equation 6.1 implies that all h/ne amplitudes should have the same functional dependence on T, as they observe. Furthermore, the damping rates b_n (the slope of the lines in figure 6.3(a)) should increase linearly with n, which is not exactly the case. To solve this problem, the author of ref.[35] explained the absence of scaling with the harmonics by the presence of thermal smearing[3]. They first studied the phase shift around the Fermi energy, and were able then to extract the effect of thermal smearing in the temperature dependence of the visibility. Above all, they have shown that thermal smearing was responsible for a decrease of the visibility but much smaller than the measured amplitudes. Regarding the dependence of b_n with n, they observe that amplitudes decay faster for n odd that even. Their argument lies on the fact that when n is even, the geometrical phase difference of electronic paths is zero, and then is less sensitive to thermal smearing. When n is even, we obtain a b_n that varies linearly with n, as expected. From these results Hansen *et al.* were able to extract the coherence length ($\sim 5\mu m \pm 1\mu m$) at 1K for ballistic 1D wires at zero magnetic field, and they found a 1/T temperature dependence. This result differs from the diffusive wires where it has been observed a $T^{-1/3}$ temperature dependence of l_φ [29]. This is the very first experiment which has shown a coherence length in disagreement with the AAK theory. One can notice that, in the same year, Seelig and Buttiker [76] have proposed a mean field theory which very well explained the results of Hansen *et al* [35]. For 1D chiral wires of the IQHE, only lower bounds to the l_φ have been determined. It has motivated us in the precise determination of the coherence length in the quantum Hall regime at $\nu = 2$.

_____

3. We will detail the notion of thermal smearing in part 6.4. The idea is that we always measure transport properties averaged on a $\sim k_B T$ energy interval. If the phase of AB oscillations depends on energy, this gives rise to thermal smearing.

6.3   Determination of l_φ

As explained in the previous part, if one wants to measure the absolute value of l_φ and not its lower bound, one needs to fulfill two conditions. First, as we want to determine the coherence length, one needs to prove its existence. It will be done by varying the size on which interferences occur. Secondly, one needs to show that the interferences have a phase which does not depend on the energy of the quasiparticle (to exclude thermal smearing). This is for these reasons that we have used the MZI which can be in principle designed in such a way that the phase is energy independent (for equal interferometer arms length). To prove that we were actually in presence of finite coherence length, we have studied three MZI of different sizes to show a scaling of the temperature dependence of the visibility with the interferometer arm length.

The experiments were performed in the IQHE regime at filling factor $\nu= 2$. The first gate G0 is tuned to fully reflect the inner edge state ($T_0{=}1$). The sizes of the three interferometers used in this study scale by up a factor $\sqrt{2}$: the length of their arms are L = 5.6μm, 8μm and 11.3μm for enclosed areas of 8.5μm^2 (referred to as small), 17μm^2 (medium) and 34μm^2 (large). [4]

We know that (see chapter 4) the oscillations can be obtained using two equivalent experimental procedures : either by superimposing a minute current to the large current of the magnet, or by changing the surface defined by the MZI using a lateral gate.
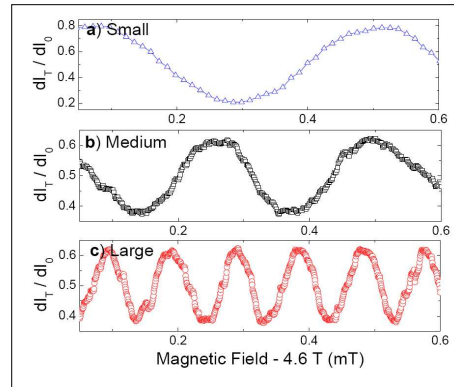
FIGURE 6.4 – Interferences revealed upon varying the magnetic flux through the surface defined by the two arms (u) and (d) of the interferometers. From the oscillation period δB we deduce the surface S = h/(eδB) of the 3 different studied MZI. In blue : The small MZI (S = 8.7±0.2 μm^2)(60% of visibility). In black : The medium MZI (S = 15.5 ± 0.4 μm^2)(30% of visibility). In red : The large MZI (S = 40.7 ± 0.8 μm^2)(30% of visibility). All these surfaces are in good agreement with the lithographic ones.

Figure 6.4 shows the AB oscillations of the transmission for the three interferometers, showing a magnetic period inversely proportional to the area of the interferometer. For precise determination of the visibility and its temperature dependence, we have always used

---

4. These values correspond to the sizes designed during the fabrication process. We can notice that the lithography precision is in good agreement with the area extracted from Aharonov Borm measurements (see figure 6.4).

the lateral gate and run the magnet in the permanent-current mode, strongly reducing the measurement noise. The maximum value of ν is always obtained at the lowest temperature. ν can reach 65 % for the small interferometer at 18mK , whereas it typically attains 20-40 % for the medium and the large interferometer (see figure 6.4(b)).

6.3.1 Temperature dependence

For each interferometer we have studied the temperature dependence of the visibility. In figures 6.5, we have plotted $ln(\nu/\nu_B)$ versus temperature, where ν_B stands for the visibility at T_B=20 mK, for the small, middle and large size sample.
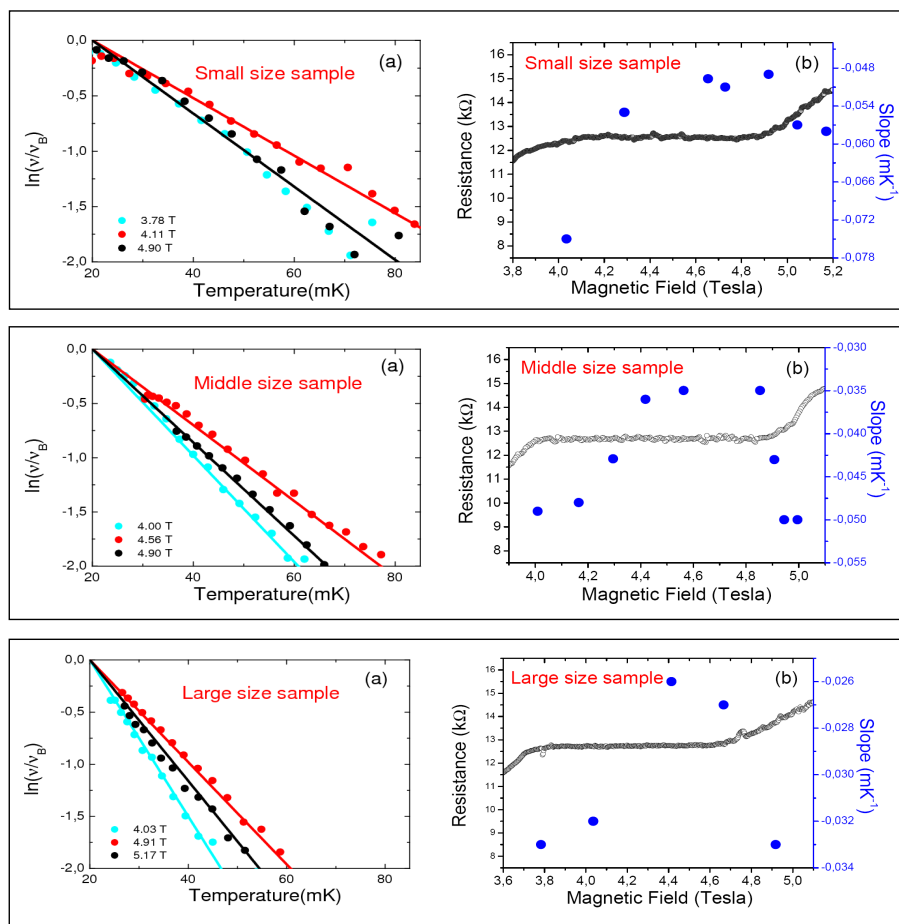
FIGURE 6.5 – (a) $ln(V/V_B)/(T-T_B)$ as a function for the temperature at three different magnetic field, for the small, middle and large samples. (b) Dependence of $ln(V/V_B)/(T-T_B)$ with the magnetic field.

Clearly, the visibility decreases with temperature in all cases, and the larger the interferometer, the stronger the temperature dependence is. More quantitatively, if a linear regression of $ln(\nu/\nu_B) = (T - T_B)/T_0$ is done, one finds that T_0^{-1} is proportional to the length of the interfering arms (see figure 6.6). In the following, we are going to show that this behavior does not result from a thermal smearing.
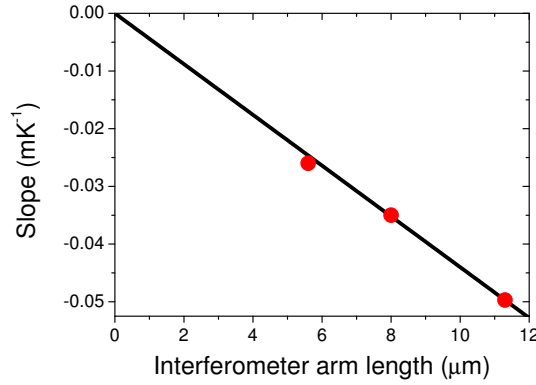
FIGURE 6.6 – Plot of the $ln(\nu/\nu_B)/(T-T_B)$=$1/T_0$ as a function of the interferometer arm length. We find that the slope is proportional to the arm length. Note that the linear regression crosses the origin.

The exponential decrease of the visibility with temperature is robust against various parameter variations, revealing an universal behavior. While the maximum visibility at the lowest temperature is affected by varying the transmission T_0 of the MZI and by applying a finite bias, the slope $ln(V/V_B)/(T-T_B)$ is found to be unaffected [68]. Moreover if one of the beam spitter G_1 or G_2 of the MZI is detuned the slope remains the same.

6.4 Phase rigidity and absence of thermal smearing

6.4.1 Definition of thermal smearing

We start from the formula 5.13[5] :

$$\delta\varphi = \frac{\epsilon \times \Delta L}{\hbar v_D}$$

where ΔL=$L_u - L_d$ is the length difference between two arms of the MZI and v_D the drift velocity. Since we work at finite temperature, the energy is averaged over a typical energy range of $k_B T$, leading to an average of the phase of the order of $k_B T \times \Delta L/\hbar v_D$. To be more precise, the formula 5.15 leads to a visibility :

$$\nu = \nu_0 \frac{\pi T}{T_S} \frac{1}{sinh(\pi T/T_S)} \tag{6.2}$$

where we have introduced $T_S = \frac{\hbar v_D}{\Delta L k_B}$ and ν_0 the visibility at zero temperature. This formula gives a quasi exponential dependence of the visibility with the temperature when $T \gtrsim T_S$. We have to prove now that the exponential decay that we have observed does not come from this effect.

_____

5. Obtained in the part 5.7.

6.4.2 Absence of thermal smearing

We have used equation 6.2 to fit our experimental data obtained for the three sizes of the MZI in order to estimate what would be the length difference between the arms of the MZI interferometer necessary to explain our results with thermal smearing. In figure 6.7 we have represented in dots experimental results, the solid lines are fit to the data using the thermal smearing formula.
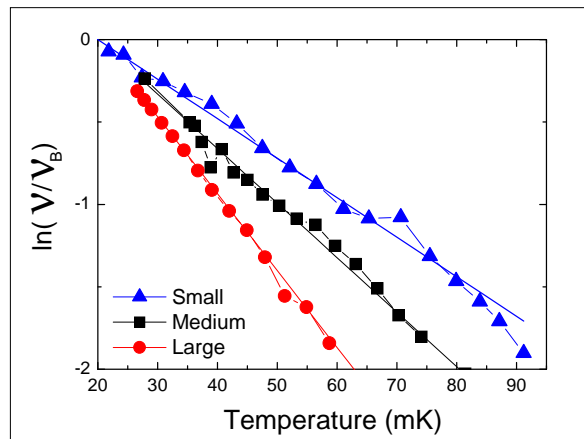
FIGURE 6.7 – We have represented in dots the experimental data. The solid lines are fit assuming the existence of thermal smearing (formula 6.2). For the small, medium, large samples (red, black, blue color respectively) one obtains T_S=66, 59, 44 mK.

It yields to T_S=66, 59, 44 mK for the small, medium and large sample respectively. Since T_S is given by the formula $T_S = \hbar v_D / \Delta L k_B$, we can extract the corresponding ΔL supposing a drift velocity equal to $5.10^4 ms^{-1}$. We find respectively for the small, medium and large sample ΔL equal to 4, 5 and 6 μm which is impossible considering the lithographic precision of our sample. But this argument is based on an estimation of the drift velocity [6]. We have another argument based on the observation of a phase rigidity as a function of energy. In case of thermal smearing, we should observe a phase variation when applying a DC bias voltage V on the interfering current. The formula 5.13, gives a phase variation with the bias :

$$\varphi(V) = \frac{eV}{k_B T_S}$$

In figure 6.8(a) we have plotted a 2D graph of the differential transmission $T(V)$ as a function of the lateral gate voltage and the dc bias, for the middle sample at 20 mK. From this measurement we have deduced the phase $\Phi(eV)$ which is shown to remain almost constant over an energy range of $\sim 16 \mu eV \sim 200$ mK (in figure 6.8(a)). As a comparison,

---

6. The drift velocity is not very well known. It should depend in principe of the electron density, magnetic field and confining potential. The cited usual values are always around $10^4 ms^{-1}$ to $10^5 ms^{-1}$. As an example in the experiment of Van der Wiel [81], one finds a discussion and a measurement of v_D (inset of the figure 3) leading to $v_D \sim 5.10^4 ms^{-1}$ at 4 Tesla.
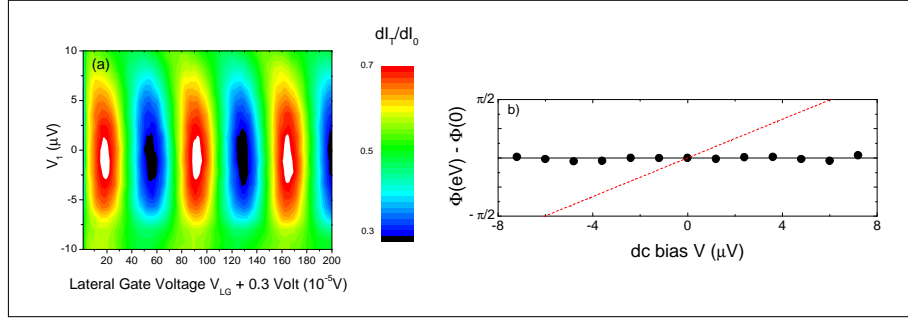
FIGURE 6.8 – (a) 2D plot of dI_T/dI_0 as a function of the lateral gate voltage V_{LG} and the DC bias V_1, for the middle sample at 20 mK. The visibility of interferences of the order of 40% decreases with V while the phase of interferences remains almost constant. (b) In black dots phase of the middle sample deduced from figure 6.8(a). In red line, the energy dependence of the phase which would be necessary to explain our observed visibility decrease with thermal smearing

the red dots of figure 6.8(b) is the phase dependence which would be required (assuming T_S=59 mK) to explain the decrease of the visibility with thermal smearing. The conclusion is straightforward : our sample does not suffer from thermal smearing. We have done the same procedure for all the three samples[7] which exhibit a phase rigidity over at least $\sim 16 \mu eV$, meaning that all our samples have negligible thermal smearing in the explored temperature range $k_B T < 16 \ \mu eV$=200 mK.

6.5 Properties of l_φ

6.5.1 Determination of l_φ

Now that we have clearly proven that the temperature dependence of ν did not result from the finite spectral width of the source we can claim that our measurements can be interpreted by the introduction of a coherence length $l_\varphi(T)$ such that :

$$\nu = \nu_0 e^{-2L/l_\varphi}$$

with

$$l_\varphi \propto T^{-1}$$

In figure 6.6 we have plotted the slope $ln(V/V_B)/(T - T_B)$ for the three samples. It is clear that the slope scales with the length of the interferometer arm defining, de facto, a coherence length $l_\varphi(T) \propto T^{-1}$. From the slope, and not from the absolute value of ν at the lowest temperature, we found a coherence length of 20 μm at 20 mK.

_____

7. This phase rigidity has been observed by every groups working on the electronic MZI with ΔL=0 [58][44].
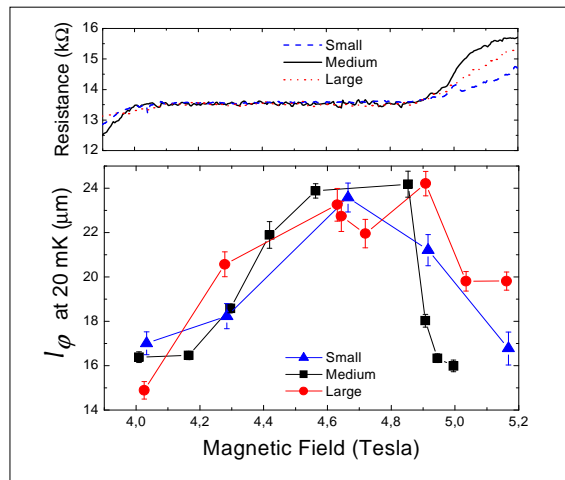
FIGURE 6.9 – (color online) **Upper panel** : The dashed, solid and dot lines are the two point Hall resistance at filling factor 2 measured for the small, the medium and the large sample respectively. l_φ has a general shape recovered by all the three samples, with a maximum at the end of the Hall plateau. **Lower panel** : Coherence length at 20 mK deduced from $L \times (T - T_B)/\ln(V/V_B)$ for the three different samples studied (L= 5.6 , 8 and 11.3 μm). The magnetic fields (x-axis) of the small and large sample has been shifted by +0.25 and -0.1 Tesla respectively, such that the plateau centers coincide for the three samples.

6.5.2   Magnetic field dependence of l_φ

The magnetic field variation of the deduced l_φ(T) is independent from the MZI size (see figure 6.9)[8].

The maximum of the coherence length is reached at the upper end of the plateau where the longitudinal resistance is usually minimum [39][9]. The magnetic field (x-axis) of the small(large) sample has been shifted by +0.2(-0.1) Tesla respectively, such that the plateau centers coincide for the three samples. This is due to a small variation of density of the samples. As one can remark, the coherence length changes for a factor close to two on the whole plateau. At that point, one may ask why we observe such a magnetic field dependence. First, just considering a drift velocity varying like 1/B and a coherence length given by $l_\varphi = v_D \tau_\varphi$, where τ_φ is a coherent time, magnetic field independent, we would think that l_φ should vary like 1/B. But it does not seem to be the case. However, our approach raises an important question : is the length L of the trajectories independent of the magnetic field ? As we will see in the next part, this is most probably not correct : the length changes with the magnetic field (probably due to disorder) leading to this non monotonous variation of l_φ with B. However before starting the next part, it is important to check if our result brings some universality or not. In the next chapter, I am going to

---

8. In order to compare the three samples at the same filling factor, we have shifted the magnetic fields (x-axis) of the small (large sample) by +0.25(-0.1) Tesla. These values center the Hall plateaus all together.

9. We have checked this independently via four points Hall resistance measurements.

compare our measured values with the different results in the literature.

6.6   Some universality ?

We can compare our results with previously available data from other groups. The first experiment on the MZI realized at $\nu = 2$ by Ji. *et al* [37] has set a lower bound $\sim 10\mu m$ to the coherence length. With a value of $\sim 20\mu m$ at 20 mK ,these experiments are in good agreement with our measured coherence length. Moreover, if one takes the pioneering results of Ji. *et al* [37] and plot them in logarithm scale, one observes that the visibility was also decaying exponentially with temperature (see figure 6.10).
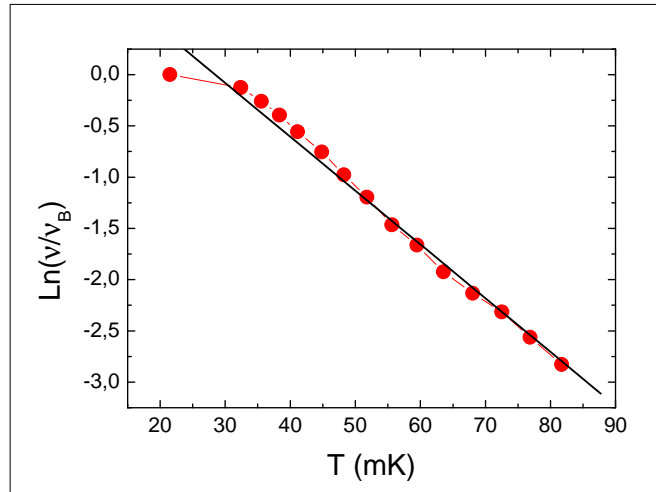
FIGURE 6.10 – Temperature dependencies of visibility for a large sample ($\sim 45\mu m^2$) obtained in the very first experiment of Ji. *et al* [37] and plot in logarithm scale. The visibility follows an exponential decay which when fitted to the dependence $\sim$ exp(-T/T_0) gives $T_0 \sim$ 52 mK (in good agreement with our measurement of T_0 for the large sample).

More recently, Litvin *et al.* have reproduced our measurements for a small and a large MZI [44]. They first considered our expression of the visibility :

$$\nu_I = \nu_0 e^{-2L/l_\varphi} = \nu_0 e^{-T/T_0} \text{ with } l_\varphi \propto T^{-1} \tag{6.3}$$

As demonstrated by the solid lines in Fig. 6.11, their data also vary exponentially with T above 45 mK. However, at lower temperatures a crossover to a weaker temperature dependence is observed. The presence of such a crossover is reflected by the extrapolated values of ν_{I0}, which exceed the allowed maximum of 100%, and the fact that the fit lines do not cross at T=0, but rather at 7 mK. Although it is notoriously hard to exclude that electron heating contributes to the apparent saturation of ν_I at T < 45 mK (in figure 6.11), the later two facts refer to the high temperature regime and indicate that the behavior

of $\nu_I(T)$ may be more complex than a simple exponential at low temperature [10]. Another strong difference with us is that they find a T_0 (see inset of the figure 6.11) that does not scale with the length of their interferometer but **with the area**, which prevents them from introducing a coherence length. Despite these important differences, their data also confirm the magnetic field dependence of T_0. They have measured T_0 on a wider interval of the magnetic field, have shown that T_0 had a maximum around $\nu = 1.5$ (see the inset of the figure 6.11) and varied from 20mK to 30mK (we obtain similar values of T_0).
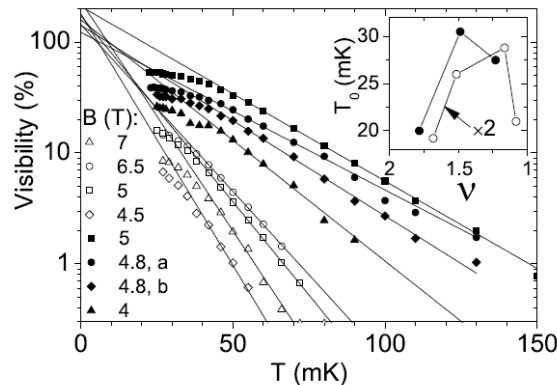
FIGURE 6.11 – (a) Temperature dependencies of visibilities for large (open symbols) and small (full symbols) MZIs at different magnetic fields. **Inset** : Characteristic temperatures T0 (2×T0) for the small (large) interferometer extracted from the exponential fits according to Equation 6.3

Another MZI experiment has confirmed our observations. Bieri *et al.* [15] have studied the visibility as a function of temperature : the visibility follows an exponential decay which when fitted to the dependence $\sim \exp(\text{-}T/T_0)$ yields for the characteristic energy scale T_0 a value of 30 mK (arm length $\sim$15μm). Finally, for several experiments on samples fabricated by different groups, with different experimental set up, different 2D gas (mobility), the coherence length seems to be of the same order for the same magnetic field. This indicates that this coherence length is more or less universal.

6.7 Conclusion

In this chapter, we have determined for the first time the value of the coherence length in the edge states at filling factor $\nu = 2$. By measuring the decay of the very high visibility of AB oscillations in MZI with the temperature on different interferometers of different sizes, we have extracted a coherence length of ~ 20 μm at 20mK. We have shown that this decay could not be attributed to thermal smearing since the phase remained rigid over an

---

10. If we look closer to the data of the middle sample, for one of the slope we also notice a saturation around 35mK. But it seems to be a spurious effect since for other slopes obtained on the same sample there is no saturation. I will explain in the next part what could be the fundamental reason for such a saturation.

interval of energy $\sim$ 200mK. Finally, we have found that this coherence length was strongly magnetic field dependent. Since then, our results have been verified in other experiments [15][44] confirming our observations.

However these measurements raise two questions :
– Why do we have a finite coherence length ?
– Why do we have a magnetic field dependence of the coherence length ?

We will answer these questions in the next part.

Direct Measurement of the Coherence Length of Edge States in the Integer Quantum Hall Regime

Preden Roulleau, F. Portier, and P. Roche

Nanoelectronic group, Service de Physique de l'Etat Condensé, CEA Saclay, F-91191 Gif-Sur-Yvette, France

A. Cavanna, G. Faini, U. Gennser, and D. Mailly

CNRS, phynano team, Laboratoire de Photonique et Nanostructures, Route de Nozay, F-91460 Marcoussis, France
(Received 15 October 2007; published 25 March 2008)

We have determined the finite temperature coherence length of edge states in the integer quantum Hall effect regime. This was realized by measuring the visibility of electronic Mach-Zehnder interferometers of different sizes, at filling factor 2. The visibility shows an exponential decay with the temperature. The characteristic temperature scale is found inversely proportional to the length of the interferometer arm, allowing one to define a coherence length l_φ. The variations of l_φ with magnetic field are the same for all samples, with a maximum located at the upper end of the quantum Hall plateau. Our results provide the first accurate determination of l_φ in the quantum Hall regime.

The understanding of the decoherence process is a major issue in solid state physics, especially in view of controlling entangled states for quantum-information purposes. The edge states of the quantum Hall effect are known to present an extremely long coherence length l_φ at low temperature [1], providing a useful tool for quantum-interference experiments [2–6]. Surprisingly, very little is known on the exact value of this length and the mechanisms that reduce the coherence of edge states. This is in strong contrast with diffusive conductors, where weak localization gives a powerful way to probe l_φ. It has been shown, in this case, that electron-electron interactions are responsible for the finite coherence length at low temperatures. In the integer quantum Hall effect (IQHE) regime, the presence of a high magnetic field destroys any time reversal symmetry needed for weak localization corrections, making such an investigation difficult. Furthermore, due to the unidimensionality of the edge states, electron-electron interactions may strongly modify the single particle picture, and one can ask whether the notion of phase coherence length is still relevant and how it depends on temperature. In this Letter, we show for the first time that one can define a phase coherence length and that it is inversely proportional to the temperature.

Though the energy redistribution length has been studied in the past [7,8], these scattering experiments do not measure the phase coherence, which requires observation of electron interference effects. So far, experiments have only been able to put a lower bound on l_φ at low temperatures [2,9–11]. The electronic Fabry-Pérot interferences occurring in ballistic quantum dots have been used since the early days of mesoscopic physics [9]. These first studies showed an exponential decay of the amplitude of the Aharonov-Bohm (AB) oscillations with temperature [10]. However, this decay was attributed to thermal smearing due to the contribution of thermally activated one particle energy levels of the dot. Furthermore, the size of the interferometers was not varied, nor

was a Fourier analysis performed of the AB oscillations that could yield an estimation of l_φ [12]. Quantum-dot systems also implicate the possible interplay of Coulomb blockade effects [13]. The Mach-Zender interferometers (MZI) [2,4,6] used in the present study do not suffer from the same limitations. First, we will show that the observed oscillations result from the interference of two paths of equal length, making thermal smearing negligible. Second, charge quantization effect leading to Coulomb blockade are irrelevant here. Last, comparison between MZI's of various sizes allows us the unambiguous determination of l_φ, as well as its dependence with temperature and magnetic field.

The sample geometry, presented in Fig. 1, is the same as in [6]. MZIs of different sizes were patterned using e-beam lithography on a high mobility two-dimensional electron gas formed at the $GaAs/Ga_{1-x}Al_xAs$ heterojunction (sheet density $n_S = 2.0 \times 10^{11}$ cm^{-2} and mobility = 2.5×10^6 cm^2/V s). The experiments were performed in the IQHE regime at filling factor $\nu = n_S h/eB = 2$ (magnetic field $B \simeq 4.6$ T). Transport occurs through two edge states. Quantum point contacts (QPCs) $G0$, $G1$, and $G2$ define electronic beam splitters with transmissions $\mathcal{T}_i$ ($i = 0$–2). In all the results presented here, the interferences were studied on the outer edge state schematically drawn as white lines in Fig. 1, the inner edge state being fully reflected by all the QPCs. The first gate $G0$ is tuned to fully transmit the outer ($\mathcal{T}_0 = 1$) edge state. The interferometer itself consists of $G1$, $G2$, and the small central Ohmic contact in between the two arms. $G1$ splits the incident beam into two trajectories (u) and (d), which are recombined with $G2$, leading to interferences. Samples have been designed such that (u) and (d) are of equal length. The sizes of the three interferometers used in this study scale by up to a factor of $\sqrt{2}$: the length of their arms are $L = 5.6$ μm, 8 μm, and 11.3 μm for enclosed areas of 8.5 μm^2 (referred to as "small"), 17 μm^2 ("medium"), and 34 μm^2 ("large"), respectively. The samples are cooled in a
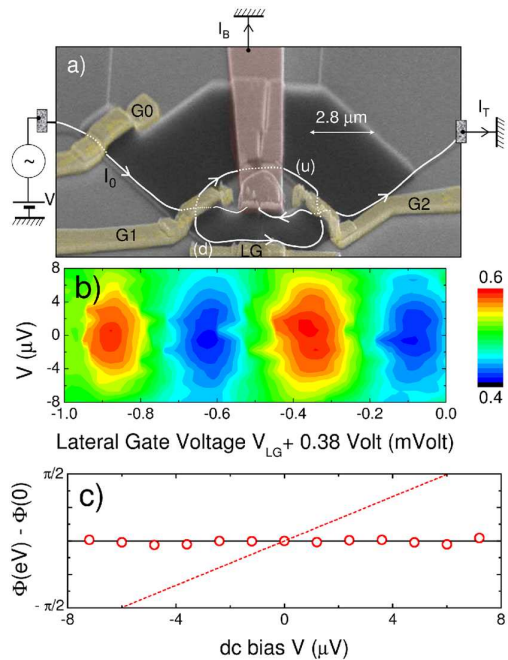
FIG. 1 (color online). (a) Tilted scanning electron microscope (SEM) view of the "small" MZI. $G0$, $G1$, and $G2$ are QPCs whose split gates are connected with gold bridges over an isolator responsible for the black color of the SEM view. LG is a lateral gate. The white line on the SEM picture represents the outer edge state. The small Ohmic contact in between the two arms collects the backscattered current I_B to the ground through a long gold bridge. (b) A 2D plot of dI_T/dI_0 as a function of the lateral gate voltage V_{LG} and the dc bias V, for the large sample at 20 mK. The visibility of interferences decreases with V while the phase of interferences remains almost constant. (c) Phase of the large sample deduced from Fig. 1(b). The dashed line is the energy dependence of the phase that would be necessary to explain our observed visibility decrease with thermal smearing.

FIG. 2 (color online). Interferences revealed upon varying the magnetic flux through the surface defined by the two arms (u) and (d) of the interferometers. From the oscillation period δB we deduce the surface $S = h/(e\delta B)$ of the 3 different studied MZI. (a) The small MZI ($S = 8.7 \pm 0.2$ μm^2). (b) The medium MZI ($S = 15.5 \pm 0.4$ μm^2). (c) The large MZI ($S = 40.7 \pm 0.8$ μm^2). All these surfaces are in good agreement with the lithographic ones (see text).

dilution fridge to temperatures ranging from 20 mK to 200 mK.

The labels are indicated in the upper part of Fig. 1. A current I_0 is injected into the outer edge state through the interferometer. The current that is not transmitted, $I_B = I_0 - I_T$, is collected to the ground with the small central Ohmic contact. I_0 is made up of a minute ac part, with the possibility to superimpose a dc bias V. The differential transmission of the interferometer is defined as $\mathcal{T} = G/G_0 = dI_T/dI_0$, where $G = dI_T/dV$ is the differential conductance and $G_0 = e^2/h$. It is measured with a standard lock-in technique using a 619 Hz frequency and a 39 pA$_{rms}$ amplitude ac bias. The corresponding bias voltage excitation (1 μV_{rms}) is always smaller than the energy scale involved. The oscillations revealing the quantum interferences can be obtained using two equivalent experimental procedures: either by superimposing a minute current to the large current of the magnet or by changing the surface defined by the MZI using a lateral gate (LG). Figure 2 shows the AB oscillations of the transmission

for the three interferometers, showing a magnetic period inversely proportional to the area of the interferometer, while Fig. 1(b) shows oscillations obtained using LG. After checking that both methods lead to the same interferences amplitude, we have always used the lateral gate and run the magnet in the permanent-current mode, strongly reducing the measurement noise. The visibility $\mathcal{V}$ of the AB oscillations is defined as the ratio of the half amplitude of the oscillation of the transmission divided by the mean value.

The maximum value of $\mathcal{V}$ is always obtained at the lowest temperature. $\mathcal{V}$ can reach 65% for the small interferometer, whereas it typically attains 20%–40% for the medium and the large interferometers [see Fig. 1(b)]. For each MZI we have studied the temperature dependence of the visibility. In Fig. 3, we have plotted $\ln(\mathcal{V}/\mathcal{V}_B)$ versus temperature, where $\mathcal{V}_B$ stands for the visibility at $T_B = 20$ mK. Clearly, the visibility decreases with temperature in all cases, and the larger the MZI, the stronger the temperature dependence. More quantitatively, if a linear regression of $\ln(\mathcal{V}/\mathcal{V}_B) = (T - T_B)/T_\varphi$ is done, one finds that T_φ^{-1} is proportional to the length of the interfering arms (inset of Fig. 3). In the following, we show that this behavior does not result from a thermal smearing.

The transmission probability through the MZI at the energy ϵ is $\mathcal{T}(\epsilon) = \mathcal{T}_1\mathcal{T}_2 + \mathcal{R}_1\mathcal{R}_2 + z\sqrt{\mathcal{T}_1\mathcal{R}_2\mathcal{R}_1\mathcal{T}_2} \times \sin[\phi(\epsilon)]$, where $z \in [0, 1]$ is a parameter accounting for phase averaging and/or decoherence, and $\mathcal{T}_i = |t_i|^2 = 1 - \mathcal{R}_i$ are the beam splitters' transmissions [14,15]. $\phi(\epsilon)$ is the AB flux across the surface $S(\epsilon)$ defined by the energy dependent edge state positions in the two inter-
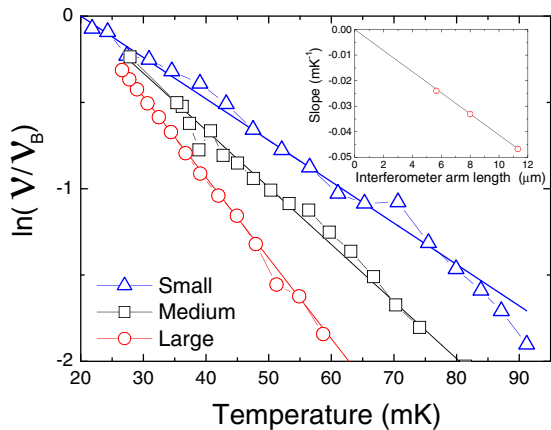
FIG. 3 (color online). $\ln(\mathcal{V}/\mathcal{V}_B)$ versus temperature for the three samples, $\mathcal{V}_B$ is the visibility measured at $T_B = 20$ mK. The measurement has been done at the magnetic field for which the visibility decay is the smallest. Inset: The slope $T_\varphi^{-1} = \ln(\mathcal{V}/\mathcal{V}_B)/(T - T_B)$ is proportional to the arm length.

fering arms, $\phi(\epsilon) = 2\pi S(\epsilon)eB/h$. When there is a finite length difference $\Delta L = L_u - L_d$ between the two arms, the surface S depends on the energy ϵ. Thus the phase varies with the energy, $\phi(\epsilon + E_F) = \phi(E_F) + \epsilon/(k_B T_S)$, where $k_B T_S = \hbar v_D/\Delta L$ [15] and v_D is the drift velocity (10^4 to 10^5 ms^{-1}) [16]. The differential conductance G at bias V and at temperature T probes the transmission probability at energy eV smeared over an energy range $k_B T$ [15]: $G(V) = G_0 \int_{-\infty}^{+\infty} f'(\epsilon)\mathcal{T}(\epsilon + eV)d\epsilon \propto \{1 + \mathcal{V}_0 < \sin[\phi(eV)]>_{k_B T}\}$, where $f'(\epsilon)$ is the derivative of the Fermi distribution. The energy dependence of the phase ϕ leads to a thermal smearing at finite temperature as the phase is blurred. A complete calculation yields a visibility decreasing like $\mathcal{V} = \mathcal{V}_0 \pi T/[T_S \sinh(\pi T/T_S)]$ [15]. In order to fit the visibility decrease with thermal smearing, this requires that $T_S \sim 66$, 59, and 44 mK, for the small, medium, and large sample, respectively [17].

On the other hand, at low temperature, T_S can be determined by measuring the phase of the interferences as a function of the dc bias V: $\phi(eV) = \phi(0) + eV/(k_B T_S)$. In Fig. 1(b) we have plotted a 2D graph of the differential transmission $\mathcal{T}(V)$ as a function of the lateral gate voltage and the dc bias, for the large sample at 20 mK. From this measurement we have deduced the phase $\phi(eV)$, which is shown to remain almost constant over an energy range of $\sim 16\ \mu$eV [Fig. 1(c)]. As a comparison, the dashed line of [Fig. 1(c)] is the phase dependence that would be required ($T_S = 44$ mK) to explain the decrease of the visibility with thermal smearing. The conclusion is straightforward: our sample does not suffer from thermal smearing. We have done the same procedure for all the three samples, which exhibits a phase rigidity over at least $\sim 16\ \mu$eV, meaning that all our samples have negligible thermal smearing in the explored temperature range $k_B T < 16\ \mu$eV $\equiv$ 200 mK. One can notice that phase rigidity with the

same order of energy range has been also observed in Ref. [18], on similar MZI [19].

The exponential decrease of the visibility with temperature is robust against various parameter variations, revealing a universal behavior. While the maximum visibility at the lowest temperature is affected by varying the transmissions $\mathcal{T}_i$ of the MZI and by applying a finite bias [6], T_φ^{-1} is found to be unaffected. In practice, the results presented here have been obtained with $\mathcal{T}_1 \sim \mathcal{T}_2 \sim 1/2$ and zero bias.

Indeed, and this is the central result of our Letter, our measurements can be interpreted by the introduction of a coherence length $l_\varphi(T)$ such that

$$\mathcal{V} = \mathcal{V}_0 e^{-2L/l_\varphi} \quad \text{with} \quad l_\varphi \propto T^{-1} \tag{1}$$

as shown in Fig. 3. $\mathcal{V}_0$ contains the temperature independent part of the visibility. In the inset of Fig. 3, we have plotted the slope $\mathcal{T}_\varphi^{-1}$ for the three samples [20]. It is clear that the slope scales with the length of the interferometer arm defining, *de facto,* a coherence length $l_\varphi(T)$ of about 20 μm at 20 mK. The magnetic field variation of the deduced l_φ is independent from the MZI size (see Fig. 4). In order to compare the three samples at the same filling factor, we have shifted the x axis of Fig. 4 by $+0.25$ T and -0.1 T for the small and large MZI, respectively. These values center the Hall plateaus all together. The maximum of the coherence length is reached at the upper
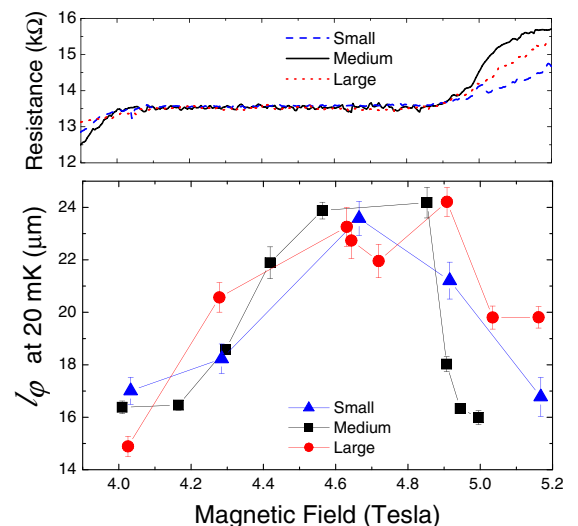
FIG. 4 (color online). Upper panel: The dashed, solid, and dotted lines are the two point Hall resistance at $\nu = 2$ measured for the small, the medium, and the large sample, respectively. l_φ has a general shape recovered by all three samples, with a maximum at the end of the Hall plateau. Lower panel: Coherence length at $T_B = 20$ mK, $l_\varphi = 2L.T_\varphi/T_B$ for the three samples studied ($L = 5.6$, 8, and 11.3 μm). The magnetic fields (x axis) of the small and large sample have been shifted by $+0.25$ and -0.1 T, respectively, such that the plateau centers coincide.

end of the plateau where the longitudinal resistance is usually minimum. However, our sample configuration does not allow us to check if it is actually the case.

Let us now compare our results with previously available data from other groups. Although the variations of $\mathcal{V}(T)$ were measured only for one interferometer size in the following experiments, it is possible to fit the data with Eq. (1) and to deduce a coherence length value at 20 mK. In the Fabry-Pérot type interferometer [Fig. (5b) of Ref. [10]], our analysis, using l_φ instead of thermal smearing, leads to $l_\varphi \sim 20$ μm at 20 mK. Although these experiments were performed with different filling factor, magnetic field, mobility, density, and geometry, surprisingly it gives the same result. The data from Ref. [2] yields also a similar l_φ, although a direct comparison is difficult without an exact knowledge of the MZI dimensions. Finally, the results of Ref. [4], again interpreted by the authors as resulting from thermal smearing, lead to $l_\varphi \sim 80$ μm at 20 mK.

What kind of mechanism is responsible for a finite coherence length varying with a T^{-1} temperature dependence? Electron-electron collisions are known to limit the coherence in non-unidimensional conductors (2D electron gas, diffusive metallic conductors). For the MZI, a finite l_φ coming from short range interaction ($l_\varphi \propto T^{-3}$), long range interaction [$l_\varphi \propto T^{-1}\ln^2(1/T)$], or curvature of the fermion dispersion ($l_\varphi \propto T^{-2}$) [21] cannot explain our findings. Alternatively, interactions with environment electrons, capacitively coupled to the arms of the interferometer, have been proposed to describe the decoherence of MZIs [22]. More specifically, decoherence is due to the thermal noise of the dissipative part of the finite frequency coupling impedance between the environment and the reservoirs. This theory leads to

$$\frac{l_\varphi}{L} = \frac{\tau_\varphi}{\tau} = \frac{\hbar}{2\pi k_B T} \frac{v_D}{L},$$ (2)

when $\pi\hbar C v_D/(Le^2) \ll 1$, C being a geometric capacitance, which represents the coupling to the environment and τ being the time of flight. For $v_D = 5.10^4$ ms^{-1} and $C/L \sim \epsilon_r\epsilon_0$, one finds $\pi\hbar C v_D/(Le^2) \ll 1$ and $l_\varphi \sim 3$ μm at 20 mK. This result agrees rather well with our measurements, although in the absence of an independent determination of v_D and C, it is not possible to be more quantitative. Moreover, the theory was developed for nonchiral wires coupled to a perfect conductor [22]. Also, one may ask what role may play the chirality and the environment of a nonperfect conductor.

We now turn to the nonmonotonic dependence of l_φ with the magnetic field B. If τ_φ is independent of B, as suggested by Eq. (2), the apparent variation of l_φ results from a variation of τ. As we have deduced l_φ assuming a constant trajectory length $l = L$, any variation of l, due to disorder, would modify the deduced $l_\varphi = \tau_\varphi L \times v_D/l$. Then, the maximum of l_φ shown in Fig. 4 corresponds to the mini-

mum of l/v_D. In a naive picture, the drift velocity v_D varies like $1/B$ [16,23] barely leading to nonmonotonic variations of l_φ. On the other hand, a nonmonotonic variation of l is all the more plausible. The maximum of l_φ occurs on the upper end of the Hall plateau where one expects minimum backscattering, thus a minimum l. Assuming this explanation is correct, the overlap of the three curves in Fig. 4 (lower panel) indicates that the variations of l scale with the geometric length of the MZI. The study of the influence of the sample disorder on l_φ and its dependence with magnetic field could bring new insights supporting our assumption.

In conclusion, we have measured the visibility of Mach-Zehnder interferometers of various sizes, operating in the IQHE regime at filling factor 2, as a function of both the temperature and the magnetic field. Our results provide a direct and reliable measurement of the coherence length found to be inversely proportional to the temperature and maximum at the upper end of the Hall plateau. The order of magnitude is compatible with theoretical predictions based on a dephasing arising from the thermal noise of the environment.

[1] T. Martin and S. Feng, Phys. Rev. Lett. **64**, 1971 (1990).
[2] Y. Ji *et al.*, Nature (London) **422**, 415 (2003).
[3] P. Samuelsson, E. V. Sukhorukov, and M. Büttiker, Phys. Rev. Lett. **92**, 026805 (2004).
[4] L. V. Litvin *et al.*, Phys. Rev. B **75**, 033315 (2007).
[5] I. Neder *et al.*, Nature (London) **448**, 333 (2007).
[6] P. Roulleau *et al.*, Phys. Rev. B **76**, 161309(R) (2007).
[7] B. W. Alphenaar, P. L. MacEuen, R. G. Wheeler, and R. N. Sacks, Phys. Rev. Lett. **64**, 677 (1990).
[8] T. Machida *et al.*, Solid State Commun. **103**, 441 (1997).
[9] B. J. van Wees *et al.*, Phys. Rev. Lett. **62**, 2523 (1989).
[10] J. P. Bird *et al.*, Phys. Rev. B **50**, 14983 (1994).
[11] I. Yang *et al.*, Phys. Rev. B **71**, 113312 (2005).
[12] A. E. Hansen *et al.*, Phys. Rev. B **64**, 045327 (2001).
[13] B. Rosenow and B. I. Halperin, Phys. Rev. Lett. **98**, 106801 (2007).
[14] F. Marquardt and C. Bruder, Phys. Rev. B **70**, 125305 (2004).
[15] V. S.-W. Chung, P. Samuelsson, and M. Büttiker, Phys. Rev. B **72**, 125320 (2005).
[16] R. C. Ashoori *et al.*, Phys. Rev. B **45**, R3894 (1992).
[17] These T_S's would imply ΔL's incompatible with the lithography precision: 5, 6, and 8 μm from small to large MZI (taking $v_D = 5.10^4$ ms^{-1}).
[18] I. Neder *et al.*, Phys. Rev. Lett. **96**, 016804 (2006).
[19] The exact origin of the phase rigidity is still under debate.
[20] These slopes are the minimum values obtained at different magnetic fields. From small to large MZI: 4.41 T, 4.91 T, and 4.85 T.
[21] J. T. Chalkers, Y. Gefen, and M. Y. Veillette, Phys. Rev. B **76**, 085320 (2007).
[22] G. Seelig and M. Buttiker, Phys. Rev. B **64**, 245313 (2001).
[23] C. W. J. Beenakker, Phys. Rev. Lett. **64**, 216 (1990).

Chapitre 7

Origin of the finite coherence length

Contents

7.1 Introduction

In this chapter, we will study the impact of the environment on the interferences. In the precedent chapter we have measured the coherence length, and have shown that it depended on the magnetic field. These measurements have raised the following questions :

Why do we have a finite coherence length ?

Where does this magnetic field dependence come from ?

These questions are usually very difficult to answer, since interfering electrons are coupled to the whole environment and in our case the environment can be the gates, electromagnetic fluctuations, nuclear spins, etc... Here, since we work at $\nu = 2$ the environment is specific : close to the interfering edge state, there is another edge state which, as we have seen, is coupled to the interfering one. It has motivated us to study more precisely the real impact of this inner edge state on the visibility of interferences realized on the outer one. We will first focus on the coupling parameter V_0 introduced in the part 5.5.1, and its magnetic field dependence. Since we work at finite temperature, the intern potential of the inner edge state fluctuates. Via the capacitive coupling, we will show that the inner edge state induces phase fluctuations of the interfering edge state.

In order to do that, we will mimic a noisy environment by partitioning the inner edge state, and study the impact on the visibility of the system. Comparing the effect of partition noise with the effect of thermal noise, we will be able then, to quantify the impact of the inner edge state on the interferences at finite temperature.

7.2 Coupling an Interferometer to a noisy environment

Several experiments have studied the coupling between an interferometer and a noisy controlled environment. Some of them are interpreted as "which path " experiments. In principle, a "which path experiment" detection means that we are able to reconstruct the interference with another experiment [14]. We are going to show that in our case the "which path" approach is not necessarily relevant.

7.2.1 Quantum dot detector

Bucks *et al.*[19] performed a which path experiment with an electronic double path interferometer [5, 6], fabricated in a high mobility 2DEG. The arms are defined by gating the 2DEG. In one arm, a quantum dot (QD) has been inserted (see figure 7.1).

A QPC is located near the QD, serving as a which path (WP) detector. It is expected that an electron passing through the QD modifies the potential nearby the QPC and hence its conductance. Even though there is no tunneling between the interferometer and the QPC-detector, the two systems are entangled by their mutual interaction. The dephasing induced by this entanglement is studied via measuring the visibility of the Ahoronov Bohm

FIGURE 7.1 – (a) A schematic description of the top electrodes and contacts of the interferometer, and the detector. The interferometer is composed of three different regions, emitter E, collector C , and base regions B on both sides of the barrier with the two slits. The right slit is in a form of a QD (with area $0.4\times 0.4\ \mu m^2$) with a QPC on its right side serving as a WP detector. (b) A top view SEM micrograph of the device. The gray areas are metallic gates deposited on the surface of the heterostructure. A special lithographic technique, involving a metallic air bridge, is used to contact the central gate that depletes the area between the two slits (it serves also as plunger gate of the QD).

conductance oscillations produced by the double path interferometer. The expression of the visibility is given by [19] :

$$\nu_D = 1 - \frac{1}{8}(\frac{\Delta T_d}{\sigma(T_d)})^2 \tag{7.1}$$

where T_d is the transmission probability of the QPC detector, ΔT_d is the sensitivity of the detector (maximum when $T_d \sim 1/2$, minimum for $T_d \sim 0$ or $T_d \sim 1$) and $\sigma(T_d)$ is the noise of the detector. For a noisy detector, $\sigma(T_d) \gg \Delta T_d$, the detector provides no which path information and $\nu_D \sim 1$. While for a quiet detector, $\sigma(T_d) \ll \Delta T_d$, one can determine, even if "in principle", the path the electron takes and consequently the interference pattern is expected to diminish. We have represented their results [19] in figure 7.2. In figure 7.2(a), they have shown the transmission probability T_d of the QPC detector, as a function of the voltage V_g applied to the right gate of the QPC detector. In figure 7.2(b), the visibility of

the Aharonov Bohm oscillations is plotted as a function of V_g for two values of the drain source voltage V_d across the detector.

We first notice that the visibility is minimum between 0 and 1/2, since there is a competition between the sensitivity of the detector and its noise, confirming the formula 7.1. Moreover, when V_d is too low, the detector is not sensitive enough to detect electrons and the visibility remains constant.

If this experiment is described as a "which path" experiment, the loss of coherence can be understood from another point of view : via looking at the direct effect of the charge fluctuations from the noisy environment on the visibility. In that case we do not need entanglement between the detector and the interferometer to suppress interferences.
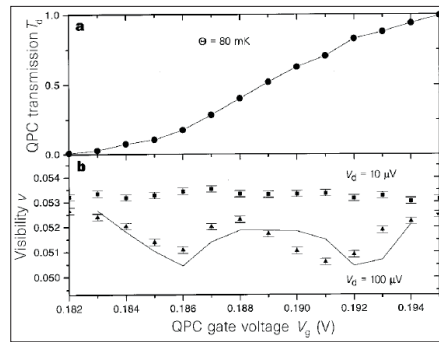
FIGURE 7.2 – (a) The transmission probability of the QPC detector, Td , as a function of the voltage applied to the right gate of the QPC detector, Vg. (b) The visibility of the Ahoronov Bohm oscillations as a function of Vg for two values of the drain source voltage across the detector, Vd .

7.2.2 Sprinzak *et al.* experiment

Sprinzak *et al.* [77] have coupled an interferometer(a double quantum dot) and a detector in the quantum Hall regime (at ν=1). Following their terminology, the detector is a noisy current, resulting from the partitioning of an edge state by a QPC. In figure 7.3, we have represented the principle of this experiment. An edge state is partitioned at the
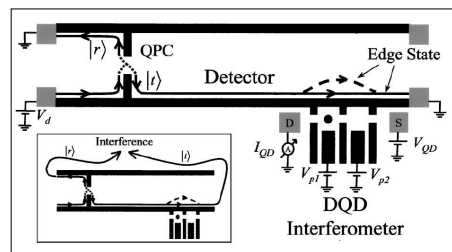
FIGURE 7.3 – A schematic of the DQD interferometer coupled to a QPC detector. The detector is a noisy edge state generated via the QPC. The interferometer is composed of a double quantum dot. What is studied here is the impact of a noisy edge state on the interferences (Sprinzak *et al.* [77]).
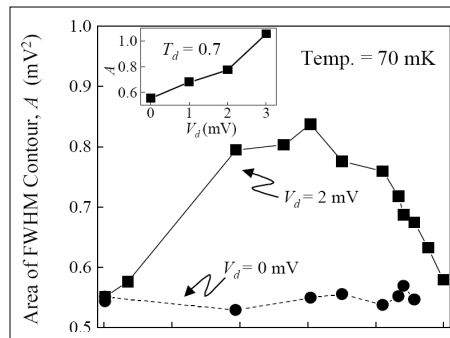
FIGURE 7.4 – The area of the contour at half peak height as a function of the transmission probability, T_d, for two values of applied bias $V_d = 0$ and 2 mV. The dependence qualitatively agrees with the expected $T_d(1 - T_d)$.

QPC. The transmitted electrons interact with the interferometer and, depending on the transmission of the QPC, the fluctuating number of electrons will have an effect on the visibility of interferences. Two different approaches can model this interaction. The first one is the "which path" approach. If we suppose that the transmitted and reflected edge state can be recombined after the interferometer[1], then we should be able to extract from the dephasing between the two paths an information about the interferometer which will, following the Bohr's complementarity principle, destroy interferences. But the loss of coherence can be understood from another point of view : via looking at the direct effect of the charge fluctuations from the noisy edge state on the visibility[2]. For a weak interaction between detector and interferometer the dephasing rate can be shown to have the form [19] :

$$\frac{1}{\tau_\varphi} = \frac{eV_d}{8\pi h}\frac{(\Delta T_d)^2}{T_d(1 - T_d)} + \frac{eV_d}{2h}T_d(1 - T_d)\gamma^2 \qquad (7.2)$$

where T_d is the transmission of QPC, ΔT_d is its variation induced by the interferometer[3], V_d is the drain source voltage on the QPC and $\gamma = \Delta\theta_t - \Delta\theta_r$ is a phase factor, with $\Delta\theta_t$ and $\Delta\theta_t$ the respective phase changes induced by the interaction with the interferometer in the transmitted and reflected electronic waves. Since the experiment is realized at $\nu = 1$, the transport is chiral and there is no feedback of the interferometer on the transmission of the QPC so ΔT_d=0 (furthermore the QPC is far away from the quantum dot). Finally the dephasing rate is proportional to the shot noise generated by the QPC. They have used a double quantum dot (QD) as an interferometer. A QD can be regarded as an electronic version of the optical Fabry-Perot interferometer, where interferences take place between the many trajectories that bounce back and forth between the two barriers connecting the QD to the leads. The interference leads to sharp resonances in the transmission through

---

1. In the inset of the figure 7.3, Sprinzak *et al.* [77] have represented a schematic representation of such an interference between the reflected and transmitted current.

2. We have preferred this point of view in the different interpretations we have used in the electronic MZI.

3. Feedback of the interferometer on the transmission of the QPC.

the QD at certain energies, each resonance has an intrinsic energy width Γ_i. When coupled to the noisy channel, dephasing leads to the broadening of the resonance peaks to $\Gamma_i + \hbar/\tau_\varphi$. We have represented in figure 7.4 the peak broadening dependence with T_d for a fixed V_d. It qualitatively follows the expression $T_d(1 - T_d)$.

7.2.3   Rohrlich *et al.* experiment
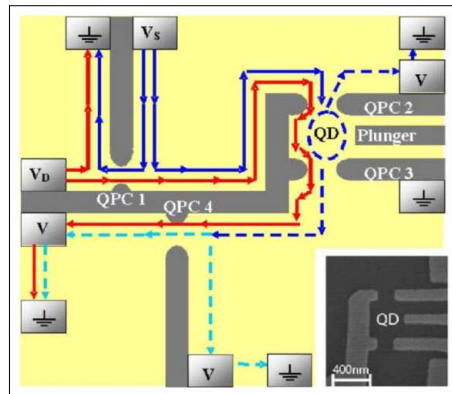
FIGURE 7.5 – Scheme of the quantum dot, defined by biased metallic electrodes (two QPCs and a "plunger gate") over a high-mobility two-dimensional electron gas (2DEG) of density $2 \times 10^{11}/\text{cm}^2$ embedded in a GaAs-AlGaAs heterojunction. The experiment is done at filling factor 2 (magnetic field of 5-7 Tesla). The inner edge state sees a Fabry Perot interferometer and the outer edge state is partitioned at a prior quantum point contact, serving as a detector. Inset : SEM micrograph of the dot, 0.4μm wide inside.

The Rohrlich *et al.*[66] experiment is very similar to the Spinzak *et al.*[77] one, except that they work at filling factor 2 and utilize one edge state as a detector and the other one as an interfering one. The interferometer is a quantum dot that acts as an interferometer of the Fabry-Perot type, composed of QPC1 and QPC2 (figure 7.5). The detector is still a noisy edge state partitioned by a quantum point. The advantage of this set up is to enhance the coupling between the detector and the interferometer. Indeed they begin to observe a strong effect on the visibility for $V_d \sim 103\mu V$ (see figure 7.6) whereas Spinzak *et al.* used to apply $V_d \sim 2mV$ to induce a detectable effect on the double quantum dot interferometer (see figure 7.4). Looking more precisely on these results, it seems that the expected $\sim exp(-T_{eff}(1 - T_{eff})V_d)$ is observed at lower bias, but that there is some deviation at higher bias. In our experiment the interferometer is an electronic Mach Zehnder and the "detector" is the inner edge state. This is the same experiment as the one realized by Neder *et al.*[59]. However as you will see in the following, our results are significantly different. We won't consider the "which path" approach, we will treat everything classically considering that the inner edge state is a noisy object that couples to the interfering edge state will reduce the visibility.
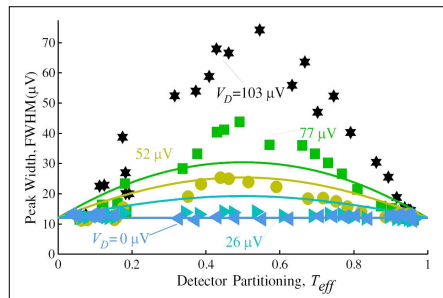
FIGURE 7.6 – Peak full width at half maximum (FWHM), as a functions of the effective detector transmission T_{eff} and detector bias. Symbols represent experimental results.

7.2.4 A true Which Path experiment ?

In principle, a "which path experiment" detection means that we are able to reconstruct the interference with another experiment. Indeed the which path experiment relies on the fact that the nearby interferometer induces a phase change in one of the propagating edge states (in the transmitted wave of the detector). If the detector is phase coherent, we should be able in principle to recombine the reflected and transmitted wave of the detector to make them interfere. The phase change gives us an information about the position of the electron in the interferometer which will destroy interferences. If we consider the "noisy environment" approach, the phase coherence of the detector is not necessary. An experimental proof to definitively keep the most adapted approach is to introduce between the QPC and the interferometer a floating ohmic contact [4] (see figure 7.7(a)).

If the partitioned edge state is fully absorbed, electrons lose their phase coherence but the environment remains noisy. Therefore if a non-coherent noisy edge state always have an effect on the visibility of oscillations, it will mean that only the second approach is more appropriated. We have represented their results in figure 7.7(b). They still observe the decay of the visibility with the dephasor, the small variation in the dephasing being attributed to the finite capacitance of the ohmic contact that shorts to ground high frequency components of the shot noise. To conclude, it seems to me that the "which path" approach is not necessary.

Similarly to the Sprinzak *et al.* experiment, we can answer the question whether coupling a noisy edge state with the MZI is a true "which path" experiment or not. We will detail in the following how to couple a noisy edge state to a MZI. We just give here the general principle of the experiment, since it is very close to the one of Sprinzak *et al.* We have represented a scheme of the experiment in the figure 7.8 where the interferometer is in red, the detector in yellow.

---

4. In our experiment "Voltage Probe" we have also used a floating ohmic contact to simulate total energy redistribution. But contrary to them, we will control the probability that electrons are dephased by the probe. In the present experiment, the gate is either open or closed.
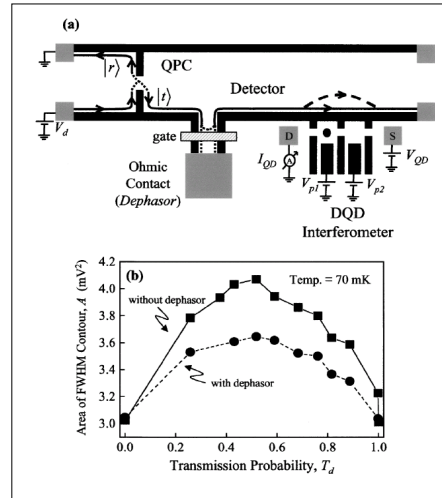
FIGURE 7.7 – (a) A schematic of the experimental setup with a floating ohmic contact introduced in the transmitted wave. The ohmic contact serves as a dephasor for the transmitted electrons. A gate in front of the ohmic contact allows removing this contact from the electrons path. (b) The area of the contour at half peak height as a function of the transmission probability, T_d, with and without the ohmic contact in the electrons path. The decrease in the dephasing rate is attributed to the non-negligible capacitance of the ohmic contact that shorts the high frequency components of the shot noise to ground, preventing them from participating in the dephasing of the Double Quantum Dot.

7.2.5   Proposal with the MZI

In the first case (see 7.8 (a)), we tune beams splitters C and B to 1/2 to obtain the maximum visibility. The detector is composed of a noisy edge state. In the first case (see 7.8 (a)), we tune the beam splitter D to 1/2 and we close the beam splitter A. Since the edge state is noisy, we will be able to destroy interferences. To check whether it is due to a which path detection or to a "noisy environment", we realize this second experiment (see figure 7.8 (b)). The beam splitter D is now closed, and the beam splitter A is set to 1/2. Before being coupled to the interferometer, the noisy edge state is fully absorbed by a floating ohmic contact. If this noisy edge state still have an effect on the interferences, it will mean the the "which path" approach is not necessary. I have not realized this experiment but I have very few doubts on what would be the result. In principle, a "which path experiment" detection means that we are able to reconstruct the interference with another experiment. This has been achieved in optics by Bertet *et al.*[14].

7.2.6   Optical experiment

Bertet *et al.*[14] have used an atomic double-pulse Ramsey interferometer, in which microwaves pulses act as beam-splitters for the quantum states of the atoms, to mimic a MZI (see figure 7.9). An atoms beam is split into two paths a and b and recombined by two beam splitters B_1 and B_2. The quantum amplitudes associated with these paths present a phase difference ϕ, swept by a retarding element. If B_1 and B_2 are macroscopic,
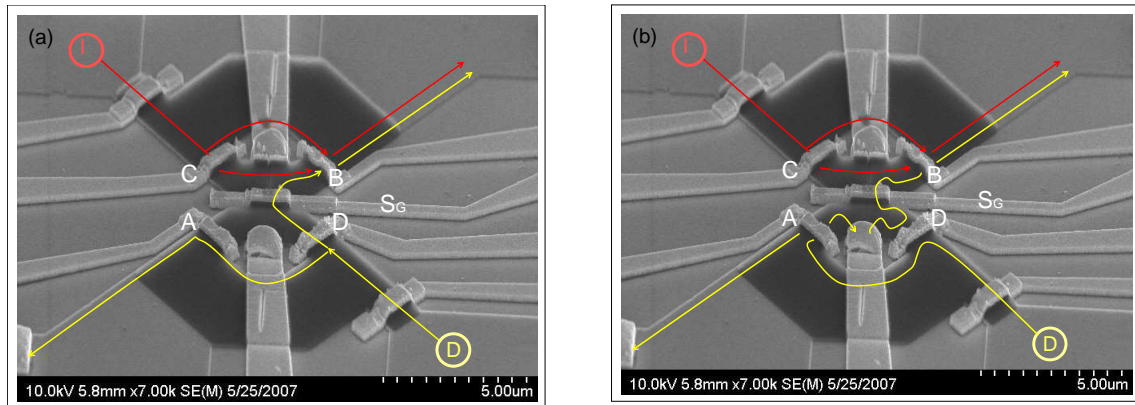
FIGURE 7.8 – Experimental configuration of my proposal. (a) We tune beams splitters C and B to 1/2 to obtain the maximum visibility. We have represented in red the interferometer, in yellow the detector is composed of a noisy edge state. We tune the beam splitter D to 1/2 and we close the beam splitter A. Since the the edge state is noisy, we will be able to destroy interferences.(b) The beam splitter D is now closed, and the beam splitter A is set to 1/2. Before being coupled to the interferometer, the noisy edge state is fully absorbed by a floating ohmic contact.

the probability for detecting the particle in detector D exhibits a sinusoidal modulation as a function of ϕ. Suppose now that B_2 is a massive classical object, and B_1 is a light plate which may rotate around an axis perpendicular to the interferometer plane. When the particle interacts with B_1, it is, with a 50 % probability, either transmitted along path a (the plate does not move) or reflected into path b (the plate receives a momentum kick, resulting in a coherent state of motion). The particle $+ B_1$ system evolves into the combined state :

$$\Psi = (1/\sqrt{(2)})(|\Psi_a > |\Psi_{B_1}(a) > +|\Psi_b > |\Psi_{B_1}(b) >)$$

where $|\Psi_a >$ and $|\Psi_b >$ represent the particle's wave packets in paths a and b and $|\Psi_{B_1}(a) >$ and $|\Psi_{B_1}(b) >$ the corresponding final states of B_1. If B_1 is light enough, it stores unambiguous information about the particle's path and $< \Psi_{B_1}(b)|\Psi_{B_1}(a) >= 0$. If B_1 is a heavy macroscopic object insensitive to the particle's momentum kick, $|\Psi_{B_1}(b) >= |\Psi_{B_1}(a) >$. The probability for detecting the particle in D is :

$$P(\phi) = \frac{1}{2}(1 + Re(< \Psi_{B_1}(b)|\Psi_{B_1}(a) > \exp(i\phi)))$$

The fringe contrast is the modulus of the scalar product of the two beam splitter final states and directly measures the degree of entanglement between the particle and B_1.

A microwave pulse R_1 (figure 7.9) acts as a beam splitter which splits the Rydberg atom's state into two energy levels e and g, then recombined by pulse R2,before being detected in D. If the R1 field, stored in a long-damping-time cavity C, is macroscopic, Ramsey fringes are visible. If the R1 field is microscopic, its photon number records information about the atom's path, suppressing the interference. We have represented their results in figure 7.10.
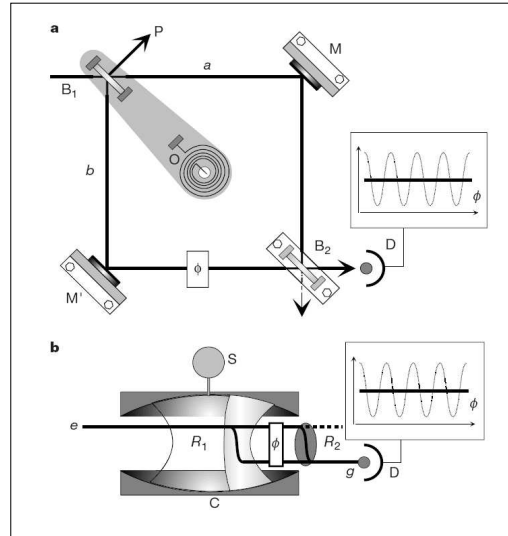
FIGURE 7.9 – Mach-Zehnder and Ramsey versions of Bohr's experiment. (a) In the Mach- Zehnder interferometer, the particle trajectory is separated by beam splitter B1 into paths a and b, folded by mirrors M and M' and recombined by beam splitter B2 into detector D. The other output port (dashed arrow) is not used. A dephasing element tunes the relative phase ϕ between the paths. B1 can rotate around an axis perpendicular to the interferometer plane, crossing it at the center O of the B1MB2M' square. A spring provides a restoring force. The moving assembly is initially in its ground state of motion. If B1 has a large mass, fringes are visible (dotted lines in inset). If B1 is microscopic, its recoil records the reflection of the particle into path b, washing out the fringes (solid lines). (b) Ramsey set-up. A Rydberg atom's state is split by microwave pulse R1 into two energy levels e and g, then recombined by pulse R2 downstream, before being detected by field-ionization in D. Interferences are obtained in the probability for finding the atom in g. A field pulse between R1 and R2 tunes the relative phase ϕ of the interfering amplitudes (Stark effect). If the R1 field, stored in a long-damping-time cavity C, is macroscopic, Ramsey fringes are visible (dotted line in the inset). If the R1 field is microscopic, its photon number records information about the atom's path, suppressing the interference (solid line).

As expected, if the R_1 field is macroscopic, fringes are visible. If R_1 is microscopic, its photon number records information about the atom's path, suppressing the interference. In this which path experiment, the information transfer between the interferometer and the detector is realized, conserving the coherence of the whole system.

7.3   Inner and outer edge state coupling

To study the real impact of the inner edge state on the visibility of interferences realized on the outer one, we must focus on the capacitive coupling between the inner and outer edge state already introduced in the part 5.5.1. In particular, we will show that this coupling is magnetic field dependent.
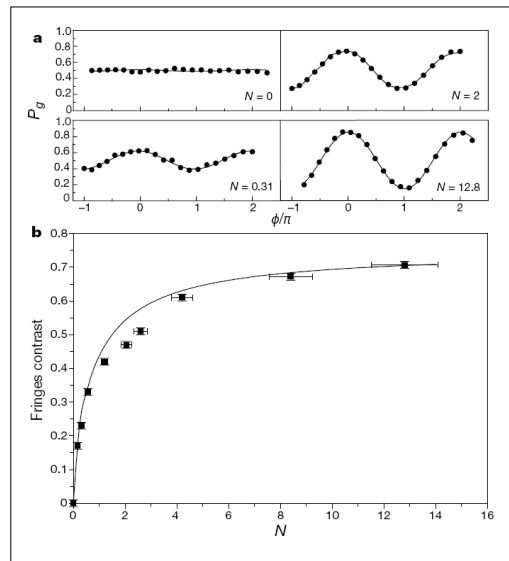
FIGURE 7.10 – From quantum to classical interferometer. (a) Ramsey interference signal recorded for various mean photon numbers N in the R1 pulse. The progressive evolution from the quantum to the classical beam-splitter case is clearly observed. (b) Fringe contrast as a function of the mean photon number N in R1. The points are experimental. The line represents the theoretical variation of the modulus of the beam-splitter final- states scalar product, multiplied by a fixed factor η that accounts for interferometer imperfections.

7.3.1   Characterizing the coupling

Here, all the measurements are realized at $\nu = 2$. We will use the inner edge state as a lateral gate. As represented in figure 7.11, we have modified the experimental set up. We separate the inner edge state (in blue) from the outer edge state that interferes (in red), using G_0 (this is the same set up that we have used in 5.5.1).

The transmissions of each edge state are measured independently with two lock-ins at two different frequencies. The inner edge state, being very close to the outer edge state is capacitively coupled to this last. By applying a bias voltage V_2 on the inner edge state one can reveal the interference pattern. As already explained, since the phase depends on the bias voltage V_2, we must take into account this capacitive coupling in the expression of the interfering part of the current $I_\sim \approx I_D \times cos(\phi - \frac{2\pi V_2}{V_0})$ where V_0 is the coupling parameter.

Figure 7.12(b) shows that we are able to sweep the phase of interferences and hence to reveal the interference pattern by sweeping V_2. This experiment was done on the large sample (arm length equal to $11.3\mu m$).

7.3.2   Magnetic field dependence of the coupling parameter

We have made here an interesting finding : the parameter V_0 depends on the magnetic field in a way which could remind the general slope of l_φ with the magnetic field. First, we have checked that the inner edge state is well defined on the whole plateau. Indeed,
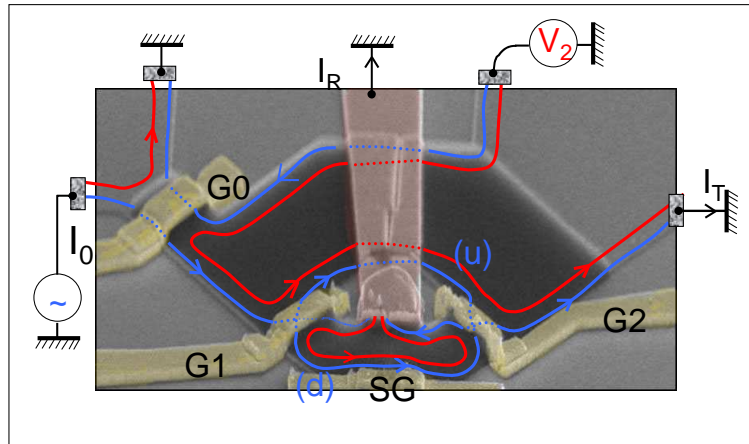
FIGURE 7.11 – Top-view scanning electron micrograph of the large device, with schematic representation of the edge states. On this representation the gate G_0 is set to 1. Two edge states are injected into the Mach-Zehnder : the outer edge-state drawn in blue, and the inner one drawn in red. Thanks to the gate G_0, one can feed the inner and outer edge states with two different bias.
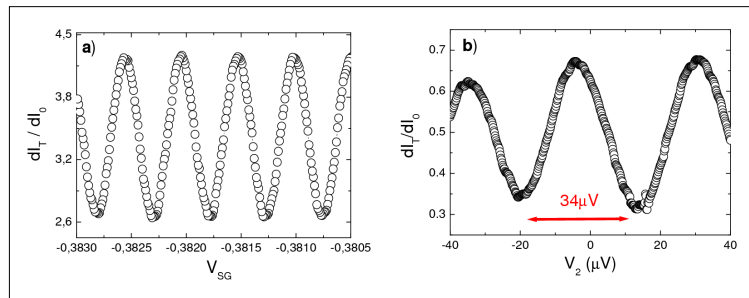
FIGURE 7.12 – (a) Phase sweeping by varying the side gate voltage V_{SG} (b) Phase sweeping by varying the bias voltage V_2, applied on S_2 (the measurements were done at 4.28 Tesla)

before characterizing the coupling one has to check if the two edge states are well defined, or more precisely, on what range of magnetic field the Hall plateau extends.

This is done either with a two point measurement in the large region of the mesa (figure 7.13) or by measuring the transmission of the inner edge state when injecting the current through S_2 with $T_0=1$ (in figure 7.14(b)).

This last experiment gives an access to the back scattering in the narrow regions of the MZI. It gives "de facto" a comparison between the filling factor in the MZI and the filling factor in the wide region. One can see on the figure 7.14(b) that the total transmitted current (T_0 is set to 1 such that in principle just the inner edge state contributes to the transport) remains equal to 1/2 and start to decrease at a magnetic field for which the Hall resistance (figure 7.13) start to decrease. This indicates that filling factor in the MZI and in the large part of the mesa are very close. We study then the dependence of the coupling parameter V_0 with the magnetic field. V_0 increases linearly from $19.2\mu V$ at 3.65 T to $48.8\mu V$ at 4.66T, and then slightly decreases (see figure 7.15 and 7.16). We have summarized the evolution of V_0 with the magnetic field in figure 7.14(a).
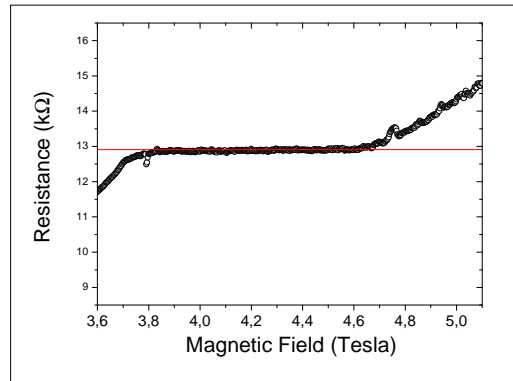
FIGURE 7.13 – Two points Hall resistance measurement. The filling factor $\nu=2$ is defined from 3.7 Tesla to 4.8 Tesla. From 4.8 Tesla to 5.2 Tesla, the Hall resistance start to increase.
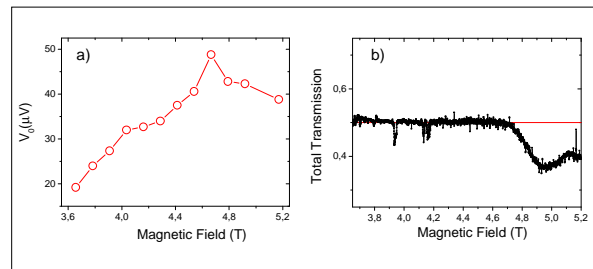
FIGURE 7.14 – (a)Dependence of V_0 on the whole plateau at $\nu=2$. We observe a monotonous increase V_0 from $20\mu V$ at 3.65Teslas to $48\mu V$ at 4.8Teslas. Between 4.8 and 5.2 Tesla, we observe a small decrease of V_0. (b) We check that the transmission of the inner edge state is well defined and equal to 1 in the interval B=3.67 T to 4.8 T. However between 4.8T and 5.2T the inner edge state is still present.
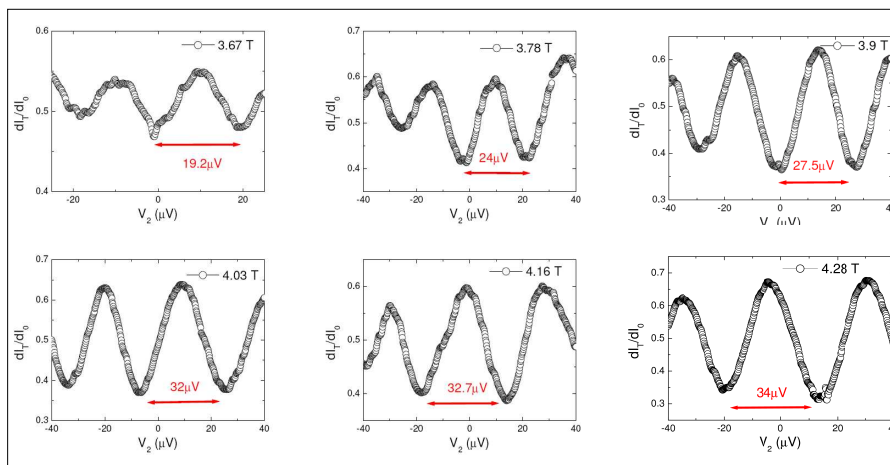
FIGURE 7.15 – Dependence of V_0 with the magnetic field in the interval B=3.67 T to 4.28 T

To conclude we have shown that the interfering edge sate is coupled to the inner edge
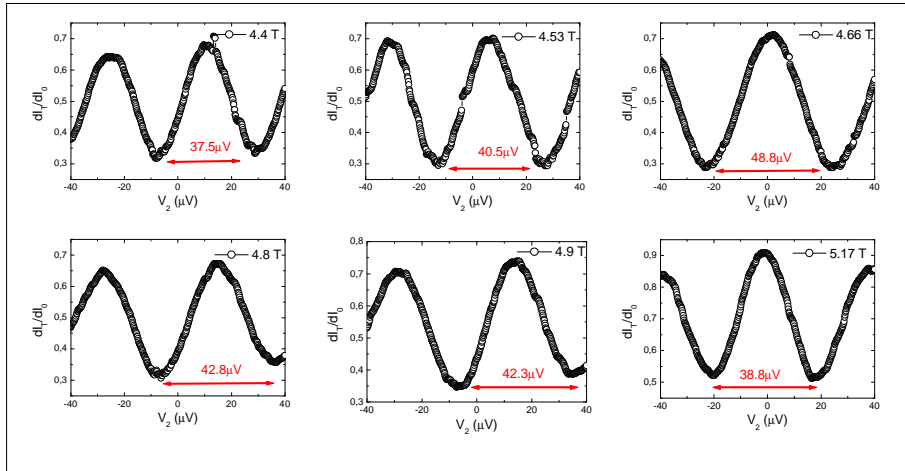
FIGURE 7.16 – Dependence of V_0 with the magnetic field in the interval B=4.4 T to 5.17 T

state. This capacitive coupling enables us to use the inner edge as a real lateral gate. We have observed that this coupling strongly depended on the magnetic field. We are going now to study the impact of a noisy inner edge state on the visibility of interferences.

7.3.3 Gaussian Noise dephasing

We have studied the impact of a noisy inner edge state on the visibility of a MZI. In this experiment, the inner edge channel is partitioned and simulates thus a noisy environment which lowers the visibility. The interaction between the inner and the outer channels was characterized before the actual dephasing experiment by first fully reflecting the biased inner edge channel emanating from S_2 (with G_0). Indeed, as we have shown in the previous part, the full reflection ($T_0 = 1$) had a strong effect on the phase of the interference pattern, which varied linearly with V_2 but with nearly no effect on the visibility. Regarding the dependence of the visibility with bias voltage V_2 for a transmission $T_{0,in}=1/2$, we have worked at different magnetic field. We have first checked that the transmission $T_{0,in}=1/2$ was well defined on the interval B=3.67 T to 5.17 T for the whole range of V_2. We never observed any lobe structure of the visibility with V_2 as Neder *et al.* [59]. (see next chapter : Observation of non Gaussian noise).

For example, at 3.9 Tesla (resp. 4.7 Tesla) we obtain a 2π shift for $V_2 = 27.5\mu V$ (resp. $V_2 = 49\mu V$) (see figure 7.17(a)).

In figure 7.17(b) we have represented the visibility decrease as a function of V_2 when $T_0=1/2$. The logarithmic scale clearly shows an exponential decrease which is very well explained by a Gaussian phase averaging of the AB phase of the MZI. The purpose of this chapter is to explain what is the Gaussian approximation and how it leads to a decrease of the visibility following $\nu \sim exp(-T_0(1-T_0)V_2/V_\varphi)$ where V_φ is a parameter.

Alternatively, we have studied the visibility for a fixed value of V_2 with the transmission of G_0. In figure 7.18 we observe an exponential decrease of the visibility proportional to $T_0(1-T_0)$ in perfect agreement with a Gaussian approximation. We do not obtain a V-shape
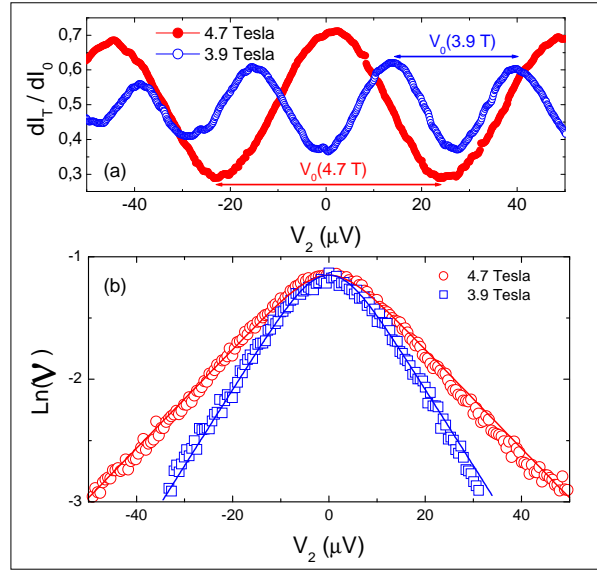
FIGURE 7.17 – (color online) **a) :**Phase sweeping by varying V_2 with $T_0 = 1$ for two different magnetic fields 4.7 and 3.9 T. The periodicity V_0 depends on the magnetic field. **b) :** Visibility decrease of the interferometer as a function of V_2 at $T_0 = 1/2$ for two different magnetic fields 4.7 and 3.9 T. The solid lines are fit to the data $V = V_0 e^{-2\pi^2 \Delta S_{22} \Delta \nu / V_0^2}$ with an electronic temperature of 25mK (for a base temperature of 20mK) and $T_0 = 1/2$. The high bias fit of the exponential decrease $V = V_0 \exp(-T_0(1 - T_0)V_2/V_\varphi)$ allows us to determine V_φ which is found to depends on the magnetic field.

as Neder *et al.* [59].
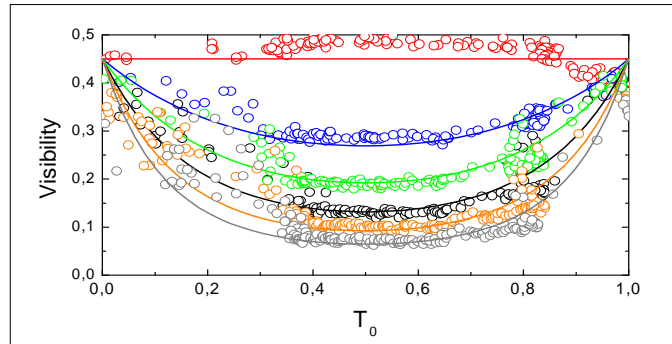
FIGURE 7.18 – (color online) Visibility decrease of the interferometer as a function of T_0 for V_2=0, 21, 31, 42, 53 and 63 μV from top to bottom. The solid lines are fits to the data using Eq. 1 with V_0=0.45, $V_\varphi = 7.2\mu V$ and T=25mK.

7.3.4   The Gaussian approximation

We detail here the Gaussian approximation. We have seen before that, due to the coupling, the phase was related to V_2 by $\delta\varphi = 2\pi V_2/V_0$. Now if V_2 fluctuates, it leads to

fluctuations of the phase. We must take into account these fluctuations in the formula of the interfering current. A phase-averaged transmission probability over these fluctuations gives :

$$\langle I_\sim \rangle = \frac{e^2}{h} V (T_1 T_2 + R_1 R_2 + \sqrt{T_1 R_2 T_2 R_1} \langle \sin(\varphi) \rangle)$$

I now assume a Gaussian phase averaging with a variance $\langle \delta\varphi^2 \rangle$. $\langle \sin(\varphi) \rangle$ becomes :

$$\langle \sin(\varphi) \rangle = \sin(\langle \varphi \rangle) e^{-\langle \delta\varphi^2 \rangle / 2}$$

where $\langle \delta\varphi^2 \rangle$ is the variance of the Gaussian distribution. $\langle \delta\varphi^2 \rangle$ is then simply related to $\langle \delta V_2^2 \rangle$ through the coupling constant, and $\langle \delta V_2^2 \rangle$ is related to the noise power spectrum S_{22} of V_2 trough an unknown bandwidth $\Delta\nu$:

$$\langle \delta\varphi^2 \rangle = (2\pi)^2 \langle \delta V_2^2 \rangle / V_0^2 = (2\pi)^2 S_{22} \Delta\nu / V_0^2 \tag{7.3}$$

If one generates partition noise on the inner edge state with the splitter G_0, the resulting excess noise :

$$\Delta S_{22} = 2e R_Q T_0 (1 - T_0) V_2 (\coth(\frac{eV_2}{2k_B T}) - \frac{2k_B T}{eV_2}) \tag{7.4}$$

leads to a visibility decreasing exponentially with V_2 when $eV_2 \gg k_B T$:

$$\nu = \nu_0 e^{-T_0(1-T_0)(V_2 - 2k_B T/e)/V_\varphi}, \tag{7.5}$$

with

$$V_\varphi^{-1} = \frac{4\pi^2 e R_Q}{V_0^2} \Delta\nu, \tag{7.6}$$

and $R_Q = 1/G_Q = h/e^2$. In equation 7.5, the unknown parameter is V_φ which is related to the bandwidth $\Delta\nu$ (Equation 7.6). This approach for the dephasing is valid only if $\Delta\nu$ is such that the fluctuations lead to a Gaussian distribution of φ. It implies that many electrons have to be involved in the dephasing during the measuring time $1/\Delta\nu$, namely that $\max(eV_2, 2k_B T) \gg h\Delta\nu$. This condition coincides with the fact that the noise power spectrum S_{22} can be considered as frequency independent.

In figure 7.17(b) we have plotted the visibility versus V_2 when $T_0 = 1/2$ at 3.9T and 4.7T. ν decreases exponentially with V_2. The solid lines are fits to the data using equation 7.5 with an electronic temperature of 25mK (for a fridge temperature of 20mK). V_φ and ν_0 are the fitting parameters. Figure 7.18 shows the visibility for different values of V_2 and T_0 at a magnetic field of 4.6 Tesla. The solid lines are fits to the data using equation 7.5 with V_φ=7.2μV and T=25mK. Clearly at high bias there is no V-shape contrary to what has been recently observed in [58] and [59]. Instead, the curves show that the Gaussian approximation is valid. The agreement is perfect when T_0 is well defined in our sample. The dispersed data on the edges in figure 7.18 coincide to a strong dependence of T_0 with the voltage applied on G_0, resulting on an energy dependent transmission T_0 [5].
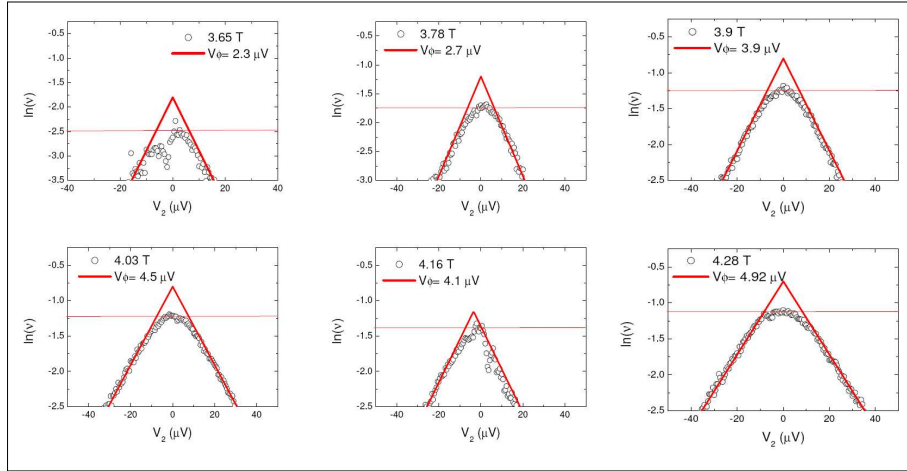
FIGURE 7.19 – Logarithm of the visibility as a function of V_2 for different magnetic field in the interval B=3.67 T to 4.28 T. From our fits we are able to extract V_φ on the whole plateau at filling factor ν=2.
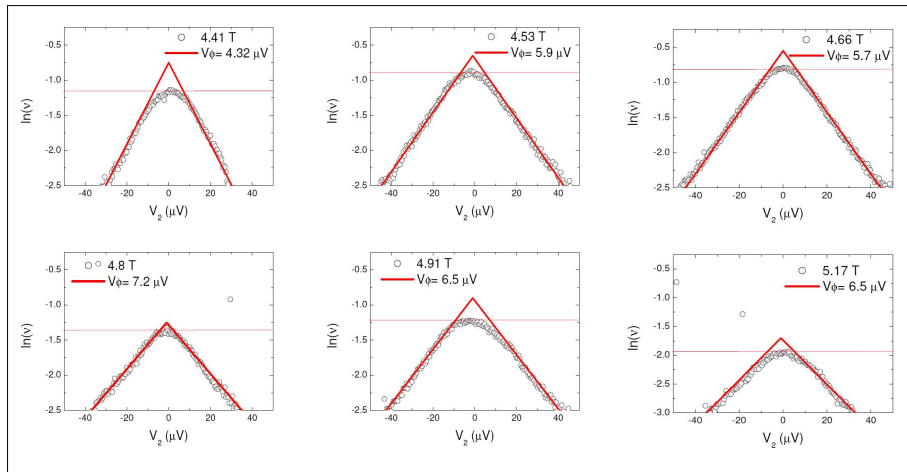
FIGURE 7.20 – Logarithm of the visibility as a function of V_2 for different magnetic field in the interval B=4.4 T to 5.17 T. From our fits we are able to extract V_φ on the whole plateau at filling factor ν=2.

7.3.5 The magnetic field dependence

In the previous part, we have shown that the coupling between the inner and the outer edge state strongly depended on the magnetic field.

To confirm our Gaussian approximation approach, we had to show that our fit (formula 7.5) is the good one on the whole plateau at $\nu = 2$ [6]. We have, thus studied the decrease of the visibility with the bias voltage V_2, at transmission T_0=1/2 for several magnetic fields. In figure 7.19 and 7.20, we have represented our experimental data in black dots,

---

5. Non linearities are more pronounced when T_0 is close to 1 and 0.

6. Indeed, we also have to show that the Gaussian approximation is valid, namely that $\Delta\nu \ll max(eV_2, k_B T)$ on the whole plateau corresponding to the filling factor ν=2.
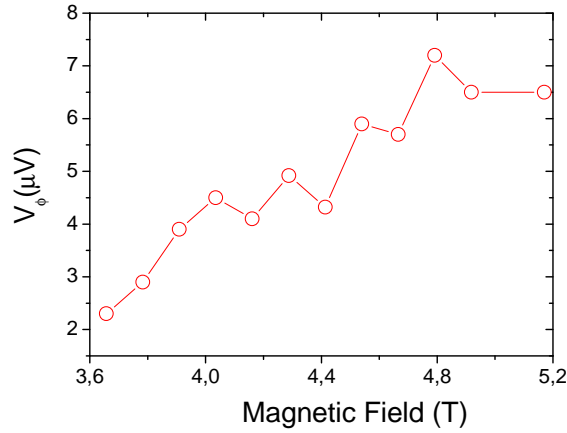
FIGURE 7.21 – Dependence of V_φ on the whole plateau at ν=2. We observe a monotonous increase V_φ from $2.4\mu V$ at 3.65Teslas to $7.5\mu V$ at 4.8Teslas. Between 4.8 and 5.2 Tesla, we observe a small decrease of V_φ.

with our fits in red solid lines from B= 3.67 Tesla to B= 5.17 Tesla. We first notice the remarkable agreement with our fit on the whole plateau. Moreover the exponential decrease strongly depends on the magnetic field : for each magnetic field, we can extract V_φ. We have summarized the evolution of V_φ with the magnetic field in figure 7.21. The general behavior of V_φ seems to be similar to V_0. We will go back to this point later.

7.4   An explanation to the finite coherence length

Now that we have characterized the impact of a noisy inner edge state, we will be able to answer to this question : where does the finite coherence length come from ? Why does the coherence length depend on the magnetic field ?

7.4.1   Impact of the inner edge state

We are now going to compare the exponential decrease of the visibility in the presence of shot noise with our previous observation that the coherence length of edge states is inversely proportional to the temperature. When $eV_2 \ll k_B T$, the noise is dominated by the Johnson Nyquist noise $S_{22}=4k_B T R_Q$. The expression 6.5 becomes :

$$\nu = \nu_0 e^{-T/T_\varphi},$$

with

$$T_\varphi^{-1} = \frac{2 \times 8\pi^2 k_B R_Q}{V_0^2} \Delta\nu, \tag{7.7}$$

Here, the factor 2 arises from the fact that the two arms of the interferometer suffer from a coupling with a noisy channel, instead of one when creating partitioning. This can

be easily understood thanks to the figure 7.22 where we have represented in white the two independent source of Johnson Nyquist noise. In the expression 7.7 the bandwidth $\Delta\nu$ is still an unknown parameter, but remains the same than when we have mimic a noisy environment [7]. We have to compare the bandwidth to the expression of V_φ given by :

$$V_\varphi^{-1} = \frac{4\pi^2 e R_Q}{V_0^2} \Delta\nu$$
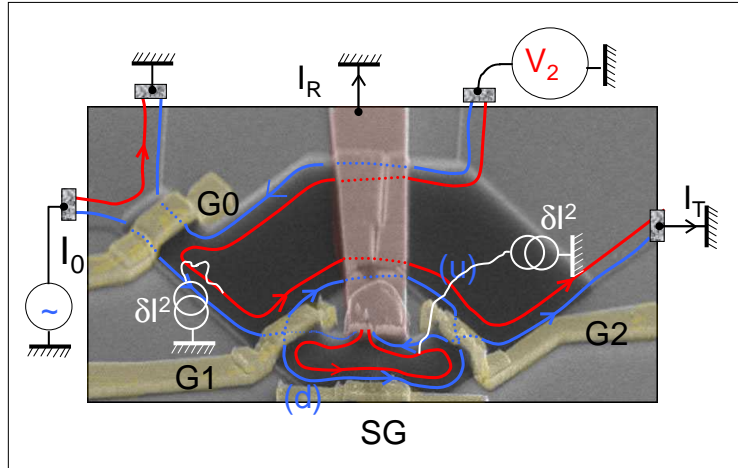
FIGURE 7.22 – The two arms of the interferometer suffer from a coupling with a noisy channel. We have represented in white the two independent sources of Johnson Nyquist noise, which lead to a finite coherence length.

We finally get :

$$\boxed{eV_\varphi = 4k_B T_\varphi} \tag{7.8}$$

If our hypothesis of a noisy inner edge state that would reduce the visibility due to thermal fluctuations is correct, we should verify experimentally the last relation between V_φ and T_φ (formula 6.8). Figure 7.23, we have collected V_0, V_φ and the general shape of T_φ obtained on the large sample on Hall plateau. Our data are in perfect agreement with equation 6.8. This definitively demonstrates that thermal noise and coupling between the two edge states are responsible for the finite coherence length.

7.4.2 An approach valid on the whole plateau $\nu = 2$

Once again this approach is valid only under the Gaussian approximation. From the measurements of V_0 and V_φ, one can deduce using equation 7.6, that $h\Delta\nu$ varies from ~ 3 to ~ 7 μeV when changing the magnetic field. This value of $h\Delta\nu$ is $\lesssim 2k_B T$, which validates our approach of Gaussian and white noise [8].

_____

7. This assumption is valid only if $\Delta\nu \ll max(eV_2, k_B T)$.

8. It can lead to a small deviation from our theory at the lowest temperature (20mK) when $eV_2 \lesssim 2k_B T$), which could explain the crossover at lower temperature with another temperature dependence (observed by Litvin *et al.*[44]).
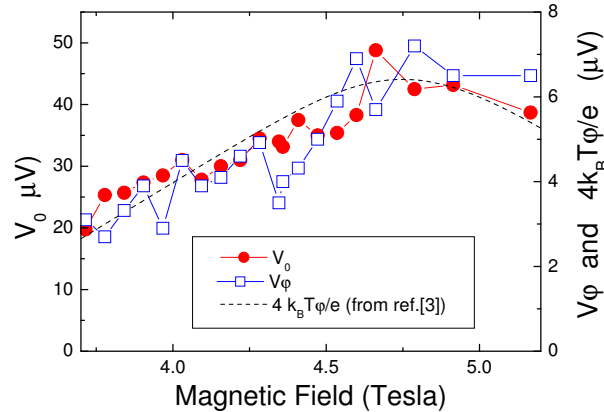
FIGURE 7.23 – (color online) V_0 and V_φ as a function of the magnetic field. The dashed line is the general behavior of $4k_B T_\varphi/e$ (right scale) measured in ref.[69], on the same sample.

The figure 7.23 also brings a valuable point for the understanding of the underlying physics : the proportionality of V_φ to V_0. This may be surprising at first sight : if $\Delta\nu$ were constant, according to equation 7.6, V_φ would scale as V_0^2. Instead as seen in figure 7.23, V_φ is proportional to V_0. We will show that, varying the magnetic field most probably changes the time of flight τ through the MZI, thus changing both the coupling between the edge states and the bandwidth $\Delta\nu$. We are going to relate V_0 and $\Delta\nu$ to microscopic parameters of the system and explain why $\Delta\nu \propto V_0$. But, before treating this point, we are going to comment different results obtained on this experiment by the Weizman's group [59][58].

7.5   Non-Gaussian noise

The first group who has studied the impact of a noisy inner edge state on the visibility of a MZI was the Weizman's group [59][58]. In their experiment, the inner edge channel served as a path detector [9] (see figure 7.11). When G_0 is tuned to partition the detector channel's (biased at V_2), electrons in the upper path of the interferometer become entangled [10] with those in the down path, resulting in a lower visibility. They interpreted this dephasing process as a "path detection", or alternatively, as a phase scrambling due to potential fluctuations in the partitioned detector channel. The interaction between the inner and the outer channels was characterized before the actual dephasing experiment by first fully reflecting the biased inner edge channel emanating from S_2 (with G_0). Indeed, as we have shown in the previous part, the full reflection ($T_0 = 1$) had a strong effect on the phase of the interference pattern, which varied linearly with V_2 ($V_0 \sim 19\mu V$ in the Weizman's experiment), but with nearly no effect on the visibility.

When G_0 was tuned to partition the inner channel ($0 < T_0 < 1$), the visibility diminished as V_2 increased. We show in figure 7.24 the dependence of the visibility on T_0 for three

_____

9. This term "path detector" refers to their "which path" detection interpretation.

10. Again this vocabulary is linked to the "which path" interpretation.
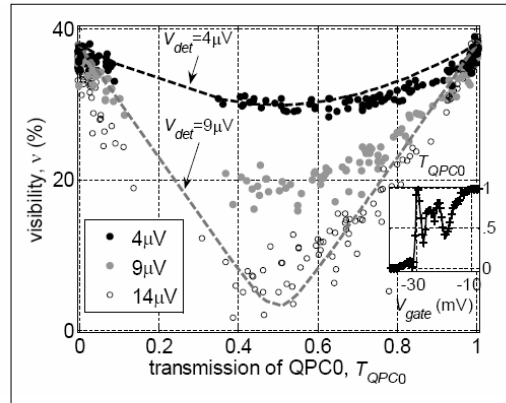
FIGURE 7.24 – Neder et *et al.*[58] experiment : The effect of partitioning the detector channel (by G_0) on the visibility of the interfering signal, at three different detector bias values. As V_2 increases, the dependance of the visibility on T_0 turns from a smooth one to a sharp V-shape (at V_2= 14μV). The dashed line is the prediction of a single detector electron model (Equation 7.9). While the model agrees with the experimental results at low bias ($4\mu V$, black line), it fails at larger bias. It predicts a V-shape dependence, but at a lower bias $V_2 = 9\mu V$ (gray line). Inset : The conductance of G_0 as a function of gate voltage shows sharp resonances. This explains the lack of visibility measurements in the range 0.1< T_0 < 0.4, and its dispersion at large detector bias (due to the dependence of the resonances on bias).

different detector voltages. As the bias V_2 increased, the visibility turned from a smooth parabolic curve to a sharp, V-shape like dependence, with a minimum at $T_0 \sim 0.5$. The dispersion among the experimental points at higher bias resulted from resonances in T_0.

To understand this result, Neder *et al.*[59] first studied a simple model where exactly one electron in the detector scrambles the phase of an interfering electron. Detector electrons were injected with a probability $1 - T_0$ into the channel that interacted with the interferometer. Depending on the presence or absence of a detector electron, the extra phase $\delta\phi$ acquired by an interfering electron fluctuated between two values $\delta\phi = \gamma V_2$ ($\gamma = \frac{2\pi}{V_0} = \frac{2\pi}{19}$ rad/μV in Neder's experiment [58]) and $\delta\phi = 0$ respectively. Averaging the $\cos(\phi)$ over the two possbilities leads to a visibility [10][77] :

$$\nu = |T_0 + (1 - T_0)e^{i\gamma V_2}| \tag{7.9}$$

For small γV_2 equation 7.9 can be expanded to second order :

$$\nu \sim 1 - \frac{1}{2}(\gamma V_2)^2 T_0(1 - T_0) \sim e^{-\frac{1}{2}(\gamma V_2)^2(T_0(1-T_0))} \tag{7.10}$$

The two broken lines in figure 7.24 are the predictions of Equation 7.9 at detector bias $V_2 = 4\mu V$ and $V_2 = 9\mu V$. For the small bias the induced phase is small ($\gamma V_2 < \pi/2$) and both equation 7.9 and 7.10 agree well with the experimental data seen in figure 7.24. However, for the larger bias the shape predicted by equation 7.9 deviates markedly from the smooth Gaussian approximation, and shows a V-shape dependence : $\nu = |1 - 2T_0|$ for $\gamma V_2 = \pi$ ($V_2 \sim 9\mu V$). In figure 7.24 this shape is observed, but at a higher detector bias

than the one predicted by equation 7.9 ($V_2 = 14\mu V$)[11].
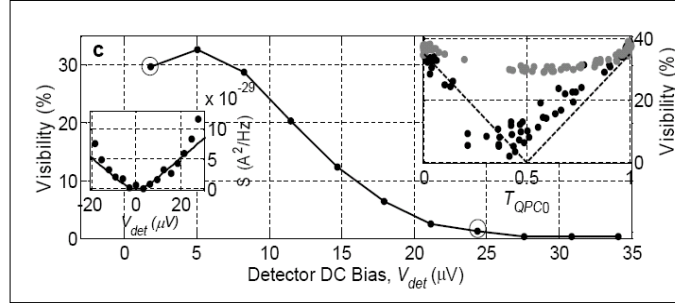
FIGURE 7.25 – Neder et *et al.*[58] experiment. Effect on a partitioned detector ($T_0 \sim 0.5$) on the interference of the MZI. For poor path detection ($V_2 = 2\mu V$) the AB oscillations are strong with visibility $\sim 30\%$, but for an accurate detection ($V_2 = 24\mu V$) the visibility drops to merely $\sim 1.5\%$; vanishing altogether as V_2 increases further. *Here $V_{det} \equiv V_2$*

Another way to study the impact of the noisy inner edge state on the interfering beam is to tune T_0 to $1/2$ and to vary V_2. In a first experiment, Neder *et al.*[58] have noticed a monotonous decay of the visibility with V_2 (see figure 7.25). In a second experiment Neder *et al.*[59] have observed completely different results. Although the bias V_2 necessary to sweep the phase per 2π is the same, they obtained a new behavior of the visibility with a non-monotonous decay (see figure 7.26). The visibility dropped to zero at $V_2 = 14\mu V$ (instead of at $9.5\mu V$ according to Equation 7.9), increased afterwards to reach another, yet smaller, maximum at $V_2 = 22\mu V$, and finally vanished at higher bias. This observation has been done in a region of G_0 gate voltages which was relatively smooth and free of resonances. Moreover, the phase of the AB oscillations increased monotonously with V_2 (see figure 7.26 b) : $\langle\delta\phi\rangle = 1 - T_0\gamma V_2$, but underwent a π phase slip when the visibility reaches zero, as expected qualitatively from 7.9[12].

Their conclusion was the following : " destruction of the interference with strong phase randomization only by a few electrons in the detector. If n$\sim \frac{eV_{det}\tau}{h}$, with τ the dwell time of an electron in the upper path of the MZI and $V_0 = 20\mu V$, they find n$\sim 1 - 2.5$ (using $\tau = \frac{L}{v_d}$, path length L$\sim 10\mu m$ and $v_d \sim (2-5).10^4 m/s^{-1}$ as an estimate of the edge channel drift velocity)". This interpretation raises however several questions. First, they obtain which seems to be two contradictory results from one paper to the other. In the first one [58], they obtain a monotonous decay of the visibility with V_2 whereas in the second one [59] they report a non monotonous decay of the visibility with V_2. Both experiments were done in the same conditions, except the fact that in the second experiment, they worked in a region of G_0 relatively smooth and free of resonances. It is not clear how their

---

11. This expression seems to us surprising. In the Neder *et al.* paper [59], this is so called the Gaussian approximation while I have shown that a Gaussian approximation leads to $\nu \sim exp(-\gamma V_2)$. The second thing is that I do not understand why the phase shift induces by one electron changes with V_2. I would expect that V_2 changes the number of electrons.

12. This result looks like the lobe pattern of the visibility with the applied bias, with a marked difference : the phase is not rigid.
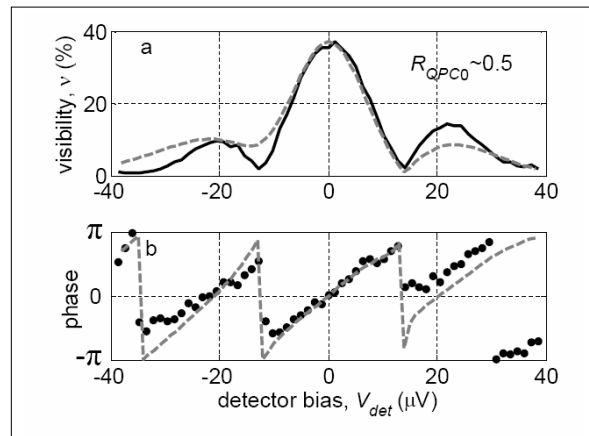
FIGURE 7.26 – Neder et *et al.*[59] experiment. Effect on a partitioned detector ($T_0 \sim 0.5$) on the interference of the MZI. Solid line : the non-monotonic behavior of the visibility has been interpreted as a sign of dephasing by non-Gaussian noise. Dashed line : prediction of an improved theoretical model, which takes into account fully the effects of binomial shot noise [59].

theoretical approach can explain their results obtained in the first experiment (the smooth decay of the visibility with the detector DC bias). Moreover, they were able to pass from a Gaussian to a non Gaussian regime only because the profile of the gate G_0 was smoother. It seems then that the noise generated in G_0 is responsible from the observed behavior. Up to now we have never succeeded to reproduce their results on non Gaussian noise. This discrepancy remains puzzling.

7.6 Theory : Finite frequency coupling

In this part, we will model the impact of the noisy inner edge state on the interfering one using a mean field approximation inspired by a work of Seelig and Buttiker [76].

7.6.1 The capacitive coupling

We first consider the capacitive coupling between edge states. Fluctuations of the charge in the gate couple to the charge in the neighboring arm of the MZI and influence electron transport in this arm. This interaction effect is taken into account by introducing a time dependent potential $V_1(x,t)$ into the Hamiltonian

$$H = -\frac{\hbar^2}{2m^*}\frac{\partial^2}{\partial x^2} + E_1 + V_1(x,t) \qquad (7.11)$$

for the upper arm [13]. Here E_1 is the sub-band energy due to the lateral confining potential of the arm and m^* is the effective mass of the electron. We make the assumption that

---

13. Here, I strictly consider the approach developed by Seelig and Buttiker [76] to evaluate the phase evolution.

the fluctuating potential factorizes in a space- and time-dependent part, writing $V_1(x,t) = h_1(x)eU_1(t)$. We will suppose for the following, that $h_1(x)$ is constant all along the length of the interferometer L. To solve the Schrödinger equation with the Hamiltonian 7.11 we make the ansatz :

$$\Psi_E(x,t) = e^{-iEt/\hbar + ik_{1,E}x + i\varphi(x,t)}$$

where $k_{1,E} = \sqrt{2m^*(E - E_1)}/\hbar$ and $\varphi(t)$ is the phase accumulated due to fluctuations. We introduce :

$$U_1(t) = \int \frac{d\omega}{2\pi} u_1(\omega) e^{-i\omega t}$$

and

$$\varphi(x,t) = \int \frac{d\omega}{2\pi} \varphi(x,\omega) e^{-i\omega t}$$

Since $h_1(x)$ is constant all along the length of the interferometer L, one obtains by WKB approximation :

$$\varphi = \int_0^\tau \frac{eU_1 dt}{\hbar}$$

This last relation allows to relate the phase noise $S_\varphi(\omega)$ to the potential noise $S_{U_1 U_1}(\omega)$:

$$S_\varphi(\omega) = 4\frac{e^2}{\hbar^2} S_{U_1 U_1}(\omega) \frac{sin^2(\omega\tau/2)}{\omega^2}$$

where $\tau = L/v_D$ is the time of flight through the MZI and L stands for the length of one arm of the interferometer.

7.6.2 Admittance matrix and noisy inner edge state

To characterize the coupling at finite frequency, one has to know how the fluctuations of the electro-chemical potential V_2 are related to the fluctuations of the internal potential U_1 seen by the electrons in the MZI. The physics is the following one : when changing V_2, the charge of the inner edge state will change. This charge will lead to a variation of the potential U_1 which will be partially screened. This is the dynamic of the screening [36][31][65][22] that we are describing here. The notations that I will used, as well as the resulting electrical circuit are represented in figure 7.27.

The admittance $G_{12}(\omega) = dI_{1,\omega}/dV_{2,\omega}$ is calculated in detail in the Annex B. We just give here the final result :

$$G_{12} = \frac{dI_1(\omega)}{dV_2(\omega)} = \frac{G_Q(1 - e^{\iota\omega\tau})}{2 + \iota G_Q(1 - e^{\iota\omega\tau})/(\omega C)}$$

with $V_2(\omega)$ the electro-chemical potential applied on S_2 , $I_1(\omega)$ the current along the outer edge state, $G_Q = e^2/h$ and C the capacitance between the inner and outer edge state. In the low frequency limit, this expression becomes :

$$G_{12}^{-1} = 2\frac{1}{G_Q(1 - e^{\iota\omega\tau})} + \frac{i}{\omega C}$$
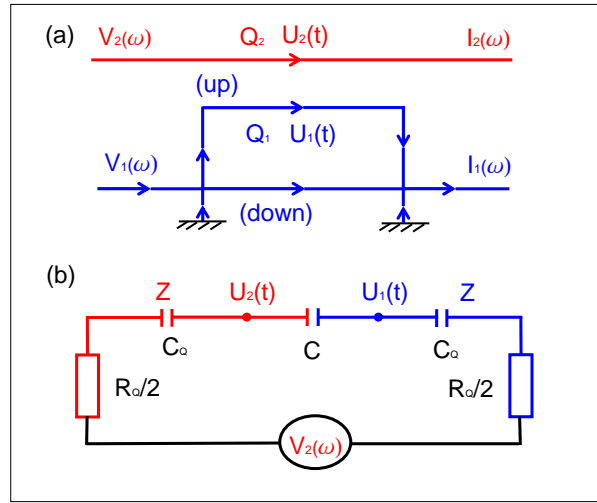
FIGURE 7.27 – a) Schematic representation of the edge states coupled by a geometrical capacitance C. b) Low frequency equivalent circuit with V_1 set to 0 V. The coupling capacitance C is in series with two relaxation resistances $R_Q/2$ accounting for the non-ideality of the two gates of the capacitor and two quantum capacitances C_Q accounting for the density of states of the edges states.

We introduce $Z(\omega) = \frac{i}{\omega G_Q(1-e^{i\omega\tau})}$ and $Z_C = \frac{i}{\omega C}$. Thus :

$$G_{12}^{-1} = 2Z + Z_C$$

which can also be written in the low frequency limit :

$$G_{12}^{-1} = \frac{i}{\omega C_Q} + \frac{R_Q}{2} + \frac{i}{\omega C} + \frac{i}{\omega C_Q} + \frac{R_Q}{2}$$

with $C_Q = G_Q\tau$. We deduce from the expression the schematic representation of the coupling between the inner and outer edge state figure 7.27. The outer edge state is composed of a quantum capacitance C_Q with a relaxation resistance $R_Q/2$ in series[36][31][65][22]. Since the lateral gate is not perfect (inner edge state), it is also composed of a quantum capacitance C_Q with a relaxation resistance $R_Q/2$ in series.

We are interested in the fluctuations of the potential $U_1(\omega)$ as a function of $V_2(\omega)$:

$$U_1(\omega) = \frac{1}{\frac{\iota}{\omega}\frac{e^2}{h}(1-e^{\iota\omega\tau})}Q_{up,2}^{tot}(\omega) = V_2(\omega)\frac{C}{2C + \frac{\iota}{\omega}\frac{e^2}{h}(1-e^{\iota\omega\tau})} \tag{7.12}$$

with $Q_{up,2}^{tot}$ the total charge in the region 2. We obtain finally for the fluctuations of the potential $U_1(\omega)$:

$$S_{U_1U_1}(\omega) = |\frac{C}{2C + \frac{\iota}{\omega}\frac{e^2}{h}(1-e^{\iota\omega\tau})}|^2 S_{22}(\omega)$$

which can also be written :

$$|G_Q(1-e^{\iota\omega\tau})|^2 S_{U_1U_1}(\omega) = |G_{12}(\omega)|^2 S_{22}(\omega)$$

We now consider the case of white partition noise $S_{22} = 2eR_QV_2T_0(1-T_0)$ (or white thermal noise $S_{22} = 2 \times 4k_BR_QT$). Using $< \delta\varphi^2 > = \int_0^\infty S_\varphi(\omega)d\omega/2\pi$, one finds :

$$V_\varphi^{-1} = \frac{e}{\hbar} \int_0^\infty \mathcal{I}(\omega)d\omega, \tag{7.13}$$

$$\text{with } \mathcal{I}(\omega) = \frac{\omega^{-2}}{1 + [\tan(\omega\tau/2)^{-1} + G_Q/C\omega]^2}.$$

In the low frequency limit $\mathcal{I}(\omega) \approx [\omega^2 + (eV_0/h)^2]^{-1}$ which leads to

$$V_0 = \pi^2 V_\varphi. \tag{7.14}$$

This is a result of importance which tells that in principle the ratio between V_0 and V_φ should be universal. It means that without screening of the interaction, whatever be the coupling and the quantum capacitance, the ratio between V_0 and V_φ should be π^2. This is not what we have observed in our experiment (we measure $V_0/V_\varphi = \pi^2/1.4$). Indeed, the approach that we have developed is very simple and we have to think now on the simplifications which are abrupt. The experimental data show that V_φ is larger than expected which means that there is less dephasing. A natural way is to include something in the model which reduces the bandwidth on which fluctuations play a role. This can be easily done by inserting screening effects which are modelled by two capacitances C_0 which mimic the capacitive coupling of the wires to the ground and will short cut the high frequency fluctuations. Indeed, this screening can also be viewed as modelling the interaction in the wire itself : the larger C_0 is, the fewer interactions there are. The next part of this chapter will be devoted to the calculation of the dephasing in presence of screening.

7.6.3 Screening of fluctuations
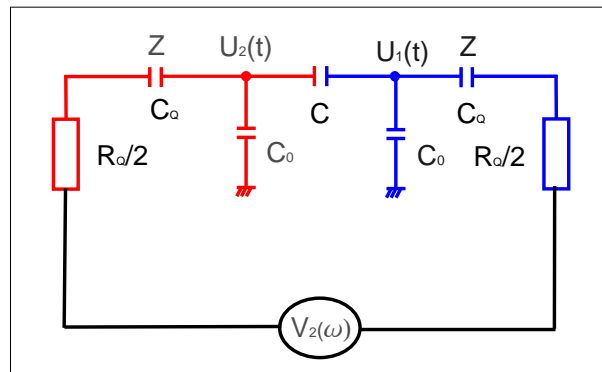
FIGURE 7.28 – Schematic representation of the screening via the introduction of two capacitances which couple the two edge states to the ground.

We model the screening of the interaction by the introduction of two capacitances C_0 which connect the two edge states to the ground. We have represented in figure 7.28 a schematic representation of the problem. A detail calculation of the new expression of V_φ is given in Appendix C. We just give here the final result :

$$V_\varphi^{-1} = \frac{4e}{\hbar} \int_0^\infty d\omega \frac{sin^2(\omega\tau/2)}{\mid R(\omega) \mid^2 \omega^2}$$

with :

$$\mid R(\omega) \mid^2 = A^2 + B^2 sin^2(\omega\tau/2) + ABsin(\omega\tau) + 2ACcotg(\omega\tau/2) + \frac{C^2}{sin^2(\omega\tau/2)} + 2BCcos(\omega\tau)$$

and :

$$A = 2(1 + 2\alpha)$$

$$B = \frac{2\gamma^{-1}}{\omega\tau}$$

$$C = \omega\tau \times \alpha\gamma(1 + \frac{\alpha}{2})$$

with $\alpha = C_0/C$ and $\gamma = C/C_Q = C/(G_Q\tau)$. Always in C, we have calculated the expression of U_1 as a function of V_2 in the low frequency limit :

$$U_1 = \frac{V_2}{2 + \gamma^{-1} + \alpha(2 + 2\gamma + \alpha\gamma)}$$

hence :

$$V_0 = \frac{h}{e\tau}(2 + \gamma^{-1} + \alpha(2 + 2\gamma + \alpha\gamma))$$

We finally obtain the following relation between V_0 and V_φ :

$$\frac{V_0}{V_\varphi} = \frac{4\pi}{\tau}(2 + \gamma^{-1} + \alpha(2 + 2\gamma + \alpha\gamma)) \int_0^\infty d\omega \frac{sin^2(\omega\tau/2)}{\mid R(\omega) \mid^2 \omega^2}$$

This integral is not easy to calculate and we have evaluated it numerically. In the screening case on has a fitting parameter which is $\alpha = C_0/C$. In figure 7.29, we have plotted the ratio $\Delta(\alpha, \gamma)$ between the theoretical $(\frac{V_0}{V_\varphi})_{theo}$ and the experimental one $(\frac{V_0}{V_\varphi})_{exp} = \pi^2/1.4$. As one can see in figure 7.29, when C_0 tends to 0, $(\frac{V_0}{V_\varphi})_{theo}$ is ~ 1.4 time larger than $(\frac{V_0}{V_\varphi})_{exp}$. Note here the range on which we have calculated $\Delta(\alpha, \gamma)$. It corresponds to the expected values of C/C_Q ($C \sim L\epsilon_0\epsilon_R \sim 1fF$ for $L=11\mu m$ and $C_Q \sim 5fF$ for $v_D = 5.10^4 ms^{-1}$) while the range of C_0/C corresponds to the range on which one obtains an agreement between experiment and theory. The yellow region corresponds to $\Delta(\alpha, \gamma)=1$ and the solid line to $C_0 \sim 0.5(CC_Q)^{1/2}$. Taking into account screening, we finally obtain a theory in agreement with the experiment.
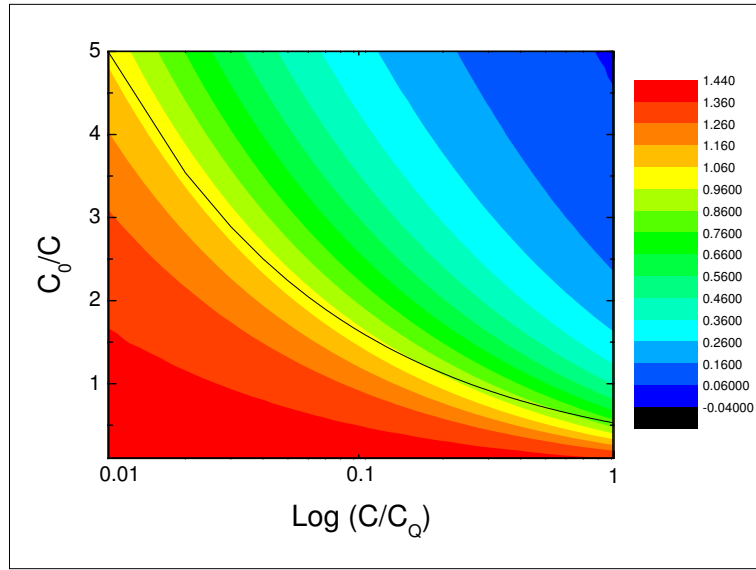
FIGURE 7.29 – Ratio $\Delta(\alpha, \gamma)$ between the theoretical $(\frac{V_0}{V_\varphi})_{theo}$ and the experimental one $(\frac{V_0}{V_\varphi})_{exp} = \pi^2/1.4$. The yellow region corresponds to $\Delta(\alpha, \gamma)=1$ and the solid line to $C_0 \sim 0.5(CC_Q)^{1/2}$.

7.7   Conclusion

In this part, we have studied the impact of the inner edge state on the interferences. We have proven that the inner edge state was responsible of the finite coherence length and of its magnetic field dependence. More precisely, we have shown that the inner edge state, via capacitive coupling, induced phase fluctuations of the interfering edge state. We have demonstrated that these phase fluctuations were generated by the thermal noise of the inner edge state.

To achieve that, we have extracted all the parameters of the problem : the capacitive coupling and the bandwidth. Mimicing an experiment of a noisy environment coupled to an interferometer, we were able to confirm that the Gaussian approximation applies. We have determined the bandwidth for different magnetic field and have validated the Gaussian approximation on the whole plateau. Assuming that the thermal noise of the inner edge state was responsible of the finite coherence length, we finally obtained this very simple relation [14] :

$$\boxed{eV_\varphi = 4k_BT_\varphi} \tag{7.15}$$

in perfect agreement with experimental data. Finally, in a last part, we have explained the proportionality between the capacitive coupling V_0 and V_φ. In particularly, we have shown that to obtain the good experimental ratio, it was necessary to insert screening effect.

The next step, now, would be to reproduce this experiment without the inner edge state namely at $\nu = 1$: we would expect a longer coherence length. However the physics of edge states at $\nu = 1$ is different from $\nu = 2$ which could lead to additional effects on the

_____

14. See 7.3.3 for the notations.

coherence length. A similar study at $\nu = 1$ would enable to answer these questions.

Noise Dephasing in Edge States of the Integer Quantum Hall Regime

P. Roulleau, F. Portier, and P. Roche

CEA Saclay, Service de Physique de l'Etat Condensé, Nanoelectronic Group, F-91191 Gif-sur-Yvette, France

A. Cavanna, G. Faini, U. Gennser, and D. Mailly

CNRS, Laboratoire de Photonique et Nanostructures, Phynano team, Route de Nozay, F-91460 Marcoussis, France

An electronic Mach-Zehnder interferometer is used in the integer quantum Hall regime at a filling factor 2 to study the dephasing of the interferences. This is found to be induced by the electrical noise existing in the edge states capacitively coupled to each other. Electrical shot noise created in one channel leads to phase randomization in the other, which destroys the interference pattern. These findings are extended to the dephasing induced by thermal noise instead of shot noise: it explains the underlying mechanism responsible for the finite temperature coherence time $\tau_\varphi(T)$ of the edge states at filling factor 2, measured in a recent experiment. Finally, we present here a theory of the dephasing based on Gaussian noise, which is found to be in excellent agreement with our experimental results.

Although many experiments in quantum optics can be reproduced with electron beams using the edge states of the Integer Quantum Hall Effect (IQHE), there exist fundamental differences due to the Coulomb interaction. As an example, the Mach-Zenhder type of interferometer in the IQHE [1] has recently allowed us to observe quantum interferences with the unprecedented 90% visibility [2], opening a new field of promising quantum information experiments. Indeed, the edge states of the IQHE provide a way to obtain "ideal" unidimensional quantum wires. However, very little is known about the decoherence processes in these "ideal" wires. Only very recently has their coherence length been quantitatively determined as well as its temperature dependence established [3]. Here, we show that the underlying mechanism responsible for the finite coherence length is the thermal noise combined with the poor screening in the IQHE regime [4].

In the IQHE, gapless excitations develop on the edge of the sample and form one dimensional chiral wires (edge states), the number of which is determined by the number of electrons per quantum of flux (the filling factor ν). In these wires, the electrons drift along the edge in a beamlike motion making experiments usually done with photons possible with electrons. The choice of the filling factor at which one obtains high visibility interferences requires a compromise between a magnetic field high enough to form well-defined edge states, and small enough to still deal with a good Fermi liquid. Naïvely, one could think that the highest visibility would have been observed at $\nu = 1$, but it is not actually the case [1]. This is most probably due to decoherence induced by collective spin excitations (Skyrmions [5]) making spin flip processes possible. In practice, the highest visibility (90% [2]) has been obtained at filling factor 2, when there are two spin polarized edge states. Here, chirality and unidimensionality prevent first

order inelastic scattering in the wires themselves [6], while tunneling from one edge to the other requires spin flip [7].

To show that the origin of the finite coherence length is related to the coupling between two neighboring edge states, we have proceeded as follow. First, we have made a which-path experiment inducing on-purpose shot noise on the inner edge state (IES) while measuring the outer edge state (OIS) interferences. The visibility decrease is shown to result from a Gaussian noise, in opposition to a recent experiment [8]. Using the parameters extracted from the which-path measurements, we are able to calculate the dephasing resulting from thermal noise (instead of shot noise). The result is in perfect agreement with our recent measurements of the finite temperature coherence length [9]. Moreover, the magnetic field dependence of the coherence length is shown to result from a variation of the coupling between the two edges. Finally, we have developed a theory which gives a full scheme of the dephasing mediated by the electronic noise.

The interferences are obtained using an electronic Mach-Zehnder Interferometer (MZI) which was patterned on a high mobility two dimensional electron gas at a GaAs/Ga$_{1-x}$Al$_x$As heterojunction (density $n_S = 2.0 \times 10^{11}$ cm^{-2} and mobility $\mu = 2.5 \times 10^6$ cm^2/V s). Measurements have been done in the quantum Hall regime, at filling factor 2 (with a magnetic field $B = 5.2$ T). In the edge states, the electrons have a chiral motion with a drift velocity of the order of 10^4–10^5 ms^{-1}. A SEM view of the sample as well as a schematic representation of the two edge states are shown in Fig. 1(a). The outer incoming edge state is split by $G1$ in two paths (a) and (b), which are recombined at $G2$ leading to interferences. SG is a side gate used to change the area S defined by the two arms of the interferometer. The current which is not transmitted through the MZ, $I_R = I_0 - I_T$, is collected to the ground
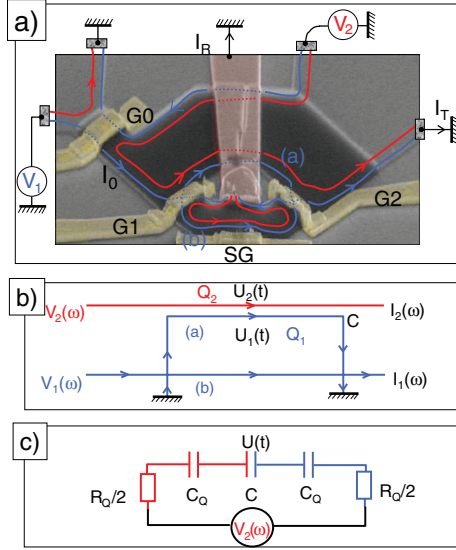
FIG. 1 (color online). (a) Tilted SEM view of the device, with schematic representation of the edge states. $G1$ and $G2$ are Quantum Point Contact (QPC) which define the two beam splitters of the Mach-Zehnder interferometer. They are set to transmission $\mathcal{T}_1 \sim \mathcal{T}_2 \sim 1/2$ for the OES, while fully reflecting the IES. The two arms (a) and (b) are $L = 11.3~\mu$m long defining an area S of 34 μm^2. The small inner Ohmic contact is connected to the ground via an Au metallic bridge. SG is a side gate. $G0$ is an additional beam splitter which makes it possible to bias the IES by V_2, while the other is biased by V_1. $G0$ is tuned such that the OES is fully reflected, while the IES is transmitted with a probability $\mathcal{T}_0$. (b) Schematic representation of the edge states coupled by a geometrical capacitance C. (c) Low frequency equivalent circuit with V_1 set to 0 V, $C_Q = \tau/R_Q$.

via the inner Ohmic contact. The differential transmission $\mathcal{T} = dI_T/dI_0$ have been measured at low temperature (~ 20 mK) by standard lock-in techniques with an ac voltage ($V_1 \sim 1\mu V_{\mathrm{RMS}}$ at 619 Hz).

It is straightforward to show that $\mathcal{T} \propto [1 + \mathcal{V}\sin(\varphi)]$, $\mathcal{V}$ being the visibility and φ the Aharonov-Bohm (AB) flux through S [9]. In the present study, we tuned the transmission $\mathcal{T}_1$ and $\mathcal{T}_2$ of the beam splitters $G1$ and $G2$ to $1/2$ in order to have a maximum visibility. The interferences are revealed by varying φ. It can be done either by applying a voltage V_{SG} on the side gate, or by applying a voltage V_2 on the IES (playing here a role similar to the side gate). In Fig. 2, we have plotted the interference pattern obtained by the two methods. The periodicity V_0 of interferences with respect to V_2 depends on the coupling between the two edge states which will be shown to be related to the time of flights through the MZI. In Fig. 4, one can notice that V_0 exhibits a large non-monotonic variation with the magnetic field on the Hall plateau at $\nu = 2$.

Any fluctuations on V_2 blur the phase. For a Gaussian distribution of the phase (we will discuss this notion later), the visibility is proportional to $e^{-\langle\delta\varphi^2\rangle/2}$ [10] where $\langle\delta\varphi^2\rangle$
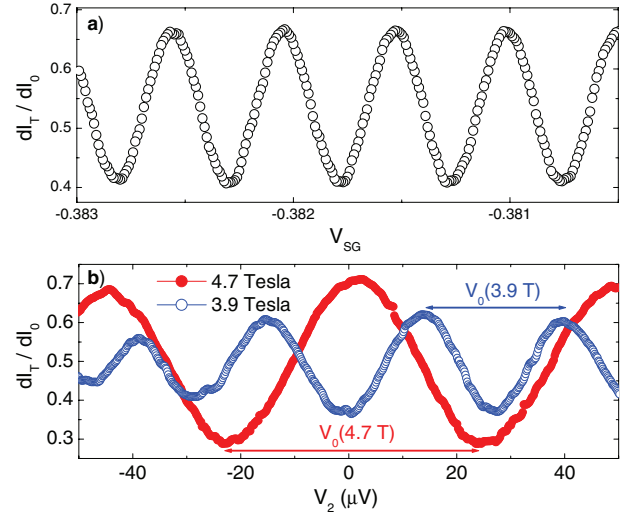
FIG. 2 (color online). (a) Phase sweeping by varying the side gate voltage V_{SG}. (b) Phase sweeping by varying V_2 with $\mathcal{T}_0 = 1$ for two different magnetic fields. The periodicity V_0 depends on the magnetic field as shown in Fig. 4.

is the variance of the Gaussian distribution. It is simply related to the noise power spectrum S_{22} of V_2 through the coupling constant and the (unknown) bandwidth $\Delta\nu$: $\langle\delta\varphi^2\rangle = (2\pi)^2\langle\delta V_2^2\rangle/V_0^2 = (2\pi)^2 S_{22}\Delta\nu/V_0^2$. If one generates partition noise on the IES tanks to the splitter G_0, the resulting excess noise $\Delta S_{22} = 2eR_Q\mathcal{T}_0(1 - \mathcal{T}_0)V_2\{\coth[eV_2/(2k_BT)] - 2k_BT/(eV_2)\}$ [11,12] leads to a visibility decreasing exponentially with V_2 when $eV_2 \gg k_BT$:

$$\mathcal{V} = \mathcal{V}_0(T)e^{-\mathcal{T}_0(1-\mathcal{T}_0)(V_2-2k_BT/e)/V_\varphi}, \tag{1}$$

$$\text{with } V_\varphi^{-1} = \frac{4\pi^2 eR_Q}{V_0^2}\Delta\nu, \tag{2}$$

and $R_Q = 1/G_Q = h/e^2$.

In Eq. (1), the unknown parameter is V_φ which is related to the bandwidth $\Delta\nu$ [Eq. (2)]. This approach for the dephasing is valid only if $\Delta\nu$ is such that the fluctuations lead to a Gaussian distribution of φ. It implies that many electrons have to be involved in the dephasing during the measuring time $1/\Delta\nu$, namely, that max(eV_2, $2k_BT$) $\gg h\Delta\nu$. This condition coincides with the fact that the noise power spectrum S_{22} can be considered as frequency independent. Note that the dephasing rate increases with V_2 because the number of involved electrons increases, not because the coupling between electrons increases with V_2 (as claimed in [8]). Figure 3 shows that our data are in remarkable agreement with Eq. (2). In Fig. 3(a), we have plotted the visibility versus V_2 when $\mathcal{T}_0 = 1/2$, for two different magnetic fields. $\mathcal{V}$ decreases exponentially with V_2. The solid lines are fits to the data using an electronic temperature of 25 mK (for a fridge temperature of 20 mK).
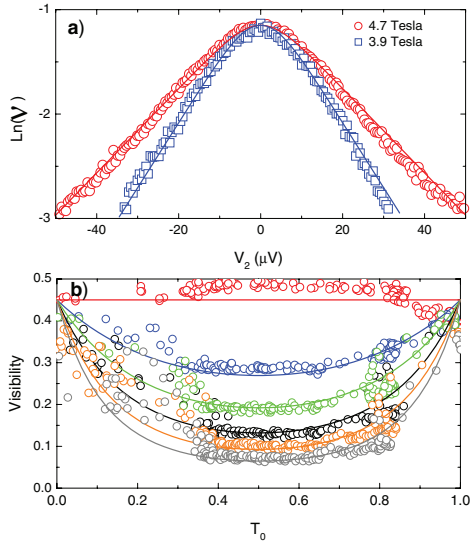
FIG. 3 (color online). (a) Visibility decrease of the interferometer as a function of V_2 at $\mathcal{T}_0 = 1/2$ for two different magnetic fields 4.7 and 3.9 T. The solid lines are fit to the data $\mathcal{V} = \mathcal{V}_0 e^{-2\pi^2 \Delta S_{22} \Delta\nu/V_0^2}$ with an electronic temperature of 25 mK (for a base temperature of 20 mK) and $\mathcal{T}_0 = 1/2$. The high bias fit of the exponential decrease $\mathcal{V} = \mathcal{V}_0 \exp[-\mathcal{T}_0(1 - \mathcal{T}_0)V_2/V_\varphi]$ allows us to determine V_φ which is found to depends on the magnetic field. (b) Visibility decrease of the interferometer as a function of $\mathcal{T}_0$ for $V_2 = 0$, 21, 31, 42, 53, and 63 μV from top to bottom. The solid lines are fits to the data using Eq. (1) with $\mathcal{V}_0 = 0.45$, $V_\varphi = 7.2$ μV, and $T = 25$ mK.

V_φ and $\mathcal{V}_0$ are the fitting parameters. The values of V_φ deduced from these measurements depend on the magnetic field in the same way as V_0. In fact, V_φ is found to be proportional to V_0 (see Fig. 4). The slope of the exponential decrease is modified by the transmission of the beam splitter following a $\mathcal{T}_0(1 - \mathcal{T}_0)$ law. Figure 3(b) shows the visibility for different values of V_2 and $\mathcal{T}_0$ at a magnetic field of 4.6 Tesla. The solid lines are fits to the data using Eq. (1) with $V_\varphi = 7.2$ μV and $T = 25$ mK. Clearly, at high bias, there is no V-shape contrary to what has been recently observed in Ref. [8]. Instead, the curves show that the Gaussian approximation is valid. Note that the agreement with our theory is perfect when $\mathcal{T}_0$ is well defined in our sample. The dispersed data on the edges in Fig. 3(b) coincide to a strong dependence of $\mathcal{T}_0$ with the voltage applied on $G0$, resulting on an energy dependent transmission $\mathcal{T}_0$ [8].

We now compare the exponential decrease of the visibility in presence of shot noise with our recent observation that the coherence length of edge states is inversely proportional to the temperature [3]. When $eV_2 \ll k_B T$, the noise is dominated by the Johnson-Nyquist noise $S_{22} = 4k_B T R_Q$. One obtains
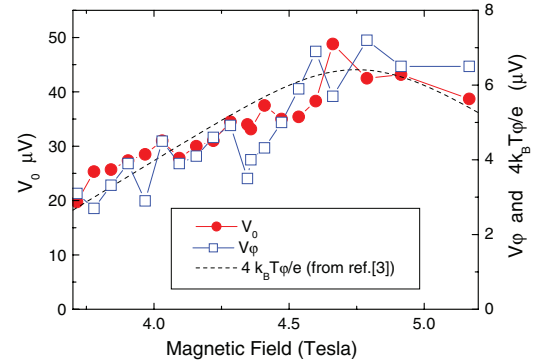
FIG. 4 (color online). V_0 and V_φ as a function of the magnetic field. The dashed line is the general behavior of $4k_B T_\varphi/e$ (right scale) measured in Ref. [3], on the same sample.

$$\mathcal{V} = \mathcal{V}_0 e^{-T/T_\varphi} \quad \text{with } T_\varphi^{-1} = \frac{2 \times 8\pi^2 k_B R_Q}{V_0^2} \Delta\nu. \quad (3)$$

Here, the factor 2 arises from the fact that the two arms of the interferometer suffer from a coupling with a noisy IES, instead of one when creating partitioning. From Eqs. (2) and (3), one gets

$$eV_\varphi = 4k_B T_\varphi. \quad (4)$$

Figure 4, which is our main result, shows that Eq. (4) is in very good agreement with our data. This demonstrates for the first time that thermal noise and coupling between the two edge states are responsible for the finite coherence length measured recently [3]. From the measurements of V_0 and V_φ, one can deduce using Eq. (2) that $h\Delta\nu$ varies from ~ 3 to ~ 7 μeV when changing the magnetic field. This value of $h\Delta\nu$ is $\lesssim \max[2k_B T, eV_2]$, which validates our approach of white and Gaussian noise [13].

Figure 4 also brings a valuable point for the understanding of the underlying physics: the proportionality of V_φ to V_0. It can be understood using a simple model where $N_2 = eV_2\tau/h$ ($\tau = L/v_D$, L stands for the interferometer arm length and v_D the drift velocity) electrons in the IES causes a dephasing of $\delta\varphi = N_2\varphi_2$ in the OES. Hence, $V_0 = 2\pi h/(e\varphi_2\tau)$ and a Gaussian distribution of N_2 due to partitioning with $\langle \delta N_2^2 \rangle = N_2\mathcal{T}_0(1 - \mathcal{T})$ leads to $\frac{\langle \delta\varphi^2 \rangle}{2} = \pi\varphi_2\mathcal{T}_0(1 - \mathcal{T}_0)/V_0$ and, therefore, $V_0 = \pi\varphi_2 V_\varphi$. Our experiment shows that $\varphi_2 \sim \pi/\sqrt{2}$, independent of the magnetic field. Indeed, this simple approach does not account from the fact that the number of electrons is not a good quantum number in an open system, nor does it gives an independent estimation of φ_2. Following the work of Seelig and Buttiker [4], we will show that interactions between the edge states, in a mean-field approximation without screening, should lead to $\varphi_2 = \pi$.

Figure 1(b) represents the description adopted here: arm (a), carrying a charge Q_1, is capacitively coupled through a capacitance C to the IES, carrying a charge Q_2. The effect

of the electrochemical potential V_2 applied on the IES can be viewed as modifying the potential U_1 felt by electrons in the OES without changing the area S of the MZI [4,10,14]. Fluctuations of U_1 result in fluctuations of the phase $\varphi = \int_0^\tau eU_1 dt/\hbar$. Within this approach, one relates U_1 to V_2, and the phase noise spectrum S_φ to S_{22}. The total charge on the capacitance is the sum of an emitted charge and a screening charge: $Q_j(\omega) = \nu(\omega)[V_j(\omega) - U_j(\omega)]$, with $\nu(\omega) = iG_Q(1 - e^{i\omega\tau})/\omega$, $x(t) = \int x(\omega)e^{-i\omega t}d\omega$, and $j = 1$ or 2. Charge neutrality ($Q_1 = -Q_2$) and $U(\omega) = U_2(\omega) - U_1(\omega) = Q_2(\omega)/C$, lead to

$$G_{12} = \frac{dI_1(\omega)}{dV_2(\omega)} = \frac{-i\omega}{C^{-1} + 2\nu(\omega)^{-1}}.$$

Figure 1(c) shows the associated low frequency equivalent circuit: the coupling capacitance C is in series with two relaxation resistances $R_Q/2$ and two quantum capacitances $C_Q = G_Q\tau$. In the zero frequency limit, one gets $U_1 = V_2/(C_Q/C + 2)$, leading to

$$eV_0/h = (2\tau^{-1} + G_Q/C). \tag{5}$$

Note that since both C and τ are proportional to L, V_0 is proportional to L^{-1}. The phase noise $S_\varphi(\omega)$ can then be related to the potential noise $S_{U_1U_1}(\omega)$ by

$$S_\varphi(\omega) = 4\frac{e^2}{\hbar^2}S_{U_1U_1}(\omega)\frac{\sin^2(\omega\tau/2)}{\omega^2}. \tag{6}$$

Equation (6) shows that the total phase fluctuations are given by potential fluctuations integrated over a $\Delta\nu \sim 1/\tau$ bandwidth. Finally, the potential fluctuations are related to the electrochemical fluctuations by

$$|\omega\nu_1(\omega)|^2 S_{U_1U_1}(\omega) = |G_{12}(\omega)|^2 S_{22}(\omega). \tag{7}$$

We now consider the case of white partition noise $S_{22} = 2eR_Q V_2 \mathcal{T}_0(1 - \mathcal{T}_0)$ (or white thermal noise $S_{22} = 2 \times 4k_B R_Q T$). Using $\langle\delta\varphi^2\rangle = \int_0^\infty S_\varphi(\omega)d\omega/2\pi$, one finds

$$V_\varphi^{-1} = \frac{e}{\hbar}\int_0^\infty \mathcal{I}(\omega)d\omega,$$
$$\text{with } \mathcal{I}(\omega) = \frac{\omega^{-2}}{1 + [\tan(\omega\tau/2)^{-1} + G_Q/C\omega]^2}. \tag{8}$$

It is noteworthy that the dephasing rates described by V_φ and T_φ scale with L^{-1}, as does V_0. As a consequence, the ratios T_φ/V_0 and V_φ/V_0 should not depend on the size of the interferometer, as confirmed by our observations. In the low frequency limit, $\mathcal{I}(\omega) \approx [\omega^2 + (eV_0/h)^2]^{-1}$ which leads to

$$V_0 = \pi^2 V_\varphi. \tag{9}$$

Numerically, we find that the equality (9) stands for all values of C/C_Q within the [0.03, 0.3] expected range [3]. Although our approach naturally explains why $V_\varphi \propto V_0$ and gives the correct order of magnitude, it overestimates

the dephasing by a factor of ~ 1.4. This discrepency can be eliminated by including the screening by the compressible regions of the 2DEG, which tend to shortcircuit high frequency fluctuations [15]. The variation of V_0 across the $\nu = 2$ plateau with a fairly constant V_0/V_φ most probably results from a variation of the effective trajectory length with B, due to the disorder, as all the microscopic parameters (namely, C_Q, C and the capacitance to ground C_0) scales with the length. However, one cannot totally exclude a more subtle variation of the microscopic structure of the edge states, leading to variations of the coupling and of the screening while keeping V_0/V_φ constant. Indeed, an independent measurement of τ would shed light on this. Last, we would like to stress that, while all of our observations are very well explained by Gaussian fluctuations, in very similar systems with a similar inter edge coupling, a different behavior has been reported in [8], which was attributed to non-Gaussian noise. The reason for such difference remains puzzling.

To conclude, we have shown that the coherence length of the edge states at filling factor 2 is limited by the Jonhson-Nyquist noise. Changing the magnetic field makes it possible to modify the coupling between the edge states and thus modifies the coherence length. Our results are well described by a mean-field approach that relates the phase randomization to the fluctuations of the electrostatic potential in the interferometer arms.

[1] Y. Ji *et al.*, Nature (London) **422**, 415 (2003).
[2] I. Neder *et al.*, Nature (London) **448**, 333 (2007).
[3] P. Roulleau *et al.*, Phys. Rev. Lett. **100**, 126802 (2008).
[4] G. Seelig and M. Buttiker, Phys. Rev. B **64**, 245313 (2001).
[5] S. E. Barrett, Phys. Rev. Lett. **74**, 5112 (1995).
[6] T. Martin and S. Feng, Phys. Rev. Lett. **64**, 1971 (1990).
[7] D. C. Dixon *et al.*, Phys. Rev. B **56**, 4743 (1997).
[8] I. Neder *et al.*, Nature Phys. **3**, 534 (2007).
[9] P. Roulleau *et al.*, Phys. Rev. B **76**, 161309 (2007).
[10] A. Stern, Y. Aharonov, and Y. Imry, Phys. Rev. A **41**, 3436 (1990).
[11] T. Martin and R. Landauer, Phys. Rev. B **45**, 1742 (1992).
[12] M. Büttiker, Phys. Rev. B **46**, 12485 (1992).
[13] This can lead to a small deviation between experiments and our theory at the lowest temperature (20 mK) when $eV_2 \leq 2k_B T$.
[14] D. Rohrlich *et al.*, Phys. Rev. Lett. **98**, 096803 (2007).
[15] The screening can be modeled by two additional capacitances C_0 connecting the edges states to the ground. This model reproduces the observed constant ratio V_0/V_φ within 5% for $C/C_Q \in [0.03, 0.3]$, provided that $C_0 \simeq 0.5(CC_Q)^{1/2}$. A more detailed study will be published elsewhere.

Chapitre 8

The Voltage Probe

Contents

8.1 Introduction

One of the major advances in the physics of quantum conductors was the scattering approach which considers the elastic scattering of in-going states toward out-going states in a ballistic conductor. It has led to numerous theoretical predictions, among which the quantification of the conductance in a quantum point contact was one of the first to be verified experimentally. A limitation of the so-called Landauer-Büttiker theory is that it treats elastic scattering. In principle, it should not be possible to determine how decoherence affects the electronic charge transfered through a quantum conductor and all its moments (current I, noise I^2, third moment ...) within this theory. This has been cunningly circumvented by adding an additional reservoir whose connection to the studied quantum circuit mimics decoherence. More precisely, quasi-particles which have been probed by this additional reservoir (the voltage probe) when going through the quantum conductor, loose their phase or, possibly, are replaced by another particle.

To demonstrate the voltage probe properties of the ohmic contact, we have realized an electronic Mach-Zehnder interferometer [37] in which one of the arms is connected to a small floating ohmic contact through a quantum point contact [49]. Our measurements constitute the first quantitative demonstration of the dephasing properties of a voltage probe in a quantum conductor [71]. [1]

In practice, the reservoirs in the physics of quantum conductors are defined as *some regions* of the conductor which absorb all incoming particles and emits particles with a Fermi statistic at the local electrochemical potential. Indeed, for an homogeneous conductor, one cannot tell exactly where are the reservoirs. They are simply put at the multiple extremities of the considered conductor exhibiting quantum properties on a size scale determined by the energy exchange length of excitations. In our experiment, the actual position of the reservoir is known : it is a small floating ohmic contact which connects a high mobility 2D electron gas to the macroscopic world. Connecting one arm of the quantum interferometer to our voltage probe through a QPC, we are able to tune the transmission probability T_P toward the voltage probe. As a result, the voltage probe reduces the visibility of the quantum interferences with a factor $\sqrt{1 - T_P}$: the probability amplitude that a particle is not probed by the small floating ohmic contact.

In a first part, I will describe the probe experiment, and show that we were able to study the amplitude and phase evolution of oscillations with T_P. Then, we will study the phase evolution introduced by a resonance near the QPC connecting one of the path to the probe, and we will show how it can be modelled. Finally, we will realize noise measurements to probe process of dephasing in the MZI at high bias, and will compare them to the case when one arm of the interferometer is connected to the floating ohmic contact.

8.2   Ohmic contact detector

8.2.1   Experimental set up

We have represented in figure 8.1 the scheme of the voltage probe experiment that we have done. The most important element is the voltage probe itself which is a small ohmic contact (with a projected surface smaller than 1 μm^2). The effect of our which path detector is straightforward to understand. We call $T1$ and $T2$ the transmissions through the beam splitters of the MZI and T_P the transmission to the voltage probe. The electron source injects an input current I_0 which has a probability $I_T/I_0 = T = t^*t$ to go through the MZI. The transmission amplitude t through the MZI is then the sum of three complex amplitudes corresponding to path (a), path (b) and the others which go through the small floating ohmic contact :

$$t = -r_1 \exp(i\phi_a)r_2 + t_1 r_P \exp(i\phi_b)t_2 + t_1 T_P \sum_j r^j \exp(i\phi_{P_j})t_2$$

---

1. This kind of voltage probe has been proposed in reference [77] but the experimental set-up was not able to exhibit its dephasing properties, since the probe was not integrated in an interferometer.
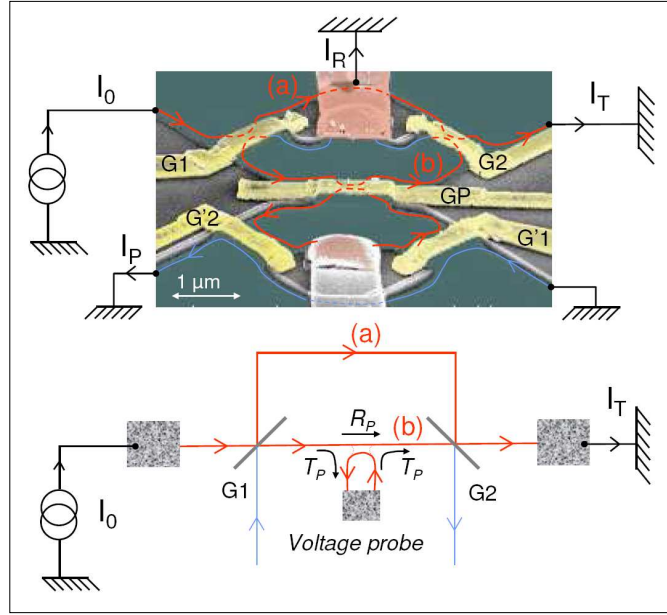
FIGURE 8.1 – The experimental setup : the MZI is designed in such a way that one arm (b) can be connected to a small floating ohmic contact. QPCs G1 and G2 are the beam splitters which split and recombine the particle trajectories. QPC GP allows to control the transmission probability T_P toward the voltage probe. G'1 and G'2 are additional QPCs which are either at pinch off in the which-path experiment or, fully open to measure the transmission through GP as a function of the gate voltage V_{GP}. The top view is a colored tilted STM view of the sample. The lines represent the edge states.

ϕ_{P_j} being random phases accumulated in the voltage probe. This leads to a transmission probability

$$T = T_1 T_2 + R_1 R_2 + \sqrt{T_1 R_2 R_1 T_2 R_P} \sin[\phi_a - \phi_b]$$

The first term of this expression corresponds to the classical term whereas the second one, which is the quantum one, oscillates with the phase difference between the two arms. The visibility of the interferences is :

$$\nu = \nu_0 \times \sqrt{R_P} \tag{8.1}$$

As expected, only the part of the wave function which does not go through the small ohmic contact contributes to the interferences. Since the mean current is not affected because the ohmic contact re-injectes all the charges that it has absorbed, the resulting visibility is given by equation (8.1). Considering the "which path" approach, the formula 8.1 tells us that electrons transmitted into the voltage probe do not interfere anymore since it would be possible "in principle" to lift the ambiguity of the particle's trajectory.

8.2.2   A specific design

In this experiment, we have to consider(see figure 8.1) 5 QPCs, G1, G2, G'1,G'2 and GP. G1 and G2 are the two beam splitters of the MZI itself, with transmissions tuned to 1/2 to obtain a maximum visibility of the interferences [69]. GP(Gate Probe), which is located

along the trajectory (b), has two functions. In the pinch-off regime, it is used to change the length of (b) in order to reveal the interference pattern. GP also serves to connect (b) to a small floating ohmic contact (the voltage probe). G'1 and G'2 are additional QPCs necessary to establish the variation of the transmission trough GP (T_P) as a function of its voltage V_{GP}. One of the two edge states (the inner one, not represented in figure 8.1) is fully reflected by G1 and G2. Thus, it does not contribute to the interferences. Here
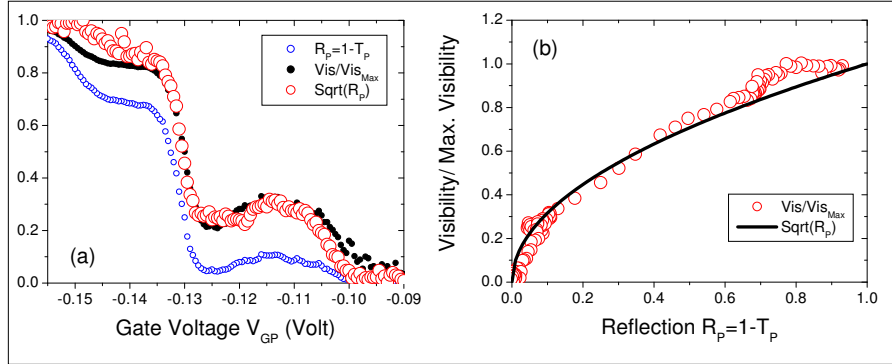
FIGURE 8.2 – (a) Normalized visibility, R_P and $\sqrt{R_P}$ as a function of V_{GP}, the voltage bias applied on GP.(b) Normalized visibility ν/ν_0 (ν_0 is inferred for $T_P = 0$) as a function of the measured transmission through the lateral gate GP. The black solid line is the $\sqrt{R_P}$ law predicted by the theory.

dephasing occurs via inelastic relaxation : the voltage probe changes the quasi particle phase and/or replace the quasi particle itself by another one. To perform a quantitative voltage probe detection, we have determined the transmission T_P as a function of V_{GP}. This is achieved by measuring $T_P = dI_P/dI_0$ with $T1 = 1$ and $T'2 = 1$. The result is shown in the figure 8.2(a). Then we closed G'1 and G'2 such that $I_P = 0$. To observe the $\sqrt{1 - T_P}$ dependence of the visibility, we need to extract the visibility of oscillations independently from the Gate voltage applied on GP. For each value of the Gate Voltage V_{GP}, we have swept the magnetic flux across the surface defined by the interferometer. The normalized visibility as a function of $R_P = 1 - T_P$ is plotted in figure 8.2. The visibility is proportional to $\sqrt{1 - T_P}$. This experiment consists in the first complete quantitative realization of the voltage probe.[2]

8.2.3 Phase evolution

We can study the phase evolution of oscillations with the gate voltage V_{GP}. A way to characterize the phase evolution of oscillations is to do a color plot of the conductance versus magnetic field (X axis) and gate voltage V_{GP} (Y axis).

Figure 8.3(a) is a color plot that shows the experimental conductance of the MZI showing Aharonov Bohm oscillations. Figure 8.3(b) represents the theoretical conductance

---

2. The measurement of T_P is realized with G'_1 and G'_2 opened ($\sim$ -0.15V), whereas the visibility dependence with T_P is done with G'_1 and G'_2 closed ($\sim$ -0.3V) which generate a small offset in the gate voltages (cross talk between gates $\sim$ 5mV).
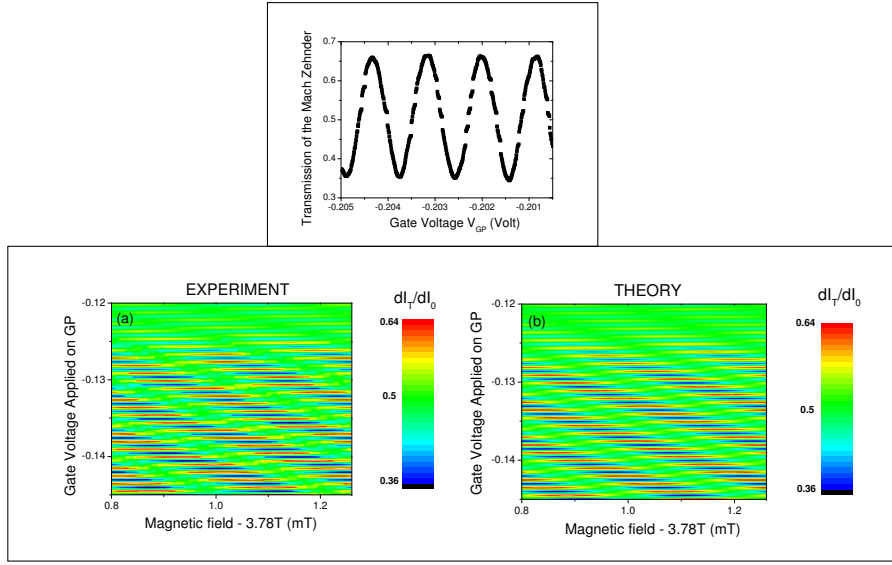
FIGURE 8.3 – Upper graph : reference of the period versus the gate voltage. We find a period of 1.15mV. Down graph : (a) Experimental data : color plot of the MZI transmission versus the gate voltage of GP (Y-axis).(b) Theoretical data : color plot of the MZI transmission versus the gate voltage of GP (Y-axis). The period versus the gate voltage (magnetic field) is 1.15mV (3.5mT). The visibility is proportional to $\sqrt{1 - T_P}$.

using the Landauer Buttiker approach, taking into account the phase evolution due both to the magnetic field and gate voltage. The visibility is set proportional to $\sqrt{1 - T_P}$. We obtain for the theoretical visibility :

$$I_\sim = \nu_0 \times \sqrt{R_P} \times cos(-\frac{2\pi V}{V_0} + \frac{2\pi B}{B_0}). \tag{8.2}$$

with $V_0 = 1.15mV$ (resp $B_0 = 3.5mT$) the necessary gate voltage(magnetic field) to observe a 2π shift of the phase.

The perfect agreement between experimental data and theory confirms that in a voltage probe set up, we can both follow transmission and phase evolution.

8.3   Study of a resonance

Figure 8.2 also gives insight in process of phase shift close to a QPC. The MZI is sensitive to phase shift occurring in each arm of the interferometer, induced by a localized state for example. The detailed study of the phase evolution of the Aharonov Bohm oscillations when we open the probe gate will enable us to study and model a resonance located close to the probe gate.

8.3.1 Effect of a resonance on the phase

In figure 8.4, we have zoomed the color plot of the figure 8.3 for V_{GP} in the interval [-0.14V,-0.13V] and [-0.12V,-0.11V]. In the interval [-0.14V,-0.13V], we obtain a linear evolution of the phase with V_{GP} as expected. However in the interval [-0.12V,-0.11V] one notices a non linear behavior of the phase with V_{GP}. This behavior is the consequence of the additional phase introduced by a resonance (see also figure 8.2(a)). The resonance close to the QPC can be understood as a coherent mechanism that modifies the trajectory of electrons (and thus the Aharonov Bohm phase).
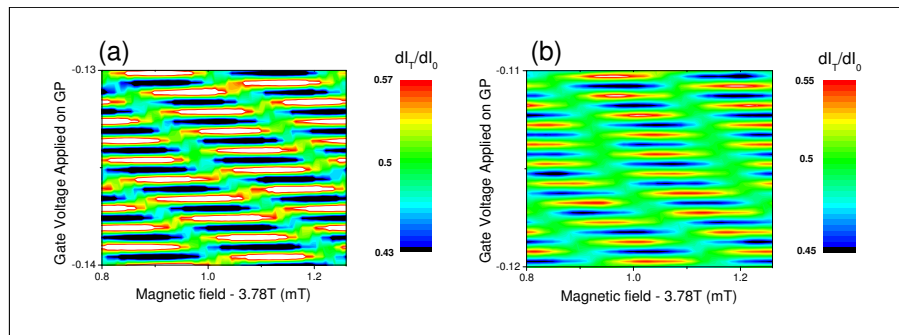
FIGURE 8.4 – Color plot of the MZI transmission versus the gate voltage of GP (Y-axis)(a) Zoom of the phase evolution for $V_{GP} = -0.14V$ to $-0.13V$. Phase evolution is linear with the voltage (b) Zoom of the phase evolution for $V_{GP} = -0.12V$ to $-0.11V$. The non linear phase evolution is the mark of the resonance (see the upper graph) that introduces an additional phase.

8.3.2 Modelling the resonance
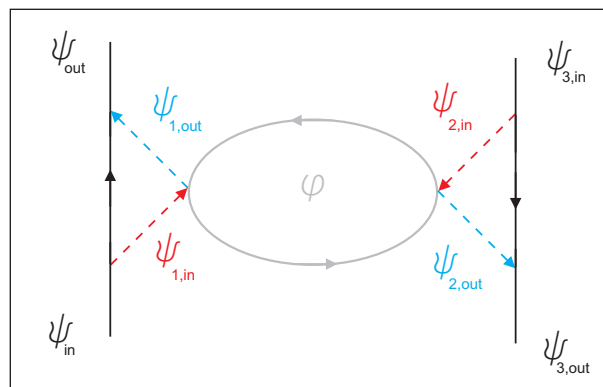
FIGURE 8.5 – Schematic representation of the resonance

We are going to model this small closed trajectory considering two counter propagating edge states as represented in figure 8.5. We can divide this model in three parts. The first one by the probability for the incoming edge state to be transmitted or reflected towards
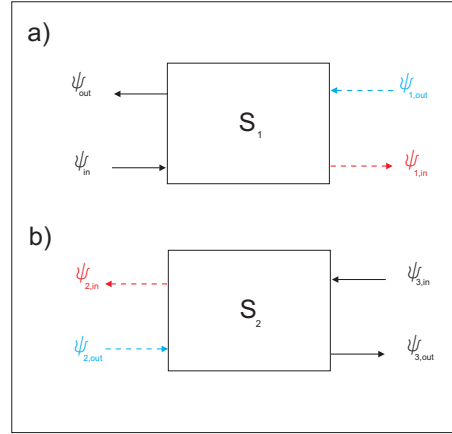
FIGURE 8.6 – Modelling the resonance in terms of scattering matrix

the resonance, modelled by the scattering matrix S_1 (figure 8.6(a)). We can express this scattering matrix in terms of reflection and transmission amplitudes :

$$S_1 = \begin{pmatrix} \psi_{out} \\ \psi_{1,in} \end{pmatrix} = \begin{pmatrix} t_1 & r_1 \\ -r_1 & t_1 \end{pmatrix} \begin{pmatrix} \psi_{1,out} \\ \psi_{in} \end{pmatrix}$$

A second composed of the localized state itself. When an electron makes the entire loop in the localized state, it accumulates the phase φ. A third part is composed of a scattering matrix S_2 (figure 8.6(b)) that models the probability for the electron to be transmitted towards the counter propagating edge state. This scattering matrix is given by :

$$S_2 = \begin{pmatrix} \psi_{2,in} \\ \psi_{3,out} \end{pmatrix} = \begin{pmatrix} t_2 & r_2 \\ -r_2 & t_2 \end{pmatrix} \begin{pmatrix} \psi_{3,in} \\ \psi_{2,out} \end{pmatrix}$$

We consider here that $\psi_{3,in} = 0$ We deduce from the scattering matrix the following expressions :

$$\psi_{out} = r_1\psi_{in} + t_1\psi_{1,out} = r_1\psi_{in} + e^{i\varphi}r_2t_1\psi_{1,in}$$

We want to express ψ_{out} as a function of ψ_{in} since we measure $\mid \psi_{out} \mid^2$:

$$\psi_{out} = (r_1 + \frac{(1 - r_1^2)r_2e^{i\varphi}}{1 + r_1r_2e^{i\varphi}})\psi_{in}$$

which finally gives for the reflection and the phase measured after this resonance :

$$R_P = \frac{\sqrt{((r_2 - r_1^2r_2)\sin(\varphi))^2 + (r_2\cos(\varphi) + r_1^2r_2\cos(\varphi) + r_1(1 + r_2^2))^2}}{1 + r_1^2r_2^2 + 2r_2r_1\cos(\varphi)}$$

$$Phase = Arctan(\frac{(r_2 - r_1^2r_2)\sin(\varphi)}{r_2\cos(\varphi) + r_1^2r_2\cos(\varphi) + r_1(1 + r_2^2)})$$

We can now compare these expressions of the phase and the transmission to our experimental data. We choose $r_1=0.18$ and $r_2=0.16$. We express φ as a function of V_{GP} :

$$\varphi = \frac{V_{GP} + 0.112}{\Delta}$$

where $\Delta = 1/220$.
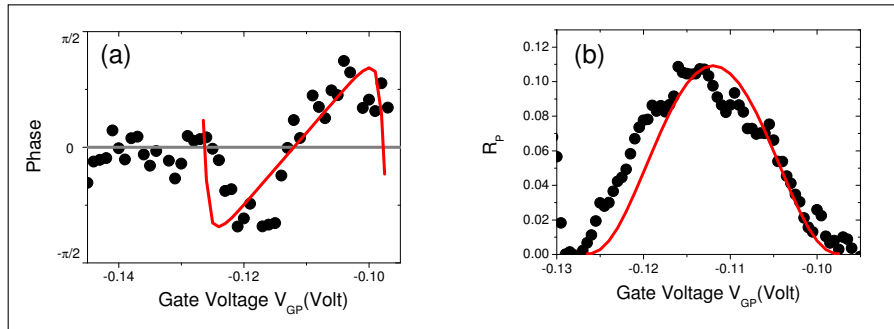
FIGURE 8.7 – (a)Black dots : transmission measured around the resonance. To obtain a symmetrical function we have subtracted from the experimental transmission the theoretical transmission. Red solid line : transmission obtained with the model of two counter propagating edge states coupled to a resonance (b)Black dots : extra phase measured due to the resonance. Red solid line : phase obtained with the model of two counter propagating edge states coupled to a resonance

We have represented, in black dots, in figure 8.7(a) the extra phase due to the resonance and 8.7(b) the transmission around the resonance, obtained experimentally. We have represented, in red solid line, in figure 8.7(a) the extra phase due to the resonance and 8.7(b) the transmission around the resonance, obtained with the theoretical model. The excellent agreement with our data suggests that this model is appropriated to understand the resonances of a QPC.

8.4   Decoherence and Phase averaging

We wish to stress that, as electrons entering the probe play no role in the interference revealed by the Aharonov-Bohm oscillations of the transmitted current, conductance measurements bring no information on the exact process at work within the probe. Do electrons reach thermal equilibrium in the probe, being re-emitted at a chemical potential that readjusts to ensure charge conservation ? Are they simply re-emitted with a random phase ? As shot noise probes the uncertainty in electron occupation in the outgoing current, noise measurement can help elucidating this point. In a a recent paper [49], Marquardt and al. have calculated shot noise in an electronic Mach Zenhder connected to a dephasing terminal, and have considered both elastic phase randomization and full energy relaxation, which one expects in our experimental set-up. In this part, we describe noise measurements with an opened gate probe first, then with a closed gate probe.

8.4.1   Decoherence in the MZ : the voltage probe approach

At that point, the small ohmic contact shows results in perfect agreement with what one can expect with a voltage probe (redistribution of the energies) or dephasing probe (the energy is kept but there is a random phase). We shall see now that one can perform different experiments to characterize the ohmic contact properties. We will start with voltage probe experiments at different temperatures. This will allow to check if the disappearance of interferences is due to a thermal smearing resulting from an effective increase of the lower trajectory length or really to dephasing and/or energy redistribution in the ohmic contact. Secondly, noise measurements will give insight into decoherence process in the MZI, in particular regarding the question of inelastic relaxation at finite DC bias. To answer to the first point, we have represented in figure (8.8)(a) the visibility as a function of temperature for two values of the lateral gate $T_P=1$ and $1/2$. For $T_P=1$ we find a linear dependence of $\ln(\nu)$ versus temperature as already studied in [69]. We have drawn in red solid line the expected result given by the same T^{-1} exponential decrease, for a lateral gate T_P tuned to 0.5. The fact that (once renormalized by the visibility at 20mK) both curves have exactly the same dependence shows that the connection to voltage probe does not introduce thermal smearing of the AB oscillations.
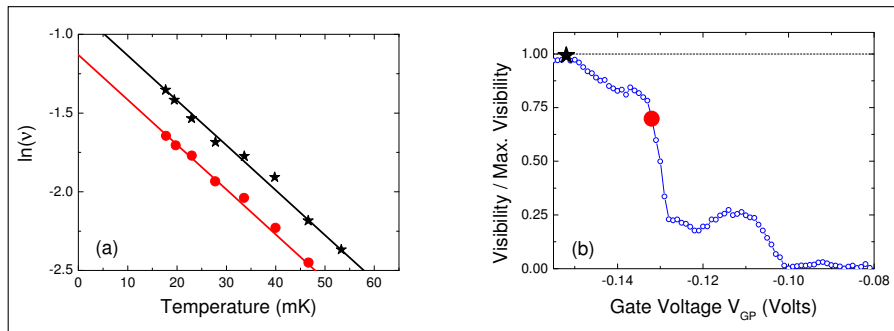
FIGURE 8.8 – (a) $\ln(\nu)$ as a function of the temperature for different values of the transmission of the lateral gate. The visibility in the case of a closed lateral gate($T_P=1$) is shown by the black stars. In red dots the visibility obtained for $T_P=1/2$. The red solid line is obtained with a simple Landeauer Buttiker approach in the case of a perfect inner ohmic floating contact. (b) the black star and the red circle show respectively the visibility/max.visibility for $T_P=1$ and $T_P=1/2$. As expected, one obtains visibility/max.visibility=1 for $T_P=1$ and ~ 0.71 for $T_P=0.5$.

Regarding the second point, the beginning of a preliminary answer is given in [37]. In their letter, Ji *et al.* have measured shot noise as a function of T_2 at $30\mu V$ DC voltage for $T_1=1/2$, under which the AB interference pattern was quenched. They found

$$S \sim 1/4 - \kappa^2 T_2(1-T_2)/2$$

with $\kappa=0.9$. [3]

_____

3. Doing this measurement, they were able to exclude complete decoherence to explain the nul visibility at $30\mu V$.

In a a recent paper [49], Marquardt *et al.* have calculated shot noise in an electronic Mach Zenhder connected to a dephasing terminal, and have treated the cases of dephasing and inelastic relaxation. The general expression of the coherent transmission in an electronic MZI connected to a dephasing terminal (see figure 8.9) is :

$$\langle T_{MZI,1}\rangle = T_1 T_2 + R_1 R_2 + 2z(t_1^\star r_1)(t_2^\star r_2)cos(\varphi)$$

where z parametrizes decoherence of the system ($z=1$ the transport is fully coherent, $z=0$
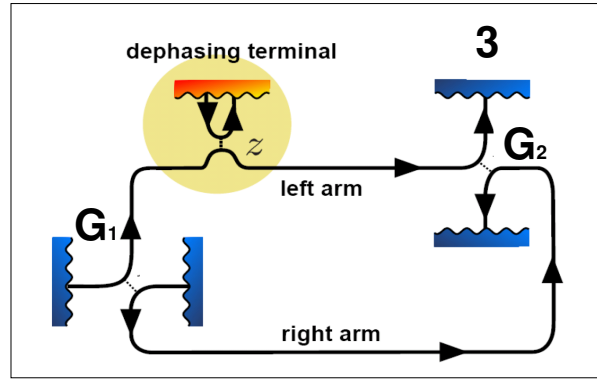
FIGURE 8.9 – At beam splitters 1 and 2 the electrons are transmitted with amplitudes $T_{1,2}$. The fictitious φ reservoir serves as a dephasing terminal. The coherence parameter z denotes the amplitude for an electron to be reflected at the beam-splitter connecting the left arm of the interferometer to the reservoir φ (thus z = 1 for fully coherent transport).

the transport is fully decoherent, see also figure 8.9). We consider here the cases of pure dephasing (averaging on the phase) and inelastic relaxation. Regarding pure dephasing, the theoretical noise measured in auto-correlation on the contact 3 (in figure 8.9) :

$$S_{33} = 2eV\frac{h}{e^2}(\langle T_{MZI,1}\rangle\langle T_{MZI,2}\rangle - 2(1 - z^2)R_A R_B T_A T_B) \qquad (8.3)$$

with $\langle T_{MZI,2}\rangle = 1 - \langle T_{MZI,1}\rangle$. For the inelastic relaxation case, it does matter whether relaxation is ascribed fully to one arm or to both arms. Marquardt *et al.* consider then two reservoirs L, R with associated amplitudes z_L, z_R. As the current only depends on $z_R z_L = z$, we write $z_L = z^\lambda$ and $z_R = z^{1-\lambda}$, where the parameter λ quantifies the asymmetry ($\lambda=1,0$ for relaxation in the left/right arm and $\lambda=1/2$ for the symmetric case). The shot noise becomes :

$$S_{33} = 2eV\frac{h}{e^2}(\langle T_{MZI,1}\rangle\langle T_{MZI,2}\rangle - 2R_1 R_2 T_2(1 + (1 - 2T_1)z^2 - R_1(z^{2(1-\lambda)} + z^{2\lambda}))) \quad (8.4)$$

for $R_A < T_A$. In the fully asymmetric case ($\lambda = 0, 1$), Marquardt *et al.* recover the formula 8.3 obtained for pure dephasing.

We have measured the shot noise as a function of T_2 at $58\mu V$ DC voltage when the lateral gate was closed(opened) $T_P=1(T_P=0)$. When the gate is closed with a 58 μV DC
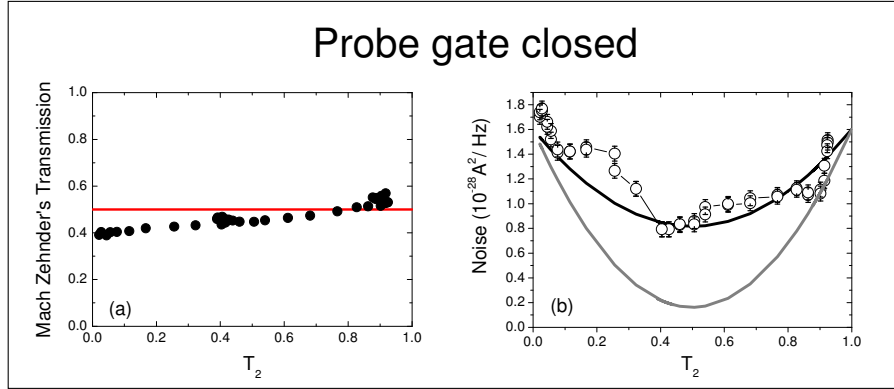
FIGURE 8.10 – (a) Mean value of the output current. Since the Mean value is equal to 0.55 when T_2=1, transmission of the first gate $T_1 \sim 0.55$. (b)Shot Noise measurement(at filling factor 2) as a function of T_2 when T_1=1/2 and the lateral gate closed. A 58 μV DC voltage is applied for the shot noise measurement (at this voltage, Aharonov-Bohm oscillations are quenched). The excess noise measured at 58 μV is shown in black circles. We have represented in black line the shot noise predicted by Marquardt *et al.*[49], in the case of zero visibility due to pure dephasing. In grey solid line is represented the inelastic relaxation case.
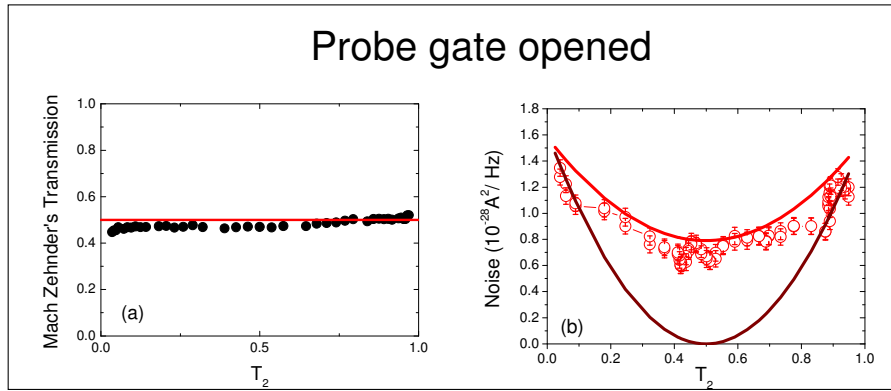
FIGURE 8.11 – (a)Mean value of the output current. Since the Mean value is equal to 0.5 when T_2=1, transmission of the first gate $T_1 \sim 0.5$. (b)Shot Noise measurement(at filling factor 2) as a function of T_{G2} when T_{G1}=1/2 and the lateral gate opened. A 58 μV DC voltage is applied for the shot noise measurement. The excess noise measured at 58 μV is shown in red circles. In red solid line, inelastic relaxation approach considering that there is no inelastic relaxation in the upper path. The dark red solid line corresponds to complete inelastic relaxation occurring in both path.

voltage, the visibility is null, thus $z \sim 0$. The formula of pure dephasing 8.3 becomes :

$$S_{33} = 2eV\frac{h}{e^2}(\langle T_{MZI,1}\rangle\langle T_{MZI,2}\rangle - 2R_1R_2T_1T_2) \qquad (8.5)$$

The study of the MZI's transmission at 58 μV, show that the transmissions of the first gate $T_1 \sim 0.5$. In figure 8.10 we have plotted in black circles the excess noise at $58\mu V$ DC voltage. The black solid line corresponds to formula 8.5 and the grey solid line to formula 8.4, in the symmetric case. The good agreement with the formula 8.5 confirms the presence of dephasing in the electronic MZI but not pure relaxation. We reproduced a

similar measurement, but for the lateral gate opened ($T_P{=}0$). We are now in the case of an inelastic relaxation in the down arm. In this case we must recover formula 8.5. In figure 8.11 we have plotted in red circles the excess noise at $58\mu V$. The red solid line corresponds to formula 8.5 and the dark red solid line to formula 8.4 in the symmetric case. Experimental data are in good agreement with formula 8.5. The small discrepancy could be attributed to a light energy relaxation occurring in the upper path, but in view of the dispersion of the points, we can hardly conclude. This result brings valuable information about the physics underlying the finite bias visibility of the MZI, which is still not yet understood. We could focus on this light energy relaxation occurring in the upper path at $58\mu V$. We could ask whether this relaxation is due to inter edge states interaction or intra edge state interaction. We do not have answer yet.

8.5   Conclusion

In this part, we have shown that a small floating ohmic contact can be used as a voltage probe which will destroy quantum interferences. The coupling between the ohmic contact and the MZI was controlled with a QPC. The decoherence in the MZI was tuned with this QPC. This is here, the first quantitative experimental realization of the theoretically widely used voltage probe. Then, we have shown that the voltage probe set up enables us to follow both the transmission and phase evolution while opening the lateral gate. We have thus studied a resonance located close to the QPC. A precise study of the phase evolution near the resonance revealed phase shift that can be very well understood modelling it by two counter propagating edge states coupled to a localized state. Finally, we have realized noise measurements to probe the energy relaxation in the floating ohmic contact. We have verified that an inelastic relaxation approach inside the ohmic contact was the good one.

This work opens new possibilities regarding the study of the voltage and dephasing probe. The most promising one being the full counting statistic of it, as recently proposed [32][33].

Tuning decoherence with a voltage probe

P. Roulleau, F. Portier, and P. Roche
Nanoelectronic group, Service de Physique de l'Etat Condensé,
CEA Saclay, F-91191 Gif-Sur-Yvette, France

A. Cavanna, G. Faini, U. Gennser, and D. Mailly
CNRS, Laboratoire de Photonique et Nanostructures,
Route de Nozay, F-91460 Marcoussis, France
(Dated: December 1, 2008)

One of the major advances in the understanding of the physics of quantum conductors has been the scattering approach which considers the elastic scattering of in-going states towards out-going states in a ballistic conductor. It has led to numerous predictions confirmed experimentally, including, for example, the quantification of the conductance in a quantum point contact. Recently, it has been used successfully to predict the behavior of the electronic Mach-Zehnder interferometer[1], and the existence of two-electrons interferences that reveal the indistinghisibility of electrons[2]. A limitation of this so-called Landauer-Büttiker theory is that it only treats elastic scattering. As a consequence, it cannot be applied directly to the description of the consequences of decoherence or energy relaxation in electronic transport. This limitation has been cunningly circumvented by theoreticians by adding an additional reservoir the connection of which to the studied quantum circuit mimics decoherence[3]. Here we show the first quantitative realization of a voltage probe with a small ohmic contact by tuning the decoherence in a quantum interferometer.

The effect of a voltage probe can be explained in the following manier. Quasi-particles which have been probed by this additional reservoir (the voltage probe) when going through the quantum conductor, loose their phase so that nothing differentiates them from the electrons of the ohmic contact. This theoretical construction is intimately linked with which-path experiments, in that when an electron is absorbed by the additional reservoir, the ambiguity of the particle's trajectory can in principle be lifted, suppressing interference effects. Energy relaxation, too, can be described within the same framework by supposing that the electrons re-injected by the voltage probe into the interferometer are at thermal equilibrium. This approach has been used to predict the two first moments of the Full Counting Statistics of the charge transmitted through an electronic Mach-Zehnder interferometer in the presence of decoherence or energy relaxation [4, 5]. In practice, a reservoir in the physics of quantum conductors is defined as *some* region of the conductor which absorbs all incoming particles and emits "new" particles with a Fermi statistics at the local electrochimical potential. Indeed, in the case of a sample larger than the electronic coherence length, one cannot tell exactly where are the reservoirs. They are simply put at the multiple extremities of the considered conductor exhibiting quantum properties on a size scale determined by the coherence length of excitations, or their energy redistribution length. For a two-dimensional electrons gas (2-DEG) in the Quantum Hall Regime, the chirality of electrical transport, occurring along one-dimensional chiral edge modes strongly suppresses electron-electron interactions. This allowed the observation of Aharanov-Bohm oscillations with unmatched visibilities, reaching 95% [2]. It makes it possible to specify the actual position of the reservoirs: the various ohmic contacts which connect the 2-DEG to the macrosopic world.

We present here an experiment where a voltage probe introduces a controlled energy redistribution in a two path electronic interferometer. To this end, we have realized an electronic Mach-Zehnder interferometer operating in the Quantum Hall Regime [1], one of the arms of which is connected to a small floating ohmic contact through a quantum point contact [5]. Our measurements constitute the first quantitative demonstration of a voltage probe in a quantum conductor. Floating ohmic contacts have already been used to enforce energy relaxation of noisy currents [6, 7] but without presenting an experimental set-up permitting the exploration of their dephasing properties. More specifically, the Quantum Point Contact (QPC), allows us to tune the transmission probability T_P towards the voltage probe. As a result, the visibility of the quantum interferences is reduced by a factor $\sqrt{1 - T_P}$, which represents the probability amplitude for a particle not to be probed by the small floating ohmic contact.

A SEM view of our MZI is represented in figure (1). Starting from a high mobility two dimensional electron gas in a GaAs/GaAlAs heterostructure with a sheet density of $n_S = 2 \times 10^{11}$ cm^{-2} and a mobility of 2.5×10^6 cm^2/Vs, we patterned the geometry of the mesa, thus the trajectory of the edge states, by e-beam lithography. The length of arms (a) and (b) is designed to be both equal to 5.7 μm yielding to an enclosed of 7.25 μm^2. In our MZI (see figure (1)), there are 5 QPCs, G1, G2,
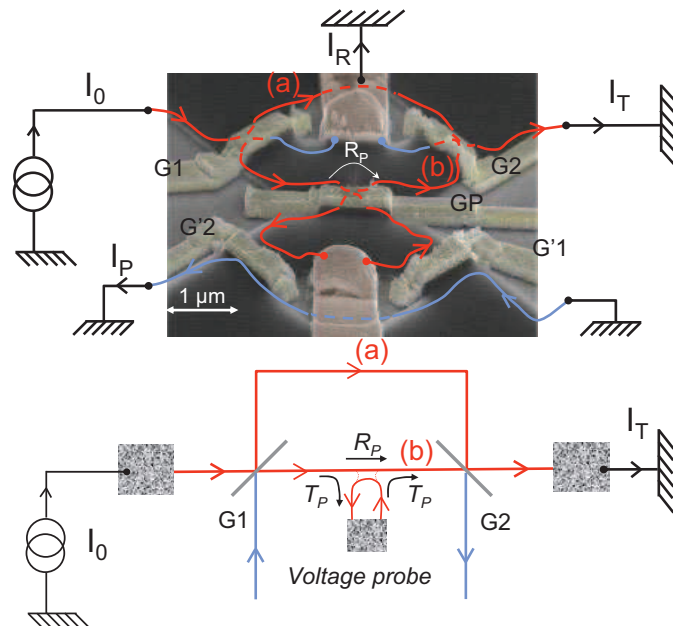
FIG. 1: The experimental setup : an electronic Mach-Zehnder interferometer is designed by electron beam lithography on a high mobility 2D electron gas in GaAs/GaAlAs heterostructure. One arm (b) can be connected to a small floating ohmic contact which plays the role of a voltage probe. QPCs G1 and G2 are the beam splitters which split and recombine the particle trajectories. QPC GP allows to control the transmission probability T_P toward the voltage probe. G'1 and G'2 are additional QPCs which are either at pinch off in the which-path experiment or, fully open to measure the transmission through GP as a function of the gate voltage V_{GP}. The top view is a colored tilted STM view of the sample. The lines represent the edge states.

G'1,G'2 and GP. G1 and G2 are the two beam splitters of the MZI itself, with transmissions tuned to 1/2 to obtain a maximum visibility of the interferences [8]. GP, which is close to the trajectory (b), has two functions. In the pinch-off regime, it is used to change the length of (b) in order to reveal the interference pattern. GP also serves to connect (b) to the bottom small ohmic contact (the voltage probe). G'1 and G'2 are additional QPCs: we first open them completely to measure a reference of the transmission trough GP (T_P) as a function of its voltage V_{GP}. Once this reference done, we permanently close them. The transmission probability through the MZI is measured by a standard lock-in technique with an AC excitation V_{AC}= 1.2 μV smaller than $k_B T/e$, ensuring that the coherence length of the source is determined by the experimental temperature. We worked at a filling factor 2 with a magnetic field of 4.6 tesla and one of the two edge states (the inner one, not represented on figure 1) is fully reflected by G1 and G2.

The interference pattern is revealed either by varying the magnetic field or V_{GP}. Hence, GP both connects the trajectory (b) to the voltage probe and sweep the phase
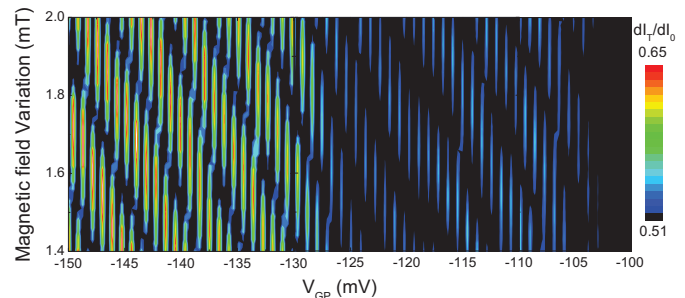
FIG. 2: Color plot of the differential transmission $\mathcal{T}$ as a function of the voltage probe gate voltage V_{GP} and the magnetic field. The color plot is set such that all the transmissions lower than the mean transmission are in black. In practice the visibility is measured by varying the magnetic field.

trough the MZI. In figure 2, a color plot of the differential transmission as a function of the magnetic field and V_{GP} is displayed. As one can remark, the amplitude of the oscillation decreases as V_{GP} increases, hence when the trajectories are more connected to the voltage probe.

This observed visibility decrease is straightforward to understand. We call T_1 and T_2 the transmissions through the beam splitters of the MZI and T_P the transmission to the voltage probe. The electron source injects an input current I_0 which has a probability $I_T/I_0 = T = t^*t$ to exit the MZI through the ohmic contact located on the right side of figure 1. As we treat a quantum circuit, T is not the sum of the transmission probability of the different trajectories $R_1 R_2 + T_1 T_2$ (path (a)+path(b)), but the squared sum of the transmission probabilities amplitudes. The transmission amplitude t through the MZI is then the sum of three complex amplitudes corresponding to path (a), path (b) and the others which go through the small floating ohmic contact:

$$t = -r_1 e^{i\phi_a} r_2 + t_1 r_P e^{i\phi_b} t_2 + t_1 T_P \sum_j r^j e^{i\phi_{P_j}} t_2 \qquad (1)$$

ϕ_{P_j} being random phases accumulated in the voltage probe, and r_i and t_i respectively stand for the reflection and transmission coefficient of electronic wavefunctions by QPC i. This leads to a transmission probability $T = T_1 T_2 + R_1 R_2 + \sqrt{T_1 R_2 R_1 T_2 R_P} \cos[\phi_a - \phi_b]$, where $R_i = |r_i|^2$, and $T_i = |t_i|^2 = 1 - R_i$. The first term of this expression corresponds to the classical term whereas the second one, which reveals the wave nature of electrons, oscillates with the phase difference between the two arms. In the Quantum Hall Regime, this phase can be shown to be equal to the Aharonov-Bohm phase corresponding to the magnetic flux threaded through the area delimited by the two interfering trajectories. It can thus be varied either by changing the length of the arm (b) or by sweeping the magnetic flux across the surface defined by the interferometer [8]. The visibility of interferences defined
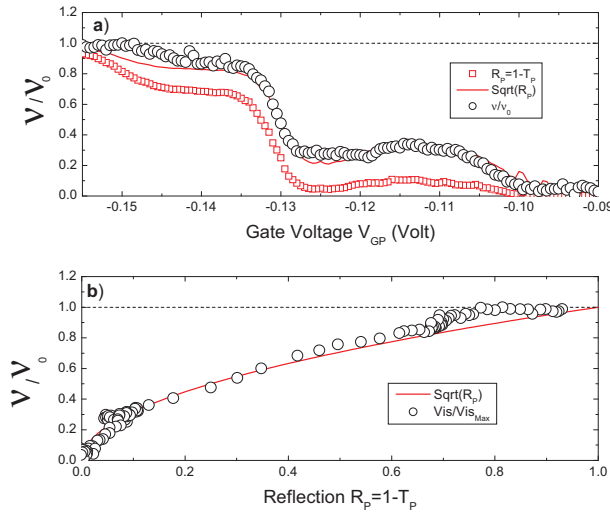
FIG. 3: Normalized visibility $\mathcal{V}/\mathcal{V}_0$ ($\mathcal{V}_0$ is inferred for $T_P = 0$). **a)** $\mathcal{V}/\mathcal{V}_0$ (black circles), R_P (red squares) and $\sqrt{R_P}$ (red line) as a function of V_{GP}. **b)** $\mathcal{V}/\mathcal{V}_0$ (black circles) as a function of the measured R_P. The solid line is the $\sqrt{R_P}$ law predicted by the theory.

as $\mathcal{V} = (T_{MAX} - T_{MIN})/(T_{MAX} + T_{MIN})$ is:

$$\mathcal{V} = \mathcal{V}_0 \times \sqrt{R_P} \qquad (2)$$

where T_{MAX} and T_{MIN} are the maximum and minimum transmission respectively. This means that, as expected, only the part of the wave function which does not go through the small ohmic contact contributes to the interferences. Equation 2 is thus a consequence of the consequence of the floating contact not affecting the mean current: all the charges that have been absorbed into it are re-injected into the circuit, so that the sum of the measured transmitted current I_T and of the current absorbed by the upper small ohmic current I_R is conserved.

In previous which path experiments using quantum conductors, the dephasing occured by coupling the electrons to a noisy electromagnetic environment [6][9][10][11]. In our set-up, electrons re-emitted into the interferometer cannot be distinguished from the other electrons of the probe. They bear a phase, reflecting their interactions with the various degrees of freedom of the floating contact, uncorrelated with the phase of the incidents electrons. Hence, they do not contribute to the quantum interferences resulting in the Aharonov-Bohm term of the transmitted current. To perform a quantitative analysis of the voltage probe detection, we determined the transmission T_P as a function of V_{GP}. This is achieved by measuring $T_P = dI_P/dI_0$ with $T_1 = 1$ and $T_2' = 1$. The result is shown in the inset of figure 3. Then we closed G'1 and G'2 such that $I_P = 0$. The normalized visibility as a function of $R_P = 1 - T_P$ is plotted in figure (2b). This is our main result, which shows a decrease of the visibility as the square root of the reflection probability, in perfect agreement with theory. It is noteworthy

that despite the small size of the ohmic contact (less than 1μ m^2), it shows no sign of Coulomb Blockade that would prevent electrons from entering it and protect quantum interferences. This is because it is connected through a metallic air bridge to a much bigger bonding pad which strongly increases its capacitance and suppresses and reduces its charging energy to a negligible level.

The phase variation $\delta\phi$ of the interferences related to the magnetic field variation δB and δV_{GP} by $\phi = 2\pi(\delta B.S + dS/dV_{GP}.\delta V_{GP})/\phi_0$, where ϕ_0 is the quantum of flux h/e leads to tilted black regions given by $\delta B.S \propto dS/dV_{GP}.\delta V_{GP}$ in figure 2. On the resonance which appears in the measurement of R_P for $V_{GP} \sim -0.115$ V, the separation between the tilted region is no longer regular, indicating that crossing the resonance a additional phase shift appears in the interferences [12]. A row determination leads to a $\sim \pi$ shift at the resonance, although our phase measurement is not precise enough to determine the exact shape of the phase variation. The absence of such phase shift in the first resonance near $V_{GP} \sim -0.145$ V explains the small discrepancy with the $\sqrt{R_P}$ law observed: when measuring R_P, all the closed trajectories at a distance lower than the coherence length [13, 14] from GP possibly lead to resonances. Here, we are in the case where the closed trajectory leading to the resonance is outside the MZI when G'1 and G'2 are at pinch off. Hence the value of the measured R_P is not the one we should take into account for the visibility decrease.

To summarize, we have shown that a small floating ohmic contact can be used as a voltage probe that can be used to destroy quantum interferences. To do so, we have used a QPC to coherently control the amplitude probability for an electron to be absorbed by the voltage probe. Then, via interference measurements, we have proved that electrons absorbed and re-emitted by the probe acquire a random phase and don't contribute to the interference process. This work opens new possibilities regarding the study of the voltage and dephasing probe. The most promising one being the full counting statistic of it, as recently proposed [15–17].

_____

[1] Y. Ji *et al.*, Nature **422**, 415 (2003).
[2] I. Neder *et al.*, Nature **448**, 333 (2007).
[3] M. Büttiker, Phys. Rev. B **33**, 3020 (1986).
[4] F. Marquardt and C. Bruder, Phys. Rev. Lett. **92**, 056805 (2004).
[5] F. Marquardt and C. Bruder, Phys. Rev. B **70**, 125305 (2004).
[6] D. Sprinzak, E. Buks, M. Heiblum, and H. Shtrikman, Phys. Rev. Lett. **84**, 5820 (2000).
[7] S. Oberholzer *et al.*, Phys. Rev. Lett. **96**, 046804 (2006).
[8] P. Roulleau *et al.*, Phys. Rev. B **76**, 161309(R) (2007).
[9] E. Buks *et al.*, Nature **98**, 871 (1998).
[10] I. Neder *et al.*, Phys. Rev. Lett. **98**, 036803 (2007).

4

[11] D. Rohrlich *et al.*, Phys. Rev. Lett. **98**, 096803 (2007).

[12] M. Avinun-Kalish *et al.*, Nature **436**, 529 (2005).

[13] P. Roulleau *et al.*, Phys. Rev. Lett. **100**, 126802 (2008).

[14] P. Roulleau *et al.*, Phys. Rev. Lett. **101**, 186803 (2008).

[15] S. Pilgram, P. Samuelsson, H. Förster, and M. Büttiker, Phys. Rev. Lett. **97**, 066801 (2006).

[16] H. Förster, P. Samuelsson, S. Pilgram, and M. Büttiker, Phys. Rev. B **75**, 035340 (2007).

[17] H. Forster, P. Samuelsson, and M. Buttiker, New Journal of Phys. **9**, 117 (2007).

Chapitre 9

Conclusion

In this PhD thesis, we have shown that the MZI proved to be a test bed to understand decoherence process in the quantum Hall regime. Studying the visibility of interferences as function of the bias voltage and the temperature, we have noticed two different behaviors : a lobe structure for the visibility as a function of the bias, and an exponential dependence for the visibility as a function of the temperature. This PhD thesis has brought new insights into these behaviors.

In the first part, I have described the electronic MZI and the experimental set up of the experiment. I have compared the different ways to reveal interferences and have shown that they were equivalent. Finally, I have shown that we have developed an original way to extract the visibility of interferences on a noisy sample.

The second part is devoted to the dependence of the visibility as a function of the bias. When two edge states are fed with the same bias, the visibility presents a monotonous decay. We have explained this monotonous dependence considering the coupling between edge states. When the inner edge state is reflected by the beam splitter G_0 we have observed single side lobe and multi side lobes at the beginning of the plateau ($\nu = 2$). We have shown that the single side lobe could be understood supposing a Gaussian phase averaging. Moreover, diluting the impinging current increased the lobe width what may be the sign of energy redistribution in the interfering edge state. We have then considered the enhancement of the visibility for small bias voltages for certain values of G_1. Taking into account the coupling between edge states, we have clarified this behavior of the visibility. There remains, nevertheless, a difference whether we consider two coupled edge states each emitted by two different sources or if we consider two edge states emitted from the same source : we do not have explanation for this result. Finally we have described another experiment where the interfering edge state is composed of a two step distribution in energy : the lobe structure is all the more affected than this two step distribution is spaced.

In a third part, we have determined for the first time the coherence length in the quantum Hall regime at $\nu = 2$. To do this, we have measured the decrease of the visibility as a function of the temperature, and have found an exponential decrease. We have done this measurement on three samples of different sizes scaling by a factor $\sim \sqrt{2}$. We have definitively excluded any spurious effect like thermal smearing, to finally determine the

coherence length l_φ at $\nu = 2$. We have found l_φ to be equal to $20\mu m$ at 20mK. Moreover we have shown a magnetic field dependence of this coherence length whose origin is treated in the fourth part.

The fourth part deals with the origin of the coherence length. We have then considered the environment of the interfering edge state, and more precisely have focused on the adjacent edge state coupled to the interfering one. We have shown, and that is one of the main result of my PhD thesis, that the finite coherence length results from this coupling with the inner edge state. In particular the inner edge state generates thermal noise, and these fluctuations induce decoherence. To demonstrate this, we have characterized this coupling on the whole plateau at $\nu = 2$, have extracted the bandwidth mimicing a noisy environment with a partitioned inner edge state and have confirmed that the Gaussian approximation applied. We have finally shown that both the origin of the coherence length and its magnetic field dependence were related to the coupling with the inner edge state.

In a last part, we have shown that a small floating ohmic contact can be used as a voltage probe which will destroy quantum interferences. To do so, we have used a QPC to control the amplitude probability for an electron to be absorbed by the voltage probe. Then, via interference measurements, we have proved that electrons absorbed and re-emitted by the probe acquire a random phase and don't contribute to the interference process. We have shown that the MZI configuration enables us to follow the phase shift in one of the arm of the interferometer. More precisely, we have followed the phase shift induced by a localized state close to the QPC and have modelled it by scattering matrix. We have realized noise measurements to probe process of dephasing in the MZI at high bias, and have compared them to the case when one arm of the interferometer is connected to the floating ohmic contact. We have verified that an inelastic approach inside the ohmic contact was the good one. This work opens new possibilities regarding the study of the voltage and dephasing probe.

The goal of this thesis was the observation of the Bell's inequalities violation in a mesoscopic conductor. Considering our visibility at finite bias, we did not have the noise sensitivity to observe neither the two-particle Aharonov Bohm effect nor the Bell's inequalities violation. The observation of the Bell's inequalities would require a higher visibility at finite bias. However, we have now a good understanding of the different process of decoherence at $\nu = 2$: this study has revealed the important role of the inner edge state. Regarding the noise sensitivity, we have begun to develop cryogenic low noise amplifiers that would reach the necessary noise sensitivity to observe first the two Aharonov Bohm effect and in the future the Bell's inequalities violation. We have encountered many technical problems during this development. An important step in the development of this experiment will be to improve these cryogenic low noise amplifiers.

Chapitre 10

Résumé/Abstract

10.1   Résumé

Ce travail est consacré à l'étude des processus de décohérence dans le régime Hall quantique entier. Ce régime est obtenu en appliquant un fort champ magnétique perpendiculaire à un système bidimensionnel d'électrons crée à l'interface entre GaAs et AlGaAs. Le transport électronique se fait alors par un ou plusieurs canaux unidimensionnels chiraux le long du bord de l'échantillon. Ces faisceaux d'électrons sont ensuite contrôlés par des lames séparatrices mésoscopiques, les contacts ponctuels quantiques. Un réglage fin de ces contacts ponctuels quantiques permet d'obtenir des interférences de la conductance. Les oscillations sont alors obtenues en balayant le champ magnétique ou en modifiant l'aire définie par les deux bras de l'interféromètre appelé interféromètre de Mach Zehnder (MZI). L'étude de la visibilité de ces oscillations en fonction de la tension drain source et de la température, nous permet de sonder la cohérence du système. L'essentiel de ces résultats a été obtenus à facteur de remplissage 2 pour lequel deux canaux de bord sont présents.

Dans un premier temps, nous avons étudié la visibilité en fonction de la tension drain source lorsque le canal interne est réfléchi et avons observé une structure en lobe. Nous avons montré qu'en présence d'un seul lobe, une moyenne gaussienne de la phase ajouté au fait que l'on mesure la conductance différentielle permettait de comprendre cette structure en lobe. Lorsque le canal interne est transmis la dépendance de la visibilité en fonction du bias devient monotone : on explique très bien ce résultat en tenant compte du couplage entre canal externe et canal interne. Dans un deuxième temps nous avons étudié la dépendance en température de la visibilité sur des MZI de différentes tailles, avons extrait pour la première fois une mesure de la longueur de cohérence de phase en régime Hall quantique à $\nu = 2$ égale à $20\mu m$ à 20mK et avons montré que $l_\varphi \sim 1/T$. Nous nous sommes ensuite intéressés à l'origine de cette longueur finie de cohérence de phase. Nous avons montré que les fluctuations thermiques du canal interne combinées au couplage entre canal interne et externe étaient la source de décohérence. Enfin dans une troisième expérience, nous avons obtenu la première réalisation expérimentale quantitative d'un objet largement utilisé en théorie : la "sonde en tension". Nous avons contrôlé le couplage de l'interféromètre vers

le contact de sonde grâce à une grille de sonde. Nous avons suivi la variation de la phase générée par un état localisé à proximité de cette grille. Enfin, des mesures de bruit nous ont permis de confirmer la relaxation en énergie dans un contact ohmique flottant. Toutes ces experiences s'incrivent dans un contexte plus général : de l'utilisation des états de bord de l'effet Hall quantique pour des expériences d'information quantique.

10.2   Abstract

This work is devoted to the study of decoherence process in the integer quantum Hall regime. This regime is reached by applying a strong magnetic field perpendicular to a bidimensional electron gas created at the interface between GaAs and AlGaAs. Current is then carried by one dimensional chiral edge channel. These electronic beams are then controlled with mesoscopic beam splitters, the quantum point contacts (QPC). A precise tuning of these QPC enable us to obtain interferences of the conductance. Then, oscillations are revealed sweeping the magnetic field or modifying the area defined by the two arms of the interferometer called Mach Zehnder interferometer (MZI). The study of the oscillations visibility as a function of the bias and the temperature enable us to probe the coherence of the system. Most of our results have been obtained at filling factor $\nu = 2$, with two edge states.

In a first part, we have studied the visibility in function of the bias when the inner edge state is reflected and have observed a lobe structure. We have shown that for a single side lobe, a Gaussian phase averaging combined with the fact that we measure the differential conductance can explain this lobe structure. When the inner edge state is transmitted, the visibility decreases monotonously in function of the bias : we have shown that it resulted from coupling between the inner and outer edge state. In a second part, we have studied temperature dependence of the visibility of different sizes MZI, and have extracted for the first time a measurement of the coherence length in the quantum Hall regime at $\nu = 2$ equal to $20\mu m$ at 20 mK and have shown that $l_\varphi \sim 1/T$. We were interested then in the origin of this finite coherence length. We have shown that thermal fluctuations of the inner edge state combined with the coupling between the inner and outer edge state were the source of decoherence. In a last experiment, we have achieved the first experimental realization of the theoretically widely used voltage probe. We have controlled the coupling between the interferometer and the voltage probe via a gate probe. We have followed the phase shift generated by a localized sate close to the probe gate. Then, noise measurements have enable us to confirm that energy relaxation occurred in a floating ohmic contact. All these experiments proceed from a more general study : the use of the edge states in the quantum Hall regime for quantum information experiments.

Annexe A

The Landauer Buttiker formalism

In this part we are going to calculate first the conductance in a 1D and ballistic system, between two reservoirs with a chemical potential difference equal to eV. If we now introduce an impurity between the two reservoirs, the Landauer Buttiker formalism provides a powerful tool to model it : the scattering matrix. We will see that each electron has a certain probability to be reflected and transmitted through. In the case of a multimode system, the scattering matrix is composed of several inputs and outputs with different transmission and reflection coefficients for each mode. We will see that in a 2D system the number of transmitted modes depends on the width of the conductor.

A.1 Quantum of conductance
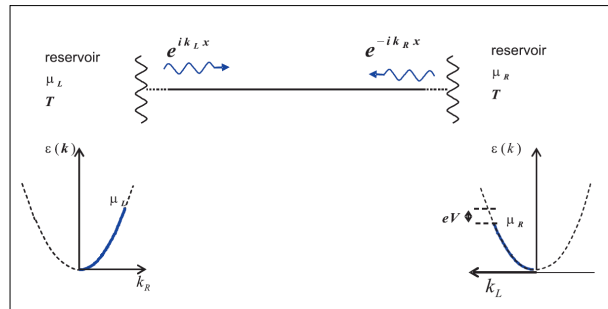
FIGURE A.1 – Ideal 1D wire : electrons from the left(right) reservoir are emitted at the chemical potential $\mu_L(\mu_R)$ with $\mu_L=\mu_R+$eV.

We consider a simple mesoscopic system : two reservoirs that inject electrons in a 1D system (cf. figure A.2). The left (right) reservoir is set to the chemical potential μ_L (μ_R) with $\mu_L=\mu_R+$eV. The injected wave function can be written : $\varphi_k=\frac{1}{\sqrt{L}}e^{ikx}$. The associated energy is $\varepsilon_k=\frac{\hbar k_n^2}{2m}$ where $k_n=\frac{2\pi n}{L}$ and L the length of the wire. To calculate the current

from the left to the right, we also need to know the density of states D(ε). The number of available states for such a system is given by (no spin) :

$$N_{states} = \frac{\Delta k}{2\pi/L} = \frac{\partial k}{\partial \varepsilon} \frac{\Delta E}{2\pi/L}$$

so :

$$D(\varepsilon) = \frac{N_{states}}{\Delta E \times L} = \frac{1}{2\pi \frac{\partial \varepsilon}{\partial k}} = \frac{1}{2\pi \upsilon(k)}$$

where $\upsilon(k)$ is the electronic velocity. We are interested in the injected current from the left to the right in an energy interval dε of the left reservoir :

$$dI = \frac{e\upsilon(k)}{L} D(\varepsilon) L d\varepsilon f_L(\varepsilon) = \frac{e}{h} d\varepsilon f_L(\varepsilon)$$

where $f_L(\varepsilon)$ is the Fermi-Dirac distribution of electrons in the left reservoir. We apply the same reasoning for the right reservoir. In the energy interval dε, the total current is given by :

$$dI = \frac{e}{h}(f_L(\varepsilon) - f_R(\varepsilon))d\varepsilon$$

so :

$$I = \frac{e}{h} \int (f_L(\varepsilon) - f_R(\varepsilon))d\varepsilon$$

For T$\ll T_F$(Fermi temperature), one obtains the very simple result :

$$I = \frac{e^2}{h}V$$

the conductance is then given by :

$$G = \frac{e^2}{h} \tag{A.1}$$

This result is fundamental. First it introduces a universal quantity e^2/h : the quantum of conductance. This quantity has the remarkable property to not depend on the studied system : no matter if the mobility or the density of the 2D system is different, the quantum of conductance is constant. Now it is used to determine the fine structure constant with precision that is comparable to the precision one gets from atomic physics [53]. It is also used as a practical and fundamental way to define the Ohm in metrology [61]. Moreover this result shows that even in the ideal case (no impurities), a wire has an intrinsic resistance. We now add an impurity in the wire : how does it modify formula A.1 ?

A.1.1 Landauer formula for a monomode conductor

We now consider an impurity in the wire. This impurity is going to reflect a part of the injected wave and reflected another one. We can model it by a scattering matrix S. We
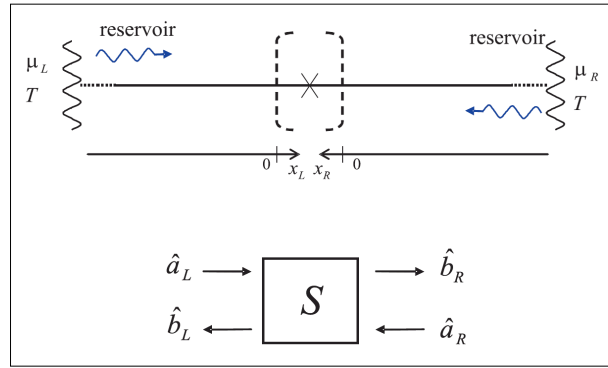
FIGURE A.2 – Schematic representation of a mesoscopic conductor, linked to reservoirs L and R. We note $\hat{a}$ amplitude of entering waves, and $\hat{b}$ exiting waves. The action of the mesoscopic conductor is modelled by a scattering matrix S that relates waves functions $\hat{a}$ to wave functions $\hat{b}$.

introduce $\hat{a}(\hat{b})$ the operators annihilation of an electron and $\hat{a}^+(\hat{b}^+$ the operators creation of an electron.

The average current [1] emitted from the left reservoir is given by [21][87] :

$$\langle \hat{I}_L \rangle = \frac{e}{h} \int d\varepsilon (\langle \hat{a}_L(\varepsilon)^+ \hat{a}_L(\varepsilon) \rangle - \langle \hat{b}_L^+(\varepsilon) \hat{b}_L(\varepsilon) \rangle)$$

We can interpret the term $\langle \hat{a}_L(\varepsilon)^+ \hat{a}_L(\varepsilon) \rangle$ as the injected current and $\langle \hat{b}_L^+(\varepsilon) \hat{b}_L(\varepsilon) \rangle)$ as the reflected one. If we replace the average values of operators by their effective values, we get for the average current :

$$I_L = \frac{e}{h} \int d\varepsilon (f_L(\varepsilon) - (|S_{L,L}(\varepsilon)|^2 f_L(\varepsilon) + |S_{L,R}(\varepsilon)|^2 f_R(\varepsilon))$$

where $S_{i,j}$ are the components of the matrix S and $f_{L,R}$ the Fermi Dirac distribution with

$$f_{L,R} = \frac{1}{1 + e^{\beta(\varepsilon - \mu_{L,R})}}$$

We distinguish in this expression three terms : $f_L(\varepsilon), |S_{L,L}(\varepsilon)|^2 f_L(\varepsilon)$ and $|S_{L,R}(\varepsilon)|^2 f_R(\varepsilon)$. $f_L(\varepsilon)$ corresponds to the current injected by the left reservoir into the system, $|S_{L,L}(\varepsilon)|^2 f_L(\varepsilon)$ is the current emitted from the left reservoir reflected by the impurities, and $|S_{L,R}(\varepsilon)|^2 f_R(\varepsilon)$ is the current from the right reservoir transmitted to the left reservoir.

Utilizing unitary properties of the matrix S [2], we can simplify the previous expression :

$$I_L = \frac{e}{h} \int d\varepsilon |S_{R,L}(\varepsilon)|^2 (f_L(\varepsilon) - f_R(\varepsilon)) \tag{A.2}$$

We set $|S_{R,L}(\varepsilon)|^2 = T(\varepsilon)$ (the transmission coefficient). Since $\mu_L = \mu_R + eV$, the conductance is equal to :

---

1. Experimentally, we measure the average current.
2. Due to the conservation of the information and of the energy during the scattering process.

$$G = \frac{I}{V} = \frac{e^2}{h} \int d\varepsilon T(\varepsilon)(-\frac{\partial f}{\partial \varepsilon})$$

For a temperature T$\ll T_F$, we obtain the fundamental relation (Landauer formula) :

$$G = \frac{e^2}{h}T(\varepsilon_F)$$

with ε_F the Fermi energy. When the conductor is perfect $T(\varepsilon_F)$=1 we find back the precedent formula *A*.1. This formula is the basis to understand electronic transport in mesosocpic physics. We will see that it can be easily generalized for a multimode systems. This formula is universal, and is applied in various systems : nanowires [17], atomic contacts [75], graphene [63] or carbon nanotubes [24].

A.1.2   2D systems

In the last part we have only considered a monomode system. Here, we treat the multimode case. The size of the scattering matrix now depends on the input and output number of modes.
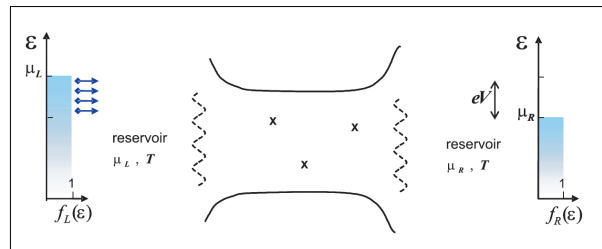
FIGURE A.3 – Schematic reprensation of a 2D reservoir. We note W_L (W_R) the left(right) reservoir width.

In the multimode case, the formula A.2 can be generalized :

$$I_L = \frac{e}{h} \int d\varepsilon(f_L(\varepsilon) - f_R(\varepsilon))Tr(S_{L,R}S_{L,R}^+)$$

where the trace is done on the different modes of the system, what can be also written :

$$I_L = \frac{e}{h} \int d\varepsilon \sum_{m=1}^{M(\varepsilon)} \{f_L(\varepsilon) + (\sum_{m'}^{M(\varepsilon)} |S_{LL,mm'}|^2 f_L(\varepsilon) + \sum_{m'}^{N(\varepsilon)} |S_{LR,mm'}|^2 f_R(\varepsilon))\}$$

We distinguish in this expression three terms : $f_L(\varepsilon)$ corresponds to electrons in the mode m injected by the left reservoir in the system. $\sum_{m'}^{M(\varepsilon)} |S_{LL,mm'}|^2 f_L(\varepsilon)$ represents electrons in the mode m' from the left reservoir reflected into the mode m by the impurities, and $\sum_{m'}^{N(\varepsilon)} |S_{LR,mm'}|^2 f_R(\varepsilon)$ represents electrons in the mode m' from the right reservoir

transmitted to the left reservoir into the mode m. We suppose that $N(\varepsilon)=M(\varepsilon)$ [3] , what simplify the general expression of the conductance :

$$G = \frac{e^2}{h} \sum_{n=1}^{N(\varepsilon)} T_n(\varepsilon)$$

where :

$$N(\varepsilon) = Int(\frac{W_L}{\lambda_F/2})$$

with W_L the left reservoir width, $T_n(\varepsilon)$ the transmittance of each mode and λ_F the Fermi length. In optics this approach would describe a wave guide : when $\lambda_F/2 > W$ the transmitted wave is evanescent. When $\lambda_F/2 = W$ a first mode can be transmitted. To transmit a second mode, one has to increase the waveguide's width until $\lambda_F = W$. In mesoscopic physics, the Quantum Point Contact(QPC) can vary the width W_L of the conductor and thus the number of transmitted modes.

---

3. In the electronic MZ, the relation $N(\varepsilon)=M(\varepsilon)$ is always verified.

Annexe B

Admittance matrix
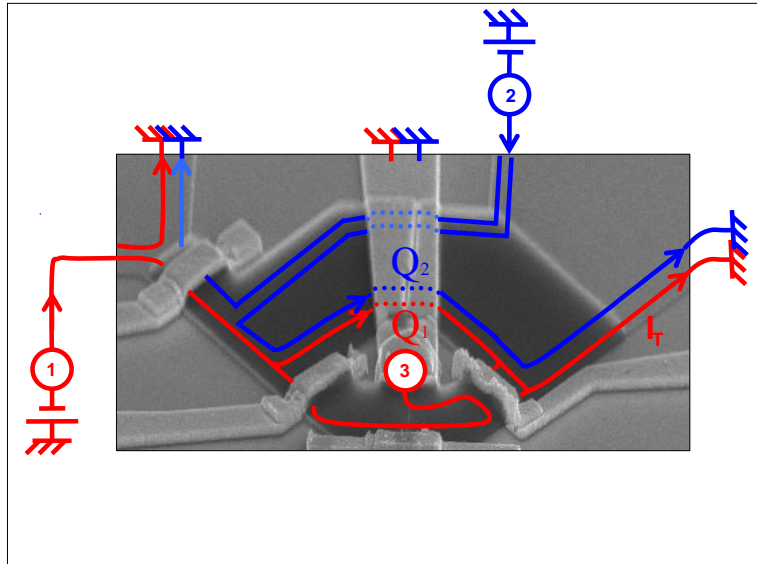
<small>FIGURE B.1 – Schematic representation of the charge injectivity : we have to consider three sources. We are interested in the charge $Q_1(Q_2)$ of the inner(outer) edge state</small>

In this part we propose the calculation of the admittance matrix $G_{12}(\omega) = dI_{1,\omega}/dV_{2,\omega}$. We concentrate on the limit $\hbar\omega \ll kT \ll E_F$. First we consider the charge density injected into the upper arm of the MZI due to a modulation of the voltage at contacts 1, 2 and 3 (the contact 3 being the inner ohmic contact connected to the mass, see also figure B.1). The charge distribution in the sample can be expressed through the Fermi-field

$$\widehat{\Psi}(\mathbf{r}, t) = \sum_{\alpha=1,2} \int \frac{dE}{\sqrt{h\nu_{\alpha,E}}} e^{-\iota E t/\hbar} \psi_\alpha(\mathbf{r}, E) \hat{a}_\alpha(E)$$

which annihilates an electron at point $\mathbf{r}$ and time t. Here $\psi_\alpha(\mathbf{r}, E)$ is a scattering state describing carriers with energy E incident from contact α. The charge density in the ring

at point $\mathbf{r}$ and time t is $\hat{\rho}(\mathbf{r},t) = e\widehat{\Psi}^\dagger(\mathbf{r},t)\widehat{\Psi}(\mathbf{r},t)$. Fourier transforming with regard to time and quantum averaging we get $\rho(\mathbf{r},t) = \langle\hat{\rho}(\mathbf{r},t)\rangle$, where

$$\rho(\mathbf{r},t) = \sum_{\alpha,\beta}\int\frac{dE}{\sqrt{\nu_{\alpha,E}\nu_{\beta,E+\hbar\omega}}}\times\psi_\alpha^*(\mathbf{r},E)\psi_\beta(\mathbf{r},E+\hbar\omega)\langle\hat{a}_\alpha(E)\hat{a}_\beta^\dagger(E+\hbar\omega)\rangle$$

The average charge may be split into an equilibrium part $\rho^{(0)}(\mathbf{r},\omega)$ and a contribution due to the external voltage $\delta\rho_\alpha(\mathbf{r},\omega)$:

$$\rho(\mathbf{r},\omega) = \rho^{(0)}(\mathbf{r},\omega) + \delta\rho_\alpha(\mathbf{r},\omega).$$

When calculating the quantum average of the charge density operator the effect of the external voltage is taken into account through the modified distribution function for charge carriers coming in from reservoir α. The distribution for contact α to linear order in the applied voltage is :

$$\langle\hat{a}_\alpha(E)\hat{a}_\beta^\dagger(E+\hbar\omega)\rangle = \delta(\hbar\omega)f_\alpha(E) + \frac{e}{h}V_{\alpha,\omega}F(E,\omega),$$

where $V_{\alpha,\omega}$ is the Fourier component to frequency ω of the voltage $V_\alpha(t)$ and $F(E,\omega)$ is defined through :

$$F(E,\omega) = \frac{f_\alpha(E) - f_\alpha(E+\hbar\omega)}{\hbar\omega}$$

When $T_0=1$ and $T_1=1/2$, the scattering states $\psi_\alpha(\mathbf{r},E)$ in the arms of the interferometer for a constant internal potential are of the form $\psi_1(\mathbf{r},E) = \psi_3(\mathbf{r},E) = \frac{\chi(\mathbf{r}_\perp)}{\sqrt{2}}exp(\iota k_E x + \iota\Phi_{up,1}(x))$ and $\psi_2(\mathbf{r},E) = \chi(\mathbf{r}_\perp)exp(\iota k_E x + \iota\Phi_{up,2}(x))$ where $\Phi_{up}(x)$ is the magnetic phase acquired going through upper arm to point x and $\chi(\mathbf{r}_\perp)$ is the transverse part of the function. We then obtain for the fluctuating part of the charge

$$\delta\rho_1(x,\omega) = \frac{e^2}{2}\int\frac{dE}{\sqrt{\nu_{1,E}\nu_{1,E+\hbar\omega}}}\times e^{\iota\omega x/\nu_E}V_{1,\omega}F(E,\omega)$$

$$\delta\rho_2(x,\omega) = e^2\int\frac{dE}{\sqrt{\nu_{2,E}\nu_{2,E+\hbar\omega}}}\times e^{\iota\omega x/\nu_E}V_{2,\omega}F(E,\omega)$$

$$\delta\rho_3(x,\omega) = \frac{e^2}{2}\int\frac{dE}{\sqrt{\nu_{3,E}\nu_{3,E+\hbar\omega}}}\times e^{\iota\omega x/\nu_E}V_{3,\omega}F(E,\omega)$$

To find the total charge $Q_{up,\alpha}^e(\omega)$ into upper arm of the MZI we integrate over the lenght of the arm $Q_{up,\alpha}^e(\omega) = \int_0^{L_{up}}dx\delta\rho_\alpha(x,\omega)$. Performing the integration we get :

$$Q_{up,1}^e(\omega) = \frac{e^2}{2h}\int dEF(E,\omega)(\frac{\iota}{\omega})(1 - e^{\iota\omega\tau})V_{1,\omega}$$

$$Q_{up,2}^e(\omega) = \frac{e^2}{h}\int dEF(E,\omega)(\frac{\iota}{\omega})(1 - e^{\iota\omega\tau})V_{2,\omega}$$

$$Q^e_{up,3}(\omega) = \frac{e^2}{2h} \int dE F(E,\omega)(\frac{\iota}{\omega})(1 - e^{\iota\omega\tau})V_{3,\omega}$$

In the limit $\hbar\omega/kT \ll 1$ we have $\int dE F(E,\omega) \sim 1$. We can rewrite the charge as $Q^e_{up,\alpha}(\omega) = e^2\nu_{up\alpha}(\omega)V_{\alpha,\omega}$ where we have introduced the injectivity $\nu_{up\alpha}(\omega)$, defined as

$$\nu_{up1}(\omega) = \frac{\iota}{\omega}\frac{1}{2h}(1 - e^{\iota\omega\tau})$$

$$\nu_{up2}(\omega) = \frac{\iota}{\omega}\frac{1}{h}(1 - e^{\iota\omega\tau})$$

$$\nu_{up3}(\omega) = \frac{\iota}{\omega}\frac{1}{2h}(1 - e^{\iota\omega\tau})$$

In the dephasing type experiments $V_1(\omega)=V_3(\omega)=0$, while $V_2(\omega)$ is varying. One finally obtains :

$$Q^e_{up,1}(\omega) = Q^e_{up,3}(\omega) = 0$$

$$Q^e_{up,2}(\omega) = e^2\nu_{up2}(\omega)V_2(\omega)$$

Now if interactions are taken into account, the excess injected charge will induce a shift in the effective internal potential, which in turn gives rise to a screening charge. This screening charge is proportional to the internal potential $eu_{up}(\omega)$ and to the total charge density available for screening $\nu_{up}(\omega)$. Thus $Q^s_{up,1}(\omega) = -e^2u_{up,1}(\omega)(\nu_{up1}(\omega) + \nu_{up3}(\omega))$ and $Q^s_{up,2}(\omega) = -e^2u_{up,2}(\omega)\nu_{up2}(\omega)$. One finally obtains for the total charge in region 1 et 2 :

$$Q^{tot}_{up,1}(\omega) = \frac{\iota}{\omega}\frac{e^2}{h}(1 - e^{\iota\omega\tau})(-U_1(\omega))$$

$$Q^{tot}_{up,2}(\omega) = \frac{\iota}{\omega}\frac{e^2}{h}(1 - e^{\iota\omega\tau})(V_2(\omega) - U_2(\omega))$$

Moreover $Q^{tot}_{up,1}(\omega)$ and $Q^{tot}_{up,2}(\omega)$ are related to the potential difference via the relation :

$$Q^{tot}_{up,1}(\omega) = -Q^{tot}_{up,2}(\omega) = C(U_1(\omega) - U_2(\omega))$$

which gives three relations for $Q^{tot}_{up,2}(\omega)$:

$$Q^{tot}_{up,2}(\omega) = C(U_2(\omega) - U_1(\omega))$$

$$Q^{tot}_{up,2}(\omega) = \frac{\iota}{\omega}\frac{e^2}{h}(1 - e^{\iota\omega\tau})(V_2(\omega) - U_2(\omega))$$

$$Q^{tot}_{up,2}(\omega) = \frac{\iota}{\omega}\frac{e^2}{h}(1 - e^{\iota\omega\tau})U_1(\omega)$$

From these relations we can extract $Q^{tot}_{up,2}(\omega)$ in function of $V_2(\omega)$.

$$Q^{tot}_{up,2}(\omega) = -V_2(\omega)\frac{C\frac{\iota}{\omega}\frac{e^2}{h}(1 - e^{\iota\omega\tau})}{2C + \frac{\iota}{\omega}\frac{e^2}{h}(1 - e^{\iota\omega\tau})}$$

The current in the arm 1 is given by $I_{1,\omega} = \iota\omega Q_{up,2}^{tot}(\omega)$. We finally obtain :

$$G_{12} = \frac{dI_1(\omega)}{dV_2(\omega)} = \frac{G_Q(1 - e^{\iota\omega\tau})}{2 + \iota G_Q(1 - e^{\iota\omega\tau})/(\omega C)}$$

with $G_Q = e^2/h$.

Annexe C

Expression of U_1 in function of V_2

C.1 Notations
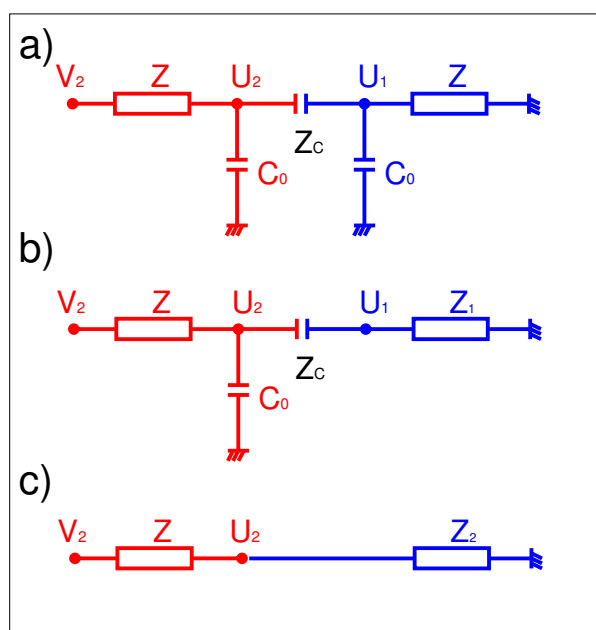
FIGURE C.1 – (a) Schematic representation of the self dephasing process via the introduction of tow capacitance for each edge state. (b) Simplification of the previous representation by the introduction of the impedance Z_1. (c) Simplification of the previous representation by the introduction of the impedance Z_2

As represented in figure C.1(a,b,c) we are going to introduce the two impedances Z_1 and Z_2 given by :

$$Z_1 = \frac{Z_0 Z}{Z_0 + Z}$$

with $Z_0 = \frac{i\omega}{C_0}$.

$$Z_2 = \frac{Z_0(Z_C + Z_1)}{Z_0 + Z_C + Z_1}$$

We can now express U_2 and U_1 in function of these impedances :

$$U_1 = \frac{Z_1 U_2}{Z_1 + Z_C}$$

$$U_2 = \frac{Z_2 V_2}{Z_2 + Z}$$

Thus :

$$U_1 = \frac{Z_1}{Z_1 + Z_C} \frac{Z_2 V_2}{Z_2 + Z}$$

We want to express the previous expression in function of Z, Z_C and Z_0.

$$U_1 = \frac{Z_0 Z_1 V_2}{(Z_0 + Z_C + Z_1)(Z_2 + Z)}$$

$$U_1 = \frac{Z_0 Z_1 V_2}{(Z_0(Z_C + Z_1) + Z(Z_0 + Z_C + Z_1)}$$

$$U_1 = \frac{V_2}{2 + \frac{Z_C}{Z} + \frac{1}{Z_0}(2Z_C + 2Z + \frac{Z_C Z}{Z_0})}$$

C.2   Low frequency limit

We introduce the parameters $\alpha = C_0/C$ and $\gamma = C/C_Q = C/(G_Q\tau)$. We start from the expression of U_1 in function of V_2 :

$$U_1 = \frac{V_2}{2 + \frac{Z_C}{Z} + \frac{1}{Z_0}(2Z_C + 2Z + \frac{Z_C Z}{Z_0})}$$

In the limit of low frequency we have :

$$\frac{Z_C}{Z} = \frac{G_Q\tau}{C} = \gamma^{-1}$$

$$\frac{Z_C}{Z_0} = \frac{C_0}{C} = \alpha$$

$$\frac{Z}{Z_0} = \frac{C_0}{G_Q\tau} = \alpha\gamma$$

So U_1 becomes :

$$U_1 = \frac{V_2}{2 + \gamma^{-1} + \alpha(2 + 2\gamma + \alpha\gamma)}$$

C.3 Expression of $< \delta\varphi^2 > /2$

We introduce $R(\omega)$ given by :

$$R(\omega) = 2 + \frac{Z_C}{Z} + \frac{1}{Z_0}(2Z_C + 2Z + \frac{Z_C V}{Z_0})$$

We are interested in $\mid R(\omega) \mid^2$:

$$\mid R(\omega) \mid^2 = \mid 2 + \frac{i}{C\omega}G_Q(1 - e^{i\omega\tau}) + \frac{2C_0}{C} + \frac{2C_0\omega}{jG_Q(1 - e^{i\omega\tau})} + \frac{2C_0^2\omega}{jCG_Q(1 - e^{i\omega\tau})}$$

$$\mid R(\omega) \mid^2 = \mid 2(1 + \frac{2C_0}{C}) + \frac{2G_Q e^{i\omega\tau/2}}{C\omega}sin(\omega\tau/2) + \frac{e^{-i\omega\tau/2}}{sin(\omega\tau/2)}(\frac{\omega C_0}{G_Q} + \frac{\omega C_0^2}{2CG_Q}) \mid^2$$

We introduce :

$$A = 2(1 + \frac{2C_0}{C})$$

$$B = \frac{2G_Q}{\omega C}$$

$$C = \frac{\omega C_0}{G_Q}(1 + \frac{C_0}{2C})$$

Thus $\mid R(\omega) \mid^2$ becomes :

$$\mid R(\omega) \mid^2 = \mid A + B\frac{e^{i\omega\tau/2}}{sin(\omega\tau/2)} + C\frac{e^{-i\omega\tau/2}}{sin(\omega\tau/2)} \mid^2$$

or :

$$\mid R(\omega) \mid^2 = A^2 + B^2 sin^2(\omega\tau/2) + AB sin(\omega\tau) + 2AC cotg(\omega\tau/2) + \frac{C^2}{sin^2(\omega\tau/2)} + 2BC cos(\omega\tau)$$

The new expression of V_φ is :

$$V_\varphi^{-1} = \frac{4e}{\hbar}\int_0^\infty d\omega \frac{sin^2(\omega\tau/2)}{\mid R(\omega) \mid^2 \omega^2}$$

We set $x = \omega\tau/2$ and obtain :

$$V_\varphi^{-1} = \frac{2e\tau}{\hbar}\int_0^\infty dx f(x)$$

with :

$$f(x) = \frac{\gamma^2 sin^2(x)}{4\gamma^2 x^2(1+\alpha)^2 + 2\gamma x sin(2x)(1+\alpha) + sin^2(x) + 8(1+\alpha)(1+\alpha/2)\alpha\gamma^3 x^3 cotg(x)}{+4\alpha^2\gamma^4 x^4(1+\alpha/2)^2\frac{1}{sin^2(x)} + 4\alpha\gamma^2 x^2 cos(2x)(1+\alpha/2)}$$

$$\text{(C.1)}$$

Bibliographie

[1] S. Adashi. Gaas and related materials. *World Scientific*, 1994.

[2] Y. Aharonov and D. Bohm. Significance of electromagnetic potentials in the quantume theory. *Phys. Rev.*, 115 :485, 1959.

[3] I.L. Aleiner, Ned.S. Wingreen, and Y. Meir. Dephasing and the orthogonality catastrophe in tunneling through a quantum dot : The which path ? interferometer. *Phys. Rev.Lett*, 79 :3740, 1997.

[4] B.W. Alphenaar, P.L. McEuen, R. G. Wheeler, and R. N. Sacks. Selective equilibration among the current-carrying states in the quantum hall regime. *Phys. Rev. Lett.*, 64 :677, 1990.

[5] B. L. Altshuler, A. G. Aronov, and D. E. Khmelnitsky. Edge states, transmission matrices, and the hall resistance. *J. Phys. C*, 15 :7367, 1982.

[6] T. Ando, A.B. Fowler, and F. Stern. *Rev.Mod.Phys.*, 54 :437, 1990.

[7] N.W. Ashcroft and N.D. Mermin. Solid state physics. *Holt, Rinehart and Winston, New York*, 1976.

[8] R.C. Ashoori, H.L. Stormer, L. N. Pfeiffer, K. W. Baldwin, and K. W. West. Edge magnetoplasmons in the time domain. *Phys. Rev. B.*, 45 :3894, 1992.

[9] A. Aspect, P. Grangier, and G. Roger. Experimental test of bell's inequalities using time- varying analyzers. *Phys. Rev. Lett.*, 49 :91, 1982.

[10] D.V. Averin and E.V. Sukhorukov. Counting statistics and detector properties of quantum point contacts. *Phys. Rev. Lett.*, 95 :126803, 2005.

[11] S.E. Barrett, G. Dabbagh, L.N. Pfeiffer, K. W. West, and R. Tycko. Optically pumped nmr evidence for finite-size skyrmions in gaas quantum wells near landau level filling $\nu = 1$. *Phys. Rev. Lett.*, 74 :5112, 1995.

[12] C.W. Beenakker. Edge channels for the fractional quantum hall effect. *Phys. Rev. Lett.*, 64 :216, 1990.

[13] J.S. Bell. On the einstein podolsky rosen paradox. *Physics*, 1 :195, 1964.

[14] P. Bertet. A complementarity experiment with an interferometer at the quantum-classical boundary. *Nature*, 411 :166, 2001.

[15] E. Bieri, M. Weiss, O. Goktas, M. Hauser, C. Schonenberger, and S. Oberholzer. Large unexpected visibility enhancement in an electronic mach-zehnder interferometer. *Phys. Rev. B*, 79 :24, 2009.

[16] J.P. BIRD, K. ISHIBASHI, M. STOPA, Y. AOYAGI, and T. SUGANO. Coulomb blockade of the aharonov-bohm effect in gaas/alxga1-xas quantum dots. *Phys. Rev. B*, 50 :14983, 1994.

[17] M. BRANDBYGE, J. SCHIOTZ, M. R. SORENSEN, P. STOLTZE, K. W. JACOBSEN, J. K. NORSKOV, L. OLESEN, E. LAEGSGAARD, I. STENSGAARD, and F. BESENBACHER. Quantized conductance in atom-sized wires between two metals. *Phys. Rev. B*, 52 :8499, 1995.

[18] C. BUIZERT, F.H.L. KOPPENS, M. PIORO-LADRIERE, I.T. VINK, S. TARUCHA, W. WEGSCHEIDER, and L.M.K. VANDERSYPEN. In situ reduction of charge noise in gaas/alxga1-xas schottky-gated devices. *Cond.Mat.*, 0808.0465, 2008.

[19] E. BUKS, R. SCHUSTER, M. HEIBLUM, D. MAHALU, and V. UMANSKY. Dephasing in electron interference by a which path detector. *Nature*, 391 :871, 1998.

[20] M. BUTTIKER. Role of quantum coherence in series resistors. *Phys. Rev. B*, 33 :3020, 1986.

[21] M. BUTTIKER. Scattering theory of current and intensity noise correlations in conductors and wave guides. *Phys. Rev. B*, 46 :12485, 1992.

[22] M. BUTTIKER, A. PRETRE, and H. THOMAS. Dynamic conductance and the scattering matrix of small conductors. *Phys. Rev. Lett.*, 70 :4114, 1993.

[23] J.T. CHALKER, Y. GEFEN, and M. Y. VEILLETTE. Decoherence and interactions in an electronic mach-zehnder interferometer. *Phys. Rev. B*, 76 :085320, 2007.

[24] L. CHICO, L.X. BENEDICT, S.G. LOUIE, and M.L. COHEN. Quantum conductance of carbon nanotubes with defects. *Phys. Rev. B*, 76 :2600, 1996.

[25] V. S. W. CHUNG, P. SAMUELSSON, and M. BUTTIKER. Visibility of current and shot noise in electrical mach-zehnder and hanbury brown twiss interferometers. *Phys. Rev. B.*, 72 :125320, 2005.

[26] D.C. DIXON, K.R. WALD, P.L. MCEUEN, and M.R. MELLOCH. Dynamic nuclear polarization at the edge of a two dimensional electron gas. *Phys. Rev. B*, 56 :4743, 1997.

[27] A. EINSTEIN, B. PODOLSKY, and N. ROSEN. Can quantum-mechanical description of physical reality be considered complete ? *Phys. Rev.*, 47 :777, 1935.

[28] J.P EISENSTEIN, H.L. STORMER, V. NARAYANAMURTI, A. Y. CHO, A.C. GOSSARD, and C.W. TU. Density of states and de haasvan alphen effect in two-dimensional electron systems. *Phys. Rev.Lett.*, 55 :875, 1985.

[29] M. FERRIER, L. ANGERS, A.C.H. ROWE, S. GUÉRON, H. BOUCHIAT, C. TEXIER, G. MONTAMBAUX, and D. MAILLY. Direct measurement of the phase-coherence length in a gaas/gaalas square network. *Phys. Rev.Lett.*, 93 :246804, 2004.

[30] D.K. FERRY and R.O. GRONDIN. Direct measurement of the phase-coherence length in a gaas/gaalas square network. *Plenum Press, New York*, 1991.

[31] G. Feve, A. Mahe, J.M. Berroir, T. Kontos, B. Placais, D.C. Glattli, A. Cavanna, B. Etienne, and Y.Jin. An on-demand coherent single electron source. *Science*, 316 :1169, 2007.

[32] H. Forster and P. Samulessonand M. Buttiker. Current voltage correlations in interferometers. *New Journal of Phys.*, 9 :117, 2007.

[33] H. Forster, P. Samulesson, S. Pilgram, and M. Buttiker. Voltage and dephasing probes : a full counting statistics discussion. *Phys. Rev. B*, 75 :035340, 2007.

[34] A. Fuhrer, P. Brusheim, T. Ihn, M. Sigrist, K. Ensslin, W. Wegscheider, and M. Bichler. Fano effect in a quantum-ring-quantum-dot system woth tunable coupling. *Phys. Rev. B*, 73 :205326, 2006.

[35] A. E. Hansen, A. Kristensen , S. Pedersen, C. B. Sørensen, and P. E. Lindelof. Mesoscopic decoherence in aharonov-bohm rings. *Phys. Rev. B.*, 64 :045327, 2001.

[36] J.Gabelli, G. Feve, J.M. Berroir, B. Placais, A. Cavanna, B. Etienne, Y.Jin, and D.C. Glattli. Violation of kirchhoff's laws for a coherent rc circuit. *Science*, 313 :499, 2006.

[37] Y. Ji, Y. Chung, D. Sprinzak, M. Heiblum, D. Mahalu, and H. Shtrikman. An electronic mach-zehnder interferometer. *Nature*, 422 :415, 2003.

[38] C. Kittel. Introduction to solid state physics. *John Wiley and Sons,New York*, 1976.

[39] K.v. Klitzing, G. Dorda, and M. Pepper. New method for high-accuracy determination of the fine-structure constant based on quantized hall resistance. *Phys. Rev. Lett.*, 45 :494, 1980.

[40] A. Kumar, L. Saminadayar, D.C. Glattli, Y. Jin, and B. Etienne. Experimental test of the quantum shot noise reduction theory. *Phys. Rev. Lett.*, 76 :2778, 1996.

[41] Ç. Kurdak, A.M. Chang, A. Chin, and T. Y. Chang. Quantum interference effects and spin-orbit interaction in quasi-one-dimensional wires and rings. *Phys. Rev. B*, 46 :6846, 1992.

[42] R.B. Laughlin. Anomalous quantum hall effect : An incompressible quantum fluid with fractionally charged excitations. *Phys. Rev. Lett.*, 50 :1395, 1983.

[43] I.P. Levkivskyi and E.V. Sukhorukov. Dephasing in the electronic mach-zehnder interferometer at filling factor 2. *Phys. Rev. B*, 78 :045322, 2008.

[44] L.V. Litvin, A. Helzel, H.P. Tranitz, W. Wegscheider, and C. Strunk. Edge channel interference controlled by landau level filling. *Phys. Rev. B*, 78 :075303, 2008.

[45] L.V. Litvin, H.P. Tranitz, W. Wegscheider, and C. Strunk. Decoherence and single electron charging in an electronic mach-zehnder interferometer. *Phys. Rev. B*, 75 :033315, 2007.

[46] A.H. MacDonald. Mesosopic quantum physics. *E.Akkermans, G.Montambaux, J.L.Pichard and J.Zinn-Justin ed., Elsevier Science, Amsterdam*, 1994.

[47] L. Mach. *Z. Instrumentenkunde*, 12 :89, 1892.

[48] T. Machida, H. Hirai, S. Komiyama, T. Osada, and Y. Shiraki. Experimental studies of the phase coherence in the quantum hall effect regime. *Sol. Sta. Com.*, 103 :441, 1997.

[49] F. Marquardt and C. Bruder. Effects of dephasing on shot noise in an electronic mach -zehnder interferometer. *Phys. Rev. B*, 70 :125305, 2004.

[50] F. Marquardt and C. Bruder. Influence of dephasing on shot noise in an electronic mach-zehnder interferometer. *Phys. Rev. Lett*, 92 :056805, 2004.

[51] T. Martin and S. Feng. Suppression of scattering in electron transport in mesoscopic quantum hall systems. *Phys. Rev. Lett.*, 64 :1971, 1990.

[52] T. Martin and R. Landauer. Wave-packet approach to noise in multichannel mesoscopic systems. *Phys. Rev. B*, 45 :1742, 1992.

[53] P.J. Mohr and B.N. Taylor. Codata recommended values of the fundamental physical constants : 2002. *Rev. Mod. Phys.*, 77 :1, 2005.

[54] N.Bohr. Can quantum-mechanical description of physical reality be considered complete ? *Phys. Rev.*, 48 :696, 1935.

[55] I. Neder and E. Ginossar. The behavior of electronic interferometers in the nonlinear regime. *Phys. Rev. Lett.*, 100 :196806, 2008.

[56] I. Neder, M. Heiblum, Y. Levinson, D. Mahalu, and V. Umansky. Coherence and phase in an electronic mach-zehnder interferometer : An unexpected behavior of interfering electrons. *arXiv*, page 0508024, 2005.

[57] I. Neder, M. Heiblum, Y. Levinson, D. Mahalu, and V. Umansky. Unexpected behavior in a two-path electron interferometer. *Phys. Rev. Lett*, 96 :016804, 2006.

[58] I. Neder, M. Heiblum, D. Mahalu, and V. Umansky. Entanglement, dephasing, and phase recovery via cross-correlation measurements of electrons. *Phys. Rev. Lett*, 98 :036803, 2007.

[59] I. Neder, F. Marquardt, M. Heiblum, D. Mahalu, and V. Umansky. Controlled dephasing of electrons by non-gaussian shot noise. *Nature Physics*, 3 :534, 2007.

[60] I. Neder, N. Ofek, Y. Chung, M. Heiblum, D. Mahalu, and V. Umansky. Interference between two indistinguishable electrons from independent sources. *Nature*, 448 :333, 2007.

[61] K.S. Novoselov, Z. Jiang, Y. Zhang, S.V. Morozov, H.L. Stormer, U. Zeitler, J.C. Maan, G.S. Boebinger, P. Kim, and A.K. Geim. Room-temperature quantum hall effect in graphene. *Sience*, 315 :1379, 2008.

[62] S. Oberholzer, E. Bieri, C. Schönenberger, M. Giovannini, and J. Faist. Positive cross correlations in a normal-conducting fermionic beam splitter. *Phys. Rev. Lett.*, 96 :046804, 2006.

[63] N.M.R. Peres, A.H. Castro Neto, and F. Guinea. Conductance quantization in mesoscopic graphene. *Phys. Rev. B.*, 76 :195411, 2006.

[64] S. Pilgram, P. Samulesson, H. Forster, and M. Buttiker. Full-counting statistics for voltage and dephasing probes. *Phys. Rev. Lett.*, 97 :066801, 2006.

[65] A. Pretre, H. Thomas, and M. Buttiker. Dynamic admittance of mesoscopic conductors : Discrete potential model. *Phys. Rev. B*, 54 :8130, 1996.

[66] D. Rohrlich, O. Zarchin, M. Heiblum, D. Mahalu, and V. Umansky. Controlled dephasing of a quantum dot : From coherent to sequential tunneling. *Phys. Rev. Lett.*, 98 :096803, 2007.

[67] B. Rosenow and B.I. Halperin. Influence of interactions on flux and back-gate period of quantum hall interferometers. *Phys. Rev. Lett.*, 98 :106801, 2007.

[68] P. Roulleau, F. Portier, P. Roche, A. Cavanna, G. Faini, U. Gennser, and D. Mailly. Finite bias visibility of the electronic mach-zehnder interferometer. *Phys. Rev. B*, 76 :161309, 2007.

[69] P. Roulleau, F. Portier, P. Roche, A. Cavanna, G. Faini, U. Gennser, and D. Mailly. Direct measurement of the coherence length of edge states in the integer quantum hall regime. *Phys. Rev. Lett*, 100 :126802, 2008.

[70] P. Roulleau, F. Portier, P. Roche, A. Cavanna, G. Faini, U. Gennser, and D. Mailly. Noise dephasing in the edge states of the integer quantum hall regime. *Phys. Rev. Lett*, 101 :186803, 2008.

[71] P. Roulleau, F. Portier, P. Roche, A. Cavanna, G. Faini, U. Gennser, and D. Mailly. Tuning decoherence with a voltage probe. *Phys. Rev. Lett.*, 102 :236802, 2009.

[72] L. Saminadayar, D.C. Glattli, Y. Jin, and B. Etienne. Observation of the e/3 fractionally charged laughlin quasiparticle. *Phys. Rev. Lett.*, 79 :2526, 1997.

[73] P. Samuelsson, E.V. Sukhorukov, and M. Buttiker. Orbital entanglement and violation of bell inequalities in mesoscopic conductors. *Phys. Rev. Lett.*, 91 :157002, 2003.

[74] P. Samuelsson, E.V. Sukhorukov, and M. Buttiker. Two particle aharonov bohm effect and entanglement in the electronic hanbury brown twiss setup. *Phys. Rev. Lett.*, 92 :026805, 2004.

[75] E. Scheer, P. Joyez, D. Esteve, C. Urbina, and M.H. Devoret. Conduction channel transmissions of atomic-size aluminum contacts. *Phys. Rev. Lett.*, 78 :3535, 1997.

[76] G. Seelig and M. Büttiker. Charge fluctuation-induced dephasing in a gated mesoscopic interferometer. *Phys. Rev. B*, 64 :245313, 2001.

[77] D. Sprinzak, E. Buks, M. Heiblum, and H. Shtrikman. Controlled dephasing of electrons via a phase sensitive detector. *Phys. Rev. Lett.*, 84 :5820, 2000.

[78] A. Stern, Y. Aharonov, and Y. Imry. Phase uncertainty and loss of interference : A general picture. *Phys. Rev. A.*, 41 :3436, 1990.

[79] E.V. Sukhorukov and V.V. Cheianov. Resonant dephasing in the electronic mach-zehnder interferometer. *Phys. Rev. Lett.*, 99 :156801, 2007.

[80] C. Texier and M. Buttiker. Effect of incoherent scattering on shot noise correlations in the quantum hall regime. *Phys. Rev. B*, 62 :7454, 2000.

[81] W.G. van der Wiel, Y.V. Nazarov, S. D. Franceschi, T. Fujisawa, J. M. Elzerman, E. W. G. M. Huizeling, S. Tarucha, and L. P. Kouwenhoven. Electromagnetic aharonov-bohm effect in a two-dimensional electron gas ring. *Phys. Rev. B*, 67 :033307, 2003.

[82] B.J. van Wees, L.P. Kouwenhoven, C. J. Harmans, J. G. Williamson, C. E. Timmering, M. E. Broekaart, C. T. Foxon, and J. J. Harris. Observation of zero-dimensional states in a one-dimensional electron interferometer. *Phys. Rev. Lett.*, 62 :2523, 1989.

[83] B.J. van Wees, H. van Houten, C. W. Beenaker, J. G. Williamson, L. P. Kouwenhoven, D. van der Marel, and C. T. Foxon. Quantized conductance of point contacts in a two-dimensional electron gas. *Phys. Rev. Lett.*, 60 :848, 1988.

[84] R.A. Webb, S. Washburn, C. P. Umbach, and R. B. Laibowitz. Observation of h / e aharonov-bohm oscillations in normal-metal rings. *Phys. Rev. Lett.*, 54 :2696, 1985.

[85] D.A. Wharam, T.J. Thornton, R. Newbury, M. Pepperand J.E.F. Frost, D.G. Peacock, D.A.Ritchie, and G.A.C.Jones. One-dimensional transport and the quantisation of the ballistic resistance. *J. Phys. C : Solid State Phys*, 21 :L209–L214, 1988.

[86] I. Yang, W. Kang, L. N. Pfeiffer, K. W. Baldwin, K. W. West, E.-A. Kim, and E. Fradkin. Quantum hall line junction with impurities as a multislit luttinger liquid interferometer. *Phys. Rev. B.*, 71 :113312, 2005.

[87] Y.M.Blanter and M.Buttiker. Shot noise in mesoscopic conductors. *Phys. Rep.*, 1 :336, 2000.

[88] S.C. Youn, H.W. Lee, and H.S. Sim. Nonequilibrium dephasing in an electronic mach-zehnder interferometer. *Phys. Rev. Lett. 100*, 100 :196807, 2008.

[89] L. Zehnder. *Z. Instrumentenkunde*, 11 :275, 1891.